Emergent phenomena in frustrated spin systems

Zur Erlangung des akademischen Grades eines

DOKTORS DER NATURWISSENSCHAFTEN

von der Fakultät für Physik

des Karlsruher Instituts für Technologie

genehmigte

DISSERTATION

von

Dipl.-Phys. Bhilahari Jeevanesan

Tag der mündlichen Prüfung: 05. Februar 2016

Referent: Prof. Dr. J. Schmalian
Korreferent: Prof. Dr. A. Shnirman

List of publications

1. Bhilahari Jeevanesan and Peter P. Orth, *Classical ground states of Heisenberg and XY antiferromagnets on the windmill lattice*, Phys. Rev. B 90, 144435, October 2014

2. Bhilahari Jeevanesan, Premala Chandra, Piers Coleman, and Peter P. Orth, *Emergent Power-Law Phase in the 2D Heisenberg Windmill Antiferromagnet: A Computational Experiment*, Phys. Rev. Lett. 115, 177201, October 2015

3. Karim Mnasri, Bhilahari Jeevanesan, and Jörg Schmalian, *Critical phenomena in hyperbolic space*, Phys. Rev. B 92, 134423, October 2015

Contents

Chapter 1

Introduction

The concept of frustration lies at the core of many emergent phenomena in condensed matter physics. Frustrated spin systems, in particular, host many surprising low-energy phenomena that have been uncovered over the years and that are not immediately obvious by looking at the microscopic degrees of freedom. Instead, these effects appear through the cooperative interplay of many degrees of freedom. Thus frustrated spin systems provide opportunities for the development of interesting models, which may turn out to have implications for experimentally realizable systems.

An instance of this paradigm is provided by the J_1-J_2 Heisenberg model [12]. This is a *geometrically frustrated* system of spins with nearest and next-nearest neighbor couplings on two sublattices. A spin model is called geometrically frustrated, if the spins on the lattice cannot simultaneously satisfy all the interactions with their neighbors. A classic example of this is provided by the Ising model on the triangular lattice with antiferromagnetic nearest neighbor couplings, a problem that was first studied by Wannier in 1950 [104]. Consider three Ising spins on a triangular plaquette as shown in Figure 1.1. No assignment of Ising variables can simultaneously satisfy all three antiferromagnetic bonds. Two spins are bound to point in the same direction and the spin system is said to be geometrically frustrated.

In a similar vein the spins in the J_1-J_2 model cannot all satisfy their antiferromagnetic bonds, since the nearest as well as the next-nearest neighbors want to point in opposite directions. The two sublattices of the J_1-J_2 model are coupled by an interaction of strength J_1, while the spins on the individual sublattices are coupled to each other with strength J_2. In a certain range where J_2 is larger than J_1 the two sublattices are fully decoupled at zero temperature and the symmetry of the ground state manifold is described by an element of $\mathrm{O}(3)/\mathrm{O}(2) \times \mathrm{O}(3)/\mathrm{O}(2)$.

The ground state degeneracy of the J_1-J_2 model is lifted for finite temperatures by the so-called *order-by-disorder* mechanism, a phenomenon discovered by Villain [102] and Henley [35] in the late 70's and 80's. While the usual effect of thermal fluctuations is to disorder a system, these authors found that in cases where the classical ground state forms a continuous manifold of energetically degenerate configurations some of these states may be entropically favored over others. This proves to be the case in the J_1-J_2 model, where a parallel or anti-parallel relative orientation of the two sublattices is entropically favored. Thus the ground state degeneracy is broken down and is now described by an element of $\mathrm{O}(3)/\mathrm{O}(2) \times \mathrm{Z}_2$, where the Z_2 part describes the relative orientation of the second lattice with respect to the first. Thus by starting with two coupled Heisenberg models, the system generates an emergent Z_2 degree of freedom. This new degree of freedom exists on every

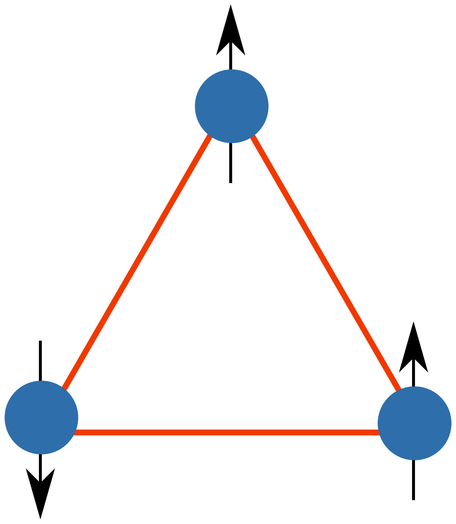

Figure 1.1: This figure shows Ising spins on the triangular lattice. The antiferromagnetic bonds between neighbors cannot be simultaneously satisfied for all three links. The model is said to be geometrically frustrated.

plaquette of the square lattice and the J_1-J_2 Heisenberg model may be said to give rise to emergent Ising degrees of freedom. In a publication of 1989 by Chandra et al. [12] the authors (CCL) showed how these degrees of freedom were capable of undergoing a phase transition. Thus at a finite temperature T_I the Ising correlation length diverges and the spins on the two square sublattices become locked relative to each other. The analysis of CCL relied on an approximate renormalization group treatment and was challenged in various numerical studies, before unambiguous proof of the correctness of their picture was provided by Weber et al. [105] in an extensive Monte Carlo study of this model.

The emergent Ising behavior found by CCL is particularly striking given the fact that according to the Mermin-Wagner theorem the microscopic Heisenberg spins themselves cannot order magnetically. Thus, despite the inability of the Heisenberg sublattices to order magnetically, their relative orientation can nevertheless develop long-range order.

An application of the CCL physics was found more than ten years later in 2000 by Melzi et al. in the compounds $Li_2VO(Si,Ge)O_4$ [57]. The authors performed NMR and magnetization measurements to show that these materials, which are well described by the J_1-J_2 model, indeed have a phase transition into collinear order. Another application of the CCL mechanism is found in the iron pnictides, where it provides an explanation for the high temperature nematic phase [23, 24].

A natural question to pose at this point is whether the CCL mechanism can be generalized to universality classes other than the Ising class. On a two-dimensional lattice the BKT phase transition comes to mind. The theory of interacting vortices developed by Berezinskii, Kosterlitz and Thouless [5, 42, 43, 44] is basically a field theory of a two-component O(2) object in the two-dimensional plane. Despite its mundanity at first sight, the model possesses an unexpected richness of phenomena. The reason for this is the fact that the low energy physics of this model has not only the usual spin-wave excitations, but also vortex excitations with different winding numbers. The latter excitations are topologically stable in two dimensions. Even in the presence of thermal fluctuations, the vortices' stability is guaranteed by the simple fact that the winding number, being a discrete quantity, cannot be changed in a continuous manner.

Of course, the physics of the BKT phase transition is not merely academic, instead, given the ubiquity of U(1) degrees of freedom, it occurs in systems such as thin superconducting films, liquid helium films and arrays of Josephson junctions.

For this reason an emergent BKT model in a system of Heisenberg spins would be a particularly striking effect. A Heisenberg spin system named the *windmill model* that might show such behavior was introduced in [72, 73]. It is one of the tasks of this thesis to provide unambiguous evidence that emergent BKT physics is indeed possible in the windmill model, which consists of a triangular- and a honeycomb-lattice.

Concerning experimental realizations, we remark that systems of cold bosonic atoms in optical lattices have been used in the past [94, 95] to investigate models of prominent frustrated magnets. These works are based on the idea that at low temperatures and for weak interactions these systems form a superfluid and the atoms at every site of the lattice have a well-defined local phase, which is a $U(1)$ degree of freedom. Thus it is possible to interpret this local phase degree of freedom as a classical planar spin. Nearest neighbor spins are coupled via tunneling of atoms between the sites. For regular tunneling of atoms between the sites, the associated coupling between the planar spins is ferromagnetic. By shaking the lattice in a periodic way, however, it is possible to add a non-zero Peierls phase to the tunneling element. In this way, it is possible to induce a change in the sign of the tunneling element which leads to an antiferromagnetic coupling between the spins. Within this approach, different links of the lattice can be addressed independently. Frustration effects have been experimentally observed on the triangular lattice via standard time-of-flight imaging [94]. Honeycomb optical lattice geometries have also been realized in the past [74, 98]. It is therefore not unreasonable to assume that the windmill lattice may be realized experimentally in the near future.

This thesis deals with frustration of two different kinds. In the first chapter we study a very fundamental kind of frustration, where an N-component $\boldsymbol{\phi}^4$ is analyzed not in regular flat space, but in hyperbolic space with a finite curvature radius R. In the latter setting, space itself frustrates spins: the volume of space surrounding a given spin grows exponentially with distance from the spin. As a consequence the correlation length has an upper bound R. Nevertheless, this system has a phase transition, that can be detected by representing the correlation function in the eigenbasis of the Laplace operator and asking when the correlation function has a scale-free form. Just at the phase transition the correlation length becomes equal to R.

With the mathematical tools that we develop in this chapter, we study certain critical exponents of this model by using a $1/N$ expansion. We find that at lowest order the critical exponents are those of three-dimensional flat space, the reason being that the saddle point equations at lowest order in $1/N$ are only defined at one point in space and are therefore oblivious to the presence of finite curvature.

The $1/N$ order correction is absent due to the finiteness of $1/R$, thus where in flat space one would have singular behavior in certain self-energy terms, in curved space these terms are regulated by the existence of a finite length scale R. Thus the critical points are in effect different from those in flat space and one can therefore conclude that an arbitrarily small value of the curvature leads to the emergence of a new fixed-point.

The following two chapters deal with the physics of a spin model that has been named the *windmill model* by the authors who introduced it [72, 73]. The name derives from the lattices' semblance to windmills once the former has been decorated by spins ordered in the 120° pattern. The lattice essentially consists of interpenetrating triangular and honeycomb lattices. In order to study the finite temperature phase diagram of this model, it is first necessary to understand the $T = 0$ phase diagram as a function of the model's coupling constants. This task is undertaken for Heisenberg and planar spins in the next chapter, where this problem is solved algorithmically by an iterative technique. This technique is a heuristic greedy algorithm and proceeds by locally minimizing the energy of randomly chosen spins. The resulting phase diagram shows the system to posses a large number of ground states. This is a consequence of the fact that the model is highly frustrated. If all couplings were ferromagnetic, the system would have a single ground state configuration, independent of the numerical value of the coupling constants, namely a trivial uniaxial order. The fact that the couplings are antiferromagnetic necessitates compromises in the spin-configurations. Thus in order to achieve a minimum total energy it is necessary for the spins to make trade-offs in nearest neighbor bonds. This leads to a large number of ground state spin-configurations, each one of which is the optimum configuration given certain values of the coupling constants, i.e. the chosen compromises are in general complicated functions of the ratios of the couplings.

Among the many phases, two are intricate non-coplanar spin-configurations. Another one of these phases is a decoupled ground-state, i.e. the triangular and the honeycomb lattice spins order by themselves, but the spins on one lattice may be globally rotated with respect to the other without incurring a cost in energy. This ground-state degeneracy gives rise to interesting physics, which is the subject of the next chapter.

The purpose of chapter 4 is to demonstrate that for Heisenberg spins this freedom in the relative orientation of the sublattices at $T = 0$ leads to emergent degrees of freedom that undergo a Berezinsky-Kosterlitz-Thouless transition. Such behavior had already been conjectured by A. M. Polyakov in a 1975 landmark paper on non-linear sigma models [75] where he suggested that an algebraically correlated phase may occur in systems of Heisenberg spins. As a way to settle this conjecture he proposed that one perform an experiment in which the non-linear sigma model is simulated by a magnetic spin system. Instead of using an experimental system, chapter 4 describes a numerical experiment that we undertook to settle this question. There it is shown unequivocally that the emergent degrees of freedom in the Heisenberg windmill model do indeed undergo a phase transition into a critical phase.

The frustration in the windmill lattice is provided by arranging the interactions in the spin system such that the spins on each triangular lattice plaquette are frustrated. In other words the bonds cannot individually minimize their energy by pointing opposite to each other. Instead they take on a 120° pattern. The order-parameter of this subsystem is an element of the group SO(3), in other words the orientation of a tripod $\{\boldsymbol{t}_1, \boldsymbol{t}_2, \boldsymbol{t}_3\}$ in spin-space describes fully the spin-configuration of the three spins on a plaquette.

The interpenetrating honeycomb lattice, has a simpler order parameter. Since the lattice is bipartite (A and B sites), the energy of this antiferromagnetically coupled system is minimized by orienting the spins on the A site opposite to the spins on the B site. The order parameter is simply a vector $\boldsymbol{n}$ in spin space, thus it is an element of O(3)/O(2).

The emergent degree of freedom is now the projection of the order parameter $\boldsymbol{n}$ onto the plane perpendicular to $\boldsymbol{t}_3$. After normalizing this projection, a U(1) degree of freedom exists for each plaquette of the lattice. This U(1) degrees of freedom are the focus of the chapter 4.

We employ large-scale Monte Carlo simulations to study the correlations of these $U(1)$

degrees of freedom. The Monte Carlo algorithm is made up of three parts, the heat-bath algorithm, the parallel-tempering subroutine and a sublattice-rotation step. In the last step the honeycomb spins are rotated relative to the triangular lattice spins in a direction that is determined to be perpendicular to the plane spanned by the triangular lattice spins. The latter are non-local moves and allow the system to explore the sixfold potential minima, which is difficult to detect by single-spin updates, since the depth of the 6-fold potential is extremely shallow.

The parallel-tempering moves are updates, where two entire spin-configurations are exchanged between neighboring temperatures. This allows the system to thermalize quickly by proposing new spin-configurations that cannot be reached by single-spin updates.

This combination of the three algorithm steps allows us to explore systems up to the size of $3 \times 180 \times 180$ spins. This is particularly important given the fact that we obtain our results by performing a finite-size scaling analysis, where large system sizes are crucial in order to obtain data collapse.

We measure the magnetization and susceptibility of the relative U(1) degrees of freedom for different system sizes and find a power law phase in a certain temperature range. For temperatures below this range we find a symmetry broken phase. The exponents associated with the the critical points show the transition to belong to the BKT universality class.

In the final chapter we summarize the main results that we obtained in this thesis.

Chapter 2

Uniform frustration in curved space

In this chapter we take the prototypical N-component ϕ^4 theory, familiar from the theory of phase transitions, and study it in the new setting of curved three-dimensional hyperbolic space.
The role of curved space is to frustrate the familiar uniaxial order, which arises in the symmetry broken state in flat space. There the ordered state corresponds to the N-component spins aligning in a common direction in spin space. This becomes impossible for geometrical reasons, since in hyperbolic space the exponentially growing volume around any given point causes correlations to decay exponentially even at the critical point. Despite this decay it is still possible to identify the critical point by representing the correlation function in the eigenbasis of the Laplacian. The critical point is identified by determining where the correlation function in this representation becomes scale-free.
In the symmetry broken phase, spins tend to align locally in the same direction. In this way the spins communicate with the neighbors and cooperatively point into a common direction. Hyperbolic space frustrates this tendency and instead the phase transition corresponds to the formation of patches of maximum size, set by the inverse of the spatial curvature κ. In contrast to an r^2dr increase in volume around a point, hyperbolic space grows with $1/\kappa^2 \sinh^2(\kappa r)dr$. Thus a spherical solution of the Laplace equation in hyperbolic space decays exponentially with distance. This has consequences for the critical exponents of thermodynamic quantities at the phase transition, a topic that is studied in the following. This chapter is based on work done in

Karim Mnasri, Bhilahari Jeevanesan, and Jörg Schmalian, *Critical phenomena in hyperbolic space*, Phys. Rev. B 92, 134423

that was published in October 2015.

2.1 Introduction

Field theory and statistical mechanics in geometries with negative curvature are of increasing interest. While a direct application to the spacetime of our universe seems to require a positive cosmological constant, a wide range of many-particle problems are closely tied to problems with negative spatial curvature. For example, field theories in hyperbolic space are increasingly studied because of its direct relation to anti-de Sitter space. The latter is essential for the duality between strong coupling limits of certain quantum field theories and higher-dimensional gravity theories[54, 32, 107]. The scaling behavior near critical points in hyperbolic space, being the Wick-rotated version of anti-de Sitter space, may therefore be of relevance in the analysis of strong coupling theories.

On the other hand, networks like the Bethe lattice, that have been studied early on in the statistical mechanics of phase transitions [47, 20, 100] and that have received renewed interest in the context of the dynamical mean-field theory of correlated fermions[30, 21], quantum spin glasses[49], or bosons[87], can be considered as a regular tiling of the hyperbolic plane [63]. To be precise, if one considers a regular tiling $\{p, q\}$, where p refers to the degree of a polygon and q to the number of such polygons around each vertex, then the Bethe lattice with coordination number q corresponds to $\{\infty, q\}$. All regular tilings of the hyperbolic plane with $(p-2)(q-2) > 4$ are possible [63]. Obviously the square lattice $\{4, 4\}$, the triangular lattice $\{3, 6\}$, and the honeycomb lattice $\{6, 3\}$, i.e. the only possible tilings with regular polygons of the two-dimensional flat space, are just excluded. It was already stressed in [63] that hyperbolic tiling might be used to interpolate between the mean-field behavior of the Bethe lattice and a lattice that might be close to the square or honeycomb lattice. This may offer an alternative approach to study corrections beyond dynamical mean-field theory. A tiling of three-dimensional hyperbolic space with dodecahedra is shown in Figure 2.1 (see [106]).

Finally, effects of uniform frustration are often captured in terms of certain background gauge fields or by embedding a theory in curved space [97, 83, 69, 70]. An interesting case of tunable uniform frustration is found by studying a given flat-space problem in curved space with inverse radius of curvature κ, an idea that was introduced in [65, 66, 81, 67]. Here, the problem of packing identical discs was studied in a hyperbolic plane. While in flat space packing in hexagonal close-packed order is possible, in hyperbolic space this order is frustrated by the fact that gaps open up between neighboring discs. This facilitated the study of packing properties as a function of frustration, where the latter can be varied by changing the spatial curvature κ.

The hyperbolic metric may also be viewed as emergent in studying the effects of frustration of packing or of the existence of negative disclinations [19]. One might thus realize packings that are not allowed in flat space, as it occurs for clusters with icosahedral local order, in terms of a non-frustrated model that is embedded in a curved geometry.

These ideas were also employed in studies of glass transitions in hyperbolic space ([86, 85]), where the authors performed molecular dynamics simulations on the hyperbolic plane for a Lennard-Jones liquid and found that the fragility of the resulting glass is tunable by varying κ.

Given these applications of negatively-curved geometries, it is an interesting question to ask how phase transitions of classical and quantum models will behave in such curved spaces. Significant numerical work has been devoted to studies of classical spin models in hyperbolic space. The thermodynamic properties of Ising spins placed on the vertices of lattices in hyperbolic space were studied in [45, 46, 3, 29]. In order to perform Monte Carlo simulations on finite two-dimensional lattices a negatively curved background is created by tessellating the hyperbolic plane with regular n-gons.

All these works have found the phase transition to follow mean-field behaviour. In particular, various critical exponents were measured and found to numerically coincide closely with mean-field exponents. One should, however, keep in mind that the detailed protocol for measuring the critical exponents in these works is somewhat different from the usual

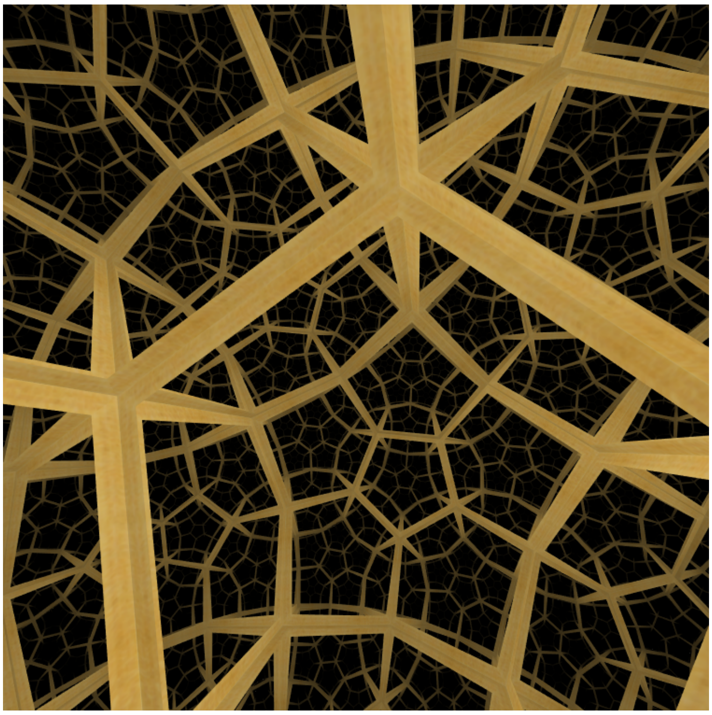

Figure 2.1: Tessellation of three-dimensional hyperbolic space by dodecahedra (created with [106])

flat space protocol.

The problem now arises to address the question of phase transitions in three-dimensional hyperbolic space. In particular, it is natural to ask, whether there is scaling as in flat d-dimensional space, or if the transition is genuinely of mean-field type. If phase transitions in hyperbolic space were of mean-field nature, it would imply for systems that are below their upper critical dimension in flat space, that an arbitrarily small curvature κ would lead to a violation of scaling. An alternative possibility is that scaling continues to be valid in hyperbolic space with a new fixed point characterized by new exponents. The above numerics would in that case indicate that some exponents take their mean-field values. Because of hyperscaling this cannot be the case for all critical exponents. In the case of a new fixed point there are obvious questions: what is the universality class and what are the critical exponents?

We answer these questions in this chapter by studying analytically the problem of an N-component continuum ϕ^4-theory in three-dimensional hyperbolic space in a large-N expansion. In the discussion section we comment on the generalization to different dimensions. Section 3.2 of this chapter contains the exposition of the ϕ^4 model in hyperbolic space. We find that the theory possesses a second order phase transition, that scaling is obeyed below the upper critical dimension of the flat space and that the exponents are given by the leading order terms of the $1/N$ expansion. To be specific, we find that the leading order $1/N$-corrections to the exponents vanish. In addition we give general arguments that support the conjecture that all higher order $1/N$-corrections should vanish as well.

The technical steps of our calculation are as follows. Using the momentum space analysis of section 2.4, we locate the critical temperature of this phase transition and find the magnetization texture of the ordered phase. In Section 2.3 we discuss the character of the phase transition and present the results of the calculations of the exponents η, ν and γ to lowest order in $1/N$. In order to meaningfully identify the critical point of this model, it is convenient to formulate the problems in momentum space. As this representation in hyperbolic space does not seem to exist in the condensed matter literature, we develop the necessary parts in section IV. With this formalism it is now possible to deal with the order $1/N$ correction to the critical exponents η and γ.

We find that the exponents η, ν and γ at lowest order are those of three-dimensional flat space and not those of a mean-field transition. However, in distinction to flat space, the $1/N$ corrections vanish. The absence of higher-order corrections is found to be the consequence of the finite curvature of hyperbolic space, which exponentially cuts off fluctuations of wavelengths longer than the curvature radius. This is in agreement with the general remarks on the regulating behavior of hyperbolic space by Callan and Wilczek in [6].

The critical exponents satisfy scaling and we discuss in the final section how our results can be understood from the scaling of the free energy in the presence of finite spatial curvature. Our results are thus in contradiction to the mean-field behavior that was found in Ref. [4]. There the mean-field behavior was supported by a Ginzburg criterion for ϕ^4-theories in hyperbolic space. This behavior was further rationalized by arguing that the Hausdorff dimension of hyperbolic space is infinite. In contradiction to this, our own results, which are obtained by performing the actual calculation, establish that the critical exponents are not mean-field exponents.

As a further result we calculated the magnetization texture of the ordered state of this model. We find that uniform magnetization develops in regions of size $1/\kappa$. Due to the exponential decay of correlations, even at the critical point, these regions will necessarily be uncorrelated in their magnetization direction.

2.2 Model and Background Geometry

The model we are considering is an N-component $\boldsymbol{\phi}^4$-theory given by the action

$$S = \int d^3x\sqrt{g}\,\frac{1}{2}\left[\mu_0\phi_i\cdot\phi_i + g^{\mu\nu}(\nabla_\mu\phi_i)(\nabla_\nu\phi_i) + \frac{u}{2N}(\phi_i\cdot\phi_i)^2\right], \tag{2.1}$$

where ∇_μ is the covariant derivative, $i = 1\ldots N$ and $\mu,\nu = 1\ldots 3$. The summation over i,μ and ν is implied. Thus we are considering here the three-dimensional version of $\boldsymbol{\phi}^4$-theory. Generalizations to different dimensions are straightforward, as we discuss in the final section. In the action, $g_{\mu\nu}$ is the metric of three-dimensional hyperbolic space, which is a maximally symmetric space with negative curvature, characterized by a single parameter, the curvature κ. The quantity g is the metric determinant and assures the proper transformation property of the action.

Hyperbolic space can be defined as one of the two (equivalent) simply-connected three-dimensional manifolds of points satisfying

$$x_1^2 + x_2^2 + x_3^2 - x_4^2 = -\frac{1}{\kappa^2} \tag{2.2}$$

inside four-dimensional Minkowski space. It is not possible to imbed this manifold in four-dimensional euclidean space, the reason being that the ambient space must have the same

symmetries in space, which it has in common with the imbedded space. The hyperbolic manifold has the symmetry of rotations and boosts and therefore Minkowski space is the proper choice as ambient space.
The coordinates x_i are the cartesian coordinates of Minkowski space. To derive a more convenient formulation, the points may be parametrized by

$$x_1 = \frac{1}{\kappa}\sinh\kappa r\sin\theta\cos\phi \tag{2.3}$$

$$x_2 = \frac{1}{\kappa}\sinh\kappa r\sin\theta\sin\phi \tag{2.4}$$

$$x_3 = \frac{1}{\kappa}\sinh\kappa r\cos\theta \tag{2.5}$$

$$x_4 = \frac{1}{\kappa}\cosh\kappa r. \tag{2.6}$$

Minkowski space has a metric that is given by

$$ds^2 = dx_1^2 + dx_2^2 + dx_3^2 - dx_4^2. \tag{2.7}$$

This induces an intrinsic metric on the hyperbolic space with line-element

$$ds^2 = dr^2 + \frac{1}{\kappa^2}\sinh^2\kappa r\left(d\theta^2 + \sin^2\theta d\phi^2\right). \tag{2.8}$$

In the limit $\kappa \to 0$ we regain three-dimensional flat space. With the radius of curvature $1/\kappa$ an additional length scale is present in hyperbolic space, which is ultimately responsible for the non-trivial magnetization texture that we derive below. Note that our results can be straightforwardly applied to quantum phase transitions in hyperbolic space, if one of the spatial coordinates is considered as imaginary time after the usual Wick rotation.

2.3 Phase transition and magnetization texture

In three-dimensional flat space the model that we consider is known to possess a second order phase transition, where the ordered state corresponds to a symmetry-broken phase with uniaxial magnetization. In contrast to flat space, it is not possible in the $N = 3$ case to identify the three scalar fields (ϕ_1, ϕ_2, ϕ_3) as vectors components in a global coordinate system, since global directions are not a well-defined concept in hyperbolic space. Consider, as shown in Fig. 2.2, three locally magnetized patches A, B, C, which are the corners of a hyperbolic planar triangle and demonstrate via a proof by contradiction, that such a global coordinate system cannot be introduced.

A basis vector at A may be chosen to be parallel-transported to B and C along the geodesics $\overline{AB}$ and $\overline{AC}$, respectively. If now we continue the parallel-transport from B to C along $\overline{BC}$, the two transported basis vectors will not match. Instead, there will be an angular defect θ between the two directions that is proportional to the enclosed area $\mathcal{A}$ of the hyperbolic triangle:

$$\theta = \mathcal{A}\kappa^2 \tag{2.9}$$

This formula follows from the fact that the vectors are parallel-transported such that the angle between the geodesic curve and the vector is a constant. Since hyperbolic triangles have angles which sum to $\pi - \mathcal{A}\kappa^2$ ([18]), we are left with the angular defect stated in

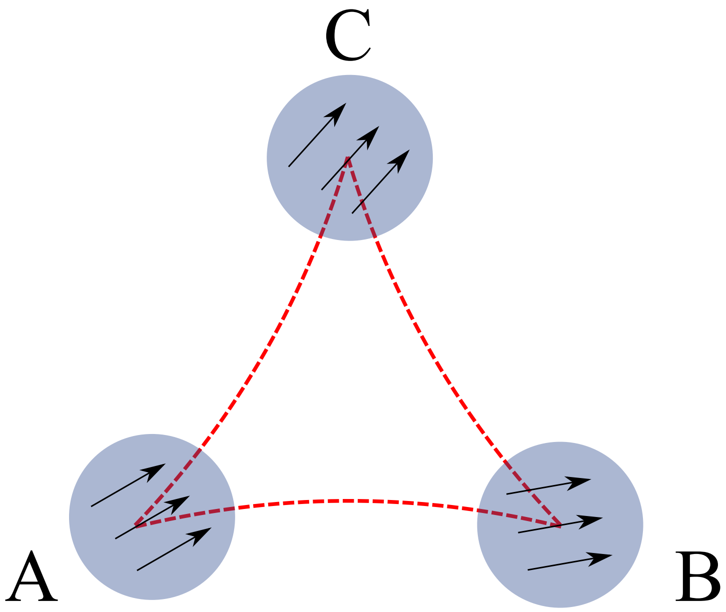

Figure 2.2: Three magnetized patches in a plane, forming a hyperbolic triangle. It is not possible to introduce a global coordinate system in which the three components (ϕ_1, ϕ_2, ϕ_3) can be interpreted as the direction of the magnetization, since parallel-transport of a basis vector from A to B and A to C, will not result in vectors that will match upon parallel-transport from B to C or vice versa.

(2.9). Thus the interpretation of (ϕ_1, ϕ_2, ϕ_3) as a three component vector in hyperbolic space is not valid.

Inside the radius of curvature, where $\mathcal{A} < 1/\kappa^2$, a uniform direction may, however, be meaningfully defined.

In order to determine the nature of the ordered state, we study the symmetry-broken state of the action S at the lowest order in a $1/N$ expansion, i.e. we peform a saddle point analysis of the partition function

$$Z = \int D\boldsymbol{\phi} \exp(-S), \tag{2.10}$$

and then include higher-order fluctuations in a systematic fashion. Here, the action S is given by:

$$S = \beta \int dV \, \frac{1}{2} \left[\boldsymbol{\phi} \left(\mu_0 - \nabla^2 \right) \boldsymbol{\phi} + \frac{u}{2N} \left(\boldsymbol{\phi} \cdot \boldsymbol{\phi} \right)^2 \right], \tag{2.11}$$

where $\nabla^2 \boldsymbol{\phi} = \nabla_\mu \nabla^\mu \boldsymbol{\phi}$ and we have defined $dV = d^3x\sqrt{g}$. We rewrite this by performing a Hubbard-Stratonovich decoupling of the $(\boldsymbol{\phi} \cdot \boldsymbol{\phi})^2$ term, whereupon the action becomes

$$S = \frac{\beta}{2} \int dV \left[\boldsymbol{\phi} \left(\mu_0 + i\lambda(\boldsymbol{x}) - \nabla^2 \right) \boldsymbol{\phi} + \frac{N}{2u} \lambda^2(\boldsymbol{x}) \right].$$

Now we integrate out all ϕ_i with the exception of the one component, along which the spins near a chosen point order and which we will label $\sigma(\boldsymbol{x})$. Moreover, we introduce a source field $h(\boldsymbol{x})$ for $\sigma(\boldsymbol{x})$. This leads to the action

$$\begin{aligned} S &= \beta \int dV \, \frac{1}{2} \left[\sigma(\boldsymbol{x}) \left(\mu_0 + i\lambda(\boldsymbol{x}) - \nabla^2 \right) \sigma(\boldsymbol{x}) + \frac{N}{2u} \lambda^2(\boldsymbol{x}) \right] \\ & \quad + \frac{N-1}{2} \mathrm{Tr} \left[\log(\mu_0 + i\lambda(\boldsymbol{x}) - \nabla^2) \right] - \beta \int dV \; h(\boldsymbol{x}) \sigma(\boldsymbol{x}) \end{aligned}$$

for the partition function $Z = \int D\sigma D\lambda \exp(-S)$.
The saddle point solutions are determined by the conditions $\frac{\delta S}{\delta\sigma(\boldsymbol{x})} = 0$ and $\frac{\delta S}{\delta\lambda(\boldsymbol{x})} = 0$, which result in the two equations

$$\left(\mu(\boldsymbol{x}) - \nabla^2 \right) \sigma(\boldsymbol{x}) = h(\boldsymbol{x}) \tag{2.12}$$

$$\mu(\boldsymbol{x}) - \mu_0 = uT \langle \boldsymbol{x} | \frac{1}{\mu(\boldsymbol{x}) - \nabla^2} | \boldsymbol{x} \rangle + \frac{u}{N} \sigma^2(\boldsymbol{x}) \tag{2.13}$$

with $\mu(\boldsymbol{x}) = \mu_0 + i\lambda(\boldsymbol{x})$.
We will use these equations to work out the critical exponents including higher-order corrections in section IV. Here, we will only analyze equation (2.12) to find the susceptibility $G^{(0)}(\boldsymbol{x}, \boldsymbol{x'}) = \delta\sigma(\boldsymbol{x})/\delta h(\boldsymbol{x'})|_{h(\boldsymbol{x'})=0}$, which, by virtue of (2.12), satisfies

$$\left(\mu(\boldsymbol{x}) - \nabla^2 \right) G^{(0)}(\boldsymbol{x}, \boldsymbol{x'}) = \delta(\boldsymbol{x}, \boldsymbol{x'}). \tag{2.14}$$

As we approach the phase transition from high temperatures, $\mu(\boldsymbol{x})$ may be assumed to be homogeneous. Using the formalism of the next section, this equation may be transformed into momentum space whereupon it becomes

$$G^{(0)}(p) = \frac{1}{\mu + \kappa^2 + p^2}, \tag{2.15}$$

where $p \geq 0$ determine the eigenvalues $\kappa^2 + p^2$ of the Laplacian. Note the presence of the 'mass term' κ^2 in the denominator. This is a consequence of the fact that the Laplace operator in hyperbolic space has a gapped eigenvalue spectrum. A criterion for the presence of the phase transition is the condition that $G^{(0)}(p)$ should diverge. The highest value of μ when this happens is $\mu = -\kappa^2$, where the $p = 0$ mode of the susceptibility diverges. Thus the phase transition takes place at $\mu = -\kappa^2$ with an order that is determined by the $p = 0$ Fourier mode. In contrast to flat space, the $p = 0$ eigenmode of the Laplace operator cannot be one of homogeneous order, in agreement with the foregoing argument about angular defects. Instead, it corresponds to a diminishing of the magnetization σ along the one direction, that we chose not to integrate out. In other words, due to the lack of a global direction of magnetization, focussing on one component of the N-component vector, entails that one is eventually considering projections of the magnetization vector instead of the full vector. The diminishing of this projection takes place according to the formula

$$\sigma(r) = \sigma_0 \frac{\kappa r}{\sinh \kappa r}, \tag{2.16}$$

where r is the geodesic distance from the origin, where the unintegrated component and local magnetization direction coincide and σ_0 is the magnitude of the magnetization at the origin. The phase transition corresponds to the formation of infinitely many patches, more precisely three-dimensional regions, of characteristic sizes $1/\kappa$, which have nearly uniform magnetization. The decay of $\sigma(r)$ in Eq. (2.16) does not imply a decay of the magnitude of the order parameter, but must be interpreted as the order parameter rotating away from the chosen direction of the vector $\boldsymbol{\phi}$.

2.4 Momentum space representation

We come now to the technical part of this work that will allow us to analyze the saddle point equations (2.12), (2.13) and compute critical exponents. In order to make progress with the calculations, it is convenient to obtain the momentum space representation of functions that are translationally invariant in hyperbolic space. Let $\psi(d_{PQ})$ be a given function of the geodesic distance between two points P and Q. The functional dependence on the two points will not have an arbitrary form, but will rather be expressed through the geodesic distance d_{PQ} between these two points. This distance is the length of the geodesic curve connecting these points. Explicit computation of this length yields the formula

$$\begin{aligned} \cosh \kappa d_{PQ} &= \cosh \kappa r \cosh \kappa r' - \sinh \kappa r \sinh \kappa r' \cos \gamma \\ \cos \gamma &= \cos \theta \cos \theta' + \sin \theta \sin \theta' \cos (\phi - \phi'). \end{aligned} \tag{2.17}$$

The fact that such a function ψ depends on the six coordinates not in an arbitrary way, but only through the geodesic distance, allows us to expand $\psi(d_{PQ})$ in terms of the eigenstates of the Laplace operator in hyperbolic space. Since hyperbolic space may be defined as the set of all points equidistant from the origin in Minkowski space, this Laplace operator is identical to the one obtained by writing down the 4-dimensional Laplace operator in angular coordinates and restricting the distance from the origin to a constant. A similar situation was considered by Fock [27], who studied the problem on a 3-sphere embedded in 4-dimensional euclidean space. The eigenfunctions of the Laplacian on this 3-sphere are the generalized spherical harmonics of three angles. Their full description was given in [27]. We find the eigenfunctions of the Laplacian in hyperbolic space by multiplying one of the angles in Fock's solution by the imaginary unit, a prescription sketched briefly in an appendix of [50].

The hyperbolic Laplacian is given by

$$\begin{aligned} \Delta &= \frac{1}{\sinh^2 \kappa r} \partial_r (\sinh^2 \kappa r \partial_r \psi) + \frac{\kappa^2}{\sinh^2 (\kappa r)} \Delta_{S^2} \\ \Delta_{S^2} &= \frac{1}{\sin \theta} \partial_\theta \left(\sin \partial_\theta \psi \right) + \frac{1}{\sin^2 \theta} \partial_\phi^2 \psi. \end{aligned} \tag{2.18}$$

The eigenfunctions are then given by

$$\psi_{qlm}(r, \theta, \phi) = \Pi_{ql}(\kappa r) Y_{lm}(\theta, \phi) \tag{2.19}$$

with eigenvalues

$$\Delta \psi_{qlm}(r, \theta, \phi) = -(\kappa^2 + q^2) \psi_{qlm}(r, \theta, \phi). \tag{2.20}$$

Here the Y_{lm} are the ordinary spherical harmonics on the 2-sphere and the Π_{pl} are special functions that solve the radial part of the eigenvalue equation

$$\frac{d^2}{dr^2} \Pi_{ql} + 2\kappa \coth \kappa r \frac{d}{dr} \Pi_{ql} - \frac{l(l+1)\kappa^2}{\sinh^2 \kappa r} \Pi_{ql}(\kappa r) = -(\kappa^2 + q^2) \Pi_{ql}(\kappa r). \tag{2.21}$$

The solutions can be expressed in a Rayleigh-type formula

$$\Pi_{ql}(x) = \frac{\sinh^l x}{M_l} \left(\frac{d^{l+1}}{d(\cosh x)^{l+1}} \right) \cos \left(\frac{q}{\kappa} x \right) \tag{2.22}$$

Table 2.1: Radial functions $\Pi_{\sigma l}(r)$ for the five lowest values of l

l	$\Pi_{\sigma l}(r)$
0	$-\operatorname{csch}(x)\sin(\sigma x)$
1	$\frac{\operatorname{csch}(x)(\coth(x)\sin(\sigma x)-\sigma\cos(\sigma x))}{\sqrt{\sigma^2+1}}$
2	$\frac{\operatorname{csch}(x)\left(\sin(\sigma x)\left(\sigma^2-\operatorname{csch}^2(x)\right)+3\sigma\coth(x)\cos(\sigma x)-2\coth^2(x)\sin(\sigma x)\right)}{\sqrt{(\sigma^2+1)(\sigma^2+4)}}$
3	$\frac{\operatorname{csch}(x)\left(\sigma\cos(\sigma x)\left(\sigma^2-4\operatorname{csch}^2(x)\right)+3\coth(x)\sin(\sigma x)\left(3\operatorname{csch}^2(x)-2\sigma^2\right)-11\sigma\coth^2(x)\cos(\sigma x)+6\coth^3(x)\sin(\sigma x)\right)}{\sqrt{(\sigma^2+1)(\sigma^2+4)(\sigma^2+9)}}$
4	$-\frac{\operatorname{csch}(x)\left(5\sigma\coth(x)\cos(\sigma x)\left(2\left(\sigma^2-5\right)-21\operatorname{csch}^2(x)\right)+\sin(\sigma x)\left(\sigma^4-35\sigma^2+15\operatorname{csch}^2(x)\left(-3\sigma^2+7\operatorname{csch}^2(x)+8\right)+24\right)\right)}{\sqrt{(\sigma^2+1)(\sigma^2+4)(\sigma^2+9)(\sigma^2+16)}}$

where

$$M_l^2 = \left(\frac{q}{\kappa}\right)^2 \left[\left(\frac{q}{\kappa}\right)^2 + 1^2\right] \dots \left[\left(\frac{q}{\kappa}\right)^2 + l^2\right] \tag{2.23}$$

is a normalization constant. The differential equation being of Sturm-Liouville form, these functions satisfy the orthogonality relation

$$\int\limits_0^\infty dr \sinh^2(\kappa r)\ \Pi_{ql}(\kappa r)\Pi_{q'l}(\kappa r) = \frac{\pi}{2}\delta(q-q'). \tag{2.24}$$

2.4.1 Addition theorem

In order to make the expansion of a given function simpler, we now wish to derive several identities. For the sake of completeness, the proof of the central identity, which was derived by Fock [27] in 1935 will be given in some detail. He obtained identities for the spherical harmonics of *spherically* curved $3d$ space, embedded in flat euclidean $4d$ space. From this identity we will derive below the corresponding identity for $3d$ hyperbolic space.
We will construct a Green's function $G(\boldsymbol{r}, \boldsymbol{r}')$ of two points $\boldsymbol{r}$ and $\boldsymbol{r}'$ with

$$\boldsymbol{r} = \begin{pmatrix} \rho\sin\alpha\sin\theta\cos\phi \\ \rho\sin\alpha\sin\theta\sin\phi \\ \rho\sin\alpha\cos\theta \\ \rho\cos\alpha \end{pmatrix}, \boldsymbol{r}' = \begin{pmatrix} \rho'\sin\alpha'\sin\theta'\cos\phi' \\ \rho'\sin\alpha'\sin\theta'\sin\phi' \\ \rho'\sin\alpha'\cos\theta' \\ \rho'\cos\alpha' \end{pmatrix}.$$

First note that the Green's function

$$G(P, Q) = \frac{1}{2R^2} + \frac{1}{2\tilde{R}^2} \tag{2.25}$$

with

$$\begin{aligned} R^2 &= |\boldsymbol{r} - \boldsymbol{r}'|^2 = \rho^2 + \rho'^2 - 2\rho\rho'\left(\cos\alpha\cos\alpha' - \sin\alpha\sin\alpha'\cos\gamma\right) \\ \cos\gamma &= \sin\theta\sin\theta'\cos(\phi-\phi') + \cos\theta\cos\theta' \end{aligned}$$

and

$$\tilde{R}^2 = \rho'^2\rho^2 + 1 - 2\rho\rho'\left(\cos\alpha\cos\alpha' - \sin\alpha\sin\alpha'\cos\gamma\right).$$

satisfies the Laplace equation, since both terms satisfy the latter independently. That this is so, is easily seen by inserting $\frac{1}{\rho^2}$ into the Laplacian of flat 4d space. Moreover, integrating around a small sphere at the origin, we have by Gauss' law

$$\int \nabla^2(\frac{1}{\rho^2})dV = \int \frac{\partial}{\partial\rho}\left(\frac{1}{\rho^2}\right)\rho^3\sin^2\alpha\sin\theta d\alpha d\theta d\phi = -2\int\frac{1}{\rho^3}\rho^3\sin^2\alpha\sin\theta d\alpha d\theta d\phi = -4\pi^2,$$

from which we conclude that

$$\nabla^2\left(\frac{1}{\rho^2}\right) = -4\pi^2\delta(\rho).$$

Since the Laplacian respects translational invariance, the functions in (2.25) will satisfy the Laplace equation as well.
Moreover, these terms satisfy

$$\left(G + \frac{\partial G}{\partial\rho'}\right)_{\rho'=1} = 0.$$

This is useful for the following application. Consider the identity

$$\begin{aligned}&\int\left(G(\boldsymbol{r},\boldsymbol{r}')\nabla^2\psi(\rho',\alpha',\theta',\phi') - \psi(\rho',\alpha',\theta',\phi')\nabla^2 G(\boldsymbol{r},\boldsymbol{r}')\right)dV'\\ &= \int\left(G(\boldsymbol{r},\boldsymbol{r}')\nabla\psi(\rho',\alpha',\theta',\phi') - \psi(\rho',\alpha',\theta',\phi')\nabla G(\boldsymbol{r},\boldsymbol{r}')\right)d\boldsymbol{S}\end{aligned}$$

and choose as integration volume the unit sphere that is defined by $\rho' = 1$. Then the surface element points radially outward. Let us furthermore assume that ψ satisfies the Laplace equation inside the unit sphere:

$$\begin{aligned}-4\pi^2\psi(\rho,\alpha,\theta,\phi) &= \int\left(G(\boldsymbol{r},\boldsymbol{r}')\frac{\partial\psi}{\partial\rho'} - \psi\frac{\partial}{\partial\rho'}G(\boldsymbol{r},\boldsymbol{r}')\right)_{\rho'=1}\sin^2\alpha\sin\theta dr d\theta d\phi\\ &= \int\left(\left[\frac{\partial\psi}{\partial\rho'} + \psi\right]G(\boldsymbol{r},\boldsymbol{r}')\right)_{\rho'=1}\sin^2\alpha\sin\theta dr d\theta d\phi.\end{aligned}$$

This is an integral equation for ψ. Now we require that ψ be a harmonic polynomial. These are homogenous polynomials of the variables x_1, x_2, x_3, x_4 that satisfy the Laplace equation. After expressing such a polynomial in spherical coordinates it will be of the form

$$\psi(\rho,\alpha,\theta,\phi) = \rho^{n-1}\Psi_n(\alpha,\theta,\phi)$$

and Ψ_n is a spherical harmonic of three angles. Inserting this ansatz into the integral equation, we obtain

$$-4\pi^2\rho^{n-1}\Psi_n(\alpha,\theta,\phi) = n\int\frac{\Psi_n(\alpha',\theta',\phi')}{\rho^2+1-2\rho\cos\omega}\sin^2\alpha'\sin\theta' d\alpha' d\theta' d\phi',$$

where we have followed Fock in defining the geodesic arc length ω

$$\cos\omega = \left(\cos\alpha\cos\alpha' + \sin\alpha\sin\alpha'\cos\gamma\right).$$

From this integral equation we can now derive very useful identities. First note ($\rho < 1$)

$$\frac{1}{\rho^2+1-2\rho\cos\omega} = \frac{1}{2i\rho\sin\omega}\left(\frac{1}{\rho e^{-i\omega}-1} - \frac{1}{\rho e^{i\omega}-1}\right) = \sum_{k=1}^{\infty}\frac{\sin k\omega}{\sin\omega}\rho^{k-1}$$

then we can compare coefficients in the integral equation, to deduce:

$$\rho^{n-1}\Psi_n(\alpha,\theta,\phi) \;=\; -\frac{n}{4\pi^2}\sum_{k=1}^{\infty}\rho^{k-1}\int \Psi_n(\alpha,\theta,\phi)\frac{\sin k\omega}{\sin\omega}\sin^2\alpha\sin\theta d\alpha d\theta d\phi$$

and hence

$$\int \Psi_n(\alpha,\theta,\phi)\frac{\sin k\omega}{\sin\omega}\sin^2\alpha\sin\theta d\alpha d\theta d\phi = \begin{cases} -\frac{4\pi^2}{n}\Psi_n(\alpha',\theta',\phi') & \text{for } k=n \\ 0 & \text{for } k\neq n \end{cases} \tag{2.26}$$

The seperation ansatz in the Laplace equation allows us to write

$$\Psi_n(\alpha,\theta,\phi) = \tilde{\Pi}_{nl}(\alpha)Y_{lm}(\theta,\phi).$$

Analogously to our previous calculation of $\Pi_{\sigma l}$ in hyperbolic space, it can be shown that

$$\begin{aligned}\tilde{\Pi}_{nl}(\alpha) &= \frac{\sin^l\alpha}{\bar{M}_l}\left(\frac{d^{l+1}}{d(\cos\alpha)^{l+1}}\right)\cos n\alpha \\ \bar{M}_l^2 &= n^2(n^2-1^2)\dots(n^2-l^2).\end{aligned}$$

Now

$$\int_0^{\pi} d\theta\sin\theta\int_0^{2\pi} d\phi\,|Y_{lm}(\theta,\phi)|^2 = 1$$

and we use Fock's convention

$$\int_0^{\pi}\tilde{\Pi}_{nl}^2(\alpha)\sin^2\alpha d\alpha = \frac{\pi}{2}$$

such that

$$\int \Psi_n(\alpha,\theta,\phi)\Psi_n^*(\alpha,\theta,\phi)\sin^2\alpha\sin\theta\; d\alpha d\theta d\phi = \frac{\pi}{2}.$$

With this and the orthogonality property of the Ψ, we deduce from (2.26)

$$\begin{aligned}\frac{\sin n\omega}{\sin\omega} &= -\frac{8\pi}{n}\Psi_n^*(\alpha,\theta,\phi)\Psi_n(\alpha',\theta',\phi') \\ &= -\frac{8\pi}{n}\sum_{l=0}^{\infty}\tilde{\Pi}_{nl}(\alpha)\tilde{\Pi}_{nl}(\alpha')\sum_{m=-l}^{l}Y_{lm}^*(\theta,\phi)Y_{lm}(\theta',\phi') \\ &= -\frac{2}{n}\sum_{l=0}^{\infty}\tilde{\Pi}_{nl}(\alpha)\tilde{\Pi}_{nl}(\alpha')(2l+1)P_l(\cos\gamma).\end{aligned}$$

This identity is correct not only for all positive integers n, but also for complex arguments. We obtain the corresponding results in hyperbolic space by letting $n = i\sigma$ and $\omega = id_H$ and introducing the $\Pi_{\sigma l}$ function

$$\Pi_{\sigma l}(r) = (-i)^l\tilde{\Pi}_{i\sigma l}(ir).$$

This results in the Rayleigh type formula

$$\Pi_{\sigma l}(r) = \frac{\sinh^l r}{M_l}\left(\frac{d^{l+1}}{d(\cosh r)^{l+1}}\right)\cos\sigma r \tag{2.27}$$

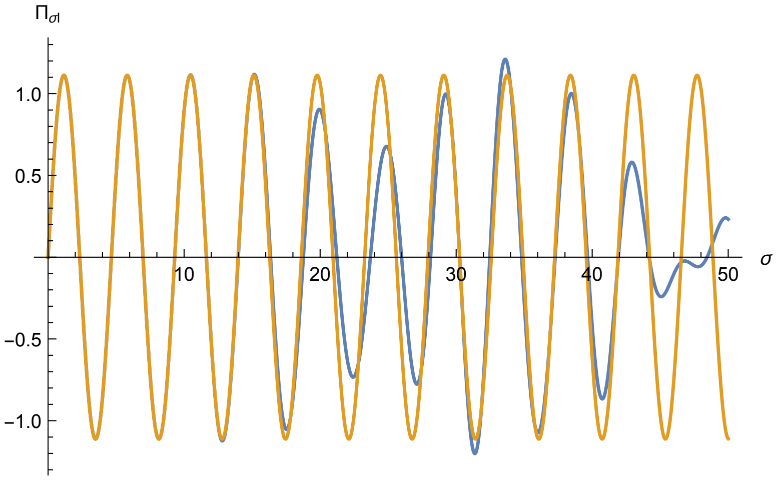

Figure 2.3: Partial sum up to $l = 30$ of (2.28) for generic values of P,Q. Orange: exact expression, blue:partial sum

$$M_l^2 = \sigma^2(\sigma^2 + 1^2)\dots(\sigma^2 + l^2).$$

The derived identity is transformed into

$$\begin{aligned}\frac{\sin\sigma d_H}{\sinh d_H} &= \frac{8\pi}{\sigma}\Psi^*_\sigma(r,\theta,\phi)\Psi_\sigma(r',\theta',\phi') = \frac{8\pi}{\sigma}\sum_{l=0}^{\infty}\Pi_{\sigma l}(r)\Pi_{\sigma l}(r')\sum_{m=-l}^{l}Y^*_{lm}(\theta,\phi)Y_{lm}(\theta',\phi') \\ &= \frac{1}{\sigma}\sum_{l=0}^{\infty}\Pi_{\sigma l}(r)\Pi_{\sigma l}(r')(2l+1)P_l(\cos\gamma) \qquad (2.28)\end{aligned}$$

and

$$\cosh d_H = \cosh r\cosh r' - \sinh r\sinh r'\cos\gamma.$$

The plot in figure 2.3 shows the convergence of the sum on the right hand side for a partial sum of $l = 30$ and generic values of P and Q. As more terms are included, the region where the partial sum (blue) does not coincide with the exact value (orange) tends to infinity.

However, we will find it more convenient to work with special functions in which the dimensionless variable σ has been replaced by q/κ, where now q is a momentum variable with dimensions of inverse length. This trivial change leads to the formula

$$\frac{\sin(qd)}{\sinh(\kappa d)} = \frac{\kappa}{q}\sum_{l=0}^{\infty}(2l+1)\Pi_{ql}(\kappa r)\Pi_{ql}(\kappa r')P_l(\cos\gamma). \qquad (2.29)$$

As a demonstration of the use of this formula, let us derive the magnetization texture of the $p = 0$ eigenmode given in (2.16). The eigenbasis expansion of $G^{(0)}$ reads

$$G^{(0)}(\boldsymbol{r},\boldsymbol{r}') = \int dp\sum_l(2l+1)G^{(0)}(p)\Pi_{pl}(\kappa r)\Pi_{pl}(\kappa r')P_l(\cos\gamma). \qquad (2.30)$$

Insertion of $G^{(0)}(p)$ from (2.15) into this equation at the critical point $\mu = -\kappa^2$, yields the real-space form of $G^{(0)}$. Now we construct the real-space form of only the $p = 0$ mode, which gives

$$\begin{aligned}\sigma(d(\boldsymbol{r},\boldsymbol{r}')) &= \lim_{p\to 0}\sum_l (2l+1)\frac{\sigma_p}{p^2}\Pi_{pl}(\kappa r)\Pi_{pl}(\kappa r')P_l(\cos\gamma)\\ &= \sigma_0\frac{\kappa d(\boldsymbol{r},\boldsymbol{r}')}{\sinh\kappa d(\boldsymbol{r},\boldsymbol{r}')},\end{aligned} \tag{2.31}$$

as claimed.

2.4.2 Extraction of coefficients and inversion formula

The identity (2.29) will be crucial in obtaining the expansion coefficients of a given function $\psi(d)$ of the geodesic distance. This distance being a non-negative quantity, the value of ψ for negative arguments is irrelevant. In particular we may redefine ψ for negative arguments such that it becomes an even function. This allows us to Fourier expand ψ as follows

$$\psi(d)\sinh\kappa d = \frac{\kappa}{2\pi^2}\int_{-\infty}^{+\infty} dp\ \psi_p p\sin(pd), \tag{2.32}$$

where we have chosen to split off a factor of $\kappa p/(2\pi^2)$ in the definition of the expansion coefficient for later convenience. Inserting (2.29) we obtain

$$\begin{aligned}\psi(d) &= \frac{\kappa}{2\pi^2\sinh\kappa d}\int_{-\infty}^{+\infty} dp\ \psi_p p\sin(pd)\\ &= \frac{\kappa^2}{2\pi^2}\int_{-\infty}^{+\infty} dp\sum_{l=0}^{\infty}(2l+1)\psi_p\Pi_{pl}(\kappa r)\Pi_{pl}(\kappa r')P_l(\cos\gamma)\end{aligned} \tag{2.33}$$

and have thereby managed to expand the arbitrary function ψ in the new basis with coefficients

$$\psi_p = \frac{\pi i}{\kappa p}\int_{-\infty}^{+\infty} dx\psi(|x|)\sinh(\kappa x)e^{-ipx}. \tag{2.34}$$

Let us briefly comment on the structure of the expansion. Note that in (2.33) the expansion coefficient ψ_p has no dependence on l. In fact, the statement of (2.33) is that any function that depends on the set of coordinates (r,θ,ϕ), (r',θ',ϕ') only through the geodesic distance of the two points, can have no explicit l or m dependence of ψ_p.
Conversely, to find the real-space function $\psi(d)$ from the knowledge of the coefficients ψ_p in the expansion (2.33) we use (2.32) which results in the inversion formula

$$\psi(d) = \frac{\kappa}{2\pi^2 i\sinh\kappa d}\int_{-\infty}^{+\infty} dp\ \psi_p p e^{ipd}. \tag{2.35}$$

2.4.3 Convolution theorem

Let f and g be two-point functions that depend on the geodesic distances d_{PQ} and d_{QR}, respectively. When we multiply these functions and integrate Q over all of hyperbolic space, the resulting function h can only depend on the geodesic distance between points P and R. This convolution will in general be difficult to carry out in real-space. The fact that the Π_{plm} and the Y_{lm} are orthogonal functions, however, allows us to reduce the convolution of f and g to a multiplication in momentum-space. This is seen explicitly by rewriting the relation

$$\int dV_Q f(d_{PQ})g(d_{QR}) = h(d_{PR}) \tag{2.36}$$

in the momentum representation (2.33) with expansion coefficients f_p, g_p, h_p and using the orthogonality relations for the radial functions and the spherical harmonics. Then this convolution formula translates into

$$f_p g_p = h_p. \tag{2.37}$$

The solution of the Dyson equation below will require knowledge about the momentum-space representation of the Dirac δ-function in hyperbolic space, which we denote by either δ_{PQ} or $\delta(\boldsymbol{r}, \boldsymbol{r}')$. We define this function by the condition that convolution of an arbitrary function $\psi(d_{PQ})$ with $\delta(d_{QR})$ must yield $\psi(d_{PR})$. Translating this condition into momentum space, we immediately read off from (2.37) the relation $\delta_p = 1$ and obtain thereby

$$\delta_{PQ} \quad = \quad \frac{\kappa^2}{2\pi^2} \int\limits_{-\infty}^{+\infty} dp \sum_{l=0}^{\infty} (2l+1)\Pi_{pl}(\kappa r)\Pi_{pl}(\kappa r')P_l(\cos\gamma). \tag{2.38}$$

Conversely, however, the multiplication of two functions in real-space does not translate into a simple convolution integral in momentum-space, but rather a double-integral. Given the product

$$f(d_{PQ})g(d_{PQ}) = h(d_{PQ}) \tag{2.39}$$

the corresponding momentum-space equation is found by employing the representation (2.35)

$$h_k = \frac{1}{4\pi^2 k} \int\limits_{-\infty}^{\infty} dp \int\limits_{-\infty}^{\infty} dq f_p g_q pq \tanh\left[\frac{p+q-k}{2\kappa}\pi\right] \tag{2.40}$$

i.e. instead of a single integral a double integral with kernel is obtained.
In the limit $k \to 0$ the symmetry properties of f_p and g_q may be used to rewrite this kernel as

$$\lim_{k\to 0} h_k = \frac{1}{8\pi\kappa} \int\limits_{-\infty}^{\infty} dp \int\limits_{-\infty}^{\infty} dq \; \frac{pq f_p g_q}{\cosh^2 \frac{\pi(p-q)}{2\kappa}}. \tag{2.41}$$

This formula will be used in section 2.8 in evaluating the corrections to the critical exponent γ. As a check of the convolution theorem and to verify all the factors of π etc., let us demonstrate the use of this identity by computing the convolution of two functions first directly and then by using the theorem. Consider

$$\begin{aligned} f(d) &= \frac{1}{\cosh^2 d} \\ g(d) &= \frac{1}{\sinh^2 d} \end{aligned}$$

and the convolution integral

$$\int dV_2 \; f(d_{12}) g(d_{23}) \equiv h(d_{13}). \tag{2.42}$$

The explicit formulas for the geodesic distance between these points (we set $\kappa = 1$) are

$$\begin{aligned} \cosh d_{12} &= \cosh r_1 \cosh r_2 - \sinh r_1 \sinh r_2 \cos \gamma_{12} \\ \cos \gamma_{12} &= \cos \theta_1 \cos \theta_2 + \sin \theta_1 \sin \theta_2 \cos(\phi_1 - \phi_2) \end{aligned}$$

and similarly for d_{23}. The straightforward way proceeds by choosing one of the points, say point 1, to be the origin. Then this integral becomes

$$h(d_{13}) = \int\limits_0^{\infty} dr_2 \int\limits_0^{\pi} d\theta_2 \int\limits_0^{2\pi} d\phi_2 \sinh^2 r_2 \sin \theta_2 f(r_2) g(d_{23}).$$

The integrand has a complicated dependence on the coordinates (r_2, θ_2, ϕ_2). We therefore solve this integral numerically.
The second way is to employ the convolution theorem. We first compute

$$\begin{aligned} f_p &= \frac{2\pi i}{p} \int\limits_{-\infty}^{+\infty} dx \, \frac{1}{\cosh^2 x} \sinh x \; e^{-ipx} = 2\pi^2 \mathrm{sech} \left(\frac{\pi p}{2} \right) \\ g_p &= \frac{2\pi i}{p} \int\limits_{-\infty}^{+\infty} dx \, \frac{1}{\cosh^2 x} \sinh x \; e^{-ipx} = \frac{2\pi^2}{p} \tanh \left(\frac{\pi p}{2} \right) \end{aligned}$$

and now transform back to real space via

$$h(d) = \frac{1}{4\pi^2 \sinh d} \int\limits_{-\infty}^{\infty} dp \; f_p g_p p \sin(pd) = \frac{\pi^2}{\sinh d} \int\limits_{-\infty}^{\infty} dp \, \frac{\sinh \frac{\pi p}{2}}{\cosh^2 \frac{\pi p}{2}} \sin(pd) = \frac{4\pi d}{\sinh d \cosh d}.$$

This is the exact expression for $h(d)$. The figure 2.4 confirms the convolution formula by comparing it with the result of the numerical integration (dots).

2.5 Critical exponents

The formalism developed in the previous sections may now be employed to analyze the saddle point equations (2.12) and (2.13). These equations describe the physics of the model

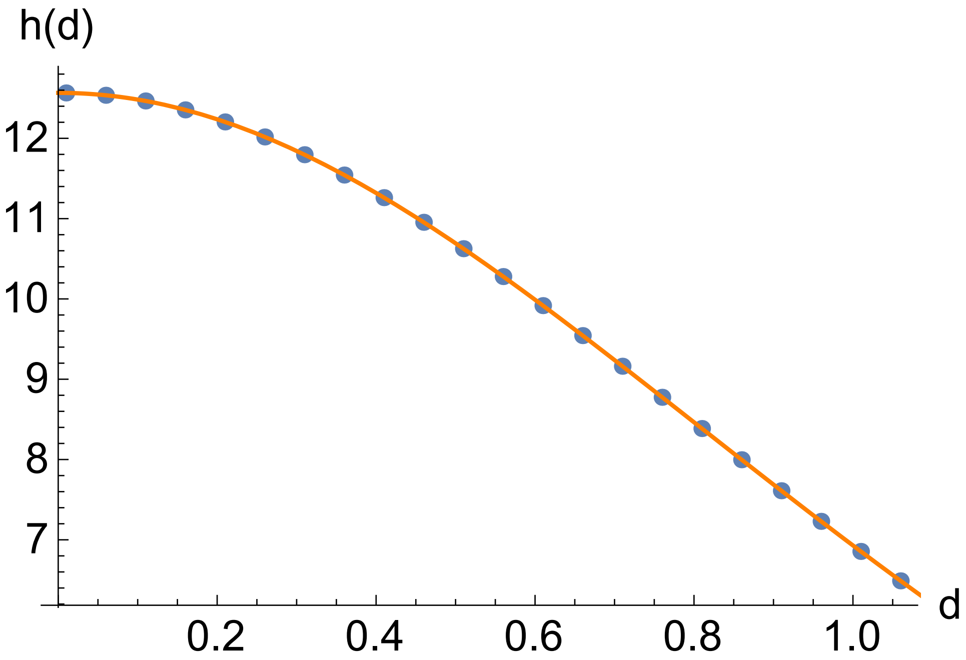

Figure 2.4: The numerical evaluation of the integral (dots) and the claimed exact expression for $h(d)$ coincide.

at lowest order in $1/N$. In principle these are only the lowest order terms in an expansion of the critical exponents in a power series in $1/N$. In flat three-dimensional space there are indeed further corrections. The main result of this work, derived in section 2.8, is to establish the absence of such corrections for η and γ in three-dimensional hyperbolic space.

We begin by computing the bare Green's function $G^{(0)}(p)$ in momentum space for constant μ in the action for $\sigma(\boldsymbol{x})$. The real-space definition of the bare $G^{(0)}(\boldsymbol{r})$ is obtained by inverting the quadratic part of the action, i.e.

$$\left(\mu - \nabla^2\right) G^{(0)}(\boldsymbol{r}, \boldsymbol{r}') = \delta(\boldsymbol{r}, \boldsymbol{r}'). \tag{2.43}$$

Inserting

$$G^{(0)}(\boldsymbol{r}, \boldsymbol{r}') = \frac{\kappa^2}{2\pi^2} \int_{-\infty}^{\infty} dp \sum_l (2l+1) G^{(0)}(p) \Pi_{pl}(\kappa r) \Pi_{pl}(\kappa r') P_l(\cos\gamma) \tag{2.44}$$

and the representation of $\delta(\boldsymbol{r}, \boldsymbol{r}')$ in (2.38), it is found that

$$G^{(0)}(p) = \frac{1}{\mu + \kappa^2 + p^2}. \tag{2.45}$$

At the critical point, $\mu = -\kappa^2$, we have a power-law dependence on p. Employing the inversion formula, we find the real-space dependence

$$G^{(0)}(\boldsymbol{r}, \boldsymbol{r}') = \frac{\kappa}{2\pi^2 i \sinh \kappa d} \int_{-\infty}^{\infty} dp \frac{p e^{ipd}}{\mu + \kappa^2 + p^2} = \frac{\kappa}{2\pi} \frac{e^{-\sqrt{\mu+\kappa^2} d}}{\sinh \kappa d}, \tag{2.46}$$

where d is the geodesic distance between $\boldsymbol{r}$ and $\boldsymbol{r}'$. Evidently, even at the critical point the Green's function decays exponentially, in accord with the previous remarks about parallel-transport.

In flat space the indicator of a phase transition is the divergence of the susceptibility. Thus one expects at the critical point $\mu = \mu_c$ the integral

$$\chi(\mu, q = 0) = 4\pi \int dr\ r^2 \chi(\mu, r)$$

to diverge. This is different in curved space, since

$$\begin{aligned} \chi_q(\mu) &= \frac{2\pi i}{q} \int dx\ \chi(\mu, x) \sinh x\ e^{-iqx} \\ &= \frac{-2\pi}{q} \int dx\ \chi(\mu, x) \sinh x\ \sin(qx). \end{aligned}$$

Thus the divergence of $\chi(q = 0)$ translates into the divergence of

$$-2\pi \lim_{q \to 0} \int dx\ \chi(\mu, x) \sinh x\ \frac{\sin(qx)}{q} \tag{2.47}$$

and not (!) of

$$\int dx\ \chi(\mu, x) \sinh^2 x, \tag{2.48}$$

as one would obtain from replacing the flat-space volume element $4\pi r^2 dr$ by $4\pi \sinh(r)^2 dr$ ($\kappa = 1$). This is the explanation for the fact that the phase transition is not at $\mu = 0$, where $\chi(\mu = 0, x) \sim e^{-2x}$. According to the wrong criterion (2.48) there would be a divergence, but not according to (2.47).

2.5.1 Critical Exponent η

Let us now proceed to the evaluation of the exponent η. At the critical point $\mu = -\kappa^2$ the power-law form of the curved-space bare Green's function in (2.45) agrees with the flat-space limit. The exponent η may therefore be defined through the relation

$$G(p) \propto \frac{\Lambda^{-\eta}}{p^{2-\eta}}. \tag{2.49}$$

We see that the bare $G^{(0)}(p)$, i.e. the lowest order form of the Green's function in an $1/N$ expansion, has $\eta = 0$.

2.5.2 Critical Exponents ν and γ

We now study the behavior of the correlation-length as the critical temperature is approached from the disordered regime by examining the saddle point equation (2.13). In

	η	γ
$\kappa = 0$	$\frac{8}{3\pi^2}\frac{1}{N} + \mathrm{O}\left(\frac{1}{N^2}\right)$	$2 - \frac{24}{\pi^2}\frac{1}{N} + \mathrm{O}\left(\frac{1}{N^2}\right)$
$\kappa \neq 0$	0	2

Table 2.2: Critical exponents in flat and hyperbolic space.

the regime $\mu > -\kappa^2$, the magnetization will be zero. We may therefore set $\sigma = 0$ and obtain

$$\mu = \mu_0 + \frac{uT}{2\pi^2}\int_0^\Lambda dq \frac{q^2}{\mu+\kappa^2+q^2} = \mu_0 + \frac{uT}{2\pi^2}\Lambda - \frac{uT}{2\pi^2}\sqrt{\mu+\kappa^2}\pi. \tag{2.50}$$

At $T = T_c$, where $\mu = -\kappa^2$, we have

$$-\kappa^2 = \mu_0 + \frac{uT_c}{2\pi^2}\Lambda, \tag{2.51}$$

which allows us to remove μ_0 from (2.50). Now close to $\mu \gtrsim -\kappa^2$, the quantity $\sqrt{\mu+\kappa^2}$ dominates over $\mu + \kappa^2$. Thus we neglect the latter and find

$$\sqrt{\mu+\kappa^2} = \frac{1}{\pi}\frac{T-T_c}{T_c}\Lambda. \tag{2.52}$$

The length ξ that diverges at the critical point is defined by

$$\xi = \frac{1}{\sqrt{\mu+\kappa^2}}, \tag{2.53}$$

which is the natural length scale of the problem. At the same time, the real-space form of the correlation function in Eq.(2.46) shows that $G^{(0)}(d)$ decays exponentially beyond the curvature $1/\kappa$, even for $\xi^{-1} = 0$. Therefore, it seems at first glance, that there is an arbitrariness in our definition of the correlation length, caused by the presence of the additional length scale $1/\kappa$ in hyperbolic space. In order to seperate the geometry-induced decay of the Green's function from the decay due to the statistical fluctuations of the field, one need only view the Green's function in the momentum basis. Then it is clear that $G^{(0)}(p)$ is of identical form as the Green's function in flat space and, just as the latter, it becomes scale invariant at T_c. Thus, our definition of the correlation length ξ is indeed the right one. The geometrical decay of $G^{(0)}(d)$ is now seen to enter by means of the $1/\sinh(\kappa d)$ factor of the transformation (2.35) from momentum-space into real-space.
The decay of the correlation function in real-space will, however, have an impact on the $1/N$ corrections of the critical exponents. Defining a critical exponent ν through ξ, we find from (2.52) and (2.53) the exponent

$$\xi \sim (T - T_c)^{-1} \to \nu = 1. \tag{2.54}$$

According to (2.15) the zero-momentum susceptibility is

$$G^{(0)}(q = 0) = \frac{1}{\mu+\kappa^2} \tag{2.55}$$

and by using (2.52) we find $\gamma = 2$.
We emphasize here explicitly the fact that both exponents are not mean-field exponents. The latter are given by $\nu_{\mathrm{MF}} = \frac{1}{2}$ and $\gamma_{\mathrm{MF}} = 1$.

2.6 Remarks about the critical point

The question we want to answer is if the ordered state $\phi = \mathrm{const}$, which minimizes the energy, can be possibly reached. We argue in the following that the correlation function

$\langle\phi(\boldsymbol{r})\phi(\boldsymbol{r}')\rangle$ always has an upper limit for the correlation length, which is never larger than $1/\kappa$. In order to see this we explicitly calculate the correlation in Gaussian approximation by solving the defining differential equation in real space. This removes any doubt that may be associated with the question of whether the momentum space formalism may have difficulties related to the fact that it cannot be used to represent the constant function.
Let us first recapitulate the way this calculation is done in flat space. We compute the correlation function by inverting the inverse propagator of the action, which defines $G(r)$

$$\mu_0 G(r) - \nabla^2 G(r) = \mu_0 G(r) - \frac{1}{r^2}\partial_r(r^2\partial_r G(r)) = \frac{1}{4\pi r^2}\delta(r) \tag{2.56}$$

in real-space. We solve this for $r > 0$ with the ansatz $G(r) = u(r)/r$:

$$u'' + \mu_0 u = 0 \rightarrow u = A\exp(-\sqrt{\mu_0}r) + B\exp(\sqrt{\mu_0}r) \tag{2.57}$$

and hence

$$G_{\text{general}}(r) = \frac{A\exp(-\sqrt{\mu_0}r) + B\exp(\sqrt{\mu_0}r)}{r}. \tag{2.58}$$

Now a point source at the origin cannot lead to an exponentially increasing solution, thus we set $B = 0$ and have

$$G(r) = \frac{A\exp(-\sqrt{\mu_0}r)}{r}. \tag{2.59}$$

The constant is determined to be $A = 1/(4\pi)$.
Notice how by looking at the critical point $\mu_0 = 0$ only, we could not have dismissed the positive exponential solution. We had to look at higher temperatures, in order to find that such a solution would not decay with distance at higher values of μ.
Let us repeat this excercise for hyperbolic space. We have

$$\mu_0 G(r) - \nabla^2 G(r) = \mu_0 G(r) - \frac{1}{\sinh^2(\kappa r)}\partial_r\left[\sinh^2(\kappa r)\partial_r G(r)\right] = \frac{\kappa^2}{4\pi\sinh^2(\kappa r)}\delta(r) \tag{2.60}$$

and solve this again for $r > 0$ with the ansatz $G(r) = u(r)/\sinh(\kappa r)$. We find

$$-u'' + (\mu_0 + \kappa^2)u = 0 \rightarrow u = A\exp(-\sqrt{\mu_0 + \kappa^2}r) + B\exp(\sqrt{\mu_0 + \kappa^2}r) \tag{2.61}$$

and hence

$$G_{\text{general}}(r) = \frac{A\exp(-\sqrt{\mu_0 + \kappa^2}r) + B\exp(\sqrt{\mu_0 + \kappa^2}r)}{\sinh \kappa r}. \tag{2.62}$$

At sufficiently high μ_0 the second solution will diverge with distance, thus we set $B = 0$ and we obtain

$$G(r) = \frac{A\exp(-\sqrt{\mu_0 + \kappa^2}r)}{\sinh \kappa r}. \tag{2.63}$$

Now let us study the two candidates for the critical point $\mu_0 = 0$ and $\mu_0 = -\kappa^2$.

Case I: $\mu_0 = 0$
Here the correlation function is given by

$$G(r) = \frac{A \exp(-\kappa r)}{\sinh \kappa r}. \tag{2.64}$$

Thus the correlation length is $1/(2\kappa)$.
In addition in momentum space this has the form

$$G((p) = \frac{A}{\kappa^2 + p^2}, \tag{2.65}$$

thus fluctuations still have a mass and therefore this cannot be the critical point.

Case II: $\mu_0 = -\kappa^2$
Here the correlation function is given by

$$G(r) = \frac{A}{\sinh \kappa r}, \tag{2.66}$$

which has a correlation length $1/\kappa$.
Moreover, in momentum space this has the form

$$G(p) = \frac{A}{p^2}, \tag{2.67}$$

thus fluctuations now do not have a mass. Therefore at $\mu_0 = -\kappa^2$ we are at the critical point. The real space correlations still decay exponentially. Therefore the ordered state with $\phi =$ const., which requires a correlation length that is infinite, will never be reached. Instead the real-space correlation attains its maximum possible value of $1/\kappa$. The $\phi =$ const. solution may have the lowest energy, but the right question to ask is not what the lowest energy state is, but what is the lowest energy state that has a correlation length that is equal to the one obtained from the correlation function. The correct answer to this is the $p = 0$ eigenmode calculated in an earlier part of this chapter.
That this seems unusual may have to do with the fact that in flat space the real-space correlation at the critical point reaches infinity, while in our problem we have an additional length scale, which allows us to define a different length $1/\sqrt{\mu_0 + \kappa^2}$, which diverges while the real-space correlation length can be read off from (2.63) to be $1/[\sqrt{\mu_0 + \kappa^2} + \kappa]$ and is never larger than $1/\kappa$.

2.7 Remarks about the lowest energy eigenfunction and the constant solution

In the same spirit as in the last section, we want to answer the question of what happens to the fully ordered $\phi =$ const. state of flat space, as κ is tuned from 0 to a finite value. We rederive the magnetization formula of the ordered state without using Fock's identity and then consider the limit $\kappa \to 0$.
The eigenfunctions of the Laplace operator in hyperbolic space are given by

$$\nabla^2 \left[\Pi_p(\kappa r) Y_{lm}(\theta, \phi)\right] = -(\kappa^2 + p^2)\Pi_p(\kappa r) Y_{lm}(\theta, \phi).$$

Let us take a general function, expressible in terms of these eigenfunctions

$$f(r,\theta,\phi) = \int\limits_0^\infty dp \sum_{l=0}^{\infty} \sum_{m=-l}^{l} f_{plm} \Pi_p(\kappa r) Y_{lm}(\theta,\phi)$$

and insert it into the gradient part of the action

$$\begin{aligned}
S_{\text{grad}} &= \int d^3x \sqrt{g} \left[-f\nabla^2 f\right] \\
&= \int dr d\theta d\phi \ \sinh^2\kappa r \sin\theta \Bigg[-\int\limits_0^\infty dp \sum_{l=0}^{\infty} f_{plm} \Pi_p(\kappa r) Y_{lm}(\theta,\phi) \\
&\quad \nabla^2 \left(\int\limits_0^\infty dp' \sum_{l'=0}^{\infty} \sum_{m'=-l'}^{l'} f_{p'l'm'} \Pi_{p'}(\kappa r) Y_{l'm'}(\theta,\phi) \right) \Bigg] \\
&= \int dr d\theta d\phi \ \sinh^2\kappa r \sin\theta \Bigg[\int\limits_0^\infty dp \sum_{l=0}^{\infty} \sum_{m=-l}^{l} f_{plm} \Pi_p(\kappa r) Y_{lm}(\theta,\phi) \left(\kappa^2 + p'^2\right) \\
&\quad \left(\int\limits_0^\infty dp' \sum_{l'=0}^{\infty} \sum_{m'=-l'}^{l'} f_{p'l'm'} \Pi_{p'}(\kappa r) Y_{l'm'}(\theta,\phi) \right) \Bigg] \\
&= \frac{\pi}{2} \int\limits_0^\infty dp \sum_{l=0}^{\infty} \sum_{m=-l}^{l} f_{plm}^2 \left(\kappa^2 + p^2\right)
\end{aligned}$$

where in the last step we used the orthonormality relations

$$\int\limits_0^\pi d\theta \int\limits_0^{2\pi} d\phi Y_{lm}^*(\theta,\phi) Y_{l'm'}(\theta,\phi) \sin\theta = \delta_{ll'} \delta_{mm'}$$

$$\int\limits_0^\infty dr \sinh^2\kappa r \ \Pi_{pl}(\kappa r) \Pi_{ql}(\kappa r) = \frac{\pi}{2} \delta(q-p).$$

The energy is obviously minimized by the $p = 0$ mode. We want to consider isotropic functions, so we only allow $l = m = 0$ components in the expansion of f, i.e. $f(r,\theta,\phi) \to F(r)$. Then we have

$$F(r) = \int\limits_0^\infty dp \ F(p) \Pi_{p0}(\kappa r),$$

where we introduced

$$F(p) \equiv f_{p00}.$$

We have

$$\Pi_{p0}(\kappa r) = \frac{\sin(pr)}{\sinh(\kappa r)}$$

and only want to keep the $p = 0$ eigenfunction. We choose

$$F(p) = -\frac{F_0}{p/\kappa} \delta(p),$$

since otherwise in the limit $p \to 0$ no component would remain (the sign is for convenience and κ is introduced since momenta are expressed in units of κ). Then we have

$$F(r) = F_0 \lim_{p\to 0} \frac{\kappa \sin(pr)}{p \sinh(\kappa r)} = F_0 \frac{\kappa r}{\sinh(\kappa r)}.$$

This is then the form of the lowest energy eigenfunction of the Laplacian. This formula was also derived in a previous section from the Fock identity, as the form of the magnetization $\sigma(r)$ of the $p = 0$ mode.

We now ask how this is related to flat space. For $\kappa \to 0$ this solution is converted into the constant solution $F(r) = F_0$. Or, saying this the other way around, the constant eigenfunction of the Laplace operator in flat space gets transformed into a decaying mode in curved space by increasing the curvature κ from 0 to a finite value.

2.8 Corrections to critical exponents

Corrections to the critical exponents η and γ are found by inspecting the self-energy. In flat space this calculation is described in [53] and we find that the general procedure carries over to hyperbolic space. This procedure consists in first determining how a correction to a critical exponent would manifest itself in the self-energy and calculating the order $O(1/N)$ diagrams to see if such contributions are present.

We start with the action (2.11). The Dyson equation in real-space reads

$$G(\boldsymbol{r}_P, \boldsymbol{r}_R) = G^{(0)}(\boldsymbol{r}_P, \boldsymbol{r}_R) + \int d\boldsymbol{r}_Q \int d\boldsymbol{r}_{Q'}\ G^{(0)}(\boldsymbol{r}_P, \boldsymbol{r}_Q)\Sigma(\boldsymbol{r}_Q, \boldsymbol{r}_{Q'})G(\boldsymbol{r}_{Q'}, \boldsymbol{r}_R) \tag{2.68}$$

and is converted to

$$G^{-1}(p) = G^{(0)-1}(p) + \Sigma(p) \tag{2.69}$$

by application of the convolution theorem. We follow [53] in rewriting this equation as

$$G^{-1}(p) = \Big(G^{(0)-1}(p) + \Sigma(0)\Big) + \Sigma(p) - \Sigma(0) \tag{2.70}$$

and redefining the new inverse bare Green's function $G^{0-1}(p)$ to be the first term, i.e.

$$G^{0-1}(p) = \mu_0 + \Sigma(0) + \kappa^2 + p^2 = \mu + \kappa^2 + p^2. \tag{2.71}$$

This has the advantage that at $T = T_c$ the 'mass' $\mu + \kappa^2$ of the bare propagator vanishes. As a consequence of this redefinition, self-energy insertions in diagrams now take the form $\Sigma(p) - \Sigma(0)$ instead of $\Sigma(p)$.

The large-N structure of the model allows us to restrict ourselves to a small number of diagrams. The calculated corrections will be exact to order $1/N$. The coupling constant u in the action is multiplied by a factor $1/N$. Due to the presence of N fields, there is a summation over the field index at every $(\phi \cdot \phi)^2$ interaction vertex. We represent this interaction term by a dashed line. On the other hand, a summation over the field index at every vertex produces a factor N. Thus the series of bubbles connected by $-u/N$ interaction lines, as shown in Figure 2.5, are all of order $1/N$ and need to be included for consistency. We denote this sum by a wiggly line and use the symbol $D(p)$. It satisfies the relation

$$D(p) = -\frac{u/N}{1 + u\Pi(p)} \approx -\frac{1}{N\Pi(p)} \tag{2.72}$$

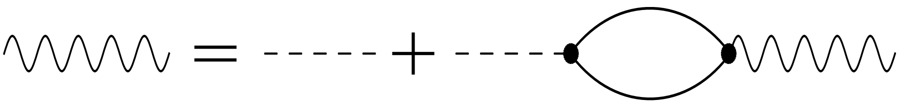

Figure 2.5: Dyson equation for the screened interaction $D(p)$

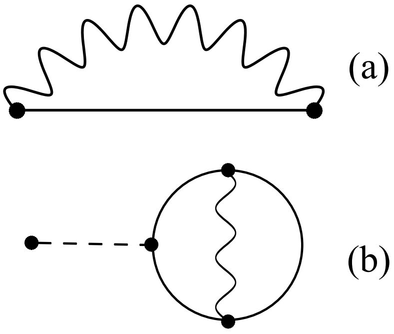

Figure 2.6: Relevant $O(1/N)$ diagrams. In flat space, diagram (a) contributes to η and diagram (b) to γ.

where $\Pi(p)$ is the polarization operator. The approximation comes from the large-u limit, which we will be considering from here on. In real-space Π is given by

$$\Pi(\boldsymbol{r},\boldsymbol{r}') = G^0(\boldsymbol{r},\boldsymbol{r}')^2 = \frac{\kappa^2}{4\pi^2}\frac{e^{-2\sqrt{\mu+\kappa^2}d}}{\sinh^2\kappa d}, \tag{2.73}$$

where d is the geodesic distance between $\boldsymbol{r}$ and $\boldsymbol{r}'$. Using (2.34) we find

$$\Pi_p(\mu) = -\frac{1}{2\pi p}\mathrm{Im}\left[\psi\left(\frac{1}{2}-\frac{ip}{2\kappa}+\frac{\sqrt{\mu+\kappa^2}}{\kappa}\right)\right], \tag{2.74}$$

where $\psi(z) \equiv \frac{d}{dz}\log\Gamma(z)$ is the digamma function. With (2.72) we find

$$D_p(\mu) = \frac{2\pi p}{N}\frac{1}{\mathrm{Im}\left[\psi\left(\frac{1}{2}-\frac{ip}{2\kappa}+\frac{\sqrt{\mu+\kappa^2}}{\kappa}\right)\right]}. \tag{2.75}$$

We present the calculation of the correction to η in detail. The calculation of the correction to γ is much more tedious and is only sketched. The result in both cases is the absence of any corrections due to the regularizing character of finite curvature.

2.8.1 Order $\mathcal{O}(1/N)$ correction of η

As we have seen $\eta = 0$ at lowest order in $1/N$. We now determine the $1/N$ correction to this result. We have defined η in (2.49). Such a correction would manifest itself in the self-energy. For large-N this critical exponent can be expanded and reads

$$G(p) \propto \frac{\Lambda^{-\eta}}{p^{2-\eta}} = \frac{\Lambda^{-\eta}}{p^2 - \eta\, p^2 \log p}, \tag{2.76}$$

i.e. a correction would lead to a $p^2 \log p$ term in the self-energy and could be found as the coefficient of such a term. In flat space there is indeed such a correction. We will now show that this $p^2 \log p$ term of flat space is regularized in hyperbolic space to behave as $p^2 \log \kappa$. The polarization operator (2.74) at the critical point $\mu = -\kappa^2$ becomes

$$\Pi(p) = \frac{1}{4p} \tanh\left(\frac{\pi}{2\kappa} p\right). \tag{2.77}$$

In flat-space the $p^2 \log p$ contribution is produced by the diagram in Figure 2.6a. To write down this term we take the real-space form of $D(p)$, which is obtained from (2.72) with (2.34)

$$D(d_{PQ}) \quad = \quad \frac{8\kappa^4 \cosh(\kappa d_{PQ})}{N\pi^2 \sinh^4(\kappa d_{PQ})}. \tag{2.78}$$

The self-energy in real-space is obtained by multiplying D with the bare Green's function

$$\Sigma(d_{PQ}) \quad = \quad 2D(d_{PQ})G^{(0)}(d_{PQ}) = \frac{8\kappa^5}{N\pi^3} \frac{\cosh(\kappa d_{PQ})}{\sinh^5(\kappa d_{PQ})}. \tag{2.79}$$

Using again formula (2.34), we can write this in momentum space as

$$\Sigma(p) \quad = \quad \frac{8(\kappa^2 + p^2)}{3N\pi^2} \times \left[\mathrm{Re}\psi\left(-\frac{3}{2} + i\frac{p}{2\kappa}\right) + \frac{2/3\, p^2}{9\kappa^2 + p^2} + \gamma - \frac{5}{2} \right], \tag{2.80}$$

where γ is the Euler-Mascheroni constant. Taking the flat-space limit $\kappa \to 0$ with fixed p, we obtain the asymptotic relation

$$\Sigma(p) \sim \frac{8}{3\pi^2 N} p^2 \left(\log \frac{p}{2\kappa} + \gamma - \frac{11}{6} \right). \tag{2.81}$$

The appearance of κ in this formula is owed to the fact that we measure all momenta in units of κ.

In the opposite regime, where p tends to 0 for fixed curvature, we have instead of a logarithmic divergence the finite value

$$\Sigma(p) \sim \frac{8\kappa^2}{3\pi^2 N} \left(\frac{17}{6} - 4\log 2 - \gamma \right). \tag{2.82}$$

This regularizing behavior of the finite curvature is shown in Figure 2.7, where we defined a quantity $\eta(p) \equiv \frac{d}{d\log p}\left[\frac{\Sigma(p)-\Sigma(0)}{p^2}\right]$, which in flat space would yield a finite η. In hyperbolic space at sufficiently small p, i.e. long length-scales, the log behavior of the self-energy (2.80) is cut off and $\eta(p)$ is suppressed to 0.

2.8.2 Order $\mathcal{O}(1/N)$ correction of γ

The exponent γ is found from the divergence of the susceptibility at $p = 0$. We find at zero-momentum for the full Green's function

$$G^{-1}(\mu(T)) \quad = \quad \mu_0(T) + \kappa^2 + \Sigma(\mu(T))$$

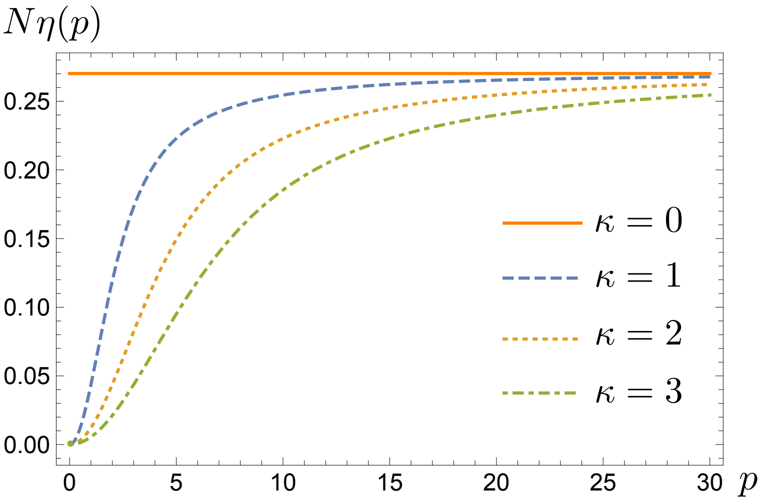

Figure 2.7: Here we have defined a function $\eta(p) \equiv \frac{d}{d\log p}\left[\frac{\Sigma(p)-\Sigma(0)}{p^2}\right]$. In flat space $\eta(p) = \frac{8}{3\pi^2 N}$, whereas in hyperbolic space it is always regularized by curvature and tends to 0 at long length-scales.

$$= \quad \mu(T) + \kappa^2. \tag{2.83}$$

In the following all calculations will be for zero external momenta, thus we have suppressed the momentum arguments. Subtracting from this equation the same equation evaluated at $T = T_c$, we find

$$\mu(T) + \kappa^2 - \Sigma\left(\mu(T)\right) + \Sigma\left(0\right) = \mu_0(T - T_c). \tag{2.84}$$

We have found $\gamma = 2$ at lowest order in section 2.5.2. Writing $1/\gamma = 1/2 - \Delta$ and using the definition of the exponent via $\mu_0(T - T_c) \sim \left(\mu(T) + \kappa^2\right)^{1/\gamma}$ for T near T_c, we obtain

$$-\Sigma\left(\mu(T)\right) + \Sigma\left(0\right) \quad \sim \quad \sqrt{\mu(T) + \kappa^2} - \Delta\sqrt{\mu(T) + \kappa^2}\log\left(\mu(T) + \kappa^2\right) \tag{2.85}$$

valid near $T \gtrsim T_c$. The first term on the right-hand side is an $O(1)$ term and was already obtained in section 2.5. It is produced by a diagram, which is obtained from diagram 2.6b by removing the internal wiggly line.

There are two $O(1/N)$ diagrams that have to be considered in computing the correction Δ, shown in Figures 2.6a and 2.6b. In flat space it can be shown that the diagram in Figure 2.6a only gives a $\sim \mu \log \mu$ correction, whereas the diagram in Figure 2.6b in fact yields a finite Δ. We shall see now that in hyperbolic space neither diagram yields a contribution to Δ, as both logarithmic divergences are regularized by κ.

Diagram (a)

We begin with the diagram in Figure 2.6a. We denote this self-energy part by $\Sigma_a(\mu)$. Using eq. (2.41) we find

$$\Sigma_a(\mu) - \Sigma_a(0) = \frac{1}{8\pi\kappa}\int_{-\Lambda}^{\Lambda} dq \int_{-\Lambda}^{\Lambda} dp\left[G_p(\mu)D_q(\mu) - G_p(0)D_q(0)\right]\frac{pq}{\cosh^2\left(\frac{\pi}{2\kappa}(p-q)\right)}. \tag{2.86}$$

The hyperbolic cosine effectively cuts off contributions with $|p-q| \gg \kappa$. Hence the q-integral may be approximated by limiting the integration to this region. Insertion of $G_p(\mu)$ and $D_q(\mu)$ from (2.45) and (2.75) and subsequent expansion in μ results in a large number of elementary integrals. All logarithmic terms stemming from these integrals are of the form $\log(c\kappa^2+\mu)$, where c is either 1 or 4. In other words, for finite κ no terms proportional to $\log\mu$ are present.

Diagram (b)

Similarly the $\sqrt{\mu}\log\mu$ divergence of the diagram 2.6b in flat-space is regularized. The self-energy expression corresponding to this diagram is obtained by noticing that diagram 2.6b is the result of attaching to the self-energy in 2.6a two legs of the interaction vertex. It is correspondingly given by

$$\begin{aligned}\Sigma_b(\mu) &= \frac{1}{8\pi\kappa}\int dq \int dq'\; qq'\; G_q(\mu)^2\left[\Sigma_a(q',\mu)-\Sigma_a(0,\mu)\right]\frac{1}{\cosh^2\frac{\pi(q-q')}{2\kappa}} \\ &\approx \frac{\kappa^2}{2\pi^2}\int dq'\; \frac{q'^2}{[(q'-2\kappa/\pi)^2+\mu+\kappa^2][(q'+2\kappa/\pi)^2+\mu+\kappa^2]}\left[\Sigma_a(q',\mu)-\Sigma_a(0,\mu)\right]\end{aligned} \tag{2.87}$$

where the same approximation as before has been made. In the integrand the momentum-dependent self-energy $\Sigma_a(q,\mu)$ is required. According to (2.40) this is given by

$$\Sigma_a(q',\mu) = \frac{1}{4\pi^2 q'\kappa}\int\limits_{-\Lambda}^{\Lambda} dp' \int\limits_{-\Lambda}^{\Lambda} dp\,\left[G_p(\mu)D'_p(\mu)-G_p(0)D'_p(0)\right] pp' \tanh\left(\frac{p+p'-q'}{2\kappa}\pi\right). \tag{2.88}$$

Inside the p-integral we approximate the tanh-function in the region $|p+p'-q| < \frac{2\kappa}{\pi}$ by its argument and outside this region by the sign-function. Then the p-integral may be carried out without a cutoff and we are left with a p'-integral. Insertion of (2.88) into (2.88) and integration over q' results in

$$\Sigma_b(\mu) = \frac{2\pi^2}{\kappa\lambda}\int\limits_0^{\Lambda} dq' \frac{q'^2}{\mathrm{Im}\psi\left(\frac{1}{2}-\frac{iq'}{2\kappa}+\frac{\lambda}{\kappa}\right)}\log\frac{(q'-2\kappa)^2+4\lambda^2}{(q'+2\kappa)^2+4\lambda^2} + R(\kappa). \tag{2.89}$$

where $R(\kappa)$ denotes terms that tend to 0 with $\kappa \to 0$. The first term on the right-hand side reproduces for $\kappa = 0$ fully the flat space formula for Σ_b. This self-energy contains the $\sqrt{\mu}\log\mu$ term. For finite κ, however, the integral in (2.89) is fully regularized and a $\sqrt{\mu}\log\mu$ term is avoided. Thus, we conclude that no singular correction to the μ dependence of the self-energy emerges, i.e. the exponent γ is also unchanged compared to the leading order $1/N$ expression given above.

2.9 Discussion

The aim of this work was to investigate critical phenomena in hyperbolic space. Our key finding is that for a ϕ^4-model embedded in hyperbolic space a new fixed point emerges at finite curvature κ. If $\kappa > 0$ the critical exponents are governed by the strong curvature limit. Interestingly, these exponents are given by leading order terms of the $1/N$ expansion. Thus, while the numerical values of the exponents are now simpler, they continue to obey hyperscaling below the upper critical dimension.

The physical state in the symmetry-broken regime is characterized by an unusual magnetization texture. This texture consists of regions of size of the order of the radius of curvature $1/\kappa$ where the vector $\boldsymbol{\phi}$ has nearly uniform direction. Beyond this region the finite value of the curvature starts to play an important role, since even at the critical point correlations decay exponentially in hyperbolic space. It is therefore not possible to establish a uniform direction of the magnetization vector.

The fact that the $\kappa \neq 0$ values of exponents are different from the flat space $\kappa = 0$ limit may be understood using standard crossover arguments as we now show using the example of magnetic susceptibility. Let $f(t, h, \kappa)$ be the singular part of the free energy density, where $t \propto (T - T_c)/T_c$ measures the distance to the critical point and h is the external field. Then the following scaling transformation holds

$$f(t, h, \kappa) = b^{-3} f\left(b^{1/\nu_f} t, b^{y_f} h, b\kappa\right), \tag{2.90}$$

with exponents ν_f for the correlation length and scaling dimension of the conjugate field $y_f = \beta_f \delta_f / \nu_f$ that refer to the flat space ($\kappa = 0$) limit. The curvature is a relevant perturbation with positive scaling dimension, i.e. the infrared behavior is governed by the infinite curvature fixed point, where all scales (except of course for the inverse ultraviolet cut-off) are larger compared to the radius of curvature. Performing the second derivative with respect to the conjugate field, we obtain the scaling expression for the order parameter susceptibility:

$$\begin{aligned} \chi(t, \kappa) &= b^{\gamma_f/\nu_f} \chi(b^{1/\nu_f} t, b\kappa) \\ &= t^{-\gamma_f} \Phi\left(\frac{\kappa}{t^{\nu_f}}\right). \end{aligned} \tag{2.91}$$

In the flat space limit $\kappa = 0$, the scaling function behaves as $\Phi(x \to 0) \to$ const. and we recover the flat space results. On the other hand, our above analysis implies that for large argument $\Phi(x \gg 1) \propto x^{-\phi}$ holds with crossover exponent

$$\phi = \frac{\gamma - \gamma_f}{\nu_f} = \frac{24}{N\pi^2}. \tag{2.92}$$

Here γ is the susceptibility exponent of the hyperbolic space obtained above. Thus, we find $\chi(t, \kappa) \propto \kappa^{-\phi} t^{-\gamma}$. The behavior $\kappa^{-\phi}$ is, at the considered order, fully consistent with the $\phi \log(\kappa)$ behavior that occured in our explicit analysis.

We have calculated the critical exponents η, γ and ν at lowest order in $1/N$ and found that these are identical to the exponents in flat three-dimensional space at lowest order. For η and γ we showed that $\mathrm{O}(1/N)$ corrections are absent. As our calculations show, the reason for this absence is the fact that correlations are exponentially decaying beyond the radius of curvature even at the critical point. The lowest order values of the exponents are computed from local quantities, which are oblivious to the finite curvature, whereas the higher-order corrections are determined through integration over the whole of hyperbolic space, wherein the finite curvature serves to cut off the long-wavelength fluctuations. For this reason, we may also surmise the absence of corrections to the other critical exponents. It is moreover plausible to assume for the same reason that higher-order corrections to the exponents will also be absent in the $1/N$-expansion. Thus we conjecture that the critical exponents we found are correct to all orders in $1/N$. We emphasize that our results establish that mean-field behavior, which [4] argued for, does not hold.

An interesting question is how our results are modified for dimensions d different from 3. The Laplacian in $d \neq 3$ dimensions is still gapped. The only modification in our lowest order $1/N$ calculations of the critical exponents would be a change of the integration measure in (2.50), from p^2 to p^{d-1}, multiplied by a numerical factor. However, this leads again the same saddle point equations as in flat space. Thus we can make the stronger statement that all critical exponents in hyperbolic space are just the leading order $1/N$ exponents of flat space. In particular, we have $\nu = \frac{1}{d-2}$ and $\gamma = \frac{2}{d-2}$ for $d \leq 4$ and mean-field exponents for $d > 4$. The upper critical dimension is $d = 4$ even for finite κ.
In summary, we conclude that the description of many-particle systems in hyperbolic space is a promising avenue to investigate uniform frustration and non-trivial critical behavior within one theoretical approach.

Chapter 3

Geometric frustration in the ground state

In this chapter we begin the study of a particular Heisenberg spin model, the so-called *windmill model*, that shows emergent critical behavior despite the fact that the lattice is two-dimensional and the couplings are short ranged as well as isotropic. That this emergent criticality is possible is owed to the fact that the Heisenberg windmill model is geometrically frustrated. *Geometric frustration* is present as soon as spins on the lattice are not able to simultaneously satisfy all bonds to neighboring spins, in the sense that each bond has a minimum energy of interaction. Instead, a compromise is achieved in which each spin minimizes its energy as much as possible.

The windmill lattice is formed out of two widely occurring lattice geometries: a triangular lattice, coupled to its dual honeycomb lattice. The phase diagram shows a rich phenomenology due to geometric frustration. One of these phases is a decoupled phase, where at $T = 0$ one sublattice is energetically decoupled from the other. This is essential for the emergence of the critical behavior that we explore in the next chapter, where we show that the relative orientation of the two sublattices allows the introduction of an emergent $U(1)$ degree of freedom, which can undergo phase transitions.

The source of frustration in this model stems from the fact that the intra- and inter-sublattice couplings are all antiferromagnetic. If all couplings were ferromagnetic, the system would have a single ground state configuration, independent of the numerical value of the coupling constants, namely a trivial uniaxial order. The fact that the couplings are antiferromagnetic necessitates compromises in the spin configurations. This leads to a large number of ground state spin configurations, each one of which is the optimum configuration given certain values of the coupling constants.

Using a combination of iterative minimization, heat-bath Monte Carlo simulations and analytical calculations, we determine the complete ground state phase diagram of both models and find the exact energies and spin configurations of the phases. The model has ground states among which are, in addition to collinear and various coplanar phases, also intricate non-coplanar phases. Different paths to experimental realizations of these spin models are outlined. Our extensive study provides a starting point for the investigation of quantum and thermal fluctuation effects.

This chapter is based on work done in

Bhilahari Jeevanesan and Peter P. Orth *Classical ground states of Heisenberg and XY antiferromagnets on the windmill lattice* Phys. Rev. B 90, 144435

that was published in October 2014.

3.1 Introduction

Insulating materials that host localized spin degrees of freedom can exhibit complex ground states and fascinating low-temperature properties. This behavior frequently arises from competing interactions that cannot be satisfied simultaneously. Prime examples are antiferromagnetic nearest-neighbor spin couplings on frustrated geometries like the two-dimensional (2D) triangular and kagome lattice or the three-dimensional (3D) pyrochlore lattice [80, 10, 62]. These systems are characterized by a large degeneracy of classical ground states. This often leads to complex states of matter and phase transitions if quantum or thermal fluctuations are present [35, 90, 15].

A triangular lattice geometry with antiferromagnetic spin couplings is realized in a large number of magnetic materials such as $\mathrm{Cs_2CuCl_2}$ [17, 16, 79], $\mathrm{Na}_x\mathrm{CoO_2}$ [99, 28], $\mathrm{NaCrO_2}$ [71, 34] and $\alpha-\mathrm{NaFeO_2}$ [56]. Another frustrated triangular material is the recently discussed cluster magnet $\mathrm{LiZn_2Mo_3O_8}$ [89, 88, 64, 26]. Here, $\mathrm{Mo_3O_{13}}$ clusters that carry a total spin $S = 1/2$ are arranged in two-dimensional triangular lattice planes that are weakly coupled along the third dimension. Another lattice geometry that exhibits frustration effects if further neighbor antiferromagnetic couplings are present is the honeycomb lattice. This lattice is dual to the triangular lattice. It is realized in various solid-state compounds and can arise by replacing one third of the magnetic ions in a triangular lattice system by a non-magnetic one. This is done, for example, in $\mathrm{Na_2Co_2TeO_6}$ or $\mathrm{Na_3Co_2SbO_6}$ [101]. Another recently discussed interesting honeycomb material is $\mathrm{Na}_{1-x}\mathrm{NiSbO_6}$, where magnetic Ni^{2+} and Ni^{3+} form a honeycomb lattice with mixed spins $S = 1/2$ and $S = 1$.

Here, we study the situation where these two lattice geometries are combined and consider spins on a honeycomb lattice that are antiferromagnetically coupled to spins situated on a triangular lattice. It has recently been shown that such a setup shows order-from-disorder effects in the regime of weakly coupled sublattices that leads to surprising new phenomena. There, an emergent $\mathbb{Z}_6$ degree of freedom has been revealed that exhibits a sequence of Berezinskii-Kosterlitz-Thouless phase transitions bracketing a critical phase [72, 73]. Experimentally, such a situation might arise, for example, in the cluster magnet $\mathrm{LiZn_2Mo_3O_8}$ at low temperatures [26] or in a material such as $\mathrm{Na}_{1-x}\mathrm{NiSbO_6}$ by replacing the non-magnetic ion Sb by a magnetic one. The progress in chemical synthesis, in particular considering the approach of using small magnetic clusters as basic units, might bring other experimental candidates in the future as well, possibly with a large spin $S > 1/2$.

Another experimental platform where classical frustrated magnetism has been investigated in recent years is based on cold bosonic atoms in optical lattices [94, 95]. At low temperatures and for weak interactions these systems form a superfluid and the atoms at site i in the lattice have a well-defined local phase ϕ_i. This local phase degree of freedom can be interpreted as a classical planar (XY) spin $\big(\cos\phi_i, \sin\phi_i\big)$. Nearest-neighbor spins are coupled via tunneling of atoms between the sites. For regular tunneling of atoms

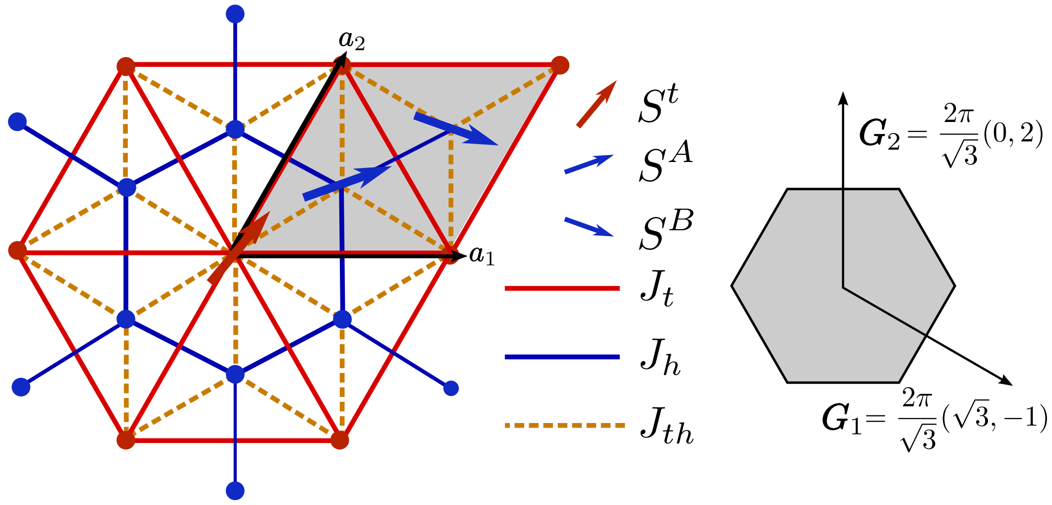

Figure 3.1: Windmill lattice. Left: The lattice may be thought of as a triangular lattice (red vertices) together with its dual honeycomb lattice (blue vertices). The model has a three-site basis. The Bravais lattice vectors are $\boldsymbol{a}_1$ and $\boldsymbol{a}_2$. The shaded region is a unit cell. Right: Reciprocal lattice vectors with first Brillouin zone.

between the sites, the associated coupling between the planar spins is ferromagnetic. By shaking the lattice in a periodic way, however, it is possible to add a non-zero Peierls phase to the tunneling element. In this way, it is possible to induce a change in the sign of the tunneling element which leads to an antiferromagnetic coupling between the spins. Within this approach, different links of the lattice can be addressed independently. Frustration effects have been experimentally observed on the triangular lattice via standard time-of-flight imaging [94]. Honeycomb optical lattice geometries have also been realized in the past [74, 98].

This serves as our motivation to extensively study the classical Heisenberg and the classical planar (XY) spin model on a lattice that combines both a honeycomb and a triangular lattice. We refer to this lattice, which is shown in Fig. 3.1, as the “windmill lattice”. Considering antiferromagnetic interactions between all nearest-neighbor pairs of spins, we determine the complete ground state phase diagram of both models. Due to competing interactions, the models turn out to show an extremely rich ground state phenomenology. For the Heisenberg model we find that next to phases where the spins order in a collinear or a coplanar fashion there exist also phases where the spins exhibit an intricate non-coplanar configuration where they arrange themselves into seperate double cones. In the windmill XY model those non-coplanar phases are replaced by other similarly involved configurations.

The structure of this chapter is as follows: in Sec. 3.2 we introduce the classical Heisenberg and planar spin models on the windmill lattice, and in Sec. 3.3 we describe the methods that we employ to obtain the ground state phase diagram. We use an “iterative minimization” technique to find a variational expression of the ground state whose energy can be analytically computed, minimized and compared to the numerical result. In Sec. 3.4 we present one of our main results: the full ground state phase diagram of the Heisenberg model on the windmill lattice as a function of exchange couplings. In Sec. 3.5, we then discuss the various ground state phases in detail. In Sec. 3.6 we analyze the planar (XY) model on the windmill lattice and determine its complete ground state phase diagram. In the appendices we provide the details on the calculation of all the ground state energies from the variational forms.

3.2 Windmill spin model

The windmill lattice that we study consists of a triangular lattice combined with its dual, honeycomb lattice. The windmill lattice can be described as a triangular Bravais lattice with a three-site basis per unit cell containing triangular, honeycomb A and B sites. The spins are positioned on the vertices of the lattice as shown in Fig. 3.1. We consider classical spins with an antiferromagnetic exchange coupling between all nearest-neighbor pairs of spins. The Hamiltonian of the windmill model reads

$$\begin{aligned} H &= J_t \sum_{\langle ij \rangle} \boldsymbol{S}_i^t \cdot \boldsymbol{S}_j^t + J_h \sum_{\langle ij \rangle} \boldsymbol{S}_i^A \cdot \boldsymbol{S}_j^B \\ &\quad + J_{th} \sum_{\langle ij \rangle, \nu = A,B} \boldsymbol{S}_i^t \cdot \boldsymbol{S}_j^\nu \end{aligned} \tag{3.1}$$

where $\langle i, j \rangle$ denotes summation over each nearest-neighbor pair, the index $\{t, A, B\}$ refers to the sublattices and J_t, J_h, J_{th} are positive, *i.e.*, antiferromagnetic, coupling constants. In the classical windmill model all spins are classical unit vectors. The vectors have three components in the case of Heisenberg spins $\boldsymbol{S}_i^\alpha = (S_{i,x}^\alpha, S_{i,y}^\alpha, S_{i,z}^\alpha)$ and two components in the case of planar (XY) spins $\boldsymbol{S}_i^\alpha = (S_{i,x}^\alpha, S_{i,y}^\alpha)$ with $\alpha \in \{t, A, B\}$.

The triangular Bravais lattice with lattice constant a is spanned by the primitive lattice vectors $\boldsymbol{a}_1 = a(1, 0)$ and $\boldsymbol{a}_2 = \frac{a}{2}(1, \sqrt{3})$. The basis vectors are given by $\boldsymbol{b}_t = (0, 0)$, $\boldsymbol{b}_A = \frac{1}{3}\boldsymbol{a}_1 + \frac{1}{3}\boldsymbol{a}_2$ and $\boldsymbol{b}_B = \frac{2}{3}\boldsymbol{a}_1 + \frac{2}{3}\boldsymbol{a}_2$. The reciprocal vectors take the form $\boldsymbol{G}_1 = \frac{2\pi}{\sqrt{3}a}(\sqrt{3}, -1)$ and $\boldsymbol{G}_2 = \frac{2\pi}{\sqrt{3}a}(0, 2)$, and are shown in Fig. 3.1.

3.3 Methodology

All the results in this chapter were obtained by using an "iterative minimization" algorithm that has been employed in the literature to discover ground state configurations of classical spin models [91, 48]. Independently we verified our results by using heat-bath Monte Carlo simulations [61] in combination with parallel tempering updates [55, 36]. We then extract variational forms of the spin configurations and determine the variational parameters by minimizing the corresponding ground state energies. We analytically find the configuration of minimal energy which determines the phase diagram and the phase boundaries.

We begin with an explanation of the iterative minimization algorithm. Starting from a randomized spin configuration, in every iteration of the algorithm a spin is chosen at random and rotated such as to minimize the interaction energy with its neighbors. Each step of the algorithm is an update of the form

$$\boldsymbol{S}_i^t \rightarrow \boldsymbol{S}_i^t = -\frac{J_t \sum_k \boldsymbol{S}_k^t + J_{th} \sum_{k,\nu} \boldsymbol{S}_k^\nu}{\| J_t \sum_k \boldsymbol{S}_k^t + J_{th} \sum_{k,\nu} \boldsymbol{S}_k^\nu \|} \tag{3.2}$$

$$\boldsymbol{S}_j^\alpha \rightarrow \boldsymbol{S}_j^\alpha = -\frac{J_h \sum_{k,\nu} \boldsymbol{S}_k^\nu + J_{th} \sum_k \boldsymbol{S}_k^t}{\| J_h \sum_{k,\nu} \boldsymbol{S}_k^\nu + J_{th} \sum_k \boldsymbol{S}_k^t \|} \tag{3.3}$$

with the index $\alpha \in \{A, B\}$. The sum over index $\nu = A, B$ runs over both honeycomb sublattices and the summation over the index k ranges over the neighbors of the spin that is being updated. This technique does not provide rigorous proofs for the correctness of the discovered phases. One difficulty that one may imagine is that the algorithm converges to a local minimum of the energy landscape. In this case a local update is not capable of improving the energy. This possibility is made unlikely by the fact that for all phases we ran the algorithm multiple times with different random initial configurations and observed that the system always converged to the same phase.

In order to discover the groundstate configurations, the algorithm was applied to a spin system with $N = L \times L = 30 \times 30$ unit cells (*i.e.*, N triangular spins and $2N$ honeycomb spins) with periodic boundary conditions. We applied the minimization algorithm for 50,000 steps. The resulting spin configurations were all explored and a mathematical description of their spin ordering was extracted, from which the energies were analytically calculated.

After the numerical search, we performed systematic runs on a lattice with $N = 12 \times 12$ unit cells to confirm the absence of further phases. This run was performed for the regime of parameters $J_h/J_t \in [0.2, \ldots, 9.4]$ in steps of 0.1 and $J_{th}/J_t \in [0.2, \ldots, 9.4]$ in steps of 0.1. At every point within this parameter range, the minimization algorithm was applied for $60,000 \times N$ iterations. Every application optimized one randomly chosen triangular lattice spin and one randomly chosen honeycomb lattice spin. The resulting energies of the converged configurations were compared to the analytically computed energies.

Some of the discovered phases have spin configurations that depend parametrically on the coupling constants such as the pitch angle in a spiral phase. Here, we computed the energy by leaving these variables, like the pitch angle, as variational parameters and obtained their value by minimizing the energy with respect to the parameters. In most cases, the results of the simulation were highly converged such that the energy per spin that emerged from the simulation numerically coincided exactly with the energy computed by minimization of the variational state. Similarly, the spin configurations (e.g. scalar products between neighboring spins) of all the simulated phases were to many digits identical to those of the phases proposed. In the few cases where the convergence was not so good, which was evidenced by the higher energy per spin value, we investigated snapshots of the spin configurations and found that the algorithm had been trapped in a local minimum with topological defects that could not be removed by local updates. Nevertheless, even in the presence of these defects the snapshots still showed ordering of the spins that were clearly those of the proposed phases.

As a final test we repeated the systematic run with Monte Carlo simulations. The simulations were carried out at 40 temperature points T_i covering the interval $[10^{-3}J_t, \ldots, 2.0J_t]$. The temperature points are chosen to be geometrically spaced [41], *i.e.*, T_{i+1}/T_i is a constant ratio. The lattice has $N = L \times L = 30 \times 30$ unit cells and we again employ periodic boundary conditions. The simulations are done in parallel for all temperatures with the spin configurations of the 40 lattices stored simultaneously. To every one of these lattices the heat-bath algorithm is applied N times. This is followed by a parallel tempering move. The latter kind of update consists in proposing for every pair of neighboring temperatures (T_i, T_{i+1}) an exchange of the full spin configurations. The proposals are accepted/rejected according to the standard Metropolis-Hastings rule. The parallel tempering algorithm helps to quickly produce uncorrelated spin configurations.

The cycle of heat-bath steps followed by parallel tempering updates was repeated a total of $10,000$ times before we finally measured the energy of the lattice with the smallest temperature.

In this way the energies were determined for the coupling constants in the parameter regime $j_h \equiv J_h/J_t \in [0.1, \dots, 10.0]$ and $\bar{J} \equiv J_{th}/\sqrt{J_t J_h} \in [0.1, \dots, 4.0]$. We found all resulting energies to be slightly larger than the analytically calculated minimum energies. This is further confirmation of the absence of ground state phases other than the ones we have found.

3.4 Ground state phase diagram of Heisenberg windmill model

The complete ground state phase diagram of the Heisenberg windmill model is shown in Fig. 4.14 as a function of the ratios of coupling constants J_t/J_h and $J_{th}/\sqrt{J_t J_h}$. Note that the vertical axis is the ratio J_t/J_h in the upper panel of the figure, while we use the inverse ratio J_h/J_t in the lower panel. The horizontal axis is $J_{th}/\sqrt{J_t J_h}$. In total, the Heisenberg model exhibits eight different ground state phases, which we describe in detail in Sec. 3.5.

The energies of the different spin configurations, measured in units of J_t, are functions of the dimensionless coupling constant ratios

$$j_h = J_h/J_t \tag{3.4}$$

$$j_{th} = J_{th}/J_t. \tag{3.5}$$

The ground state energy $E(j_h, j_{th})$ is defined as the energy of the spin configuration with the lowest energy, and the ground state phase is described by this spin configuration.

As a function of the couplings j_h and j_{th} there will eventually be level crossings where the energies of the spin configurations with the lowest two energies switch places [31]. A phase transition occurs at a crossing of the energies of two different spin configurations. Exactly at the transition point, their energies match, but their (higher order) derivatives will generally not be the same. According to the usual Ehrenfest classification of phase transitions, the order of the phase transition is determined by the lowest order of the derivative of the ground state energy $E(j_h, j_{th})$ with respect to the tuning parameter, j_h or j_{th}, that exhibits a singularity. In the phase diagram we have indicated the order of the phase transition by the labels 1^{st} and 2^{nd} for first and second order phase transitions.

Some of the discovered phases are continuously connected to each other, and exactly at the level crossing the spin configurations are identical. We often denote those phases in the phase diagram by the suffix a or b. In this case both the energies as well as the first order derivatives of the energies will match at the transition point. The second order derivatives, however, will in general not be equal. The phase transitions between phases that are continuously deformed into each other at the transition are therefore always of second order.

There are two special points in the phase diagram, where multiple phases become energetically degenerate. These are the points $(j_h, j_{th}/\sqrt{j_h}) = (1/4, 1)$ and $(j_h, j_{th}/\sqrt{j_h}) = (1, 2)$. One would not expect a large number of unrelated phases to coincide at one point. In fact, one can prove a simple result similar to the Gibbs phase rule [22] about the number of generically coinciding, energically degenerate phases. Let $E_1(j_h, j_{th}), E_2(j_h, j_{th})$ and $E_3(j_h, j_{th})$ be the energies of three minimum energy phases. The requirement that these energies should coincide at a point (j_h, j_{th}) is expressed by the conditions

$$E_1(j_h, j_{th}) = E_2(j_h, j_{th}) \tag{3.6}$$

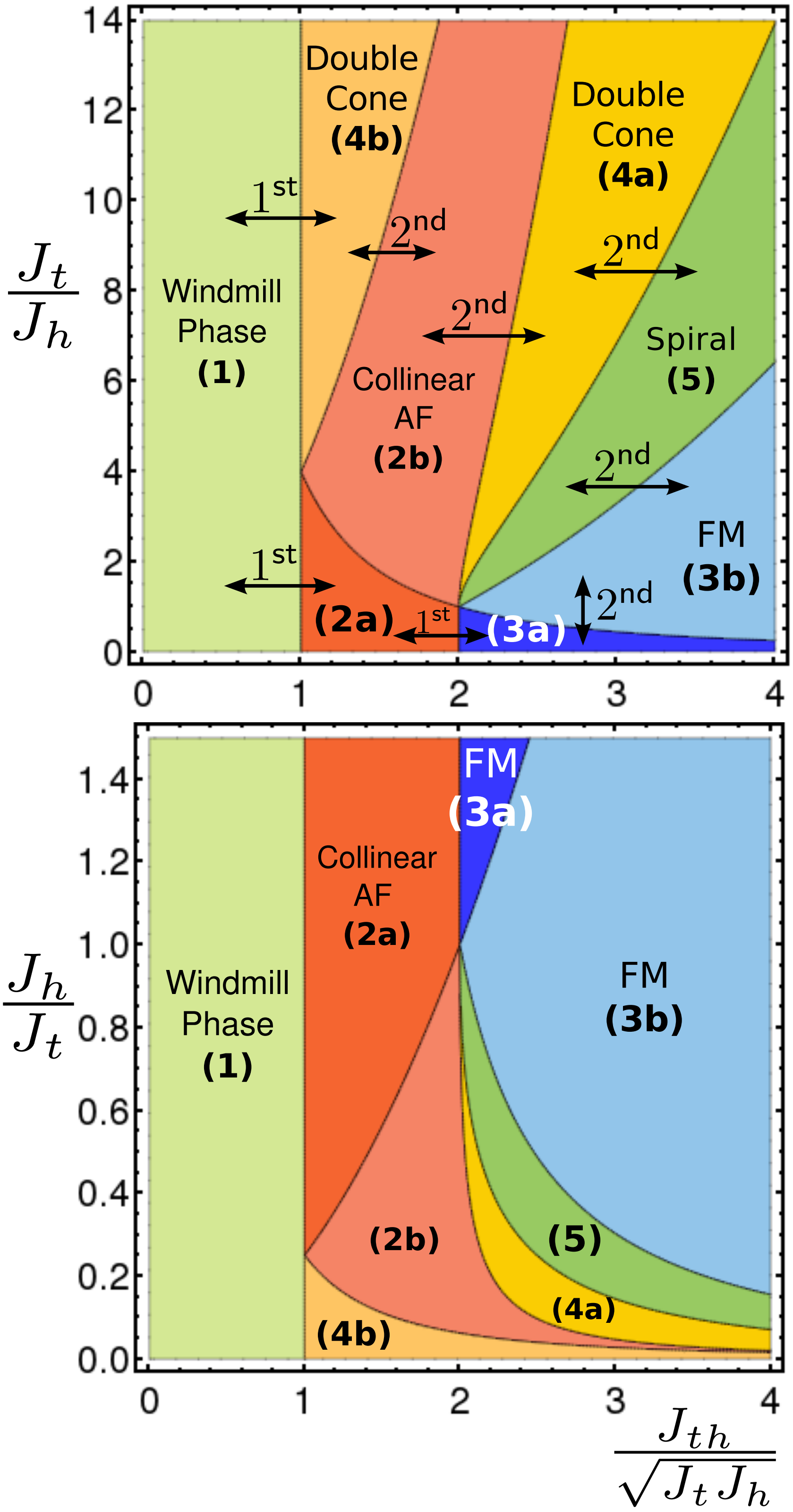

Figure 3.2: Ground state phase diagram of the Heisenberg model on the windmill lattice as a function of the dimensionless ratios of coupling constants J_t/J_h and $J_{th}/\sqrt{J_t J_h}$. In the upper figure we use the y-axis label J_t/J_h while in the lower figure we use the inverse ratio J_h/J_t. The different phases are described in detail in Sec. 3.5. The order of the phase transition between the phases is indicated above the arrows. The non-coplanar phases are labelled $(4a)$ and $(4b)$.

$$E_2(j_h, j_{th}) = E_3(j_h, j_{th}) \tag{3.7}$$

which can be expected to be a solvable system in j_h and j_{th}, since the number of variables equals the number of conditions. Equating a larger number of energy functions will generally result in an overdetermined, unsolvable system, unless the energy functions are related to each other in a special way. Thus the number of generically coincident points is limited to three.

In the ground state phase diagram in Fig. 4.14 there are, however, seven phases coinciding at the point $(j_h, j_{th}/\sqrt{j_h}) = (1, 2)$ and four phases coinciding at the point $(j_h, j_{th}/\sqrt{j_h}) = (1/4, 1)$. This is possible because a number of these phases are related to each other in the way described above, *i.e.*, they continuously transform into each other at the degeneracy point.

Let us consider the point $(j_h, j_{th}/\sqrt{j_h}) = (1, 2)$ in more detail. The detailed description of the different phases can be found below in Sec. 3.5. Exactly at the point $(j_h, j_{th}/\sqrt{j_h}) = (1, 2)$ there are two energetically equal ground state configurations, which are those of phase (2*b*) and phase (3*b*) (see Secs. 3.5.2 and 3.5.3). In the limit $(j_h, j_{th}/\sqrt{j_h}) \to (1, 2)$ the spin configurations of all the surrounding phases are equal to the configuration of one of these two phases. All these phases must, therefore, meet at this point in the phase diagram. Obviously phase (2*a*) deforms into (2*b*) and phase (3*a*) into (3*b*). The half-opening angles of the conical phase (4*a*) (see Sec. 3.5.4) go to zero in this limit, which yields a spin configuration identical to the one of phase (2*b*). Similarly, the spiral angle of phase (5) (see Sec. 3.5.5) goes to zero resulting in a spin configuration that is identical to the one of phase (3*b*).

A similar line of reasoning explains the degeneracy at the point $(j_h, j_{th}/\sqrt{j_h}) = (1/4, 1)$. Here, phases (4*b*) and (2*a*) turn into (2*b*). The opening angle α_t of the double cone configuration tends to zero as the border to region (2b) is approached. This border includes the degeneracy point, as shown in the phase diagram.

3.5 Ground state phases

In the following we describe the phases that were found in a broad search of the two-dimensional parameter space $(j_h = J_h/J_t, j_{th}/\sqrt{j_h} = J_{th}/\sqrt{J_t J_h})$. The phases are labelled as shown in the phase diagram in Fig. 4.14. In describing these phases we adopt the convention of placing the spins in the coplanar phases in the S_x-S_y-plane in spin space. In many of the following phases there is an additional degeneracy in that a certain symmetry may be broken along different directions of lattice space. In such cases we adopt one particular direction for the description of the phase and follow this with a discussion about the symmetry properties. Next to the figures with the spin arrangements are shown the positions of the ordering wave vectors in the Brillouin zone with the wave vectors of the honeycomb lattice as blue points and triangular lattice as red points.

In some of the following ground state phases the symmetry of the lattice is broken. This can manifest itself, for example, in stripes of equal spin orientation along a certain direction in lattice space. In such cases, one can obtain a distinct, but energetically degenerate ground state by means of a rotation of all spins in lattice space around an arbitrary triangular site. The description of such a rotated state is complicated by the fact that the windmill lattice has a three site basis. The operation of rotating the lattice by 60° will in general also involve a reattribution of honeycomb spins to their respective unit cells and a possible relabeling of A into B site spins and vice versa. In order to avoid such complications, our description in the following will always be of only one lattice configuration. The other symmetry related configurations are discussed.

The differerent phases are characterized by their order parameter manifold. This manifold is defined as the symmetry group, whose elements transform a given spin configuration into a distinct, but energetically degenerate configuration. A simple (anti-)ferromagnetic state in the Heisenberg model thus has the order parameter manifold $O(3)/O(2)$, since it is characterized by a normalized unit vector in the direction of magnetization $\boldsymbol{n}$. Global rotations around an axis that is not (anti-)parallel to a given magnetization $\boldsymbol{n}$ yield another energetically degenerate ground state spin configuration. In Table 3.4 we list the order parameters manifolds of the various ground state phases.

We measure energies in units of NJ_t, where N is the number of spins on the triangular lattice. The energies of the ground state spin configurations can be analytically calculated and are given in Table 3.2. We refer to Appendix B for the details. Finally, in Table 3.3 we list the functional forms of the boundaries between the phases, which are calculated from the explicit form of the energies and the conditions for the existence of phases. The same table also contains the order of the phase transitions between two neighboring phases. For completeness we also include in these tables the additional phases found in the planar windmill model that is discussed in Sec. 3.6.

Phase	Order Parameter Manifold (Heisenberg model)
1	$SO(3) \times O(3)/O(2)$
2a, 2b	$O(3)/O(2) \times O(2) \times \mathbb{Z}_3$
3a	$O(3)/O(2) \times O(2)$
3b	$O(3)/O(2)$
4a	$SO(3) \times \mathbb{Z}_3$
4b	$SO(3) \times \mathbb{Z}_3$
5	$SO(3) \times \mathbb{Z}_3$

Table 3.1: Order parameter manifold of the ground state phases of the Heisenberg windmill model. The elements of these group manifolds transform energetically degenerate ground state spin configurations into each other.

Phase	Energies E/NJ_t	Condition
1	$-\frac{3}{2} - 3j_h$	none
2a	$-1 - 3j_h - \frac{j_{th}^2}{2j_h}$	$2j_h \geq j_{th}$
2b	$-1 - j_h - 2j_{th}$	$2j_h \leq j_{th}$
3a	$3 - 3j_h - \frac{3}{2}\frac{j_{th}^2}{J_h}$	$2j_h \geq j_{th}$
3b	$3 + 3j_h - 6j_{th}$	$2j_h \leq j_{th}$
4a	see (B.42)	$j_{th}^2 \geq 4j_h$, $\sigma \leq 1 \leq \rho$
4b	$-\frac{3}{2} - j_h - 2j_{th}^2$	$2j_{th} \leq 1$
5	$-\frac{3}{2} - \frac{(2j_{th}-j_h)^2}{2}$	$\lvert 1 + j_h - 2j_{th} \rvert \leq 2$
XY I	$-\frac{3}{2} - \frac{(2j_{th}+j_h)^2}{2}$	$j_{th} + j_h/2 \leq 1/2$
XY II	see Eq. (B.63))	$j_{th}^2 \geq 2j_h$, $\rho \leq 1 \leq \sigma$

Table 3.2: Energies of the different ground state spin configurations of the Heisenberg and XY windmill model.

3.5.1 Decoupled windmill phase (1)

In the “decoupled windmill” phase (1) the spins on the triangular lattice are arranged in a 120° configuration while the honeycomb spins exhibit Néel order. This phase exists in a large region of the phase diagram where $J_{th} \leq \sqrt{J_t J_h}$. The spin configuration of phase (1) is shown in Fig. 3.3, and an analytical expression is given by

$$\boldsymbol{S}^t(\boldsymbol{r}) = \begin{pmatrix} \cos(\boldsymbol{Q}^t \cdot \boldsymbol{r}) \\ \sin(\boldsymbol{Q}^t \cdot \boldsymbol{r}) \\ 0 \end{pmatrix} \tag{3.8}$$

$$\boldsymbol{S}^A(\boldsymbol{r}) = \begin{pmatrix} \cos(\boldsymbol{Q}^A \cdot \boldsymbol{r}) \\ \sin(\boldsymbol{Q}^A \cdot \boldsymbol{r}) \\ 0 \end{pmatrix} \tag{3.9}$$

$$\boldsymbol{S}^B(\boldsymbol{r}) = -\boldsymbol{S}^A(\boldsymbol{r})\,. \tag{3.10}$$

Here, $\boldsymbol{r} = n\boldsymbol{a}_1 + m\boldsymbol{a}_2$ is a Bravais lattice vector and the ordering wave vectors read in the basis of the reciprocal lattice vectors as

$$\boldsymbol{Q}^t = \pm(1/3, -1/3) \tag{3.11}$$

$$\boldsymbol{Q}^{A,B} = (0,0)\,. \tag{3.12}$$

The triangular ordering vectors are thus given by $\boldsymbol{Q^t} = \pm(\boldsymbol{G}_1/3 - \boldsymbol{G}_2/3) = \pm 2\pi(\frac{1}{3}, -\frac{1}{\sqrt{3}})$ and are located, as shown in Fig. 3.3, at the corners of the first Brillouin zone. Only two of those six corners are non-equivalent, *i.e.*, cannot be reached by adding a reciprocal lattice vector. We have chosen to place the honeycomb spins in the same plane as the triangular lattice spins. This is only done for convenience, since in this configuration the spins on the triangular lattice are decoupled from the spins on the honeycomb lattice: global rotations of spins on either of the two sublattices do not cost any energy. The sign of the different wave vectors $\boldsymbol{Q}^t$ corresponds to different chiralities of the 120°-order.

Phases	Phase Boundary	Order of transition
1 : 2a	$j_{th}^2 = j_h$	1
1 : 4b	$j_{th}^2 = j_h$	1
2a : 2b	$j_{th} = 2j_h$	2
2b : 4b	$j_{th} = \frac{1}{2}$	2
2b : 4a	$2j_h = \sqrt{2} j_{th}^{3/2} - j_{th}$	2
2a : 3a	$j_{th}^2 = 4j_h$	1
3a : 3b	$j_{th} = 2j_h$	2
3b : 5	$j_{th} = \frac{3}{2} + \frac{1}{2} j_h$	2
4a : 5	$j_h + 1 = j_{th}$	2
1: XY I	$6j_h = (2j_{th} + j_h)^2$	1
1 : 2b	$2j_{th} = 2j_h + 1/2$	1
XY I : 2b	$j_h + 2j_{th} = 1$	2
2b : XY II	$2j_{th}^2 = j_{th} + j_{th} j_h + 4j_h$	2
5 : XY II	$E_5 = E_{\text{XY II}}$	1

Table 3.3: Parametric location of the phase boundaries and order of the phase transition between different phases in the ground state phase diagram of the Heisenberg and XY windmill model (see Figs. 4.14 and 3.11).

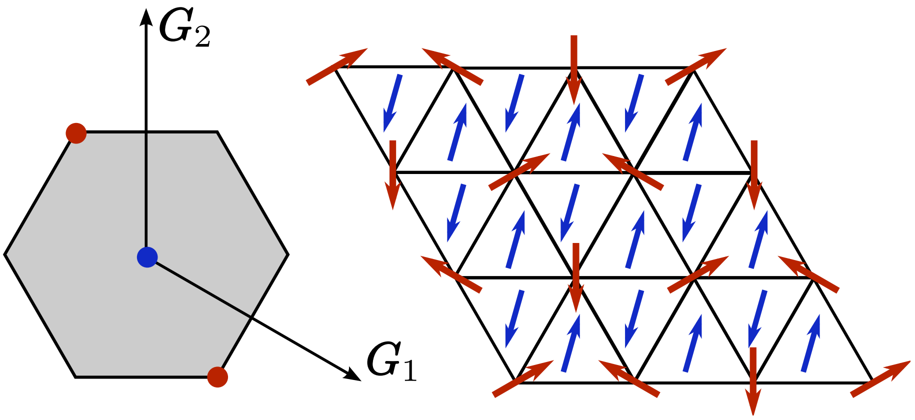

Figure 3.3: Decoupled windmill phase (1). In this phase the two sublattices are decoupled. The triangular lattice spins have a 120° order, whereas the honeycomb spins are Néel ordered. Left: Ordering wave vectors for honeycomb (yellow) and triangular (red) lattice

To find the order parameter manifold of this phase, we first divide the tripartite triangular lattice into X, Y and Z-sites, where the different sites correspond to the three possible directions of triangular lattice spins in the 120° configuration. Consider a plaquette of X-, Y- and Z-site spins and let $\boldsymbol{t}_2$ be a unit vector along the spin on the X-sites $\boldsymbol{S}_X$. Then define the unit vector $\boldsymbol{t}_1$ to be parallel to the component of the spin $\boldsymbol{S}_Y$ on the Y sites that is orthogonal to $\boldsymbol{S}_X$. Finally, define the unit vector $\boldsymbol{t}_3 = \boldsymbol{t}_1 \times \boldsymbol{t}_2$. The triad $(\boldsymbol{t}_1, \boldsymbol{t}_2, \boldsymbol{t}_3)$ that is defined in this way is the local order parameter for the 120° phase. The vector $\boldsymbol{t}_3$ is essential to encapsulate the chirality of the ordering, *i.e.*, XYZ ordering versus XZY. The chirality on a triangular plaquette is defined to be negative (positive), if the rotation of spins going from site X to Y to Z is (counter)clockwise. If the plane of triangular spin order is given by the x-y-plane of real-space, as is assumed in Fig. 3.3, a positive (negative) chirality corresponds to the unit vector $\boldsymbol{t}_3$ pointing out-of (into) the plane. The chirality of the configuration can be changed by performing a π-rotation around an axis that lies in the plane of the triangular spins. The order parameter manifold of the triangular lattice spins is thus given by $SO(3)$.

The order parameter of the honeycomb lattice spins can be defined by a unit vector $\boldsymbol{n}$ that points along the direction of the A-site spins, and global rotations around an axis that is not parallel (or anti-parallel) to $\boldsymbol{n}$ yield other energetically degenerate spin configurations. The order parameter manifold of the "decoupled windmill" phase (1) is thus given by $SO(3) \times O(3)/O(2)$.

We finally mention that at finite temperatures, it was shown in Refs. [72, 73] that thermal (or quantum) fluctuations around this ground state lead to a finite temperature phase diagram with $\mathbb{Z}_6$ order and an emergent critical phase.

3.5.2 Collinear antiferromagnetic phase/canted ferromagnetic phase $(2a)$ and $(2b)$

This is a planar phase in which the spins on the triangular sublattice are collinearly ordered, *i.e.*, ferromagnetically along one lattice direction and antiferromagnetically along the others. The A/B honeycomb sublattices are each collinear canted ferromagnets with spins on the B sites that are antiparallel to two of the neighboring spins on the A-site.

The spin configuration is shown in Fig. 3.4. We have chosen the direction of one of the triangular lattice spins to be along the S_x-axis of spin space. An analytical expression of the spin configuration in this phase is given by

$$\begin{aligned}
\boldsymbol{S}^t(\boldsymbol{r}) &= \begin{pmatrix} \cos(\boldsymbol{Q}^t \cdot \boldsymbol{r}) \\ 0 \\ 0 \end{pmatrix} && (3.13)\\
\boldsymbol{S}^A(\boldsymbol{r}) &= -\begin{pmatrix} \cos(\theta + \boldsymbol{Q}^A \cdot \boldsymbol{r}) \\ \sin\theta \\ 0 \end{pmatrix} && (3.14)\\
&= \begin{pmatrix} -j_{th}/(2j_h)\cos(\boldsymbol{Q}^A \cdot \boldsymbol{r}) \\ -[1 - j_{th}^2/(4j_h^2)]^{1/2} \\ 0 \end{pmatrix} && (3.15)\\
\boldsymbol{S}^B(\boldsymbol{r}) &= -\boldsymbol{S}^A(\boldsymbol{r}) && (3.16)
\end{aligned}$$

with

$$\begin{aligned}
\theta &= -\cos^{-1}\left(\frac{j_{th}}{2j_h}\right) && (3.17)\\
\boldsymbol{Q}^t &= \boldsymbol{Q}^{A,B} \in \{(1/2,0),(0,1/2),(1/2,1/2)\}\,. && (3.18)
\end{aligned}$$

The form of θ was obtained by taking it as a variational parameter and minimizing the energy found from the explicit evaluation of the Hamiltonian (we refer to Appendix B.1 for details).

Note that θ is undefined for $j_{th} > 2j_h$. In this latter range the minimum is instead found at $\theta = 0$. The region where this phase is hosted is denoted $(2b)$ in the phase diagram. The transition between this configuration and one of finite θ is accompanied by a discontinuity of the second derivative of the energy as a function of the coupling constants, *i.e.*, the phase transition between the phases $(2a)$ and $(2b)$ is of second order.

The order parameter is given by defining the direction of one triangular lattice spin and by specifying one direction in lattice space in which the spins are collinear with the chosen spin. For the latter there are three possible choices. The honeycomb spins arrange themselves in a plane that contains the triangular spins and enclose a certain angle θ with the triangular spins. Global $O(2)$ rotations of the honeycomb spins around an axis parallel to the triangular spins yield energetically degenerate spin configurations. The order parameter manifold of the phases $(2a)$ and $(2b)$ is thus given by $O(3)/O(2) \times O(2) \times \mathbb{Z}_3$.

3.5.3 Ferromagnetic phases $(3a)$ and $(3b)$

In phase $(3a)$ all three sublattices are separately ferromagnetically ordered. The spins on the honeycomb A and B sites enclose an angle θ with the triangular spins, but point in mirror opposite directions with respect to the triangular spins. The spin configuration is depicted in Fig. 3.5. Let the direction of $\boldsymbol{S}^t$ be the S_x-axis of spin space. An analytical expression of the spin configuration reads

$$\boldsymbol{S}^t(\boldsymbol{r}) = \begin{pmatrix} 1 \\ 0 \\ 0 \end{pmatrix} \qquad (3.19)$$

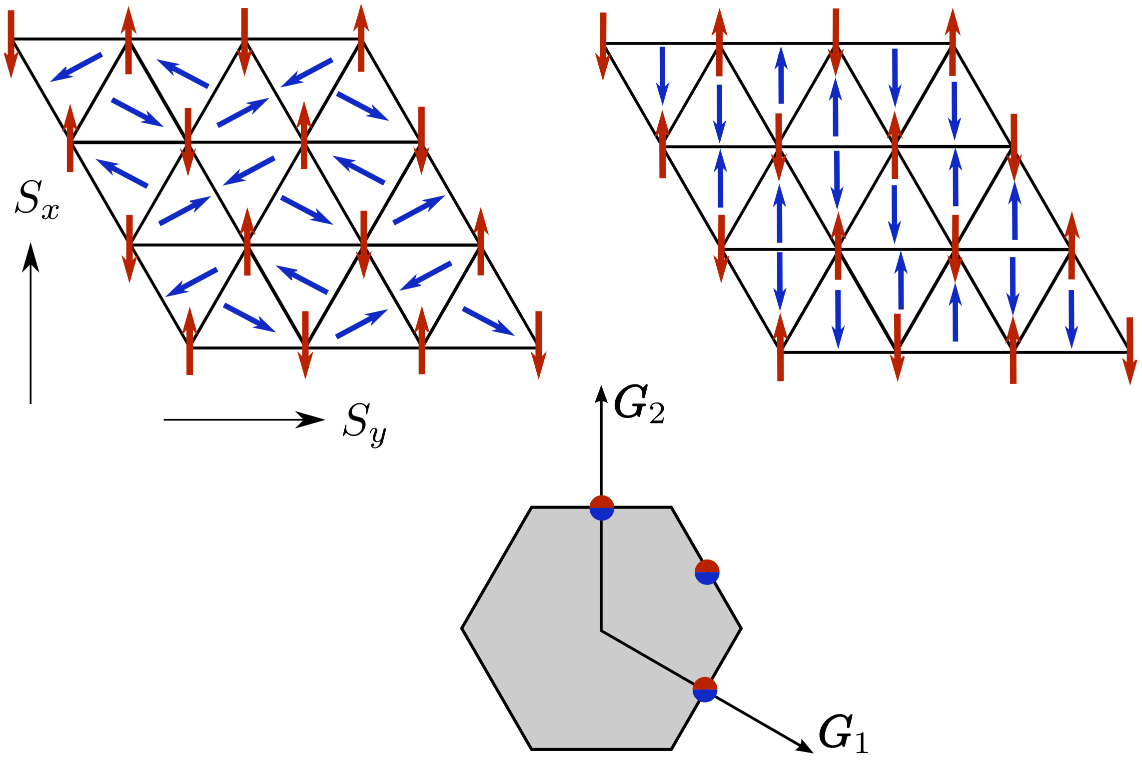

Figure 3.4: Collinear Antiferromagnet/Canted Ferromagnet (left: $(2a)$, right: $(2b)$). Phase (2a) can exist only for $j_{th} < 2j_h$, when this inequality is violated, phase (2b) minimizes the energy. In configuration (2a) the honeycomb spins can be globally rotated around the triangular spin direction without any cost in energy. The ordering wave vectors of both lattices are identical.

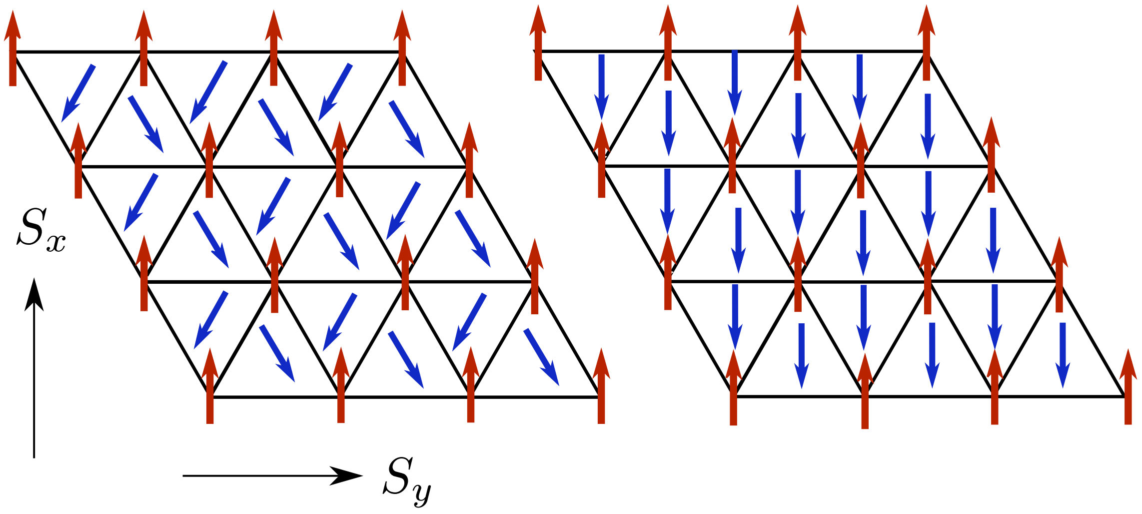

Figure 3.5: Left: (3a), right: (3b). All three sublattices are ferromagnetically ordered. In phase (3a) the relative angles between the lattices is tunable by changing j_{th}. However, once $j_{th} \geq 2j_h$ the spins become locked in the configuration (3b).

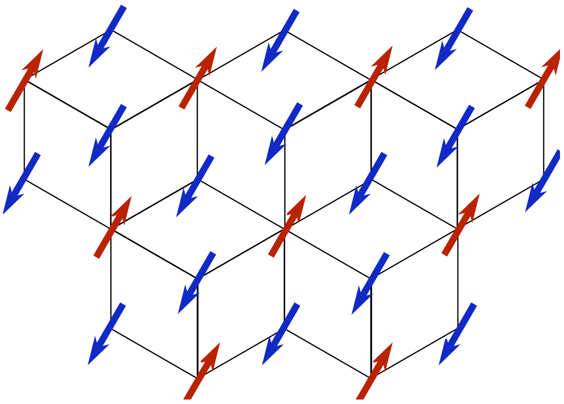

Figure 3.6: The Figure shows the *dice lattice* obtained in the limit of large $J_{th} \gg J_t, J_h$. This is effectively the lattice for phase (3b). Red (blue) arrows lie on triangular (honeycomb) lattice sites.

$$\boldsymbol{S}^A(\boldsymbol{r}) = \begin{pmatrix} \cos\theta \\ \sin\theta \\ 0 \end{pmatrix} = \begin{pmatrix} -j_{th}/(2j_h) \\ [1 - j_{th}^2/(4j_h^2)]^{1/2} \\ 0 \end{pmatrix} \tag{3.20}$$

$$\boldsymbol{S}^B(\boldsymbol{r}) = \begin{pmatrix} \cos\theta \\ -\sin\theta \\ 0 \end{pmatrix} = \begin{pmatrix} -j_{th}/(2j_h) \\ -[1 - j_{th}^2/(4j_h^2)]^{1/2} \\ 0 \end{pmatrix} \tag{3.21}$$

with

$$\cos(\theta) = -\frac{j_{th}}{2j_h}. \tag{3.22}$$

The ordering wave vectors are all identically zero, which corresponds to ferromagnetic order.

Once again the variational parameters become undefined for $j_{th} > 2j_h$. The minimum for this region is instead found at $\theta = \pi$ and the corresponding phase is denoted $(3b)$ in the phase diagram. This phase is the one that would be obtained in the limit of infinite J_{th} and finite J_t, J_h. Such a limit corresponds to a lattice where there is a vanishingly small coupling within the triangular lattice and within the honeycomb lattice, but a dominant inter-sublattice coupling J_{th}. The resulting bipartite lattice is depicted in Fig. 3.6 and is known as the *dice lattice*. It is the dual of the kagome lattice and has been studied in the literature in various contexts[103].

The order parameter manifold of this phase is defined by the direction of the triangular lattice spin. The energy of phase $(3a)$ remains invariant, however, if we rotate all honeycomb spins around an axis parallel to the triangular spin, which corresponds to an $O(2)$ symmetry. Therefore, the order parameter manifold of phase $(3a)$ is given by $O(3)/O(2) \times O(2)$, whereas that of phase $(3b)$ is equal to $O(3)/O(2)$.

3.5.4 Double cone phases $(4a)$ and $(4b)$

Spins in the phases $(4a)$ and $(4b)$ exhibit a non-coplanar arrangement. In phase $(4a)$, spins on the triangular and the honeycomb lattice lie on separate double-cones. The phase $(4a)$

is shown in Figs. 3.7 and 3.8. The double cone structure is depicted in Fig. 3.7 and the arrangement of the spins on the lattice is clearly illustrated in Fig. 3.8. As one moves horizontally in lattice space along $\boldsymbol{a}_1$ ($\boldsymbol{a}_2$) from one site to the next, the spins advance by an azimuth angle of θ (2θ). In other words, the spins in the figure labelled by the same angles share a common plane in spin space. Additionally, they alternately lie on upper and lower cones, which is represented by blue and red in Fig. 3.8. We are showing only one of the six symmetry-related ground states. The others are obtained by rotating the lattice through an angle of $(2\pi/6)n$ with $n = 1, \ldots, 5$.

Non-coplanar ground states, similar to the ones we have found, have also been discovered in Heisenberg models on triangular, square, pyrochlore and octahedral lattices [33, 93, 91, 48]. The interest in such phases stems from the fact that non-coplanar spin orderings are expected to give rise to an anomalous Hall effect[96], due to the non-vanishing spin chirality. Moreover, considering quantum fluctuations it is expected that non-coplanar classical ground states give rise to chiral spin liquid phases [82, 91, 59].

To describe this configuration we choose the opening axis of the cones to be the S_z-axis. Then the spins are described by

$$\boldsymbol{S}^t(\boldsymbol{r}) = \begin{pmatrix} \sin(\alpha_t)\cos(\boldsymbol{Q}_1\cdot\boldsymbol{r}) \\ \sin(\alpha_t)\sin(\boldsymbol{Q}_1\cdot\boldsymbol{r}) \\ \cos(\alpha_t)\cos(\boldsymbol{Q}_2\cdot\boldsymbol{r}) \end{pmatrix} \tag{3.23}$$

$$\boldsymbol{S}^A(\boldsymbol{r}) = \begin{pmatrix} -\sin(\alpha_h)\cos(\boldsymbol{Q}_1\cdot\boldsymbol{r}+\theta) \\ -\sin(\alpha_h)\sin(\boldsymbol{Q}_1\cdot\boldsymbol{r}+\theta) \\ -\cos(\alpha_h)\cos(\boldsymbol{Q}_2\cdot\boldsymbol{r}) \end{pmatrix} \tag{3.24}$$

$$\boldsymbol{S}^B(\boldsymbol{r}) = \boldsymbol{S}^A(\boldsymbol{r}+\boldsymbol{a}_1) \tag{3.25}$$

with ordering wave vectors

$$\boldsymbol{Q}_1 = \pm\frac{1}{2\pi}(\theta, 2\theta) \tag{3.26}$$

$$\boldsymbol{Q}_2 = (1/2, 0) \tag{3.27}$$

The ambiguity in sign corresponds to two possible orderings that are related by a π-rotation in lattice space. Four other orderings are possible, that correspond to the remaining rotated states

$$\boldsymbol{Q}_1 = \pm\frac{1}{2\pi}(\theta, -\theta) \tag{3.28}$$

$$\boldsymbol{Q}_2 = (1/2, 1/2) \tag{3.29}$$

and

$$\boldsymbol{Q}_1 = \pm\frac{1}{2\pi}(2\theta, \theta) \tag{3.30}$$

$$\boldsymbol{Q}_2 = (0, 1/2). \tag{3.31}$$

The angles α_t and α_h are the half-opening angles of the respective cones. The angle θ is the difference in the azimuthal angle, as shown in Fig. 3.7. These three angles $\{\alpha_t, \alpha_h, \theta\}$ are functions of the coupling constants. By solving the minimization problem (see Appendix B.3) for the set of variables $\{\alpha_t, \alpha_h, \theta\}$, one finds the solution

$$\sin\alpha_t = \sqrt{\frac{1-\sigma^2}{\rho^2-\sigma^2}} \tag{3.32}$$

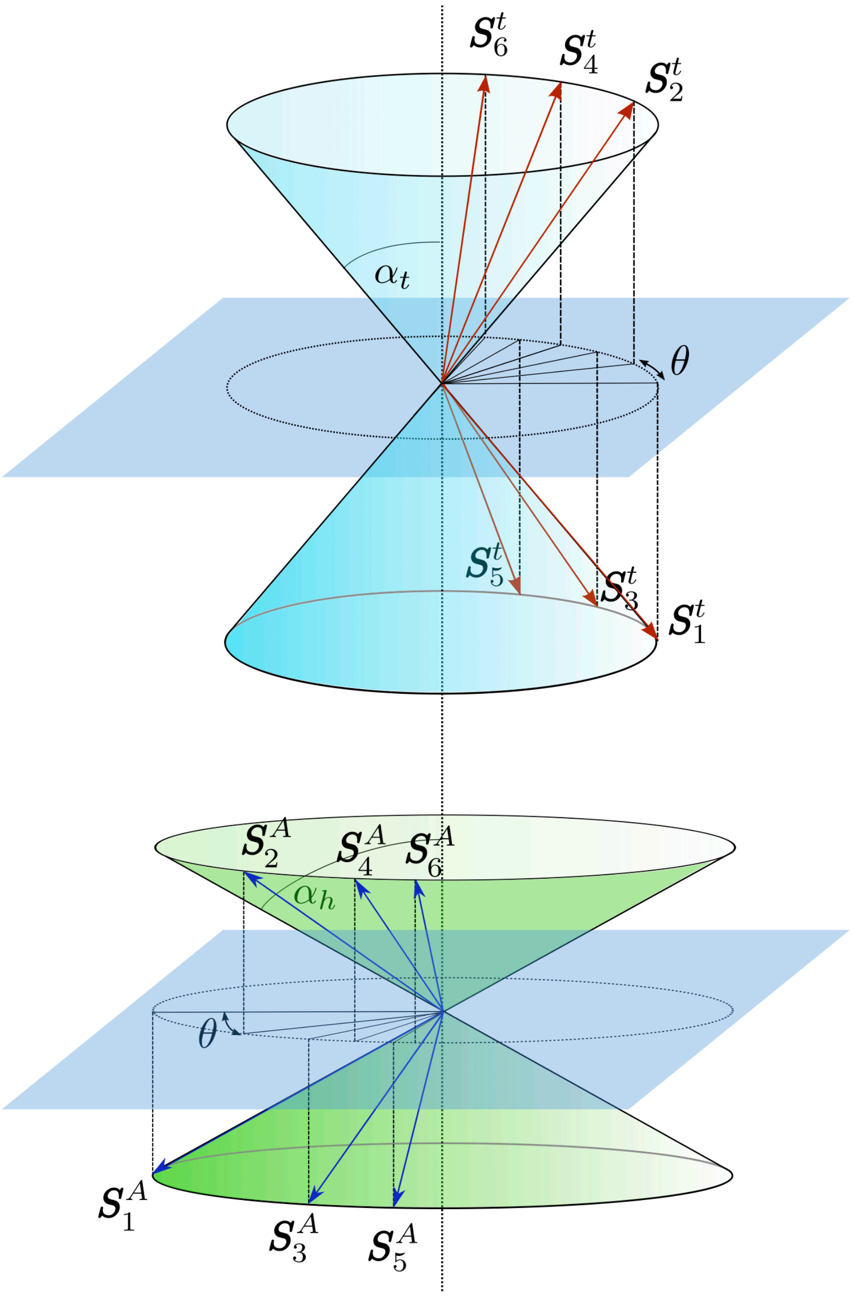

Figure 3.7: Double Cone Phase ($4a$). Spins on the triangular (top) and the honeycomb lattice (bottom) lie on separate double cones with different opening angles α_t and α_h. In the figures we use the notation $\boldsymbol{S}_{n+1}^{t,A,B} = \boldsymbol{S}_1^{t,A,B}(\boldsymbol{r} + n\boldsymbol{a}_1)$ and $\boldsymbol{S}_{2n+1}^{t,A,B} = \boldsymbol{S}_1^{t,A,B}(\boldsymbol{r} + n\boldsymbol{a}_2)$.

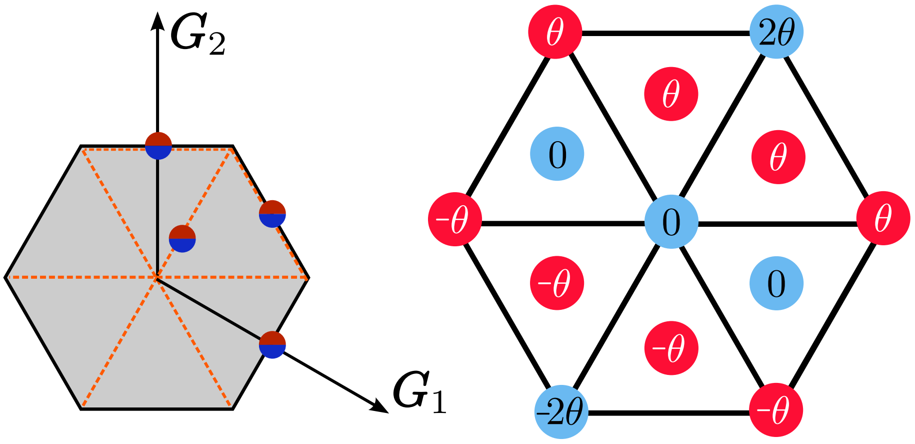

Figure 3.8: Double Cone Phase $(4a)$. Left: $\boldsymbol{Q}$ vectors of all sublattices are identical. The phase contains one of the three $\boldsymbol{Q}$ vectors on the boundary and one from the dashed lines. Specifying θ determines the exact position of the $\boldsymbol{Q}$ vector on the dashed lines. Right: Scheme of spin orientations on the lattice. Let the middle reference spin be on the upper double cone of the triangular lattice. The blue (red) spins lie on upper (lower) cones. The angles describe by how much a spin's azimuthal angle differs from that of the reference spin.

$$\sin\alpha_h = \sqrt{\frac{1-\sigma^2}{\rho^2-\sigma^2}}\rho \tag{3.33}$$

$$\cos\theta = j_{th}\frac{j_{th}-\sqrt{j_{th}^2-4j_h}}{4j_h} = \frac{j_{th}}{2}\rho \tag{3.34}$$

with

$$\rho \equiv \frac{\sin\alpha_h}{\sin\alpha_t} = \frac{j_{th}-\sqrt{j_{th}^2-4j_h}}{2j_h} \tag{3.35}$$

$$\sigma \equiv \frac{\cos\alpha_h}{\cos\alpha_t} = \frac{j_{th}\left(j_{th}-\sqrt{j_{th}^2-4j_h}\right)^2}{8j_h^2}. \tag{3.36}$$

Generally both angles α_t, α_h are nonzero.

Another solution to the minimization problem exists, for which $\rho = 0$. The corresponding phase is denoted by $(4b)$ and is shown in Fig. 3.9. In this configuration the honeycomb lattice spins are aligned with the cone axis, while the triangular lattice spins lie again on a cone with variable half-opening angle

$$\cos\alpha_t = 2j_{th}\,. \tag{3.37}$$

Consecutive triangular lattice spins rotate by an angle of $\theta = 2\pi/3$ around the cone axis.

The order of both phases may be described by first specifying the cone axis and one of the triangular lattice spins. Once this choice is made, there is a further degeneracy due to the freedom in rotating the lattice, as explained above. Thus there are six energetically degenerate configurations. These six possibilities may be further classified into two

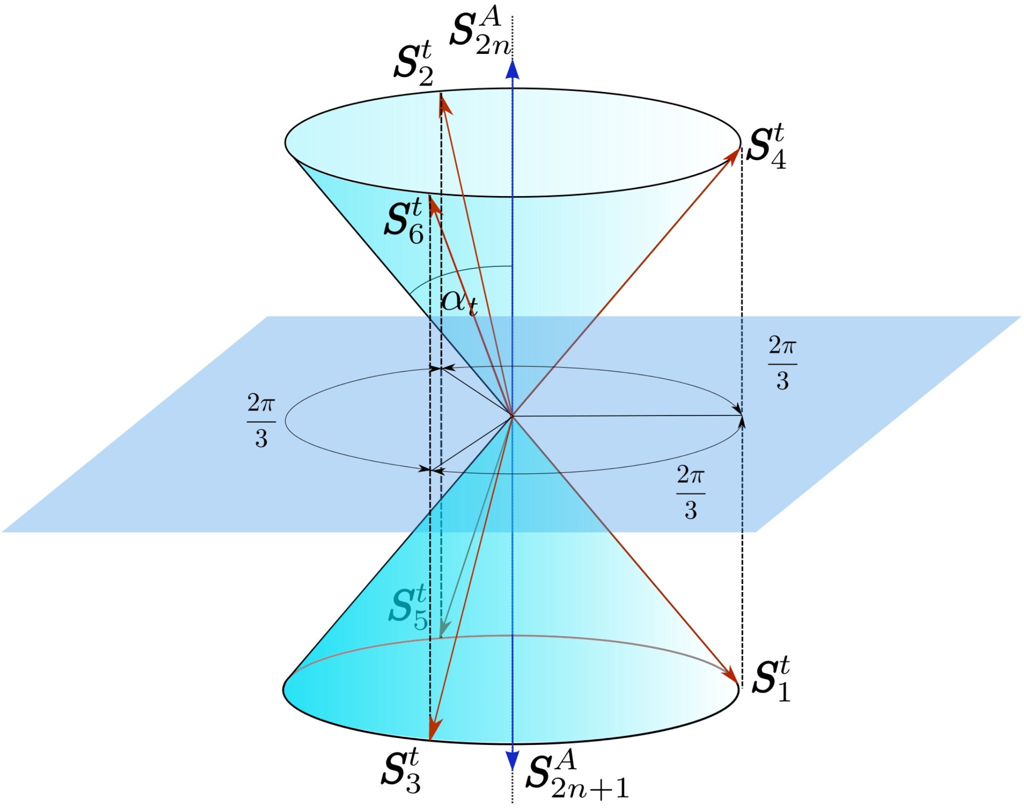

Figure 3.9: Double Cone Phase ($4b$). The spins on the honeycomb lattice align with the cone axis, while the spins on the triangular lattice lie on a double cone with half-opening angle $\cos\alpha_t = 2j_{th}$ and advance by a fixed angle of $\theta = \frac{2\pi k}{3}$ when translated by $\boldsymbol{a}_k$.

chiralities: three cover the configurations that describe a right handed screw around the cone axis when advancing in the $\boldsymbol{a}_1$ direction and three describe a left handed screw. In specifying the cone axis, we may encode the chirality of the spins via the direction of the cone axis vector. The chirality can thus be reversed by a π-rotation around an axis that lies in the plane orthogonal to the cone axis. The order in this phase is therefore described by an element of $SO(3) \times \mathbb{Z}_3$.

3.5.5 Incommensurate spiral phase (5)

In phase (5) the spins are arranged in a coplanar incommensurate spiral as shown in Fig. 3.10. The spin configuration takes the form

$$\boldsymbol{S}^t(\boldsymbol{r}) = \begin{pmatrix} \cos(\boldsymbol{Q}\cdot\boldsymbol{r}) \\ \sin(\boldsymbol{Q}\cdot\boldsymbol{r}) \\ 0 \end{pmatrix} \tag{3.38}$$

$$\boldsymbol{S}^A(\boldsymbol{r}) = -\begin{pmatrix} \cos(\boldsymbol{Q}\cdot\boldsymbol{r}+\theta) \\ \sin(\boldsymbol{Q}\cdot\boldsymbol{r}+\theta) \\ 0 \end{pmatrix} \tag{3.39}$$

$$\boldsymbol{S}^B(\boldsymbol{r}) = -\begin{pmatrix} \cos(\boldsymbol{Q}\cdot\boldsymbol{r}+2\theta) \\ \sin(\boldsymbol{Q}\cdot\boldsymbol{r}+2\theta) \\ 0 \end{pmatrix}, \tag{3.40}$$

where the ordering wave vector is given by

$$\boldsymbol{Q} = \pm\frac{1}{2\pi}(\theta, 2\theta). \tag{3.41}$$

with the angle θ defined via

$$\cos\theta = -\frac{1}{2}\left(1 + j_h - 2j_{th}\right). \tag{3.42}$$

As for the double cone phase, the sign ambiguity of $\boldsymbol{Q}$ describes the chirality. Four further symmetry related configurations exist and are described by the $\boldsymbol{Q}$ vectors

$$\boldsymbol{Q} = \pm\frac{1}{2\pi}(2\theta, \theta) \tag{3.43}$$

and

$$\boldsymbol{Q} = \pm\frac{1}{2\pi}(\theta, -\theta). \tag{3.44}$$

The right-hand side of Eq. (3.42) must satisfy

$$|(1 + j_h - 2j_{th})| \leq 2\,. \tag{3.45}$$

For parameters that violate this inequality the minimum is instead found at either $\theta = 0$ or $\theta = \pi$. The former case is identical to phase (3*b*) and the latter one to phase (2*b*).

In the spiral phase the triangular lattice spins have the same order parameter manifold as the 120° ordered spins of phase (1). This is clear, since the 120° order is just a special case of this incommensurate spiral phase. An incommensurate spiral phase on the windmill lattice, however, can appear in three distinct types, as described above, three of each chirality. The order parameter manifold of the incommensurate spiral phase is thus equal to $SO(3) \times \mathbb{Z}_3$.

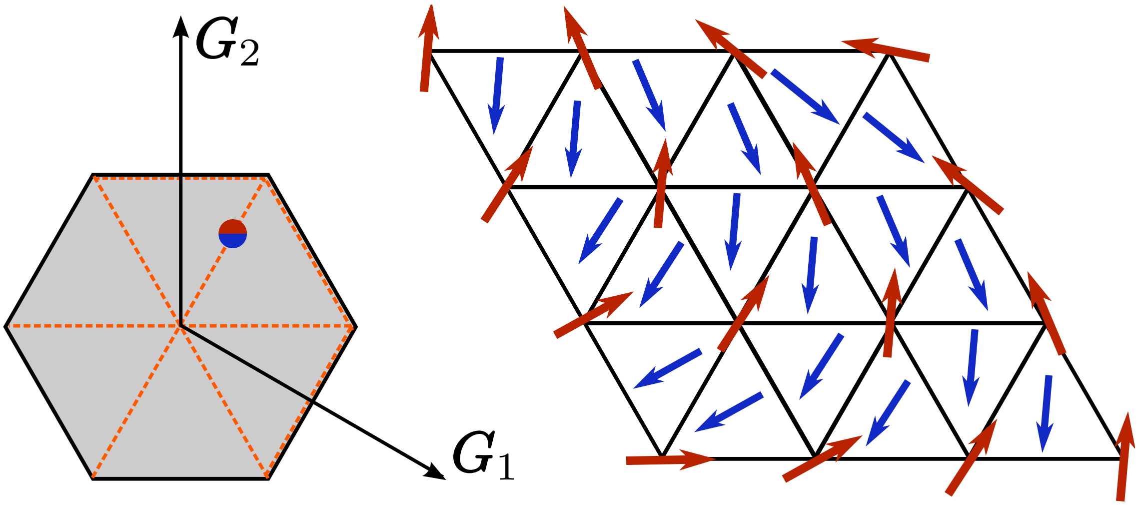

Figure 3.10: Phase (5). Left: $\boldsymbol{Q}$ vector is identical for all sublattices. It lies on one of the dashed lines and is determined by θ. Right: The spins exhibit incommensurate spiral order. The spiral can be either left-handed or right-handed.

3.6 Planar (XY) windmill model

We now discuss the XY windmill model, where planar (XY) spins $\boldsymbol{S}_i^\alpha = (S_{i,x}^\alpha, S_{i,y}^\alpha)$, $\alpha \in \{t, A, B\}$, are placed on the vertices of the windmill lattice (see Fig. 3.1). This case is particularly interesting given the recent advances in the field of ultracold atoms, where XY spins with nearest-neighbor antiferromagnetic interactions were successfully simulated on a triangular lattice [94, 95]. The lattice is created by means of standing wave laser fields. The atoms are trapped in and tunnel between the local minima of this optical lattice. At low temperatures, the system becomes superfluid and the atoms have well-defined local condensate phases ϕ_i at every site i of the lattice. This U(1) degree of freedom plays the role of the XY spins $\boldsymbol{S}_i = (\cos\phi_i, \sin\phi_i)$. The nearest-neighbor spin couplings are determined by the tunneling amplitudes of atoms that move between the different laser field minima. For normal quantum mechanical tunneling between the sites, the corresponding spin interaction is always ferromagnetic, favoring a locking of the condensate phases to the same value. In contrast, it was recently demonstrated that the tunneling element acquires a non-zero Peierls phase by periodically shaking the optical lattice and an

Phase	Order Parameter Manifold (planar model)
1	$O(2) \times SO(2)$
2a, 2b	$SO(2) \times \mathbb{Z}_6$
3a	$SO(2) \times \mathbb{Z}_2$
3b	$SO(2)$
5	$O(2) \times \mathbb{Z}_3$
XY I	$O(2) \times \mathbb{Z}_3$
XY II	$O(2) \times \mathbb{Z}_3$

Table 3.4: Order parameter manifolds in the planar windmill model.

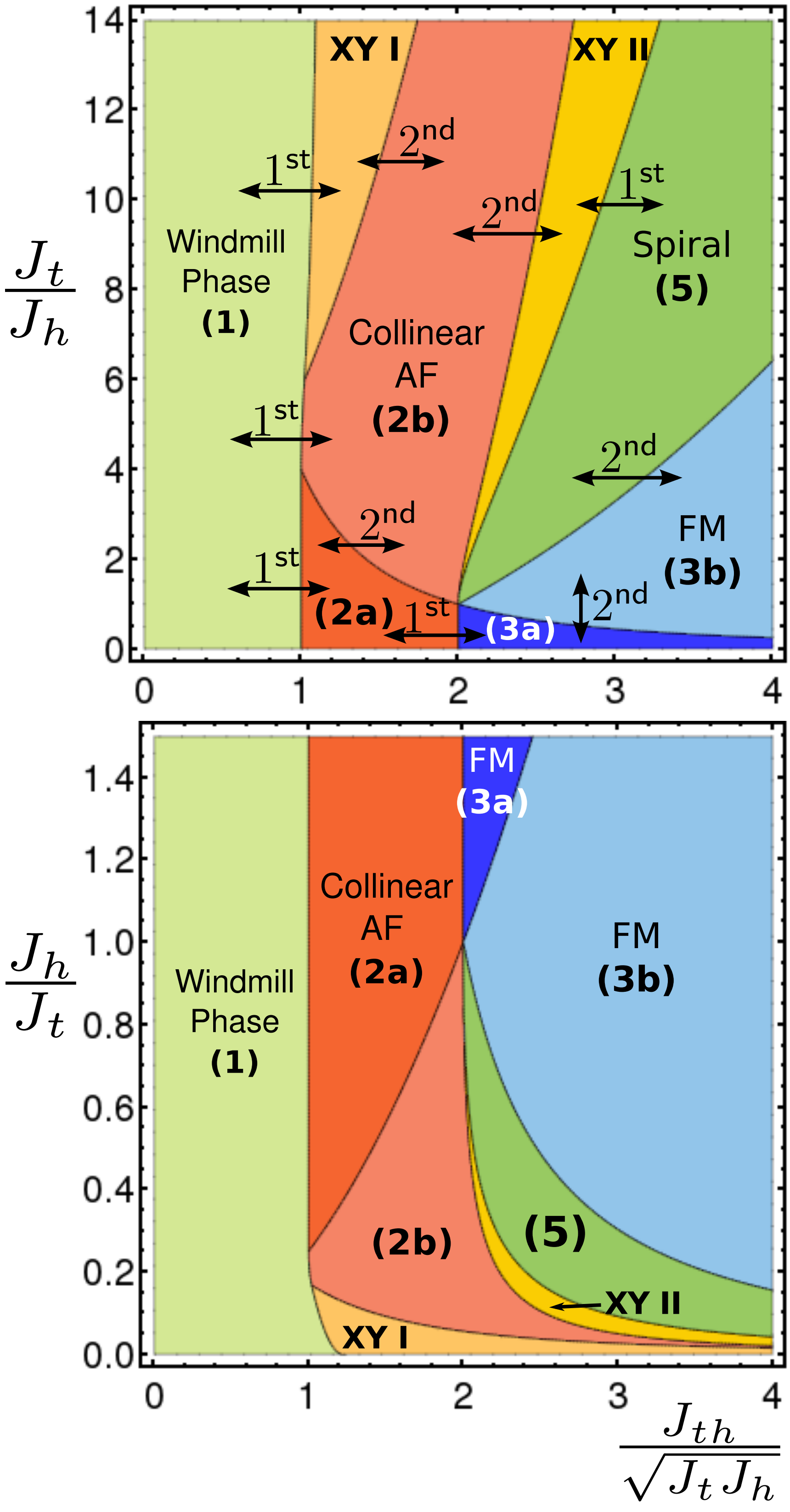

Figure 3.11: Ground state phase diagram of the XY windmill model. The top figure has as the vertical axis J_t/J_h, while in the lower panel it is J_h/J_t . The 6 planar phases of the Heisenberg windmill model reappear, with two additional phases labelled (XY I) and (XY II)

antiferromagnetic coupling of local XY phases on a triangular lattice was experimentally realized [94, 95]. As honeycomb optical lattice geometries have also been successfully implemented in various groups [74, 98, 40], it is entirely feasible to realize the XY windmill model using cold bosonic atoms in optical lattices.

We have determined the full phase diagram of the XY windmill model. It is shown in Fig. 3.11. We note that a coplanar state that minimizes the energy for Heisenberg spins has to minimize the energy for XY spins, as well. Thus, compared to the results for the Heisenberg windmill model the only major modification in the phase diagram, apart from a quantitative shift of the phase boundaries, takes place in the regions where the Heisenberg model exhibits non-coplanar phases. These regions are now largely occupied by two new planar phases, (XY I) and (XY II), which we describe below.

Of the two highly degenerate points in the phase diagram of the Heisenberg model, only one remains in the planar model: at the point $(j_h, j_{th}/\sqrt{j_h}) = (1, 2)$ six phases meet. Like in the case of the Heisenberg model, this high degeneracy is explained by the fact that all six phases deform into either phase $(2b)$ or phase $(3b)$ in the limit $(j_h, j_{th}/\sqrt{j_h}) \to (1, 2)$. Thus there are only two distinct phases present at this point. In particular, phase (XY II) transforms into phase $(2b)$, as we explain below.

3.6.1 Incommensurate alternating spiral phase (XY I)

In place of the non-coplanar phase $(4b)$ we now find a new planar phase. We denote this phase by (XY I). It is an incommensurate spiral phase with the directions of spins alternating from one site to the next. It is shown in Fig. 3.12. It may be described as a twisted Néel-ordered configuration. The spin configuration is given by

$$\boldsymbol{S}^t(\boldsymbol{r}) = \begin{pmatrix} \cos(\boldsymbol{Q}\cdot\boldsymbol{r}) \\ \sin(\boldsymbol{Q}\cdot\boldsymbol{r}) \end{pmatrix} \tag{3.46}$$

$$\boldsymbol{S}^A(\boldsymbol{r}) = \begin{pmatrix} \cos(\boldsymbol{Q}\cdot\boldsymbol{r}+\theta) \\ \sin(\boldsymbol{Q}\cdot\boldsymbol{r}+\theta) \end{pmatrix} \tag{3.47}$$

$$\boldsymbol{S}^B(\boldsymbol{r}) = \begin{pmatrix} \cos(\boldsymbol{Q}\cdot\boldsymbol{r}+2\theta) \\ \sin(\boldsymbol{Q}\cdot\boldsymbol{r}+2\theta) \end{pmatrix} \tag{3.48}$$

with ordering wave vectors

$$\boldsymbol{Q} = \pm\frac{1}{2\pi}(\theta+\pi, 2\theta)\,, \tag{3.49}$$

and an angle θ that is defined by

$$\cos\theta = \frac{1}{2}\left(1 + j_h + 2j_{th}\right)\,. \tag{3.50}$$

The chiralities are encoded in the sign of $\boldsymbol{Q}$. Four further symmetry related phases are possible with $\boldsymbol{Q}$ vectors

$$\boldsymbol{Q} = \pm\frac{1}{2\pi}(2\theta, \theta+\pi) \tag{3.51}$$

and

$$\boldsymbol{Q} = \pm\frac{1}{2\pi}(\theta+\pi, \pi-\theta). \tag{3.52}$$

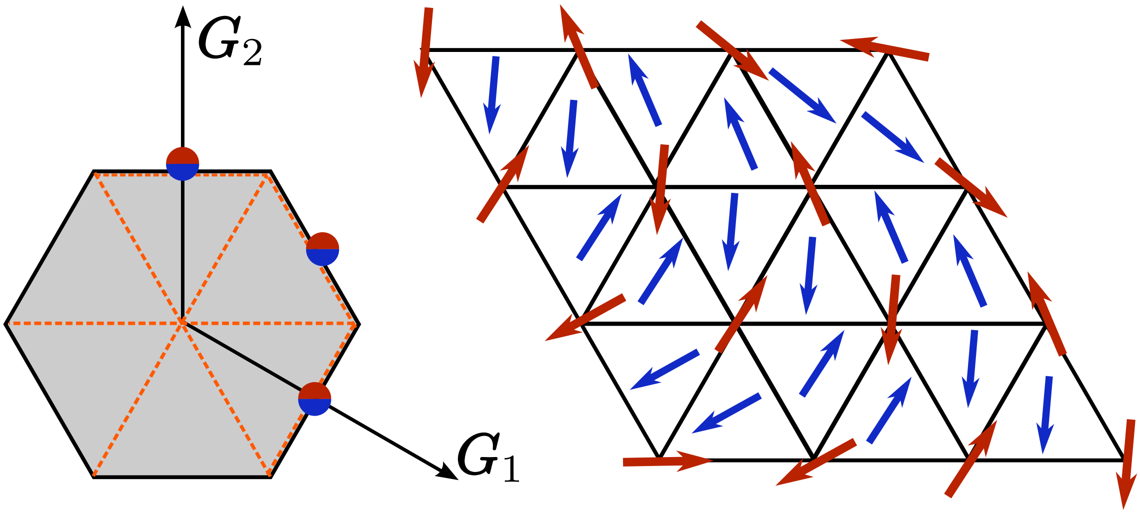

Figure 3.12: Phase (XY I). Left: $\boldsymbol{Q}$ vectors are identical for all sublattices. By specifying θ the wave vectors come to lie either on the boundary or on the dashed lines. Right: The spins arrange themselves in an incommensurate, alternating spiral.

Imposing the condition that the angle θ be real, yields

$$j_h + 2j_{th} \leq 1. \tag{3.53}$$

This phase is never an energy minimum for the Heisenberg model, since the non-coplanar phase (4b) includes the whole range of existence of phase (XY I) and has a smaller energy.

Like in the case of the incommensurate spiral phase (5), the order parameter of phase (XY I) is determined by giving the direction of two triangular lattice spins and by specifying one of the three $\boldsymbol{Q}$ vectors. Hence, its manifold is $O(2) \times \mathbb{Z}_3$.

3.6.2 Canted ferromagnetic phase (XY II)

The phase (XY II) is found in the former region of the non-coplanar phase ($4a$) in the phase diagram. It is depicted on the left of Fig. 3.13. All spins lie symmetrically about a line, which we choose in the following to be the x-axis.

The spin configuration is related to the double-cone state, since it can be obtained by forcing the double-cone azimuth angle θ to be zero (see Eqs. (3.23)-(3.25)). The spin configuration is given by

$$\boldsymbol{S}^t(\boldsymbol{r}) = \begin{pmatrix} \cos(\alpha_t) \\ \sin(\alpha_t + \boldsymbol{Q}\cdot\boldsymbol{r}) \end{pmatrix} \tag{3.54}$$

$$\boldsymbol{S}^A(\boldsymbol{r}) = \begin{pmatrix} -\cos(\alpha_h) \\ -\sin(\alpha_h + \boldsymbol{Q}\cdot\boldsymbol{r}) \end{pmatrix} \tag{3.55}$$

$$\boldsymbol{S}^B(\boldsymbol{r}) = \begin{pmatrix} -\cos(\alpha_h) \\ \sin(\alpha_h + \boldsymbol{Q}\cdot\boldsymbol{r}) \end{pmatrix} \tag{3.56}$$

with

$$\boldsymbol{Q} \in \{(1/2,0),(0,1/2),(1/2,1/2)\}. \tag{3.57}$$

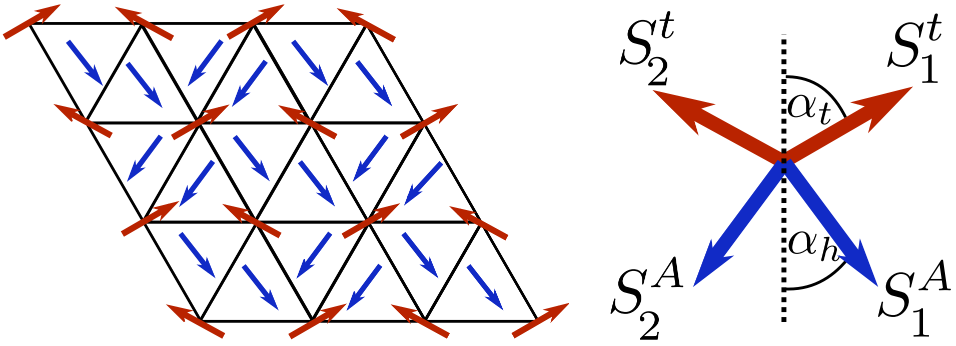

Figure 3.13: Left: Phase (XY II). The spins on all three sublattices alternate between two positions. These two positions may be viewed as reflections along a mirror line that is common to all three sublattices. Right: Shown are spins from the triangular lattice (red) and (A-site) honeycomb lattice (blue) at neighboring lattice sites along $\boldsymbol{a}_1$. The vertical line is a mirror line, analogous to the mirror plane of the double cone phase. The spins are aligned ferromagnetically along $\boldsymbol{a}_2$.

The angles α_h and α_t are given by

$$\sin\alpha_t = \sqrt{\frac{1-\sigma^2}{\rho^2-\sigma^2}} \tag{3.58}$$

$$\sin\alpha_h = \sqrt{\frac{1-\sigma^2}{\rho^2-\sigma^2}}\rho \tag{3.59}$$

with

$$\begin{aligned} \sigma &\equiv \frac{\cos\alpha_h}{\cos\alpha_t} \\ &= \frac{2}{3j_{th}} + \frac{j_{th}}{3j_h} - \sqrt{\left(\frac{2}{3j_{th}} + \frac{j_{th}}{3j_h}\right)^2 - \frac{1}{j_h}} \end{aligned} \tag{3.60}$$

$$\rho \equiv \frac{\sin\alpha_h}{\sin\alpha_t} = 3\sigma - \frac{4}{j_{th}}\,. \tag{3.61}$$

As we approach the high degeneracy point $(j_h, j_{th}/\sqrt{j_h}) = (1, 2)$, it is straightforward to show from (3.58)-(3.61) that $\alpha_h, \alpha_t \to \pi/2$ as the degeneracy point is approached and (XY II) becomes identical to phase ($2b$).

Concerning the lattice symmetry of this phase, we note that from the configuration shown in Fig. 3.13 two further energetically degenerate phases are obtained by rotation of the lattice by (i) 120° and (ii) 240°, respectively. Hence, the order parameter manifold in this phase is equal to $O(2) \times \mathbb{Z}_3$.

3.7 Conclusions

We have determined the complete ground state phase diagram of both the classical Heisenberg and the planar (XY) spin models on the windmill lattice. Like the well-known J_1-J_2-model on the square lattice, the windmill model couples a lattice to its dual lattice.

In the windmill model this is a triangular lattice coupled to its dual honeycomb lattice. Competing antiferromagnetic interactions between the spins lead to a rich ground state phenomenology with collinear, coplanar, incommensurate spiral and non-coplanar phases. We discussed different routes to an experimental realization of these spin models. Based on our results and recent finite temperature studies of the Heisenberg windmill model in the regime of weak sublattice coupling, the region of phase (1), we expect interesting physics to emerge in the presence of quantum and thermal fluctuations.

Chapter 4

Emergent critical phase in a frustrated magnet

A fundamental result in statistical physics is the theorem proved by Mermin and Wagner [58, 76, 108] according to which N-component spin systems, with $N \geq 2$, in two-dimensional space, coupled via short-range interactions are not capable of developing long-range order. The reason for this is, roughly speaking, that the resulting Goldstone modes of such a symmetry-broken phase would immediately destroy the order.

Despite the fact that the Mermin-Wagner theorem prohibits long-range order of the microscopic spins, it does not make any constraining statements about emergent degrees of freedom. One may therefore imagine a scenario, where one has two sublattices of Heisenberg spins, which cannot develop long-range order by themselves, but where the relative orientation of these sublattices defines new degrees of freedom. If these degrees of freedom are discrete, the theorem does not forbid them from developing long-range order via a finite temperature phase transition.

This is indeed what was found in the so called J_1-J_2 model [12], which is a frustrated Heisenberg model on two coupled square lattices. Here the emergent degrees of freedom are Ising variables. Thus as the temperature of the system is lowered and the correlation length of the Heisenberg spins stays finite, there is a critical temperature T_c, where the correlation length of the Ising variables becomes infinite. This is an instance of a 2D Heisenberg spin system exhibiting an Ising phase transition.

In his pioneering work on this subject [75], A. M. Polyakov pointed out a similar possibility by speculating that a 2D Heisenberg magnet might develop *algebraic order*; he further suggested that this possibility might be explored experimentally. Hence a natural question to pose at this point is whether one can generalize the J_1-J_2 model in such a way that the system develops emergent XY-spin degrees of freedom that can undergo phase transitions into an *algebraically ordered* phase. Recently Orth, Chandra, Coleman and Schmalian (OCCS) [72, 73] have proposed that frustration can provide a mechanism to realize Polyakov's conjecture; these authors constructed a frustrated model of Heisenberg spins, in which the emerging spin system is a planar XY model with a 6-fold potential. A pure XY model, i.e. not an emergent one, with such a potential was shown by J. V. José et al. [39] to have a low-temperature $\boldsymbol{Z}_6$-symmetry broken region and a high-temperature disordered region. These two regions enclose a middle regime in which the emergent XY model has a power law phase.

In this chapter a computational experiment is performed that detects the development of an emergent XY order parameter with power-law correlations in the 2D Heisenberg windmill model, confirming the OCCS mechanism and its realization of the Polyakov conjecture. The OCCS mechanism relies on the formation of a multi-spin U(1) order parameter describing the *relative* orientation of the magnetization between a honeycomb and a triangular lattice. The development of fluctuation-induced $\mathbb{Z}_2$ order in the J_1-J_2 Heisenberg model [12] is thought to be responsible for the high temperature nematic phase observed in the iron-pnictides [24, 23, 105, 7]. In the OCCS mechanism, the emergent $U(1)$ order parameter is subject to a $\mathbb{Z}_6$ order-by-disorder potential at short distances. At intermediate temperatures this potential is irrelevant (in the renormalization group sense) and scales to zero at long distances, leading to emergent power-law correlations. Remarkably, the stiffness of the emergent U(1) order parameter remains finite in the infinite system, despite the short-range correlations of the underlying Heisenberg spins. In this XY manifold the binding of logarithmically interacting defect vortices leads to ordering via two consecutive transitions that belong to the Berezinskii-Kosterlitz-Thouless (BKT) universality class [72, 73, 39].

The analysis of the emergence of the planar XY model with 6-fold potential from the windmill Hamiltonian, which we define more precisely below, was undertaken in [72, 73] in a renormalization group calculation. In this treatment several approximations had to be made, which, though plausible, weaken the strength of the authors' arguments. The difficulties are the following:

- the calculations are performed on the continuum model in a long-wavelength approximation; thus the lattice structure of the theory is lost, which leaves open the possibility that short-wavelength fluctuations could preempt the scenario via unanticipated transitions into different phases [8, 14, 13]
- the middle regime is treated in an approximation, where coplanarity is hard coded into the analysis, while in fact fluctuations out of the plane are always present
- the RG gives only order of magnitude values of the phase-transition and crossover temperatures, thus a quantitative phase diagram is lacking; the latter is particularly important in order to assess whether the power law regime is present in a broad region or if it only appears in a narrow slice of the phase diagram

In this work we remove these difficulties by simulating the model in a Monte Carlo calculation, which allows an unbiased treatment of the problem.
This chapter is based on work done in

Bhilahari Jeevanesan, Premala Chandra, Piers Coleman, and Peter P. Orth, *Emergent Power-Law Phase in the 2D Heisenberg Windmill Antiferromagnet: A Computational Experiment*, Phys. Rev. Lett. 115, 177201

that was published in October 2015.

In the first section we recapitulate the essential ideas of the J_1-J_2 Heisenberg model. The focus is on demonstrating the Ising phase transition computationally. This was done first in [105] by C. Weber et al.. We reproduce some of these results.
As a preparation for the study of the windmill lattice with emergent algebraic order,

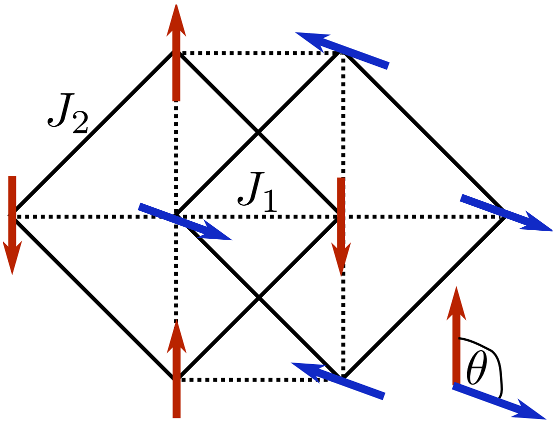

Figure 4.1: The J_1-J_2 model. It consists of two interpenetrating sublattices with two spin species (red and blue). The two species are coupled within the same sublattice by a coupling J_2 and spins from different sublattices are coupled by J_1.

the next section summarizes some results from BKT theory, before the actual problem is treated in the subsequent section.

4.1 Emergent Ising order in the frustrated J_1-J_2 model

The J_1-J_2 model is a short-range Heisenberg spin model, where the spins are placed on the vertices of two interpenetrating square lattices (see Fig. 4.1). Now one can differentiate between the two sublattices (red and blue in the Fig. 4.1) and define coupling constants that depend on the sublattice type. We denote by $J_2 \geq 0$ the coupling of nearest neighbor spins on the same sublattice, while $J_1 \geq 0$ denotes nearest neighbor couplings of spins on different sublattices. The Hamiltonian of this model is given by

$$H = J_1 \sum_{\langle\langle ij \rangle\rangle} \boldsymbol{S}_i \cdot \boldsymbol{S}_j + J_2 \sum_{\langle ij \rangle} \boldsymbol{S}_i \cdot \boldsymbol{S}_j . \tag{4.1}$$

In the following we will consider the regime, where $J_2 \gg J_1$. The opposite regime, $J_1 \gg J_2$, is trivial in the sense that the $T = 0$ ground state consists of antiferromagnetically ordered spins. The diagonal bonds only serve to enhance fluctuations, but this does not yield interesting low energy phenomena.

This is in stark contrast to the opposite regime of $J_2 \gg J_1$, which we want to discuss in the following. At $T = 0$ the red and blue spins order antiferromagnetically. However, in this configuration there is no preferred relative angle between the red and blue spins. In other words, the system has a degenerate ground state and any choice of angle θ in Fig. 4.1 leads to the same energy. Thus at $T = 0$ the two sublattices are fully decoupled and may be individually rotated relative to the other sublattice. However, as the temperature is increased thermal fluctuations are present, which lift this degeneracy of the ground state and couple the two lattices. This takes place by a mechanism that has been termed order-by-disorder and was worked out by Villain [102] and Henley [35]. We present a full calculation of the order-by-disorder mechanism for the windmill model in appendix E. Here, we instead give an intuitive picture of how this mechanism works. Consider in Fig. 4.2 the action of the red spins on the middle blue spin. At low temperatures almost all

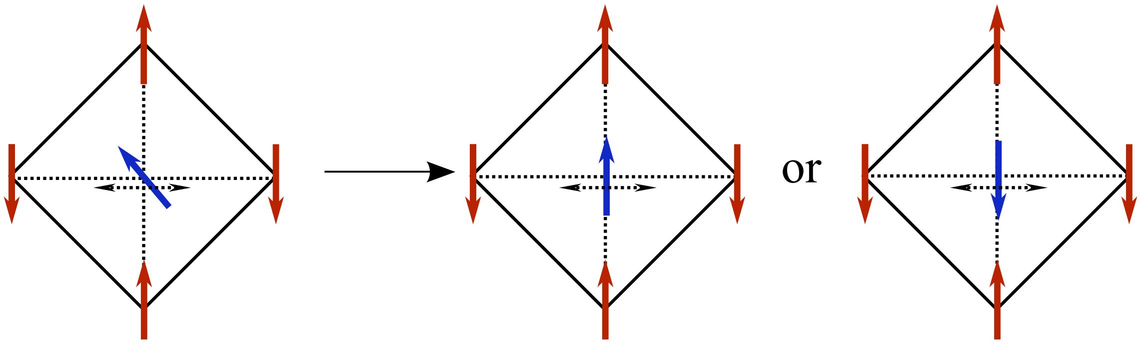

Figure 4.2: Order-by-disorder mechanism: The small fluctuations of the red spins induce a Weiss field (dashed arrow) that is felt by the blue spin. In the figure the field acts mostly in a horizontal direction. The blue spin will spent most of its time in the vertical position, which offers a pocket where it is left undisturbed. There are two such preferred orientations.

the red spins surrounding a blue spin point in the same direction, but they also fluctuate slightly around this position, generating a mostly horizontally aligned Weiss field for the blue spin. The latter is randomly acted on by these fluctuations and will, of course, spend most of its time in an orientation from which these fluctuations cannot easily remove it. In the figure such an orientation is given by a vertical alignment, so there are two possible directions which minimize fluctuations. This is the origin of the emergent Ising degree of freedom: the two sublattices prefer to be in one of two orientations, i.e. the two settings $\theta = 0$ and $\theta = \pi$ are entropically favored over the other possibilities.

Given the existence of such emergent Ising degrees of freedom, it is an interesting question to ask, if these spins can undergo a phase transition. That this was in fact possible was shown using the renormalization group in [12]. Given the approximations that became necessary in these authors' line of reasoning, this fact required a more unambiguous demonstration. Work undertaken in [105] showed, using Monte Carlo simulations and a finite size scaling analysis, that the picture of [12] was essentially correct, although some minor modifications were required close to the boundary of the two regimes of J_2/J_1. Since the analysis in [12] was essentially a low-energy continuum theory, this first order transition between the two regimes of J_2/J_1 values and fluctuations in and out of the neighboring phase, led to effects that are not captured in a perturbation theory around one regime, while the Monte Carlo simulation is naturally capable of exploring such fluctuations.

In order to demonstrate the Ising phase transition in this Heisenberg system, the full Heisenberg model is treated in Monte Carlo simulations and statistical averages are calculated of the emergent degrees of freedom. The emergent Ising variables are defined per plaquette according to the rule (see Fig. 4.3)

$$\sigma = \frac{(\boldsymbol{S}_1 - \boldsymbol{S}_3) \cdot (\boldsymbol{S}_2 - \boldsymbol{S}_4)}{|\boldsymbol{S}_1 - \boldsymbol{S}_3||\boldsymbol{S}_2 - \boldsymbol{S}_4|}.$$

Having defined the Ising variables, the authors of [105] went on to measure the Ising susceptibility defined by

$$\chi_{\text{Ising}} = \frac{N}{T}\left(\langle M^2\rangle - \langle M\rangle^2\right)$$

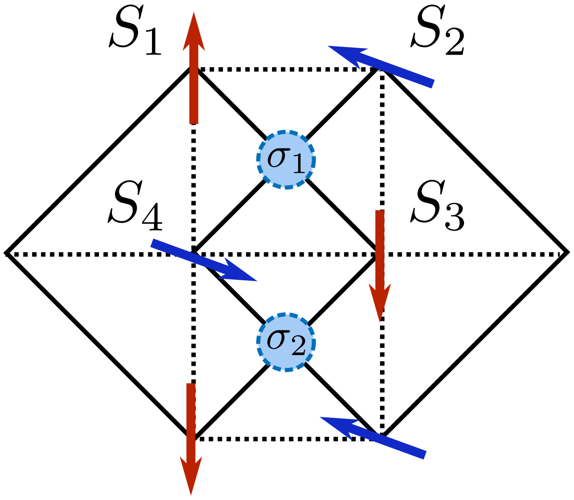

Figure 4.3: Emergent Ising degrees of freedom

where M is the Ising magnetization given by

$$M = \frac{1}{N}\sum_{\alpha}\sigma_{\alpha}.$$

We have repeated these simulations and obtained full agreement with the authors (Fig. 4.4). The figure shows the finite-size scaling of the susceptibility. As the system size is increased, it is clearly seen that the susceptibility develops a sharp peak. The position of the peak allows us to read off a transition temperature of about $T_c \approx 0.198 J_1$. A more precise value is obtained by measuring the correlation length ξ and extrapolating the ξ^{-1} vs. T/J_1 plot linearly and determining where the line intersects the temperature axis. In this way the authors find $T_c \approx 0.196 J_1$ (Fig. 4.5).

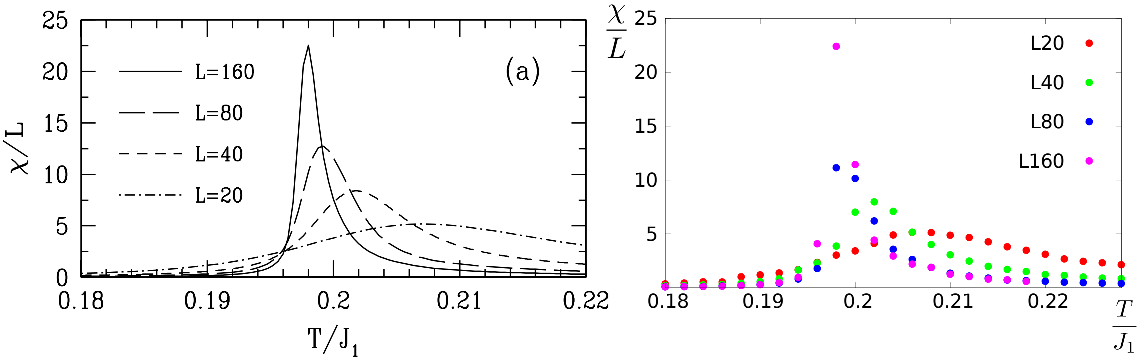

Figure 4.4: Susceptibility for the emergent Ising degrees of freedom defined per plaquette. We obtain agreement (right) with the authors of [105] (left). Reprinted with permission from [105] (http://dx.doi.org/10.1103/PhysRevLett.91.177202), Copyright (2003) by the American Physical Society.

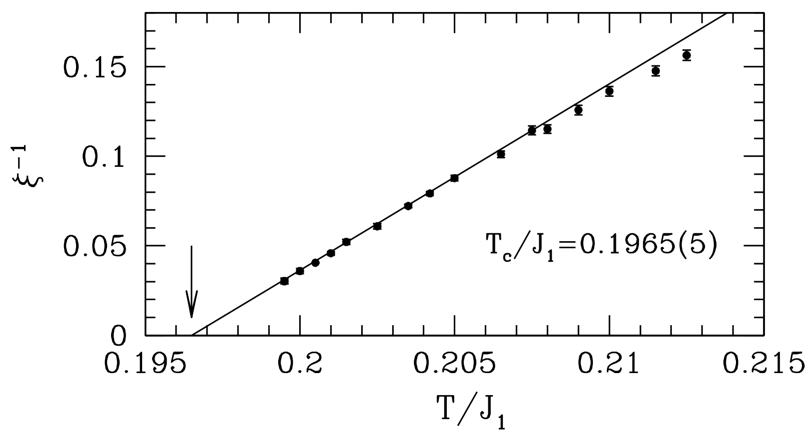

Figure 4.5: Ising correlation length as function of temperature for J_1-J_2 model. Reprinted with permission from [105] (http://dx.doi.org/10.1103/PhysRevLett.91.177202), Copyright (2003) by the American Physical Society.

4.2 BKT transitions and the power-law phase

When we turn to the Heisenberg windmill model below, we will see that in the coplanar regime it effectively behaves like an XY model. This is demonstrated below by performing Monte Carlo simulations and extracting the properties of the phase transition in a finite-size scaling analysis suited to BKT transitions and by determining the critical exponent η at the upper and lower phase transition.
We first derive some results from the theory of BKT transitions following [1, 9, 5, 42, 44] for the square lattice without any symmetry breaking potential. This allows us to extract the theoretical value for η, the form of the free energy near the transition and from this the behavior of the susceptibility close to the transition.

4.2.1 High-temperature phase

We consider an XY-Hamiltonian on the square lattice given by

$$H = -J \sum_{\langle ij \rangle} \boldsymbol{S}_i \cdot \boldsymbol{S}_j = -J \sum_{\langle ij \rangle} \cos(\theta_i - \theta_j). \tag{4.2}$$

and ask for the behavior of the correlation function

$$G_{ij} = \langle \boldsymbol{S}_i \boldsymbol{S}_j \rangle = \langle \cos(\theta_i - \theta_j) \rangle.$$

In the limit of large temperatures, we can expand the partition function in a high-T expansion. This is a representation of the partition function as a sum over configurations that consist of closed loops on the lattice (see Fig. 4.6). To derive this representation we expand the partition sum for small β as

$$Z = \mathrm{Tr}[\exp(-\beta H)] \approx \prod_i \left(\int_0^{2\pi} d\theta_i \right) \prod_b [1 + \beta J \cos(\theta_{b_1} - \theta_{b_2})],$$

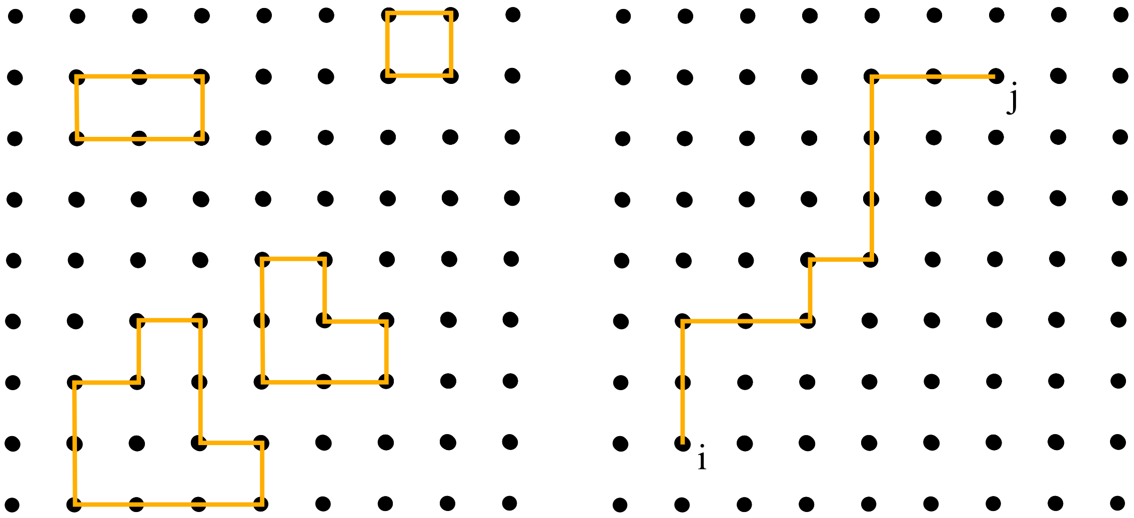

Figure 4.6: High-temperature expansion. Left: The partition function can be represented as a sum over closed-loop configurations. Right: The correlation function $\langle \boldsymbol{S}_i \cdot \boldsymbol{S}_j \rangle$ is obtained by summing over all configurations (appropriately weighted) that connect site i to site j. One such configuration is shown here.

where the second product ranges over all nearest-neighbor bonds b in the lattice and b_1, b_2 denote the two sites that belong to this bond. In computing Z, we obtain integrals of the type

$$I = \int_0^{2\pi} d\theta \cos(\theta - \theta_1)\cos(\theta - \theta_2)\ldots\cos(\theta - \theta_n).$$

If the number of cosines in this product is odd, i.e. if n is odd, this integral is zero. This is shown by noting first that the integration is over a full period. Therefore a translation of θ by π cannot change the value of this integral. However, the cosines obtain a sign change and we therefore obtain the relation:

$$I = I(-1)^n$$

thus if n is odd we have $I = 0$.

Diagrammatically this means that the only contributing configurations are those where the number of edges incident on a lattice site is even. Such configurations cannot have loose ends (these would be vertices with an odd number of incident edges) and are therefore closed loops.

By this logic, considering the correlation function $G_{ij} = \langle \cos(\theta_i - \theta_j) \rangle$ we conclude that the only contributions to this function come from those configurations that connect site i to j (see right lattice in Figure 4.6). The lowest order in βJ that contains such a configuration is $(\beta J)^{d_{ij}}$, where d_{ij} is the distance between sites i and j (not the straight line distance, since we have to follow the horizontal and vertical bonds of the lattice, but rather the closely related Manhattan distance [1] between these sites). Then

$$\langle \boldsymbol{S}_i \cdot \boldsymbol{S}_j \rangle \sim (\beta J)^{d_{ij}} = \exp\left(-\frac{d_{ij}}{1/|\log(\beta J)|}\right)$$

---

[1] Let $\boldsymbol{u} = (u_1, u_2)$ and $\boldsymbol{v} = (v_1, v_2)$ be the position vectors to two sites on the square lattice. The Manhattan distance between between these points is defined as $d = |u_1 - v_1| + |u_2 - v_2|$.

and we deduce that the correlation function decays exponentially with a correlation length given by

$$\xi \equiv \frac{1}{|\log(\beta J)|}.$$

4.2.2 Low-temperature phase

Now we want to consider the low-temperature phase for this Hamiltonian. We will find that this limit suggests algebraic behavior for the correlation function. This behavior is suggestive, but not conclusive proof, since the following arguments are based on a Gaussian approximation, while interactions may modify this picture. To analyze interactions we will perform an RG treatment in a later section.
In the limit of low temperatures it is permissible to rewrite the Hamiltonian in a continuum approximation. We expand the cosines in (4.2) and drop an additive constant to obtain

$$H \approx \frac{J}{2} \int d^2x \, (\nabla\theta)^2 . \tag{4.3}$$

The correlation function G_{ij} can be written as

$$G_{ij} = \langle \cos(\theta(\boldsymbol{r}) - \theta(\boldsymbol{r}')) \rangle = \mathrm{Re}\langle e^{i(\theta(\boldsymbol{r})-\theta(\boldsymbol{r}'))} \rangle = e^{-\frac{1}{2}\langle(\theta(\boldsymbol{r})-\theta(\boldsymbol{r}'))^2\rangle},$$

where in the last step we used the fact that H is Gaussian. We proceed to evaluate the exponent. The Green's function in Fourier space is read off from (4.3):

$$\begin{aligned} \langle \theta_{\boldsymbol{q}} \theta_{\boldsymbol{q}'} \rangle &= \delta(\boldsymbol{q}+\boldsymbol{q}') G_q \\ G_{\boldsymbol{q}}^{-1} &= \beta J q^2 \end{aligned}$$

Then

$$\begin{aligned} \langle (\theta(\boldsymbol{r}) - \theta(\boldsymbol{r}'))^2 \rangle &= 2\int \frac{d^2q}{(2\pi)^2}(1 - e^{i\boldsymbol{q}\Delta\boldsymbol{r}})G_q = \frac{2}{\beta J}\int_0^{1/a} \frac{dq}{q} \int_0^{2\pi} \frac{d\phi}{(2\pi)^2}(1 - e^{iq\Delta r\cos\phi}) \\ &= \frac{1}{\pi\beta J}\int_0^{1/a} dq \, \frac{1 - J_0(q\Delta r)}{q} = \frac{1}{\pi\beta J}\int_0^{\Delta r/a} d\lambda \, \frac{1 - J_0(\lambda)}{\lambda} \end{aligned}$$

where J_0 is the zero-order Bessel function. In order to separate the logarithmic dependence on the cutoff from the finite parts in this integral, we rewrite the integral as

$$\begin{aligned} \int_0^{\Delta r/a} d\lambda \, \frac{1 - J_0(\lambda)}{\lambda} &= \int_0^1 d\lambda \, \frac{1 - J_0(\lambda)}{\lambda} + \int_1^{\Delta r/a} d\lambda \, \frac{1 - J_0(\lambda)}{\lambda} \\ &= \int_0^1 d\lambda \, \frac{1 - J_0(\lambda)}{\lambda} + \log\left(\frac{\Delta r}{a}\right) - \int_1^{\infty} d\lambda \, \frac{J_0(\lambda)}{\lambda} + \int_{\Delta r/a}^{\infty} d\lambda \, \frac{J_0(\lambda)}{\lambda} \\ &= \gamma - \log 2 + \log\left(\frac{\Delta r}{a}\right) + \int_{\Delta r/a}^{\infty} d\lambda \, \frac{J_0(\lambda)}{\lambda}. \end{aligned}$$

The last integral is negligible for large $\Delta r/a$, since it vanishes asymptotically as $\sim (\Delta r/a)^{-3/2}$. This finishes the calculation and we obtain for large Δr

$$\langle (\theta(\boldsymbol{r})) - \theta(\boldsymbol{r}'))^2 \rangle = \frac{1}{\pi\beta J}\left(\gamma - \log 2 + \log\left(\frac{\Delta r}{a}\right)\right)$$

and therefore

$$G(\Delta r) = e^{-\frac{1}{2}\langle(\theta(\boldsymbol{r})-\theta(\boldsymbol{r}'))^2\rangle} \sim \left(\frac{a}{\Delta r}\right)^{\frac{1}{2\pi\beta J}} . \tag{4.4}$$

We see that the correlation function at low temperatures decreases algebraically. Accepting this fact, we have to conclude that there must be a transition from the disordered phase at high temperatures to the algebraically ordered phase at low temperatures, characterized by a diverging correlation length. This result was derived in a Gaussian approximation. The Hamiltonian, however, possesses low energy excitations, namely vortices that have not been taken into account so far. The Figure 4.7 shows a snapshot of a Monte Carlo simulation of ferromagnetically coupled XY spins at low temperatures. The system would be perfectly ordered were it not for the three clearly visible vortex defects. These excitations are non-perturbative in nature, since the winding number associated with a vortex cannot be changed continuously.

4.2.3 Vortices and spin stiffness

Starting with the low-energy form of the theory in (4.3), we now consider besides the spin-waves also vortex excitations. This is most conveniently accomplished by phrasing the problem in a hydrodynamic language. A velocity vector $\boldsymbol{u}$ is introduced that is defined by

$$\boldsymbol{u} \equiv \nabla\theta.$$

Let us now consider a vortex with winding number 1. Going around the vortex in a closed loop, the value of θ starts at 0 and will increase by a total of 2π upon a full turn. But such a change forces θ to make a jump back to the initial value of 0, if we consider the θ-field to be single-valued. Thus around a vortex

$$\oint d\boldsymbol{l}\cdot\boldsymbol{u} = \oint d\boldsymbol{l}\cdot\nabla\theta \neq 0,$$

whereas if θ had been an analytic function, we would have obtained 0. The non-analytic behavior can be subsumed into a vortex contribution to the field $\boldsymbol{u}$ in the following way. We sepearate $\boldsymbol{u}$ into a sum of two parts $\boldsymbol{u}_1$ and $\boldsymbol{u}_2$. One part $\boldsymbol{u}_1$ represents pure potential flow, i.e. $\nabla\times\boldsymbol{u}_1 = 0$ and therefore, $\oint d\boldsymbol{l}\cdot\boldsymbol{u}_1 = 0$. The other part $\boldsymbol{u}_2$ contains the vortex contribution. Say we have vortices in our system and the i-th vortex is centered at $\boldsymbol{r}_i$ and has winding number n_i. Then the line integral around this vortex produces $\oint d\boldsymbol{l}\cdot\boldsymbol{u}_2 = 2\pi n_i$. On the other hand we have

$$\oint d\boldsymbol{l}\cdot\boldsymbol{u}_2 = \oint d^2x\nabla\times\boldsymbol{u}_2 = 2\pi n_i.$$

This means that the vortex at $\boldsymbol{r}_i$ contributes $2\pi\hat{\boldsymbol{z}}n_i\delta(\boldsymbol{r}-\boldsymbol{r}_i)$ to $\nabla\times\boldsymbol{u}_2$. Then the collection of all vortices is captured by

$$\nabla\times\boldsymbol{u}_2(\boldsymbol{r}) = 2\pi\hat{\boldsymbol{z}}\sum_i n_i\delta(\boldsymbol{r}-\boldsymbol{r}_i). \tag{4.5}$$

Note that we have introduced the third dimension for convenience into the problem.
To solve this equation we notice that according to the Helmholtz theorem in two dimensions

a field $\boldsymbol{u}_2$ can be represented as a gradient of a smooth scalar function and the rotation of the vector $\psi\hat{\boldsymbol{z}}$. Inserting this ansatz into (4.5), we obtain

$$\nabla \times (\nabla \times (\psi\hat{\boldsymbol{z}})) = -\nabla^2\psi\hat{\boldsymbol{z}} = 2\pi\hat{\boldsymbol{z}}\sum_i n_i\delta(\boldsymbol{r}-\boldsymbol{r}_i). \tag{4.6}$$

This is a Poisson equation in two dimensions with point sources. The potential in this case is known to be logarithmic and one obtains the total potential by the superposition principle:

$$\psi = \sum_i n_i V(|\boldsymbol{r}-\boldsymbol{r}_i|) = \sum_i n_i \log|\boldsymbol{r}-\boldsymbol{r}_i|,$$

where we introduced the potential $V(|\boldsymbol{r}|) \equiv \log|\boldsymbol{r}|$. The point of the decomposition $\boldsymbol{u} = \boldsymbol{u}_1 + \boldsymbol{u}_2$ is that insertion into the Hamiltonian (4.3) shows how the spin-wave part $\boldsymbol{u}_1$ and the vortex contribution $\boldsymbol{u}_2$ can be seperated into non-interacting parts. Thus, inserting the decomposition into (4.3)

$$H = \frac{J}{2}\int d^2x\ (\boldsymbol{u}_1+\boldsymbol{u}_2)^2 = \frac{J}{2}\int d^2x\ (\nabla\phi)^2 + 2\nabla\phi\cdot\nabla\times(\psi\hat{\boldsymbol{z}}) + (\nabla\times(\psi\hat{\boldsymbol{z}}))^2\,,$$

where we wrote $\boldsymbol{u}_1 = \nabla\phi$ and $\boldsymbol{u}_2 = \nabla\times(\psi\hat{\boldsymbol{z}})$. The cross term vanishes, since upon partial integration a gradient acts on the curl operator. With $\nabla\times(\psi\hat{\boldsymbol{z}}) = \hat{\boldsymbol{z}}\times\nabla\psi$, the third term becomes $(\hat{\boldsymbol{z}}\times\nabla\psi)^2 = \hat{\boldsymbol{z}}^2(\nabla\psi)^2 - (\hat{\boldsymbol{z}}\cdot\nabla\psi)^2 = (\nabla\psi)^2$. Thus we finally have for the action the form

$$H = H_S + H_V = \frac{J}{2}\int d^2x\ (\nabla\phi)^2 + (\nabla\psi)^2,$$

which shows that the spin-wave H_S and vortex sectors H_V are fully decoupled. In particular, the computation of the partition function can be undertaken seperately for the two sectors. A phase transition due to vortex physics must therefore be obtainable by just studying the part of the partition function that is due to vortices.
We begin by inserting the general form of ψ after partially integrating the $(\nabla\psi)^2$ term

$$\begin{aligned} H_V &= \frac{J}{2}\oint \psi(\nabla\psi)d\boldsymbol{A} - \frac{J}{2}\int d^2x\ \psi\nabla^2\psi \\ &= \frac{J}{2}\oint \psi(\nabla\psi)d\boldsymbol{A} + \frac{J}{2}2\pi\sum_{i,j} n_i n_j \log V(|\boldsymbol{r}_i-\boldsymbol{r}_j|). \end{aligned}$$

In order to discard the surface term, we want to send the integration surface to infinity. At large $|\boldsymbol{r}|$, far away from all the sources $\boldsymbol{r}_i$, $\psi(\boldsymbol{r}) \approx \sum_i n_i \log|\boldsymbol{r}|$. Thus in order for the surface term to vanish, $\sum_i n_i$ must hold. All other combinations of $\{n_i\}$ are infinitely costly in the thermodynamic limit.
Thus we assume $\sum_i n_i = 0$ to hold and discard the surface term. In the remaining Hamiltonian

$$H_V = J\pi\sum_{i,j} n_i n_j \log V(|\boldsymbol{r}_i-\boldsymbol{r}_j|)$$

we have a divergence, whenever $i = j$. This is obviously an artifact of the continuum approximation. The singularity at the center of the vortex is regularized by the presence of the lattice. We remove the $i = j$ terms and add by hand the cost E_n of a vortex core with winding number n to the Hamiltonian:

$$H_V = \sum_i E_{n_i} + 2\pi J \sum_{i<j} n_i n_j \log V(|\boldsymbol{r}_i - \boldsymbol{r}_j|)$$

One can now argue that at low temperatures only the $n_i = \pm 1$ sectors contribute. This is due to the fact that the ratio of vortex-energy to vortex-entropy is lowest for winding number ± 1. Thus by decreasing the temperature sufficiently it is always possible to justify the omission of the higher winding number sectors.

The partition function of the vortex part is now given by

$$\begin{aligned} Z_V &= \sum_{N=0}^{\infty} \frac{1}{N!^2} \prod_{i=1}^{2N} \int d\boldsymbol{x}_i \ \exp\left(-\beta\ 2NE_{\pm 1} - 2\pi\beta J \sum_{i<j} n_i n_j \log V(|\boldsymbol{r}_i - \boldsymbol{r}_j|) \right), \\ &= \sum_{N=0}^{\infty} \frac{y_0^{2N}}{N!^2} \prod_{i=1}^{2N} \int d\boldsymbol{x}_i \ \exp\left(-2\pi\beta J \sum_{i<j} n_i n_j \log V(|\boldsymbol{r}_i - \boldsymbol{r}_j|) \right), \end{aligned}$$

where N is the number of positive and negative vortex pairs, i.e. a total of $2N$ vortices. The factor $N!^2$ accounts for over-counting the configurations in the integral over the positions of the vortex centers. Since reattributing the labels among all the positive winding vortices and negative winding vortices does not change the configuration, we have to divide by $N!$ twice. We also introduced the fugacity $y_0 \equiv \exp(-\beta E_{\pm 1})$.

The vortex partition function obviously represents a two-dimensional system of N positive and N negative charges interacting by the Coloumb force. The BKT phase transition in this picture is the transition from a state in which positive and negative charges are bound together as dipoles to a high-temperature phase, where one has a plasma of free charges. Once the dipoles unbind, the interaction between charges is screened and one obtains an exponentially decaying correlation function.

In order to detect this transition, we introduce a renormalized stiffness, which is defined by the response of the system to a gradient twist on the spins. The Hamiltonian so far has the form $H = \frac{J}{2} \int d^2x\ \boldsymbol{u}^2$ with $\boldsymbol{u} = \boldsymbol{u}_1 + \boldsymbol{u}_2$, but now we add a constant vector $\boldsymbol{V}$, such that we have

$$H[\boldsymbol{V}] = \frac{J}{2} \int d^2x\ \ (\boldsymbol{u}_1 + \boldsymbol{u}_2 + \boldsymbol{V})^2 .$$

The reason we call this $\boldsymbol{V}$ a twist is that in terms of the old variable θ, we have performed the transformation $\theta \to \theta + \boldsymbol{V} \cdot \boldsymbol{r}$, i.e. we are twisting the spins in the direction of $\boldsymbol{V}$ with (linearly) increasing angle.

The stiffness of the system is now measured by how the free energy responds to such a $\boldsymbol{V}$. We define the renormalized stiffness J_{ren} by

$$F[V] - F[0] = -T \log \text{Tr}[e^{-\beta H[\boldsymbol{V}]}] + T \log \text{Tr}[e^{-\beta H[0]}] = \frac{J_{\text{ren}}}{2} V^2 + \mathcal{O}(V^4).$$

Calculating $F[V]$ straightforwardly, we obtain

$$\begin{aligned} F[V] &= -T \log \text{Tr}[e^{-\beta H[\boldsymbol{V}]}] = -T \log \text{Tr}[\exp(-\beta \frac{J}{2} \int d^2x\ \ (\boldsymbol{u} + \boldsymbol{V})^2)] \\ &= \frac{J}{2} L^2 V^2 - T \log \text{Tr}[e^{-\beta H[0]} \exp(-\beta J \int d^2x\ u_i V_i)] \end{aligned}$$

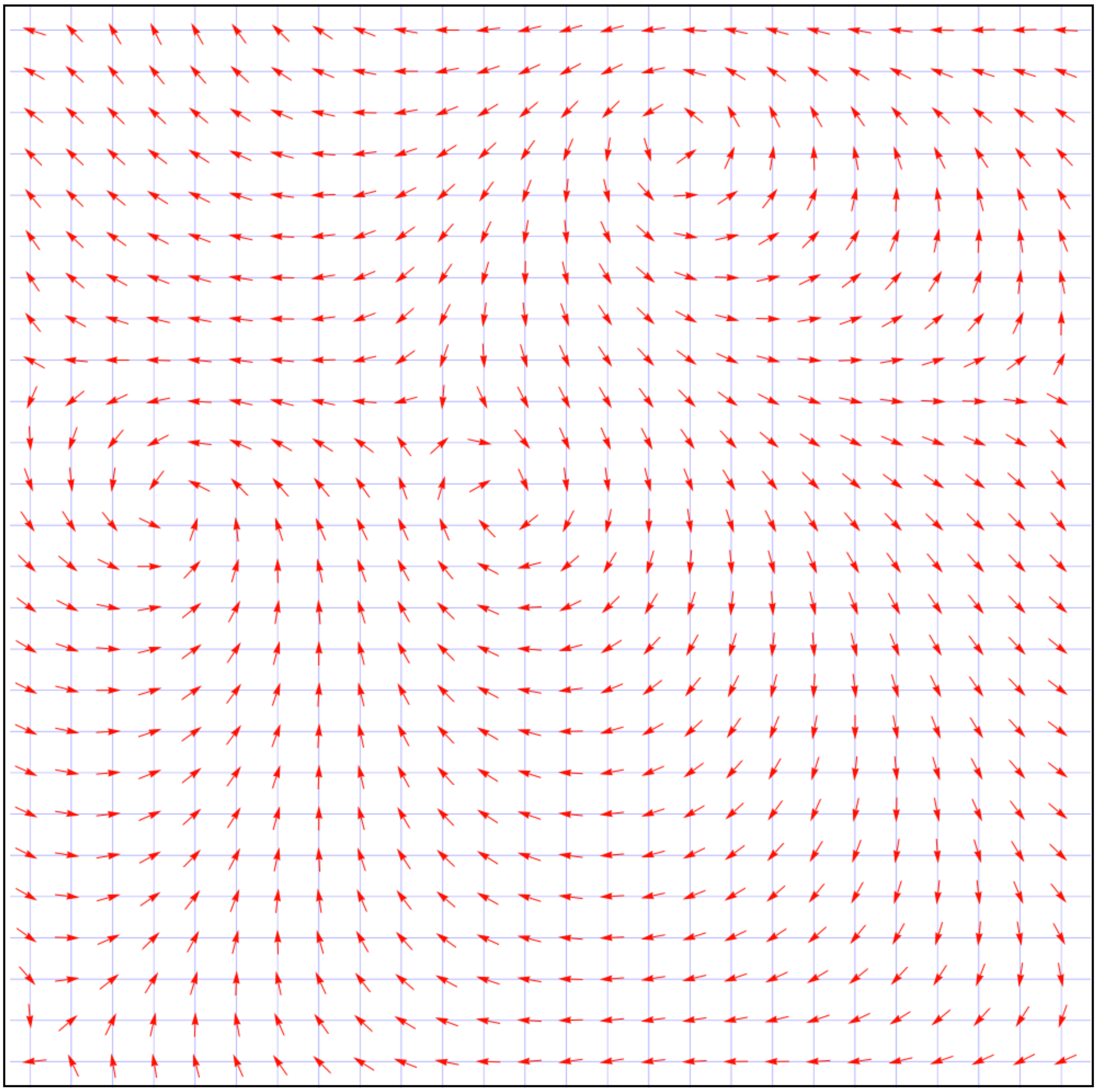

Figure 4.7: Snapshot of a spin configuration obtained from our Monte Carlo simulation of the ferromagnetic XY model on the square lattice. Three vortex defects are clearly visible for this system of 26 × 26 spins.

$$
\begin{aligned}
&= \frac{J}{2}L^2V^2 + F[0] - T\log\left\langle \exp(-\beta J\int d^2x\; u_iV_i)\right\rangle \\
&= \frac{J}{2}L^2V^2 + F[0] - \frac{J^2}{2T}\int d^2x \int d^2x' \;\left\langle u_i(\boldsymbol{x})u_j(\boldsymbol{x}')\right\rangle V_iV_j + \mathcal{O}(V^4) \qquad (4.7)
\end{aligned}
$$

where summation over i is implied, L^2 is the area of the system and the average is computed with respect to the untwisted system, i.e. using $H[0]$. In the last line we expanded up to quadratic order in V, since this is all that is required to compute the renormalized stiffness. We have shown above that the action of the system factorizes into spin-wave and vortex excitations. We can therefore consider both separately. In the decomposition $\boldsymbol{u} = \boldsymbol{u}_1 + \boldsymbol{u}_2$ the $\boldsymbol{u}_1$ term contains the spin-wave excitations. Being a gradient of an analytic potential function, these will not contribute. For instance $\int d^2x\langle u_{1i}(\boldsymbol{x})u_{1j}(\boldsymbol{x}')\rangle = \langle\int d^2x\partial_i\phi(\boldsymbol{x})u_{1j}(\boldsymbol{x}')\rangle = 0$, since on the boundary we have $\phi =$ const.. Thus we have shown that spin-wave contributions do not renormalize the system's stiffness and we may therefore restrict our attention to the vortex sector of the action.

Moreover, since the system respects translational invariance, $\langle u_i(\boldsymbol{x})u_j(\boldsymbol{x}')\rangle$ is a function of $\boldsymbol{x}-\boldsymbol{x}'$ only. Thus the double integral in eq. (4.7) obtains a volume factor once we change to difference coordinates. The remaining integral is the $\boldsymbol{q}=0$ component of the expectation value $\langle u_{2i}(\boldsymbol{q})u_{2j}(-\boldsymbol{q})\rangle$. First we notice that since we are averaging with respect to the $\boldsymbol{V}=0$ Hamiltonian, the system is isotropic. Thus the expectation value is a tensor in i and j and therefore has to be a linear combination of δ_{ij} and q_iq_j. Since $\nabla\cdot\boldsymbol{u}_2(\boldsymbol{x})=0$ for the vortex part, we conclude that $\boldsymbol{q}\cdot\boldsymbol{u}_2(\boldsymbol{q})=0$ holds. Thus $\langle u_{2i}(\boldsymbol{q})u_{2j}(-\boldsymbol{q})\rangle \sim (\delta_{ij}-q_iq_j)$. In the $\boldsymbol{q}\to 0$ limit only the δ_{ij} term is present. Using the definition of the renormalized stiffness, we obtain

$$\begin{aligned} J_{\text{ren}} &= J - \frac{J^2}{2V^2T}\int d^2q\ \langle u_{2i}(\boldsymbol{q})u_{2i}(-\boldsymbol{q})\rangle\, V_i^2 \\ &= J - \frac{J^2}{2T}\int d^2x\ \langle \boldsymbol{u}_2(\boldsymbol{x})\boldsymbol{u}_2(0)\rangle\,. \end{aligned}$$

We recall that $\boldsymbol{u}_2(\boldsymbol{x}) = \hat{\boldsymbol{z}}\times\nabla\psi(\boldsymbol{x}) = \hat{\boldsymbol{z}}\times\nabla\sum_i n_iV(|\boldsymbol{x}-\boldsymbol{x}_i|)$, where V is the Green's function in two dimensions. It therefore satisfies $\nabla^2V(\boldsymbol{x}) = -2\pi\delta(\boldsymbol{x})$ and therefore $V(\boldsymbol{q}) = -\frac{2\pi}{q^2}$. Fourier transforming $\boldsymbol{u}_2(\boldsymbol{x})$, we obtain

$$\boldsymbol{u}_2(\boldsymbol{q}) = -\hat{\boldsymbol{z}}\times\boldsymbol{q}\sum_i\frac{2\pi n_i}{q^2}e^{-i\boldsymbol{q}\boldsymbol{x}_i}$$

and hence we obtain

$$\int d^2x\ \langle\boldsymbol{u}_2(\boldsymbol{x})\boldsymbol{u}_2(0)\rangle = \frac{1}{(2\pi)^2}\lim_{\boldsymbol{q}\to 0}\langle\boldsymbol{u}_2(\boldsymbol{q})\boldsymbol{u}_2(-\boldsymbol{q})\rangle = \lim_{\boldsymbol{q}\to 0}\frac{1}{L^2}\sum_{i,j}\frac{\langle n_in_j\rangle}{q^2}e^{-i\boldsymbol{q}(\boldsymbol{x}_i-\boldsymbol{x}_j)}.$$

In the $\boldsymbol{q}\to 0$ limit only the $\boldsymbol{q}^2$ order term of the exponential survives. The lower order terms are both zero, since we have the $\sum_i n_i = 0$. Thus

$$J_{\text{ren}} = J - \frac{J^2}{2L^2T}\sum_{i,j}\langle n_in_j\rangle(\boldsymbol{x}_i-\boldsymbol{x}_j)^2.$$

It can be shown that the correlator $\langle n_in_j\rangle$ to order y_0^2 is given by

$$\langle n_in_j\rangle = -2y_0^2\left(\frac{|\boldsymbol{x}_i-\boldsymbol{x}_j|}{a}\right)^{-2\pi J/T}.$$

For the renormalized stiffness this gives

$$\begin{aligned} J_{\text{ren}} &= J - \frac{J^2}{2L^2T}\sum_{i,j}\langle n_in_j\rangle(\boldsymbol{x}_i-\boldsymbol{x}_j)^2 = J - \frac{J^2}{2L^2T}\sum_{i,j}\langle n_in_j\rangle(\boldsymbol{x}_i-\boldsymbol{x}_j)^2 \\ &= J - 4\pi^3y_0^2\frac{J^2}{aT}\int_a^\infty dr\left(\frac{r}{a}\right)^{3-2\pi J/T}. \end{aligned}$$

For $J/T > 2/\pi$ this integral is convergent and yields a finite decrement in stiffness. However, for $J/T \leq 2/\pi$ the integral diverges. It is nevertheless possible to extract further

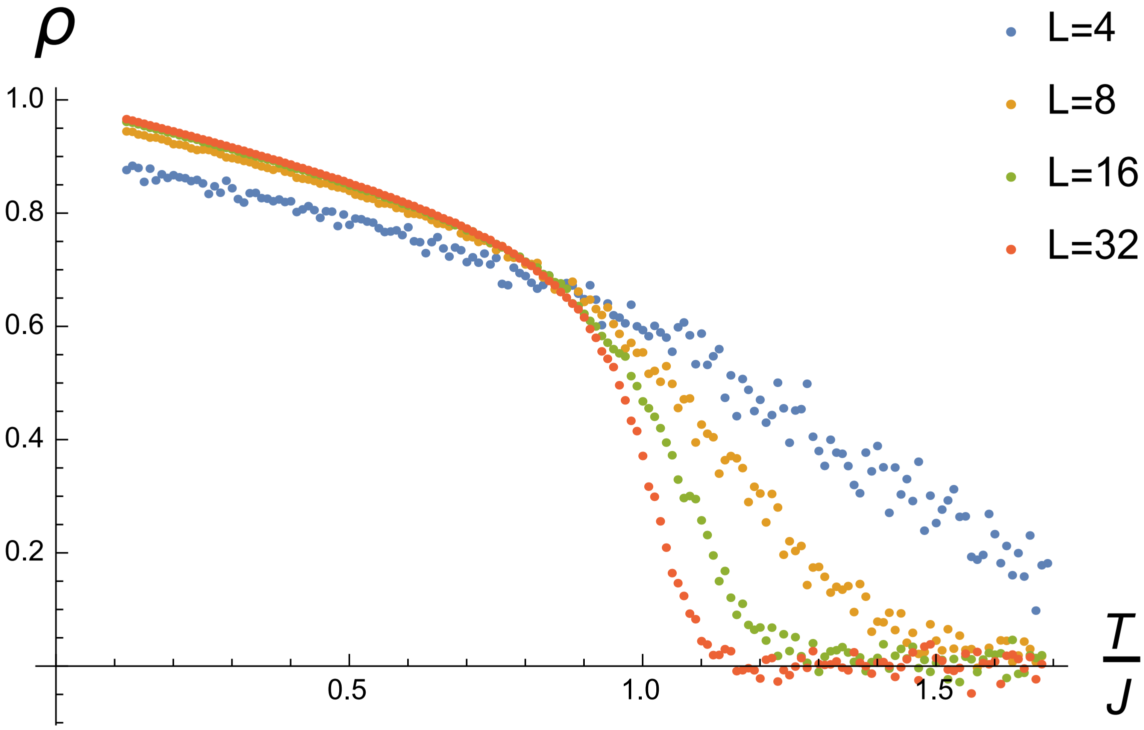

Figure 4.8: Shown are the results from our Monte Carlo simulations that measured the spin stiffness of a ferromagnetic XY model on a square lattice for sizes $N = 4 \times 4, 8 \times 8, 16 \times 16$ and 32×32 with the jump between $T/J = 0.9, \ldots, 1.1$ clearly visible.

information about the renormalization of the stiffness by constructing a flow equation. We carry out a small, finite part of the short-scale real-space integration, namely in the interval $[a, a \cdot b]$, where $b > 1$, and formally keep the remaining, divergent integral. We rescale the latter such that it formally looks identical to its previous form. Carrying out these steps and introducing $l = \log b$ and $K = J/T$, we obtain the two flow equations

$$\frac{dK^{-1}(l)}{dl} = 4\pi^3 y^2(l) \tag{4.8}$$

$$\frac{dy(l)}{dl} = [2 - \pi K(l)]\, y(l). \tag{4.9}$$

We see that for $K > 2/\pi$, the fugacity decreases to zero. This can be understood from the fact that the flow equations describe the effect of coarse-graining on $K(l)$ and $y(l)$. In the phase where the vortex pairs are bound one cannot tell by looking on very large scales, if a vortex is present. Thus the fugacity is small on large scales. The first equation tells us that in this case the coupling K flows to a constant. Thus the whole line of $y = 0$ with $K > 2/\pi$ consists of attractive fixed points.

In the other limit, when $K < 2/\pi$, the fugacity increases and K^{-1} also increases. This is the large-temperature disordered limit. Thus the phase transition is signaled by a jump in the renormalized stiffness from 0 in the high-temperature phase to a finite value of $2/\pi$ in the BKT-ordered regime.

We have carried out a Monte Carlo simulation to demonstrate this jump in stiffness and the result is shown in Figure 4.8. The simulated system consists of XY spins on a square lattice and the stiffness is calculated by using formulas derived according to the scheme described in appendix C. With increasing system size the sharpness of the jump is apparent and in the thermodynamic limit, $L \to \infty$, one would obtain a discontinuity. We can treat the differential equations (4.8) and (4.9) analytically near the origin by substituting $\Delta = K^{-1} - \pi/2$. Then

$$\begin{aligned} \frac{d\Delta(l)}{dl} &= 4\pi^3 y^2(l) \\ \frac{dy(l)}{dl} &= \frac{4}{\pi} y(l)\Delta(l), \end{aligned}$$

where we neglected terms of order Δ^2 and higher in the second equation. We obtain an invariant combination of Δ and y by noting that $\Delta\Delta' - \pi^4 yy' = 0$, thus

$$\Delta^2 - \pi^4 y^2 = c, \tag{4.10}$$

with a constant c. The collection of these curves for all c form the lines of flow shown in Figure 4.9.

We have shown in (4.4) that the correlation function decays as $G(\Delta r) \sim (\Delta r/a)^{1/(2\pi K)}$. Now we find that K gets renormalized and at the critical point it has the value $K_{\text{ren}} = 2/\pi$, i.e. $G(\Delta r) \sim (\Delta r/a)^{1/4}$. Thus the critical exponent η, which is defined in two dimensions by $G(\Delta r) \sim (\Delta r/a)^{-\eta}$ takes on the value $\eta = 1/4$ at the phase transition and decreases continuously with temperature.

Finally we want to obtain the behavior of the correlation length with temperature as the critical point is approached from above. In order to derive the formula for this, we notice first that the constant c vanishes at the critical point. Close to, but in a region larger than T_c we can linearize c as $-b^2(T - T_c)$, for some positive constant b. Then we can use the equation (4.10) to eliminate y^2 from the first flow equation to obtain

$$\frac{d\Delta}{dl} = 4\pi^3 y^2 = \frac{4}{\pi}\left(\Delta^2 + b^2(T - T_c)\right),$$

which can be integrated to yield

$$\frac{4}{\pi} l = \frac{1}{b\sqrt{T - T_c}} \tan^{-1}\left(\frac{\Delta}{b\sqrt{T - T_c}}\right)$$

The flow equations are valid only as long as Δ and y are small, therefore the integration can only be carried out until either Δ or y is of the order of 1. The flow parameter l will by then have reached a value l^*, which is defined by letting $\Delta = 1$ in the previous equation

$$l^* = \frac{\pi^2}{8b\sqrt{T - T_c}},$$

where we used that $\tan^{-1} x \to \pi/2$ for $x \to \infty$. The correlation length has then grown to the value

$$\xi = ae^{l^*} = a \exp\left(\frac{\pi^2}{8b\sqrt{T - T_c}}\right).$$

This relation will be used below in the finite-size scaling analysis.

As a last remark on this topic we point out that the singular part of the free energy density, f, behaves as ξ^{-2}, since we are in two dimensions. Thus we obtain

$$f \sim \exp\left(-\frac{\pi^2}{4b\sqrt{T - T_c}}\right),$$

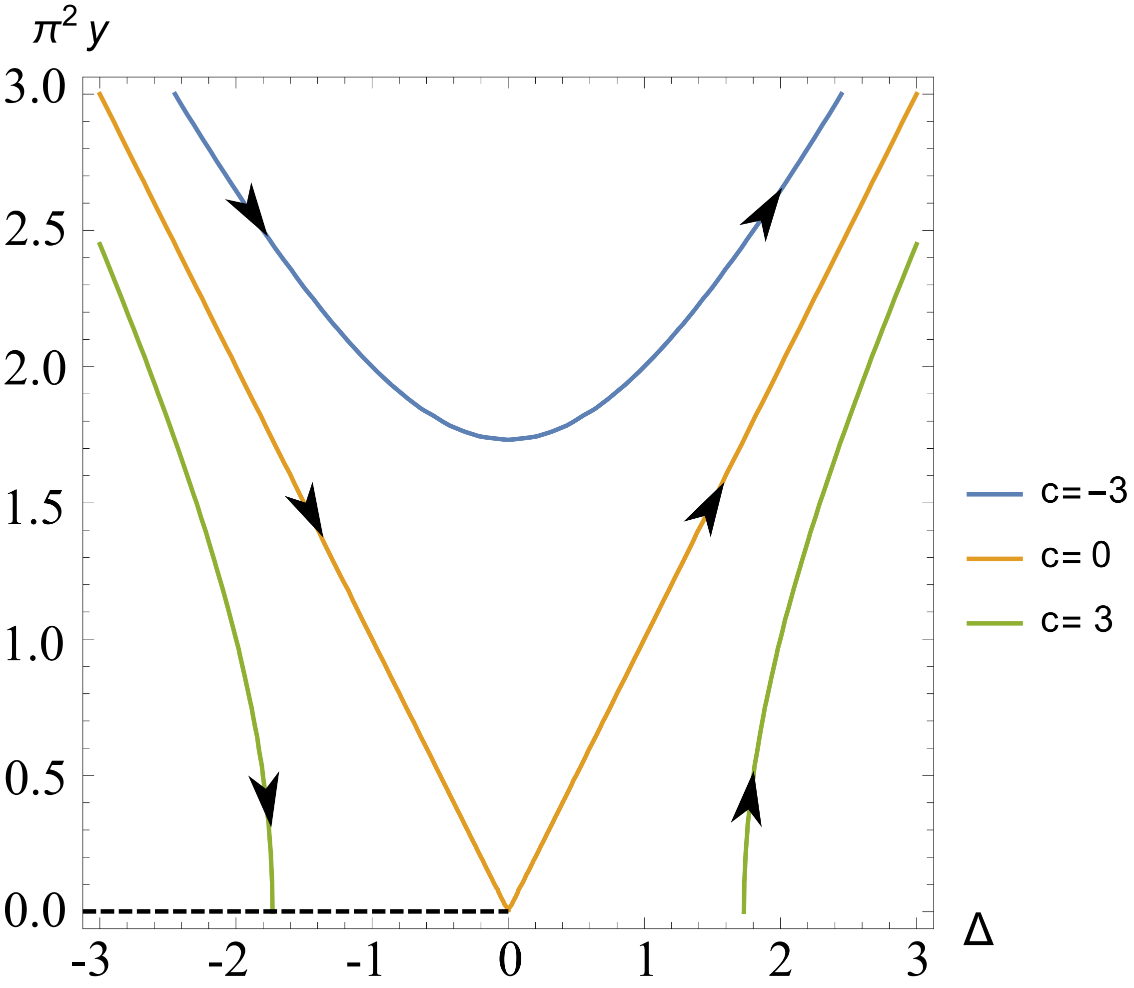

Figure 4.9: BKT flow lines. The left half-line of $y = 0$ consists of attractive fixed points (dashed line).

which shows that the free energy and all its finite-order derivatives are analytic at $T = T_c$. For this reason the BKT transition is sometimes called an infinite order phase transition.

4.2.4 Six-fold potential

In pioneering renormalization group work J. V. José et al. [39] undertook an extensive study of planar spin models on the square lattice in the presence of *external fields*, where each spin $\boldsymbol{S}_i$ is exposed to a symmetry breaking potential of the type $h_n \cos(n\theta_i)$, with θ_i being the XY degree of freedom of the spin.

We will only be interested in the case $n = 6$, which is the order-by-disorder potential for the Heisenberg windmill lattice (see appendix E). The result of the analysis in [39] is shown in the phase diagram in Figure 4.10. At high temperatures the effect of the presence of a finite six-fold potential is to renormalize the transition temperature T_1 between the disordered and the algebraically correlated regime. As the temperature of the system is lowered, one encounters another phase transition, the reason being the h_6 term in the Hamiltonian. The system possesses a fixed point where all spins fall into a common

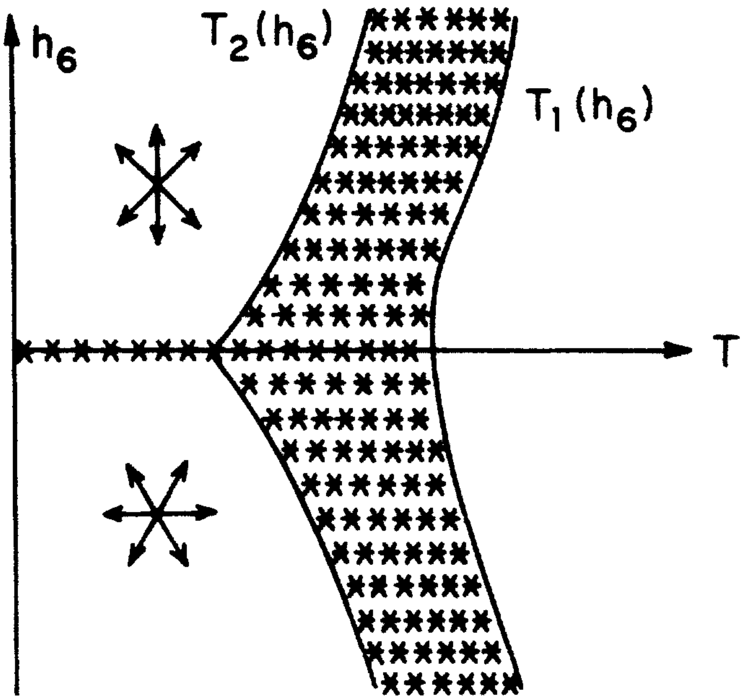

Figure 4.10: Finite temperature phase diagram from J.V. José et al. [39]. The authors find that an XY spin model in a six-fold symmetry breaking potential of strength h_6 develops a critical region inside a temperature interval $[T_2(h_6), T_1(h_6)]$. Reprinted with permission from [39] (http://dx.doi.org/10.1103/PhysRevB.16.1217), Copyright (1977) by the American Physical Society

minimum of the six-fold potential. As is clear from the phase diagram, the physics for arbitrarily small symmetry breaking fields h_6 is different from the $h_6 = 0$ behavior.
In [39] it was also found that the critical exponent η, which is $\eta_> = \frac{1}{4}$ at the upper temperature, decreases continuously until $T = T_2$. There it reaches the value $\eta_< = \frac{1}{9}$. These values of the critical exponent will also be determined in the Monte Carlo simulations below and thereby serve as evidence that the universality class of the transitions is BKT.

4.3 Heisenberg windmill magnet and emergent power-law phase

The model treated in this section provides the answer to the question of how the J_1-J_2 model may be generalized to produce other types of emergent degrees of freedom. This so-called Heisenberg windmill magnet was introduced and studied in [72, 73]. The model is defined by the Hamiltonian

$$H = J_{tt} \sum_{\langle ij \rangle} \boldsymbol{S}_i^t \cdot \boldsymbol{S}_j^t + J_{hh} \sum_{\langle ij \rangle} \boldsymbol{S}_i^h \cdot \boldsymbol{S}_j^h + J_{th} \sum_{\langle ij \rangle} \boldsymbol{S}_i^t \cdot \boldsymbol{S}_j^h \tag{4.11}$$

with positive coupling constants. According to our results in chapter 3, we are in the decoupled regime, as long as $J_{th} \leq \sqrt{J_{tt} J_{hh}}$ is provided, where the emergent phase we

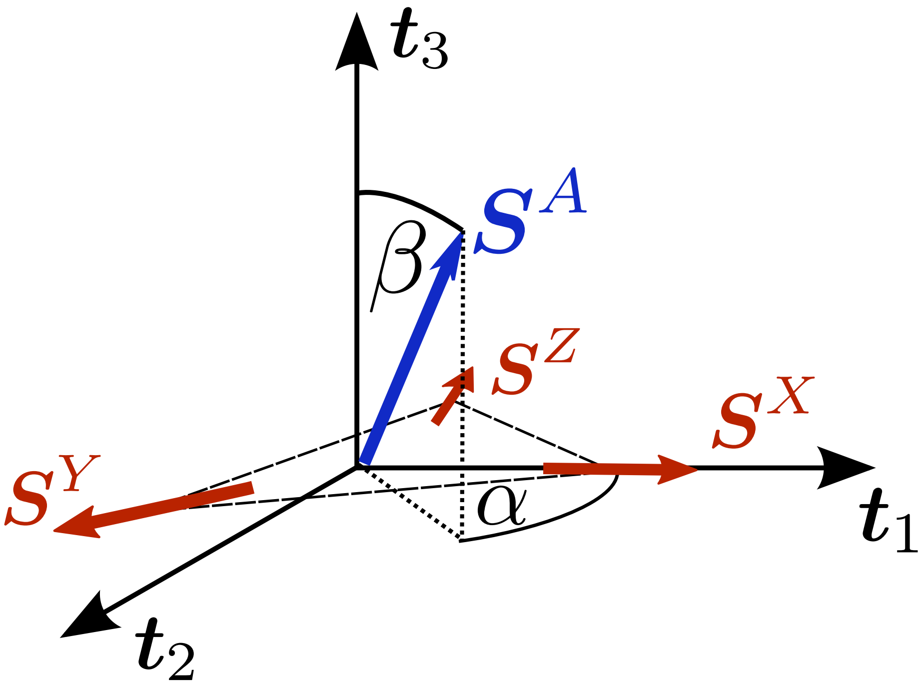

Figure 4.11: The relative orientation of an A-site honeycomb spin is described by giving its spherical coordinates in a tripod system that is constructed from the triangular lattice spins. The latter define a plane and thereby a direction perpendicular to it.

are interested in occurs. As a reminder, the $T = 0$ ground state is characterized by coplanar 120° order of the triangular spins and Néel order of the honeycomb spins (see Fig. 4.16) [38]. This order has $\mathrm{SO}(3) \times \mathrm{O}(3)/\mathrm{O}(2)$ symmetry and is described by five Euler angles $(\theta, \phi, \psi) \times (\alpha, \beta)$. As shown in Fig. 4.11, the angles (α, β) describe the orientation of the honeycomb spins relative to the coordinate system $\boldsymbol{t}_\gamma$ $(\gamma = 1, 2, 3)$ set by the triangular spins. The Euler angles (θ, ϕ, ψ) relate $\boldsymbol{t}_\gamma$ to a fixed coordinate system. While the relative orientation can be changed without energy cost at $T = 0$, thermal fluctuations induce order-by-disorder potentials [102, 90, 35]. These potentials arise due to the fact that low-energy fluctuations around a given ground state have entropies that depend on α and β, a dependence that is captured via the free-energy. Considering Gaussian thermal fluctuations around the classical ground state, one finds a contribution to the free energy equal to (see [10] for the general procedure and the appendix E in this thesis for the derivation of the following formula)

$$\frac{F_{\mathrm{pot}}}{NT} = \cos(2\beta)\left[0.131\frac{J_{th}^2}{\bar{J}^2} - 10^{-4}\frac{J_{th}^6}{\bar{J}^6}\cos^2(3\alpha)\right]. \tag{4.12}$$

The first term forces the spins to become coplanar ($\beta = \pi/2$) below a coplanarity crossover temperature T_{cp} . More precisely, long-wavelength excitations out of the plane acquire a mass and are gapped out for $T < T_{cp}$. The second term shows that the remaining U(1) relative angle α is subject to a $\mathbb{Z}_6$ potential.

In order to study this model and the emergent phases, we developed a Monte Carlo code that is capable of demonstrating unequivocally the existence of the phase transitions, critical exponents, universality classes and the exact phase diagram.

As a means of dealing with the feeble order-by-disorder $\boldsymbol{Z}_6$-potential and the rather large system sizes that are required for the finite-size scaling analysis, it was necessary to implement a three-step thermalization procedure. We employ large-scale parallel tempering classical Monte-Carlo simulations to obtain the finite temperature phase diagram shown in Fig. 4.16. As the emergent order parameter is a multi-spin object, a specific non-local Monte-Carlo updating sequence consisting of three sub-routines had to be designed: (i) a heat bath step [61] in which a randomly chosen spin is aligned within the local exchange field of its neighbors according to a Boltzmann weight; (ii) a standard parallel tempering move [55, 36] for which we run parallel simulations at 40 temperature points and switch neighboring configurations according to the Metropolis rule; finally step (iii) is necessary in order to include the effect of the minute $\mathbb{Z}_6$ order-by-disorder potential. It works by selecting a (global) rotation axis perpendicular to the average plane of the triangular spins, which exhibit (local) 120° order, and rotate all honeycomb spins around this axis by a randomly chosen angle and accept or reject by the Metropolis rule. This series of three algorithm steps was applied at least for 9×10^5 Monte-Carlo steps of which the first half is discarded to account for thermalization.

In the next three sections we will describe the steps of this algorithm in succession. The pseudo-code below shows how these three steps fit together structurally.

Algorithm Three-step Monte Carlo algorithm

```
for ($i = 1, i \leq$ Thermalization Steps, $i = i + 1$) do
    for ($l = 1$, $l \leq$ number of lattices $L$, $l = l + 2$) do
        ParallelTempering ($l, l + 1$)
    end for
    for ($l = 2$, $l \leq$ number of lattices, $l = l + 2$) do
        ParallelTempering ($l, l + 1$)
    end for
    for ($l = 1$, $l \leq$ number of lattices, $l = l + 1$) do
        Heatbath($l$)
    end for
    for ($l = 1$, $l \leq$ number of lattices, $l = l + 1$) do
        GlobalRotation($l$)
    end for
end for
for ($i = 1, i \leq$ Measurement Steps, $i = i + 1$) do
    for ($l = 1$, $l \leq$ number of lattices, $l = l + 1$) do
        Measure($l$)
    end for
end for
```

The first outer for-loop is for the purpose of thermalization, i.e. we allow the $L = 40$ lattices to equilibrate before any measurements are undertaken. Attached to every lattice is a unique temperature. The parallel tempering move is the only step in the algorithm that can change the associated temperatures. All steps in the program are parallelized and each thread handles one lattice at a time. In order to avoid collisions, i.e. instances where two threads try to modify the same lattice in the memory, we perform the parallel tempering in two separate for-loops by considering first only the switches between lattice pairs $(1, 2), (3, 4), (4, 5), \ldots$ and only in the second loop do we consider the switch of pairs

$(2,3),(4,5),(6,7),\ldots$. This is the reason for the two for-loops that carry out parallel tempering moves.
Once thermalization is finished the measurements are carried out. Before we describe what is measured, we first turn to the three algorithm steps in turn.

4.3.1 The heat bath algorithm

Arguably the simplest way to simulate a classical system of Heisenberg spins is a Monte Carlo simulation using the standard Metropolis rule [60, 68]. The algorithm in this case works by randomly choosing a spin and proposing a new orientation for it. The acceptance rule for this move is to calculate the change in energy ΔE associated with this change in spin direction. The Metropolis rule is given by

$$\begin{cases} \Delta E \leq 0 & \text{always accept,} \\ \Delta E \geq 0 & \text{accept with probability } e^{-\beta \Delta E}. \end{cases}$$

Although this algorithm is always worth a try given its simplicity and straightforward implementation, it is highly unsuited for the windmill model due to its computational inefficiency. The acceptance ratio (i.e. the fraction of all the proposed moves that are accepted) near the temperatures at which the interesting physics takes place can be on the order of 10^{-3} or even smaller. Thus most of the proposed moves get rejected, entailing a large averaging time for expectation values. Even with highly parallelized code, working on multiple cores, the required statistical averages could not be computed for reasonable system sizes after many days of computation time.

We resort, therefore, to a technique called the *heat bath* method [61, 68], which is also a single spin algorithm. However, in contrast to Metropolis Monte Carlo, with this technique every step leads to a change of the spin configuration. The stochastic element enters not through the acceptance or rejection of a proposed step, but by means of a rotation angle that is a function of a random number.
A single step of the algorithm consists in selecting a spin $\boldsymbol{S}_i$ at random and in updating only $\boldsymbol{S}_i$, while leaving the remaining spins untouched. The interaction with the neighbors of $\boldsymbol{S}_i$ is seen as the field with respect to which the spin can orient itself. If $\boldsymbol{S}_i$ were randomly moving in the field of the other spins, while the latter are held fixed, the probability distribution of finding this spin oriented with spherical angles inside the intervals $[\theta, \theta + d\theta]$ and $[\phi, \phi + d\phi]$ is calculated by

$$\frac{\exp\left(-\beta H\left(\{\boldsymbol{S}_j\}\right)\right)}{\int\limits_{\boldsymbol{S}_i} \exp\left(-\beta H\left(\{\boldsymbol{S}_j\}\right)\right)} \sin\theta d\theta d\phi = \frac{\exp\left(-\beta F \cos\theta\right) \sin\theta d\theta d\phi}{\int\limits_0^{2\pi} \int\limits_0^{\pi} d\phi d\theta \sin\theta \exp\left(-\beta F \cos\theta\right)} \tag{4.13}$$

where the integration is only over the spin we are considering. In going to the second expression, we used the fact that all terms in the Hamiltonian not containing $\boldsymbol{S}_i$ will cancel. The surviving terms are the interactions that involve $\boldsymbol{S}_i$. The sum of these interactions has been rewritten by introducing the vector

$$\boldsymbol{F}(i) = \begin{cases} J_{tt} \sum_{j(i)_t} \boldsymbol{S}_j + J_{th} \sum_{j(i)_h} \boldsymbol{S}_j, & i \text{ in triangular lattice} \\ J_{hh} \sum_{j(i)_h} \boldsymbol{S}_j + J_{th} \sum_{j(i)_t} \boldsymbol{S}_j, & i \text{ in honeycomb lattice} \end{cases}$$

where θ is the angle between $\boldsymbol{F}$ and spin $\boldsymbol{S}_i$ and we treat $\boldsymbol{F}$ as the z-axis. Noticing that the probability distribution is independent of ϕ we choose the $\phi = 0$ plane to be the one spanned by $\boldsymbol{F}$ and $\boldsymbol{S}_i$. The notation $j(i)$ stands for the neighbor number j of spin i. The denominator of the probability distribution is easily calculated:

$$\int_0^{2\pi} d\phi \int_0^{\pi} d\theta \sin\theta \exp\left(-\beta F \cos\theta\right) = \frac{4\pi}{\beta F} \sinh\left(\beta F\right).$$

The probability of finding the spin with an angle smaller than θ and arbitrary azimuth angle is given by

$$R(\theta) = \frac{\int_0^{2\pi} d\phi \int_0^{\theta} d\theta' \sin\theta' \exp\left(-\beta F \cos\theta'\right)}{\int_0^{2\pi} d\phi \int_0^{\pi} d\theta \sin\theta \exp\left(-\beta F \cos\theta\right)} = \frac{1}{2\sinh\left(\beta F\right)} \left[e^{-\beta F \cos\theta} - e^{-\beta F}\right]. \tag{4.14}$$

Now $R(0) = 0,\ R(\pi) = 1$. Hence, for a uniform distribution of R the probability of finding a value in the interval $[R(\theta), R(\theta + d\theta)]$ is equal to the probability of having a spin with angle between θ and $\theta + d\theta$.

Therefore the algorithm will work as follows. A random number R is generated in the interval $[0, 1]$. From (4.14) we can find the corresponding θ

$$\cos\theta = -\frac{1}{\beta F} \log\left[R e^{\beta F} + (1 - R) e^{-\beta F}\right].$$

The transformation on the azimuth angle is simpler as there is no energy change associated with an update of ϕ. Thus let R' be another random number in the interval $[0, 1]$. Then choose ϕ simply by

$$\phi = 2\pi R'.$$

This completes the description of how the algorithm works. It is obvious that any configuration of spins can in principle be reached by a series of such operations, thus ergodicity is satisfied. It is similarly easy to demonstrate [68] that detailed balance is satisfied by virtue of the fact that a move between two configurations with angles θ and θ' is given by (4.13):

$$p(\theta) p(\theta \to \theta') = p(\theta') p(\theta' \to \theta)$$

Concerning the runtime, the computational effort in this algorithm mostly stems from the rotation of spins to their new configuration. Let the old spin be $\boldsymbol{S}$ and the new one be $\boldsymbol{S}'$ and the angle these make with $\hat{\boldsymbol{F}}$ be θ and θ' respectively. Let $\hat{\boldsymbol{F}}$ be the unit vector in the direction of the field and $\hat{\boldsymbol{n}}$ the normalized component of $\boldsymbol{S}$ perpendicular to $\hat{\boldsymbol{F}}$. We have for the unit vector

$$\begin{aligned} \hat{\boldsymbol{n}} &= \frac{\boldsymbol{S} - (\boldsymbol{S} \cdot \hat{\boldsymbol{F}}) \hat{\boldsymbol{F}}}{\mathcal{N}} \\ \mathcal{N} &= \sqrt{1 - (\boldsymbol{S} \cdot \hat{\boldsymbol{F}})^2}. \end{aligned}$$

The new spin vector can be straightforwardly expressed in terms of the three perpendicular unit vectors $\hat{\boldsymbol{F}}, \hat{\boldsymbol{n}}, \hat{\boldsymbol{F}} \times \hat{\boldsymbol{n}}$:

$$\begin{aligned} \boldsymbol{S}' &= \cos\theta' \hat{\boldsymbol{F}} + \sin\theta' \cos\phi' \hat{\boldsymbol{n}} + \sin\theta' \sin\phi' \hat{\boldsymbol{F}} \times \hat{\boldsymbol{n}} \\ &= \frac{\sin\theta' \cos\phi'}{\mathcal{N}} \boldsymbol{S} + \left[\cos\theta' - \frac{\sin\theta' \cos\phi'}{\mathcal{N}} \boldsymbol{S} \cdot \hat{\boldsymbol{F}}\right] \hat{\boldsymbol{F}} + \frac{\sin\theta' \sin\phi'}{\mathcal{N}} \hat{\boldsymbol{F}} \times \boldsymbol{S} \end{aligned}$$

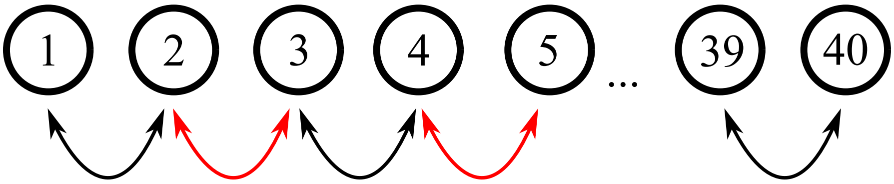

Figure 4.12: This figure illustrates the concept of the parallel tempering algorithm. Lattice configurations with neighboring temperature values are proposed to be swapped. Using a Metropolis-type rule this switch is either accepted or rejected. Since the code is parallelized, we first propose switches of the odd-numbered lattices with their right neighbors (black) and do the same same for even number lattices (red) in the next run (see text for explanation).

4.3.2 Parallel tempering

In order to improve the speed of thermalization, it is useful to add a parallel tempering step. This algorithm was discovered by [55, 36], for a pedagogical exposition see [41]. Our simulation runs 40 independent copies of the windmill lattice in parallel, we denote these copies by $S_1, S_2, \ldots, S_{40}$, which are all at different temperatures, expressed by the function $T(S_i)$. The parallel tempering move consists in proposing a switch between configurations that have neighboring temperatures (see Fig. 4.12). In practice it is computationally far less costly to switch the temperatures instead of the spin configurations, i.e. a switch $T(S_i) \leftrightarrow T(S_j)$ is performed, where S_i and S_j are systems that are neighbors in temperature space. Let the two configurations have energies E_i and E_j and let the current temperatures of these systems be T_i and T_j, respectively. Then the joint probability for these two systems to be in these configurations at their respective temperatures is given by the product

$$P_{ij} = \frac{e^{-E_i/T_i}}{Z}\frac{e^{-E_j/T_j}}{Z},$$

where Z is the partition function of the system. Upon switching the temperatures of the two systems we would obtain the joint probability

$$P'_{ij} = \frac{e^{-E_i/T_j}}{Z}\frac{e^{-E_j/T_i}}{Z}.$$

Detailed balance is guaranteed, if the proposed switch is accepted or rejected according to the rule

$$\begin{cases} P_{ij} \le P'_{ij} & \text{always accept} \\ P_{ij} \ge P'_{ij} & \text{accept with probability } \frac{P'_{ij}}{P_{ij}} = \exp\left[(E_i - E_j)(\frac{1}{T_i} - \frac{1}{T_j})\right]. \end{cases}$$

4.3.3 The global rotation step

The effect of the $\boldsymbol{Z}_6$ order-by-disorder potential is so feeble that its effect cannot be detected by running the previous two algorithm steps for a reasonable time. It is necessary to allow the system to explore configurations that are of nearly equal energy, but are not easily accessible due to the fact that these cannot be reached by the update of a single spin. In a later section we define the temperature T_{cp}, below which the system is almost

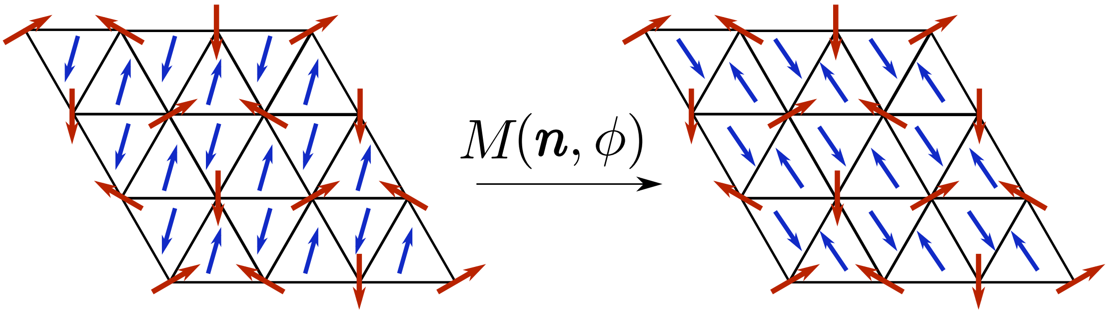

Figure 4.13: The rotation operation $M(\boldsymbol{n},\phi)$ is applied to the honeycomb spins. The direction of the rotation axis $\boldsymbol{n}$ is selected to be a vector, that is on average perpendicular to the plane of the triangular lattice vectors. Thus in the figure $\boldsymbol{n}$ points in the direction perpendicular to the plane of drawing.

coplanar. Thus fluctuations out of the plane cost energy. However, the $\boldsymbol{Z}_6$ is weak enough that a rotation of the honeycomb lattice relative to the triangular lattice costs almost no energy. The third step in our three-step algorithm, therefore, consists in proposing a rotation of the whole honeycomb lattice relative to the triangular lattice around a certain axis described by the unit vector $\boldsymbol{n}$. This axis is determined as the average direction perpendicular to the plane of the triangular lattice spins. An angle ϕ is chosen randomly in the interval $[0, 2\pi]$ and a rotation of all the honeycomb spins around $\boldsymbol{n}$ by ϕ is proposed. The related energy change ΔE due to such a move is calculated and the move is accepted with probability $\min[1, \exp(-\beta\Delta E)]$.

We now need to solve the following task in order to implement the algorithm. Given a rotation axis $\boldsymbol{n}$, what is the matrix corresponding to a rotation around this axis by angle ϕ? Let $\boldsymbol{s}$ be an arbitrary vector and let $\boldsymbol{p}$ be the unit vector along the component of $\boldsymbol{s}$ perpendicular to $\boldsymbol{n}$. Then

$$\boldsymbol{p} = \frac{\boldsymbol{s} - (\boldsymbol{n}\cdot\boldsymbol{s})\boldsymbol{n}}{\sin\theta}$$

where

$$\boldsymbol{s}\cdot\boldsymbol{n} = \cos\theta.$$

Then the rotated version of $\boldsymbol{s}$ has the same component along $\boldsymbol{n}$, but the perpendicular component gets rotated by

$$\cos\phi\sin\theta\ \boldsymbol{p} + \sin\phi\sin\theta\ \boldsymbol{n}\times\boldsymbol{p}$$

thus the total transformed vector is

$$\begin{aligned}\boldsymbol{s}' &= \cos\phi\sin\theta\ \boldsymbol{p} + \sin\phi\sin\theta\ \boldsymbol{n}\times\boldsymbol{p} + \cos\theta\ \boldsymbol{n}\\ &= \cos\phi\ \boldsymbol{s} + (1-\cos\phi)\cos\theta\ \boldsymbol{n} + \sin\phi\ \boldsymbol{n}\times\boldsymbol{s}\end{aligned}$$

rewriting this in matrix form, we obtain

$$\boldsymbol{s}' = M\boldsymbol{s}$$

with

$$M_{ij}(\boldsymbol{n},\phi) \equiv (1-\cos\phi)n_i n_j + \cos\phi\delta_{ij} - \sin\phi\epsilon_{ijk}n_k$$

with an implicit sum over k.

4.3.4 Extraction of critical exponents by finite-size scaling analysis

Having found means of approaching the problem numerically, we now need to demonstrate the existence of the claimed phase transitions. We achieve this by measuring the magnetization and susceptibility of the emergent degrees of freedom. The latter are defined precisely below. We use the finite-size scaling of the magnetization to demonstrate the phase transition at $T = T_<$ and the susceptibility to demonstrate the phase transition at $T = T_>$.

A phase transition in a spin system described by statistical mechanics can only occur, if it has an infinite number of degrees of freedom. This is seen most clearly by inspecting the partition function

$$Z = \sum_{\text{configurations}} e^{-\beta E}. \tag{4.15}$$

If the number of degrees of freedom is finite, then the sum over all configurations is obtained by a finite number of integrations over angle variables, i.e. the integration intervals are all finite. Then Z is an analytic function of β.

In order for the partition function, and hence the free energy, to show singular behavior at a finite $\beta_c = 1/T_c$, it is necessary to have a system with an infinite number of angle variables. For this reason it will never be possible to observe an actual phase transition by simulating a finite system of spin degrees of freedom. One is therefore faced with the task of establishing the existence of a phase transition of a thermodynamic system by studying finite systems. This problem is solved by the theory of finite-size scaling [11, 84, 25], which predicts how thermodynamical variables are affected by finite system size. In particular it predicts functional forms for thermodynamical variables in terms of the system size L. This allows us to rescale the measured magnetization and susceptibility data in such a way that all the measurements for different system sizes come to lie on one (L-independent) curve.

The key observation in finite-size scaling theory is the fact that the finite system behaves like the infinite system if the correlation length ξ is much smaller than the system size L. The system's behavior gets modified as soon as $\xi \approx L$. This will inevitably happen close to phase transitions, where the correlation length diverges. The singularities that occur in the thermodynamic limit are associated with this diverging correlation length and are regulated by L in a finite system. In particular divergences are rounded off.

In order to demonstrate how finite-size scaling relations are deduced, we will now derive the L-dependence of the magnetization m. The scaling hypothesis for finite systems reads

$$m(t, L) = L^{\sigma} \tilde{\phi}\left(\frac{\xi}{L}\right), \tag{4.16}$$

where $t = (T - T_c)/T_c$ is the reduced temperature and $\tilde{\phi}(x)$ is a universal (i.e. independent of system size) function. The correlation length ξ is the value of the infinite system. Near the phase transition ξ shows a power law behavior $\xi \sim t^{-\nu}$. We can insert this form into the right hand side and define a new function ϕ, in which the temperature enters the argument linearly:

$$m(t, L) = L^{\sigma} \phi\left(tL^{1/\nu}\right),$$

Exactly at the critical point $t = 0$ the magnetization has a power-law dependence on the system size. However, if we are slightly away from the critical point and look at larger and larger systems, eventually L will be much larger than ξ and the system should behave as it does in the thermodynamic limit, i.e. $m \sim t^{-\beta}$. This gives the condition

$$\lim_{L\to\infty} m(t, L) = \lim_{L\to\infty} L^{\sigma}\phi\left(tL^{1/\nu}\right) \tag{4.17}$$

and in order to have the same functional dependence on t on both sides, we must have

$$\lim_{x\to\infty} \phi\left(x\right) \sim x^{-\beta}.$$

This in turn gives an L-dependence on the right hand side of (4.17) of the form $L^{\sigma-\beta/\nu}$. Since a finite-size dependence should not occur in the limit of $L \gg \xi$, we can conclude that $\sigma = \beta/\nu$ holds. Thus we have the finite-size scaling law for the magnetization

$$m(t, L) = L^{\beta/\nu}\phi(tL^{1/\nu}).$$

This is the approriate scaling-form for phase transitions with finite ν and β values. However, the BKT phase transition is characterized by an exponential singularity in the free energy. In particular, we have shown above that $\xi \sim \exp(a/\sqrt{t})$. Here we can return to the scaling ansatz in eq. (4.16) and argue as before: for $L \gg \xi$ we must get an L-independent behavior on the right hand side, thus

$$\tilde{\phi}(x) \sim x^{\sigma}, \text{ as } x \to 0.$$

Furthermore, in the system of infinite size the magnetization depends on the correlation length via the relation

$$m \sim \xi^{-\eta_{<}/2},$$

from which we can deduce $\sigma = -\eta/2$. This gives a scaling ansatz, which is appropriate for BKT transitions, of the form

$$m = L^{-\eta_{<}/2}\tilde{\phi}(L^{-1}\exp(a_{<}/\sqrt{t})) \tag{4.18}$$

with $t = \frac{T_{<}-T}{T_{<}}$. By following the same line of arguments we can deduce from the behavior of the susceptibility in the infinite system,

$$\chi = \xi^{2-\eta_{>}},$$

the scaling ansatz

$$\chi = L^{2-\eta_{>}}\tilde{\phi}(L^{-1}\exp(a_{>}/\sqrt{t})) \tag{4.19}$$

with $t = \frac{T-T_{>}}{T_{>}}$.
If we now scale the data from measurements of χ and m for various values of L by these formulas, the curves for different L will collapse onto single curves for a certain setting of parameters $\{a_{>}, \eta_{>}, a_{<}, \eta_{<}\}$. By performing this fit and obtaining a data collapse the phase transition is demonstrated and the universality class is furthermore confirmed by seeing if $\eta_{>}$ and $\eta_{<}$ agree with the values $\eta_{<} = 1/9$ and $\eta_{>} = 1/4$, which are the exponents of the planar spin model in a sixfold symmetry breaking field [39].

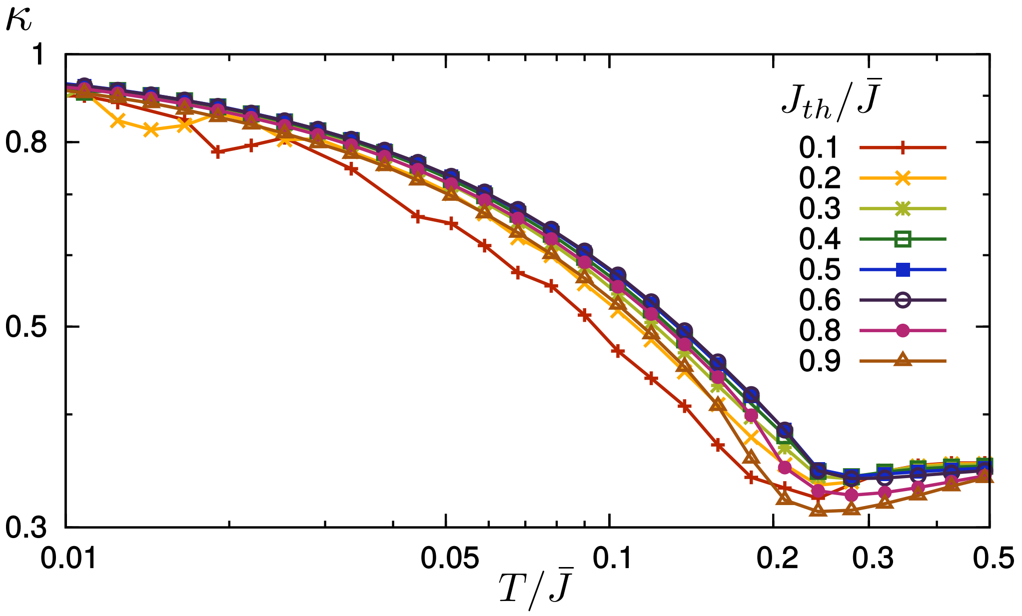

Figure 4.14: Coplanarity κ as a function of temperature for various values of $J_{th}/\bar{J}$ for system size $L = 60$.

4.3.5 Coplanar Crossover

As remarked above, the free energy has a dependence on the chosen ground state, that is given by

$$\frac{F_{\text{pot}}}{NT} = \cos(2\beta)\left[0.131\frac{J_{th}^2}{\bar{J}^2} - 10^{-4}\frac{J_{th}^6}{\bar{J}^6}\cos^2(3\alpha)\right]. \tag{4.20}$$

The first term of this equation forces the system to become coplanar with $\beta = \pi/2$. In other words, the honeycomb lattice spins are forced to lie in the plane spanned by the triangular lattice spins.

This coplanarity crossover is determined in the Monte-Carlo simulations by measuring the coplanarity

$$\kappa = 1 - \frac{3}{N}\sum_{j=1}^{N}\langle\cos^2\beta_j\rangle\,, \tag{4.21}$$

where $\cos\beta_j = \boldsymbol{S}_j^A\cdot\left(\boldsymbol{S}_j^t\times\boldsymbol{S}_{j+\delta_{tt}}^t\right)$ with δ_{tt} being a nearest-neighbor vector on the triangular lattice. The result is shown in the plot in Fig. 4.14. In order to understand this plot it is useful to consider the two extremes. At very high temperatures, where no relative spin configuration is preferred, a straightforward averaging over all orientations of the three spins yields

$$\begin{aligned}\left\langle[\boldsymbol{h}\cdot(\boldsymbol{t}_1\times\boldsymbol{t}_2)]^2\right\rangle &= \frac{1}{(4\pi)^2}\int_0^{\pi}d\theta_1\sin\theta_1\int_0^{2\pi}d\phi_1\int_0^{\pi}d\theta_2\sin\theta_2\\ &\quad\times\int_0^{2\pi}d\phi_2\,(\sin\theta_1\cos\phi_1\sin\theta_2\sin\phi_2-\sin\theta_1\sin\phi_1\sin\theta_2\cos\phi_2)^2\end{aligned}$$

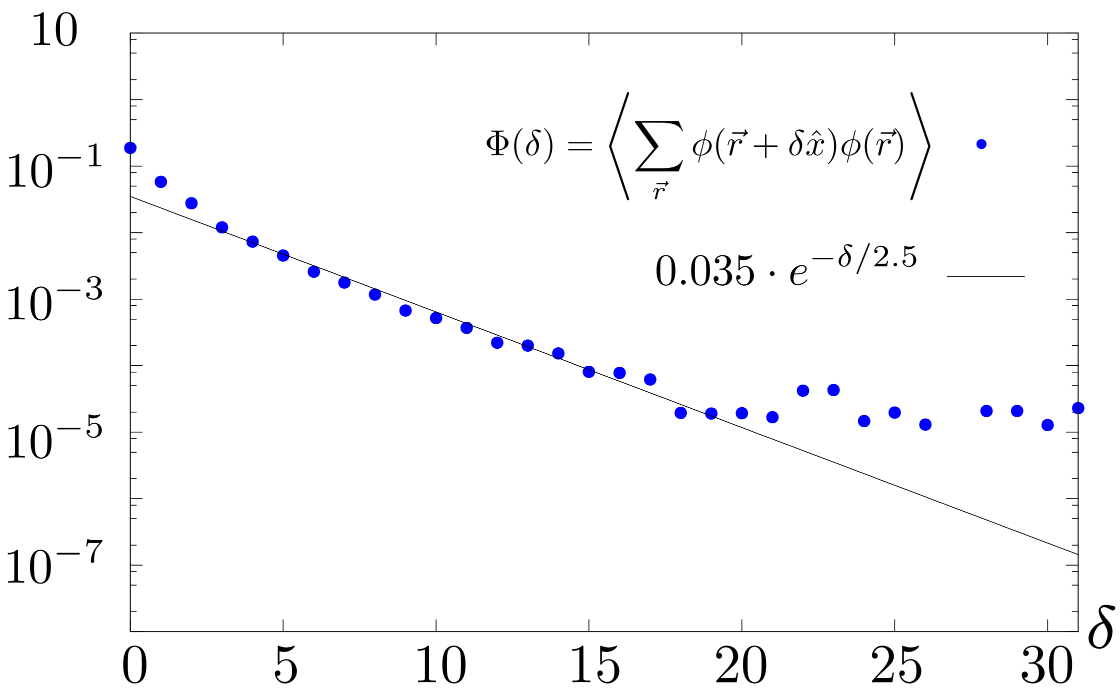

Figure 4.15: Coplanar correlations $\Phi(\delta)$ for $T = 0.2J_{tt}$ for a system of size $L = 60$. The solid line signifies exponential decay of Φ with a typical decay length of less than 3 sites. Since the system is satisfies periodic boundary conditions, only the region away from $\delta = 30$ should be explored.

where we used the fact that the quantity we are averaging is a scalar and the coordinate system may thus be rotated in such a way that h points along the z-axis. The integrals are straightforward to calculate and one obtains

$$\left\langle [\boldsymbol{h} \cdot (\boldsymbol{t}_1 \times \boldsymbol{t}_2)]^2 \right\rangle = \frac{2}{9}.$$

We have N such tripods and therefore the coplanarity is given by

$$\kappa = 1 - \frac{3}{N}\frac{2N}{9} = \frac{1}{3}.$$

In the opposite regime a completely coplanar state occurs and we have all $\beta_j = \pi/2$ and therefore $\kappa = 1$. For local triangular 120° and honeycomb Néel order that is uncorrelated with each other one finds $\kappa = 0$. Our Monte-Carlo results show that coplanarity develops as soon as $T \lesssim 0.25\bar{J}$ and κ smoothly approaches unity for lower temperatures. Interestingly, κ depends only weakly on J_{th} as long as $J_{th} \gtrsim \bar{J}/10$. We define the location of the coplanar crossover T_{cp} shown in Fig. 4.16 to be the location of the minimum of κ. Note that down to the lowest temperatures we observe substantial out-of-the plane fluctuations and $\kappa < 1$. In order to assess the origin of these fluctuations, we have measured the *coplanar correlation* defined by

$$\Phi(\delta) \equiv \left\langle \sum_{\boldsymbol{r}} \phi(\boldsymbol{r})\phi(\boldsymbol{r} + \delta\hat{x}) \right\rangle$$

where

$$\phi(\boldsymbol{r}) \equiv \boldsymbol{h}(\boldsymbol{r}) \cdot (\boldsymbol{t}_1(\boldsymbol{r}) \times \boldsymbol{t}_2(\boldsymbol{r})).$$

Clearly $\Phi(\delta)$ is a measure of how well the out of plane fluctuations are correlated. The result of the measurement is shown in figure 4.15. Over a large range the correlation may be fitted with an exponential (solid line in the figure). The decay happens on the order of 2 to 3 lattice sites. Thus we conclude that fluctuations in this temperature regime are of a short-range nature.

4.3.6 Z_6 symmetry breaking

Below the coplanar crossover temperature T_{cp} one may define emergent XY spins $\boldsymbol{m}_j$ at all Bravais lattice sites via projecting the honeycomb spin $\boldsymbol{S}_j^A$ (or $\boldsymbol{S}_j^B \approx -\boldsymbol{S}_j^A$) onto the plane that is spanned by the three nearest-neighbor triangular spins. After normalizing we obtain

$$\boldsymbol{m}_j = \frac{(\boldsymbol{S}_j^A \cdot \boldsymbol{t}_{1,j}, \boldsymbol{S}_j^A \cdot \boldsymbol{t}_{2,j})}{\|(\boldsymbol{S}_j^A \cdot \boldsymbol{t}_{1,j}, \boldsymbol{S}_j^A \cdot \boldsymbol{t}_{2,j})\|} = (\cos\alpha_j, \sin\alpha_j)\,. \tag{4.22}$$

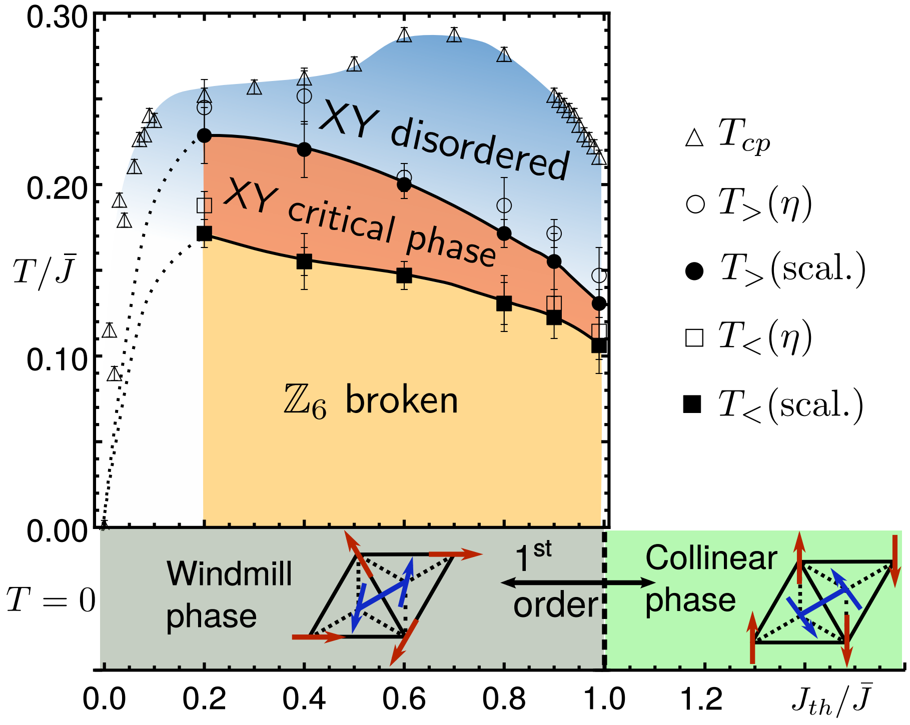

Figure 4.16: Finite temperature phase diagram of classical windmill Heisenberg antiferromagnet as a function of inter-sublattice coupling $J_{th}/\bar{J}$, $\bar{J} = \sqrt{J_{tt}J_{hh}}$. Below a coplanar crossover temperature T_{cp} , emergent XY spins appear and undergo two BKT phase transitions: at $T_>$ from a disordered to a critical phase with algebraic order and then at $T_<$ into a $\mathbb{Z}_6$ symmetry broken phase with discrete long-range order. At zero temperature the system undergoes a first order transition at $J_{th} = \bar{J}$ from a 120°/Néel ordered windmill phase to a collinear phase.

We study the behavior of these emergent spins in the remainder of this paper. The local triangular triad $\boldsymbol{t}_{\gamma,j}$ is defined as follows: the spins on the triangular lattice are first partitioned into three classes $\{\boldsymbol{S}_j^{t,X}, \boldsymbol{S}_j^{t,Y}, \boldsymbol{S}_j^{t,Z}\}$ as shown in Fig. 4.14. One then defines $\boldsymbol{t}_{1,j} = \boldsymbol{S}_j^{t,X}$ and $\boldsymbol{t}_{2,j}$ to point along the component of $\boldsymbol{S}_j^{t,Y}$ that is perpendicular to $\boldsymbol{t}_{1,j}$. Finally, $\boldsymbol{t}_{3,j} = \boldsymbol{t}_{1,j} \times \boldsymbol{t}_{2,j}$ completes the local triad. We show below that although the system exhibits out-of-the plane fluctuations and $\kappa < 1$, the emergent spins $\boldsymbol{m}_j$ decouple from these fluctuations and behave as U(1) degrees of freedom.

To map out the low-temperature phase diagram we analyze the correlations of the emergent spins $\boldsymbol{m}_j$ in the following. First we define the total magnetization as

$$\boldsymbol{m} = \frac{1}{N}\sum_{j=1}^{N} \boldsymbol{m}_j = |\boldsymbol{m}|(\cos\alpha, \sin\alpha)\,. \tag{4.23}$$

The magnetization amplitude $|\boldsymbol{m}|$ depends on the (linear) system size L, in particular, it vanishes in the absence of long-range order for $L \to \infty$. Performing the Monte-Carlo average the plots in Figures 4.22-4.25 show the behavior of the magnetization with temperature for different system sizes. We also show the dependence of $\langle|\boldsymbol{m}|\rangle$ with system size L in Fig. 4.17(a). While it vanishes faster than algebraic at large temperatures, it exhibits power-law scaling $\langle|\boldsymbol{m}|\rangle \propto L^{-\eta(T)/2}$ with $0 < \eta \lesssim 0.3$ for intermediate temperatures, a key signature of a critical phase. At the lowest temperatures, the exponent approaches zero and the magnetization saturates. To directly prove that the system develops (discrete) long-range order, we show the direction of the magnetization vector expressed as $\langle\cos(6\alpha)\rangle$ in Fig. 4.17(b). Clearly, $\langle\cos(6\alpha)\rangle$ approaches its saturation value of unity at low temperatures and large system sizes. The relative phase vector $\boldsymbol{m}$ points into one of the six directions preferred by the $\mathbb{Z}_6$ potential in Eq. (4.20). The honeycomb spins are then aligned with one of the three triangular spin classes $\{S^{t,X}, S^{t,Y}, S^{t,Z}\}$, in agreement with the general order-from-disorder mechanism that spins tend to align their fluctuation Weiss fields to maximize their coupling [35].

To determine the universality class of the phase transition and the transition temperatures $T_>$ and $T_<$, which partition the regimes of algebraic and long-range ordering, we perform a finite-size scaling analysis of the XY susceptibility and magnetization for various values of $J_{th}/\bar{J}$ [11, 37, 78, 77, 51]. As shown in Fig. 4.26 we obtain perfect data collapse using a BKT scaling ansatz. Since the susceptibility diverges when the system enters a critical phase, we can detect the upper transition at $T_>$ by analyzing

$$\chi(T, L) = \frac{N}{T}\big\langle|\boldsymbol{m}|^2\big\rangle = \frac{1}{NT}\Big\langle\big|\sum_j \boldsymbol{m}_j\big|^2\Big\rangle \tag{4.24}$$

for different temperatures T and system sizes L. We employ a BKT ansatz for the correlation length $\xi_> = \exp\big(a_>\sqrt{T_>}/\sqrt{T - T_>}\big)$ with $a_>$ being a non-universal constant. Since $\chi(T, \infty) \sim \xi_>(T)^{2-\eta_>}$ in the infinite system, it holds that $\chi(T, L) = L^{2-\eta}Y_\chi(\xi_>(T)/L)$ with a universal function $Y_\chi(x)$. For $J_{th} = 0.6\bar{J}$ we extract the values $T_> = 0.200(4)\bar{J}$, $a_> = 1.9(3)$ and $\eta_> = 0.25(1)$ from optimizing the collapse. This agrees very well with the theoretically expected value $\eta_> = 1/4$ [39].

Performing the analysis for other values of J_{th} yields data collapse of similar quality with a value $\eta_> = 0.25$ within error bars. This determines $T_>$(scal.) and the upper phase transition line in Fig. 4.16. As an independent way to determine $T_>$, we use the power-law scaling of the magnetization with the system size L, which is expected to be

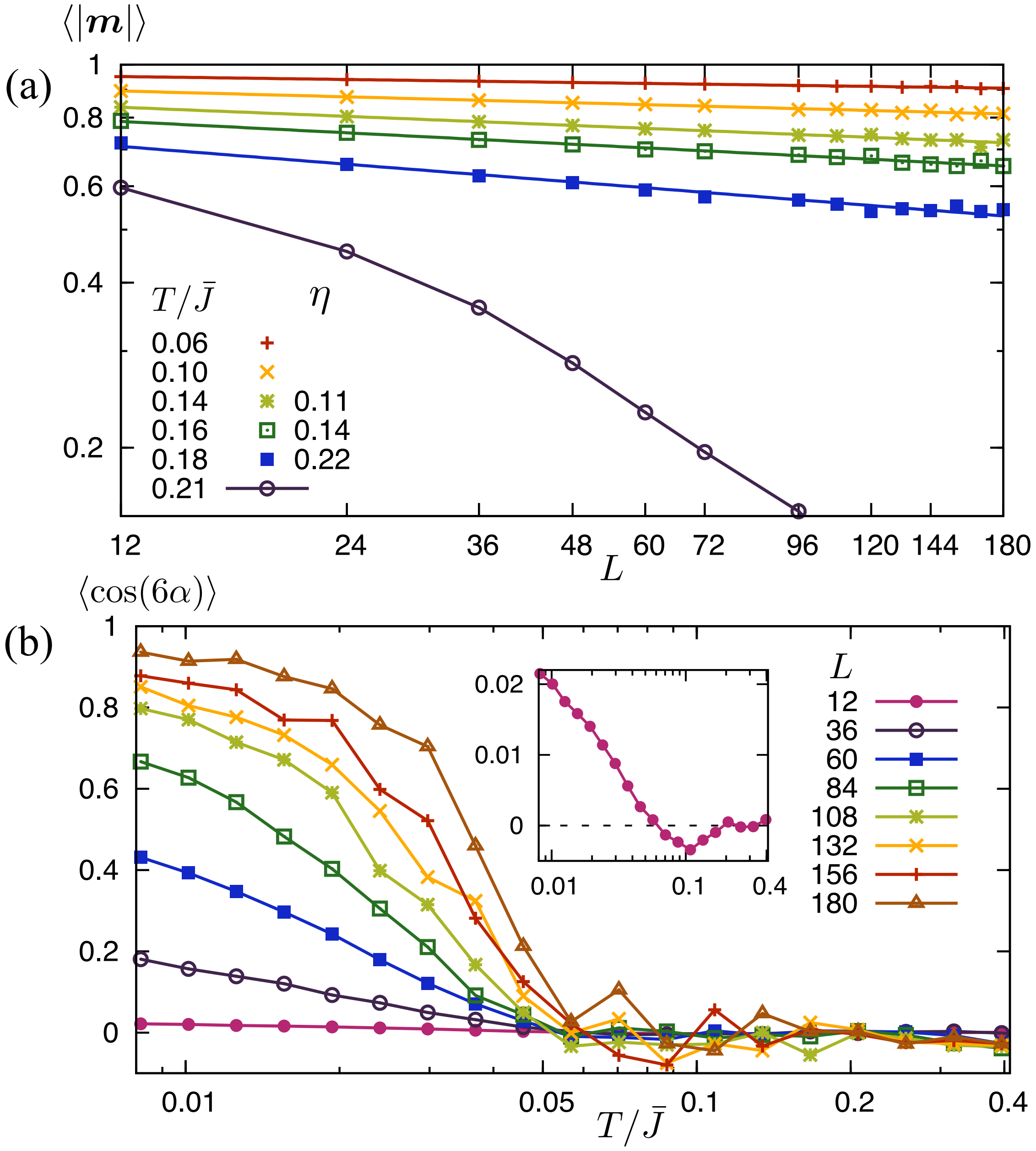

Figure 4.17: (a) XY magnetization amplitude $\langle|m|\rangle$ as a function of linear system size L for various temperatures $T/\bar{J}$ and fixed $J_{th}/\bar{J} = 0.8$. On a double logarithmic plot it exhibits linear scaling within the critical phase with indicated floating exponent $\eta(T)$. It bends down in the disordered phase. Due to the finite system size we cannot clearly observe a saturation (at a finite value) at low temperatures, but η approaches zero in a linear fit. (b) Direction of the magnetization expressed as $\langle\cos(6\alpha)\rangle$ as a function of T for $J_{th} = 0.9\bar{J}$. A non-zero value signals breaking of the six-fold symmetry at low temperatures $T < T_<$. Inset shows $L = 12$.

$\langle|\boldsymbol{m}|\rangle \propto L^{-\eta/2}$ with $\eta = 1/4$ at the upper transition. This yields $T_>(\eta)$ included in Fig. 4.16. The two temperatures agree within error bars with $T_>(\eta)$ being systematically

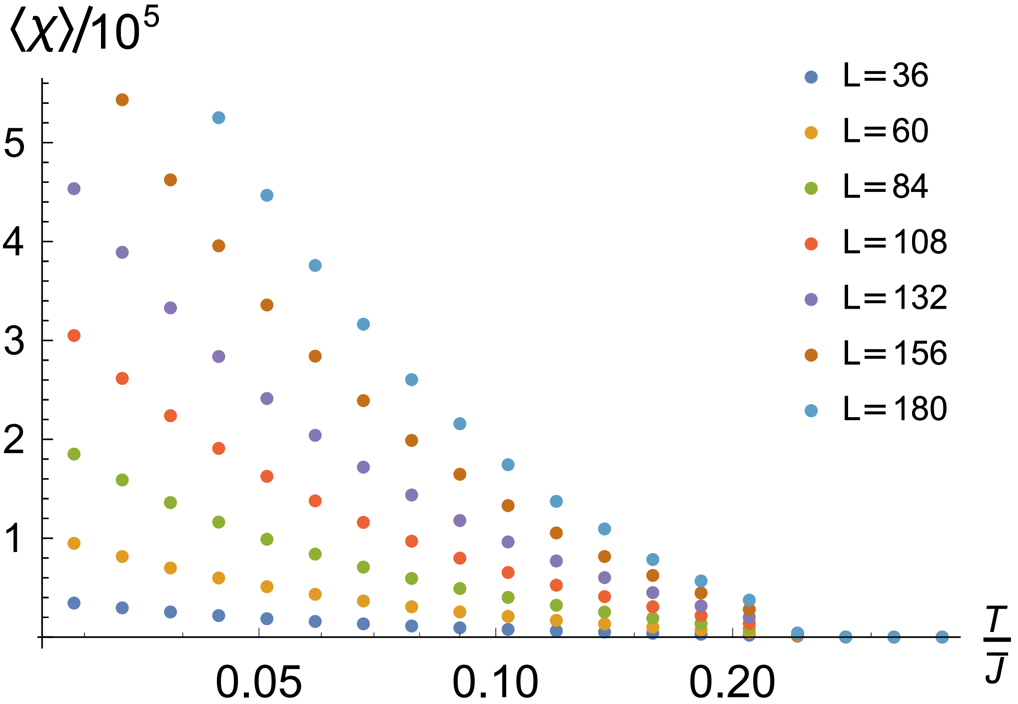

Figure 4.18: Susceptibility of emergent degrees of freedom as function of temperature for $J_{th} = 0.4\bar{J}$

slightly larger. Finally, we note that we have also tried to achieve data collapse using a scaling ansatz corresponding to a second order phase transition, but the resulting collapse is worse in this case, especially for data points close to the phase transition.

To determine the lower transition temperature $T_<$ we perform a finite size scaling analysis of the magnetization amplitude $\langle|\boldsymbol{m}|(T,L)\rangle$. Since it holds in the infinite system that $\langle|\boldsymbol{m}|(T)\rangle \propto \xi(T)_<^{-\eta_</2}$ with correlation length $\xi_< = \exp\big(a_<\sqrt{T_<}/\sqrt{T_< - T}\big)$ and non-universal factor $a_<$, it follows for a finite system that $\langle|\boldsymbol{m}|(T,L)\rangle = L^{-\eta_</2} Y_m(\xi_<(T)/L)$, where $Y_m(x)$ is a universal function. In Fig. 4.26(b) we show the best data collapse for $J_{th} = 0.6\bar{J}$ which yields $T_< = 0.18(1)$, $\eta_< = 0.11(1)$ and $a_< = 5.0(5)$. This is in good agreement with the theoretically expected value of $\eta_< = 1/9$ at the lower transition [39, 8].

Two independent ways to obtain $T_<$ are (i) to investigate the power-law scaling of $\langle|\boldsymbol{m}|\rangle$ with system size and (ii) to directly look for the symmetry breaking as indicated by the quantity $\langle\cos(6\alpha)\rangle$. Using the first method, we find that our data can be fitted to $\log\langle|\boldsymbol{m}|\rangle \propto -\frac{\eta(T)}{2}\log L$ with a temperature-dependent slope $\eta(T)$ that is monotonically decreasing over the full range $0 < T < T_>$. At high temperatures, we find $\eta(T_>) \approx 0.25$ (as expected) and we define $T_<(\eta)$ as the temperature where $\eta(T_<) = 1/9$. The fact that the system appears to be critical within our simulation even for lower temperatures (with an exponent $\eta < 1/9$) is a simple consequence of the fact that the system size is much smaller than the correlation length [37, 51]. If we were able to reach larger system sizes in the simulation, we would eventually see a saturation of $\langle|\boldsymbol{m}|\rangle$ to a finite value.

Next we discuss the second method to detect $T_<$, namely direct observation of symmetry-breaking. We see in Fig. 4.17(b) that $\langle\cos(6\alpha\rangle$ approaches unity at low temperatures and

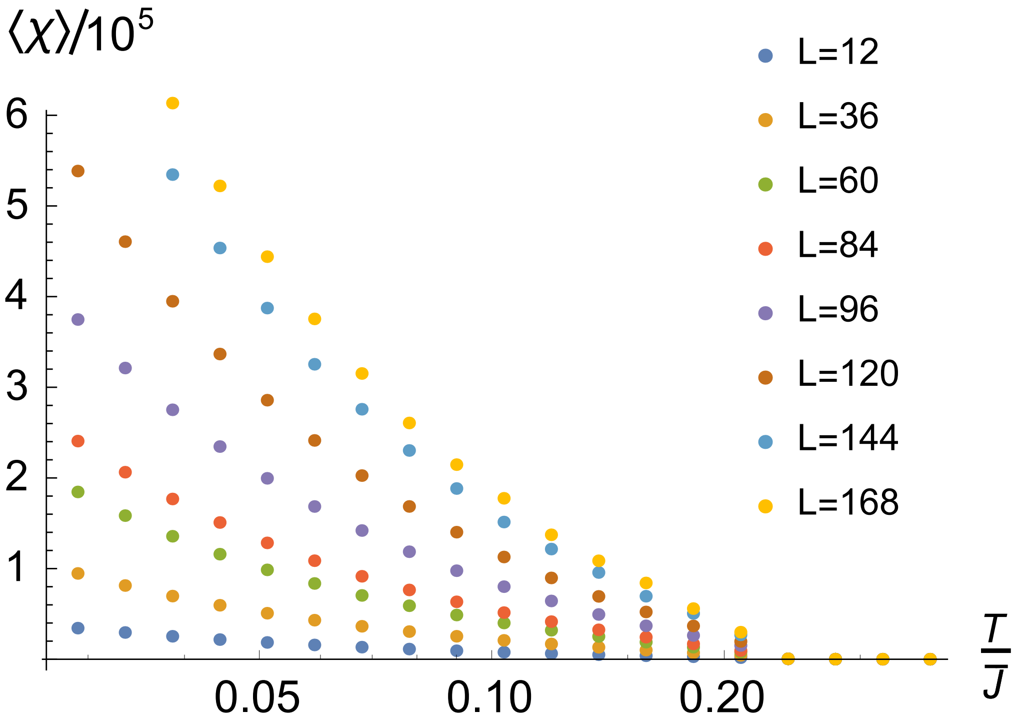

Figure 4.19: Susceptibility of emergent degrees of freedom as function of temperature for $J_{th} = 0.6\bar{J}$

large system sizes. In a finite-size system, we can observe this ordering only for not too small values of $J_{th} \geq 0.8\bar{J}$ because the bare value of the order-from-disorder six-fold potential scales with $(J_{th}/\bar{J})^6$ with an additional small numerical prefactor 10^{-4} [see Eq. (4.20)]. While the lower phase transition occurs when this potential becomes relevant at long length scales, independently of the bare value, the finite system size serves as a cut-off of the scaling making an effect of the potential only visible at sufficiently large bare values. To extract the transition temperature $T_<$ from $\langle\cos(6\alpha)\rangle$ we have to take into account that while at low temperatures the Gaussian order-from-disorder potential predicts free energy minima at $\alpha = 2\pi n/6$ (in agreement with our simulation), at intermediate temperatures we observe in the finite size system a tendency of the spins to prefer a relative direction corresponding to a negative value of $\langle\cos(6\alpha)\rangle$ [see inset in Fig. 4.17(b)]. This is presumably a result of nonlinear spin fluctuations around the classical ground state order, similarly to the effect of quenched disorder [35]. We thus identify the transition temperature $T_<(\mathbb{Z}_6)$ as the location of the minimum of $\langle\cos(6\alpha)\rangle(T)$ which yields temperatures that are within error bars in agreement with the ones predicted from scaling.

We note that in the critical phase that develops for $T \in [T_<, T_>]$, the phase α behaves as a perfect, decoupled XY order parameter. Once the vortices bind at the BKT transition $T_>$, the ensemble of thermodynamically accessible states divides up into distinct degenerate subspaces, each defined by a pair of winding numbers $\{n_x, n_y\}$ with

$$n_l = \int_0^L \frac{dx_l}{2\pi} \nabla_l \alpha(x), \qquad (l = x, y), \tag{4.25}$$

where L is the linear size of the system, indicating the presence of an emergent topological

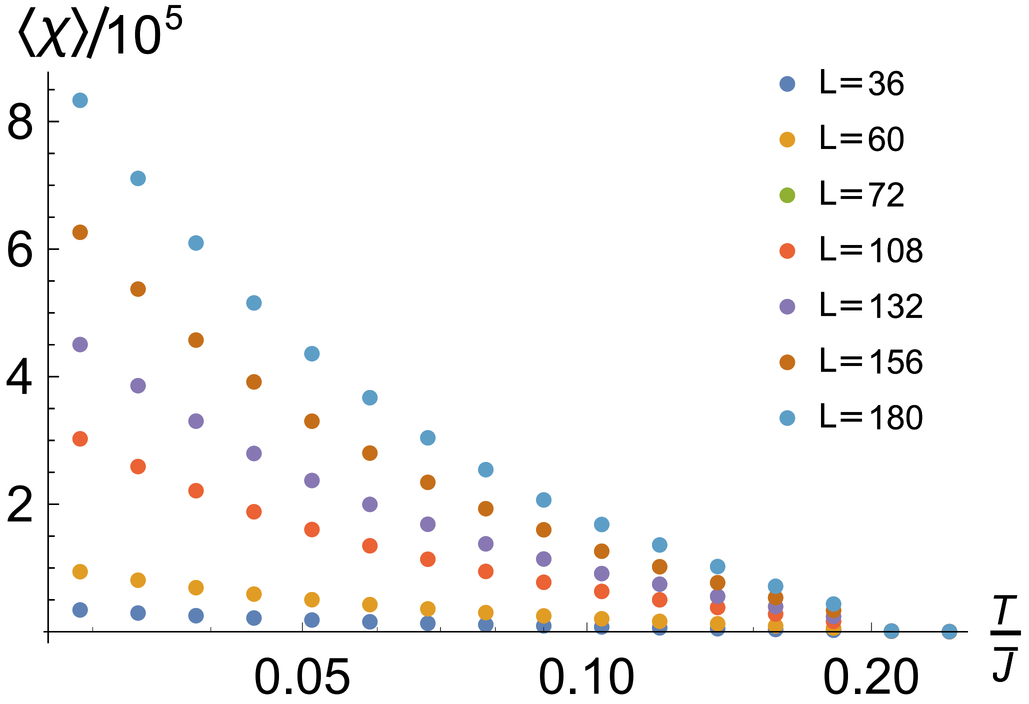

Figure 4.20: Susceptibility of emergent degrees of freedom as function of temperature for $J_{th} = 0.8\bar{J}$

phase [44]. The multiple degeneracies of this state confirm the Polyakov hypothesis that a power-law phase is possible with a degenerate vacuum.

In conclusion, employing extensive parallel-tempering Monte-Carlo simulations, we have presented conclusive evidence for an emergent critical phase in a 2D isotropic classical Heisenberg spin model at finite temperatures. This realizes the Polyakov conjecture [75] that Heisenberg magnets can develop algebraic order if they exhibit a vacuum degeneracy. Using finite size scaling we have shown that the transitions are in the Berezinskii-Kosterlitz-Thouless universality class and determined the transition temperatures. At low temperatures, we find direct evidence of long-range order in the relative orientation of the spins via breaking of a discrete six-fold symmetry induced by an order-from-disorder potential.

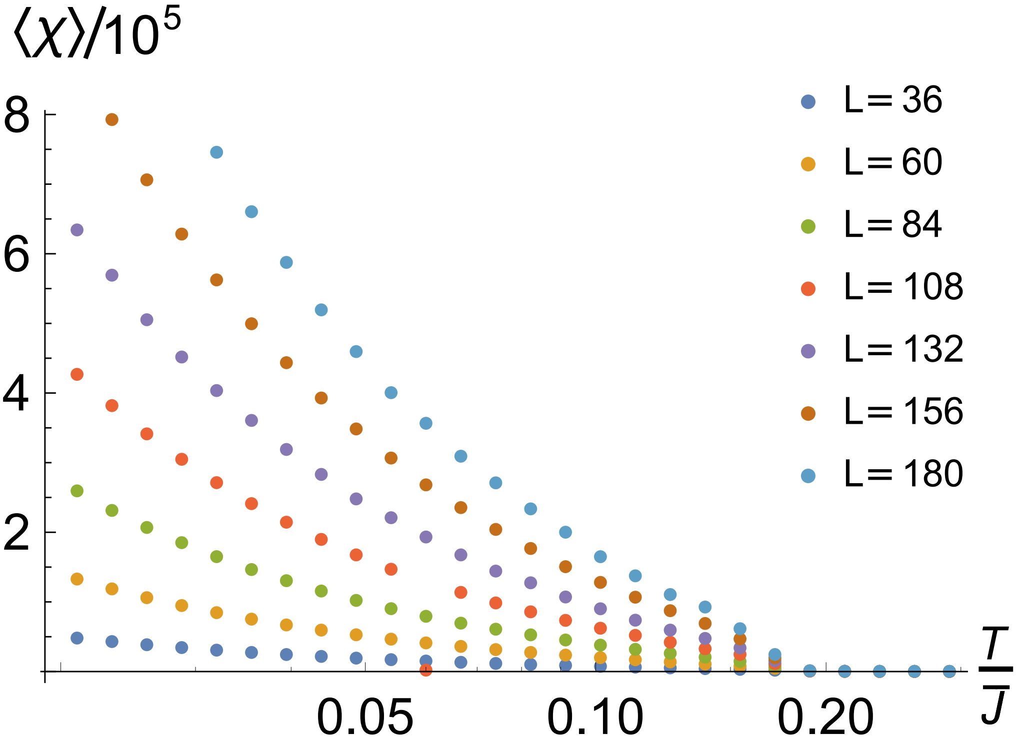

Figure 4.21: Susceptibility of emergent degrees of freedom as function of temperature for $J_{th} = 0.92\bar{J}$

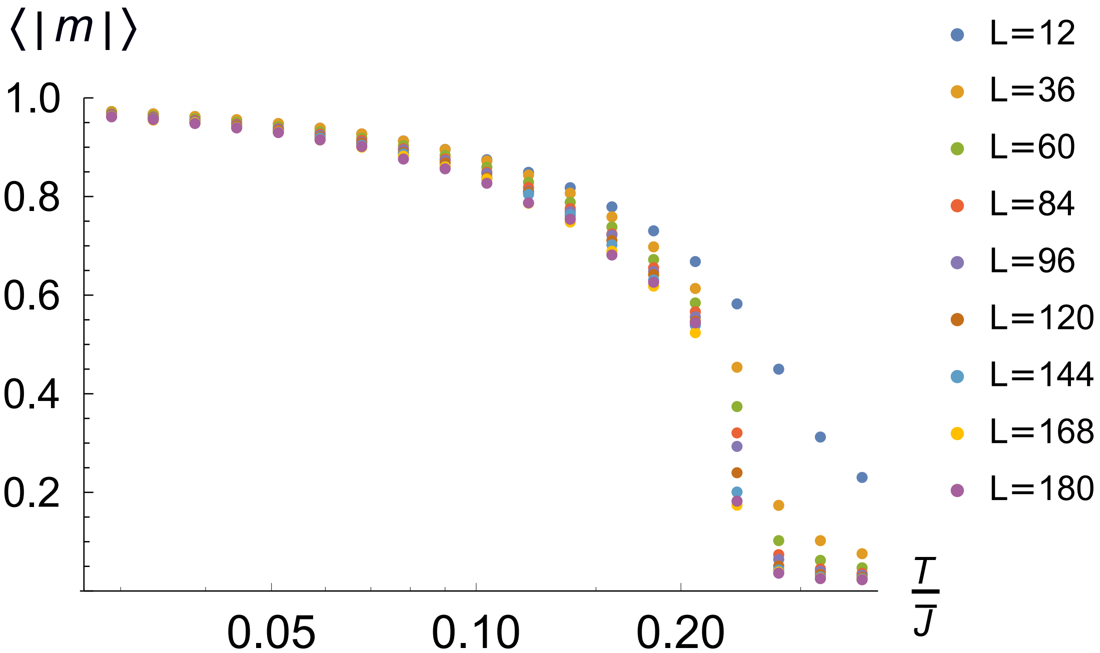

Figure 4.22: Magnetization of emergent degrees of freedom as function of temperature for $J_{th} = 0.4\bar{J}$

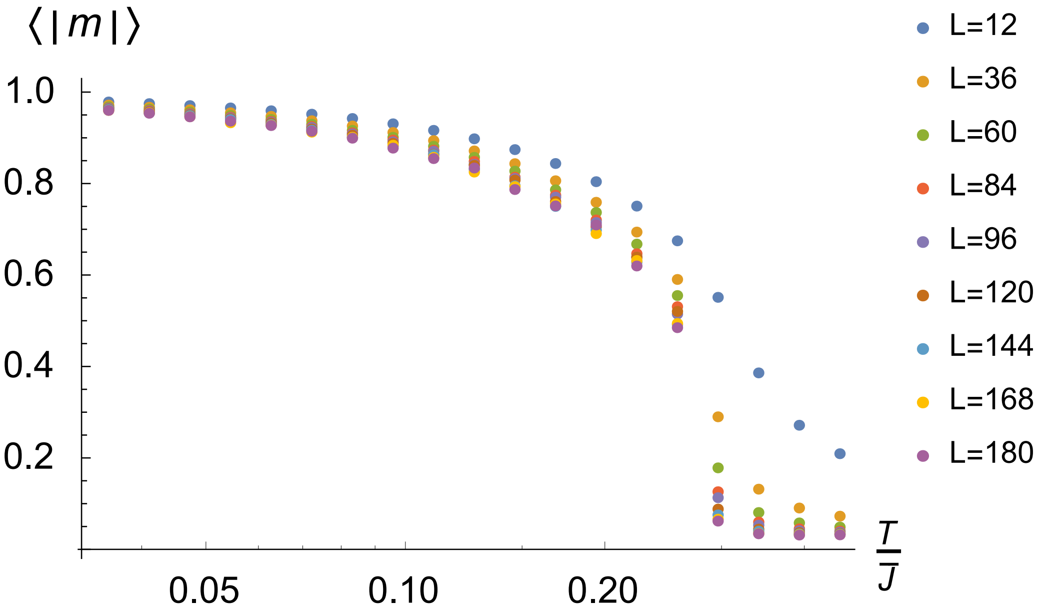

Figure 4.23: Magnetization of emergent degrees of freedom as function of temperature for $J_{th} = 0.6\bar{J}$

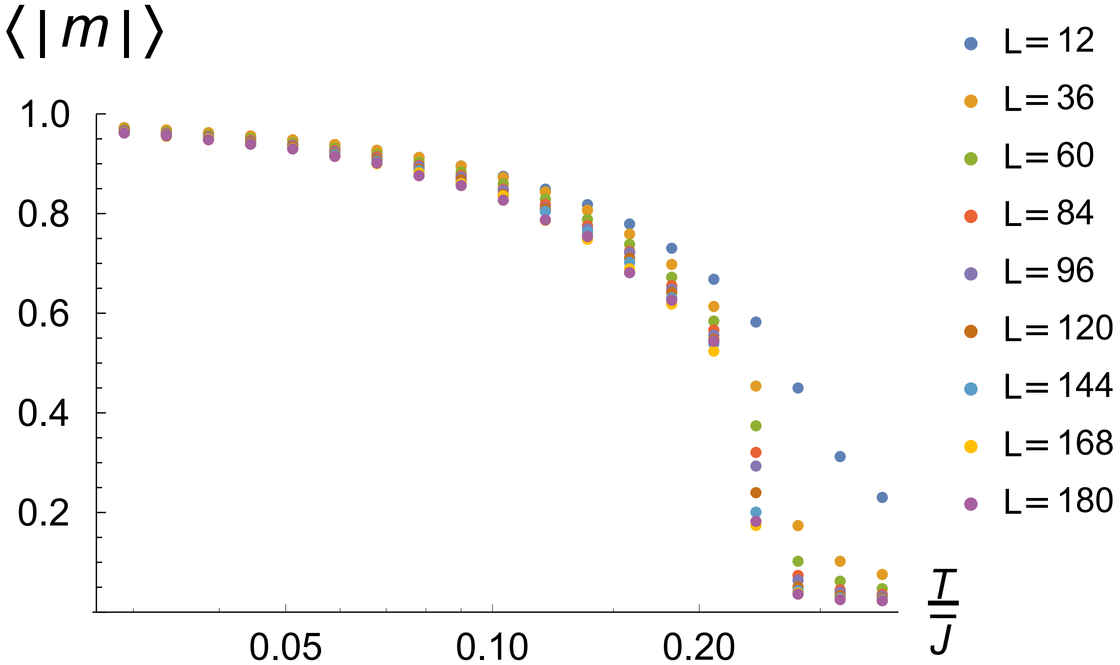

Figure 4.24: Magnetization of emergent degrees of freedom as function of temperature for $J_{th} = 0.8\bar{J}$

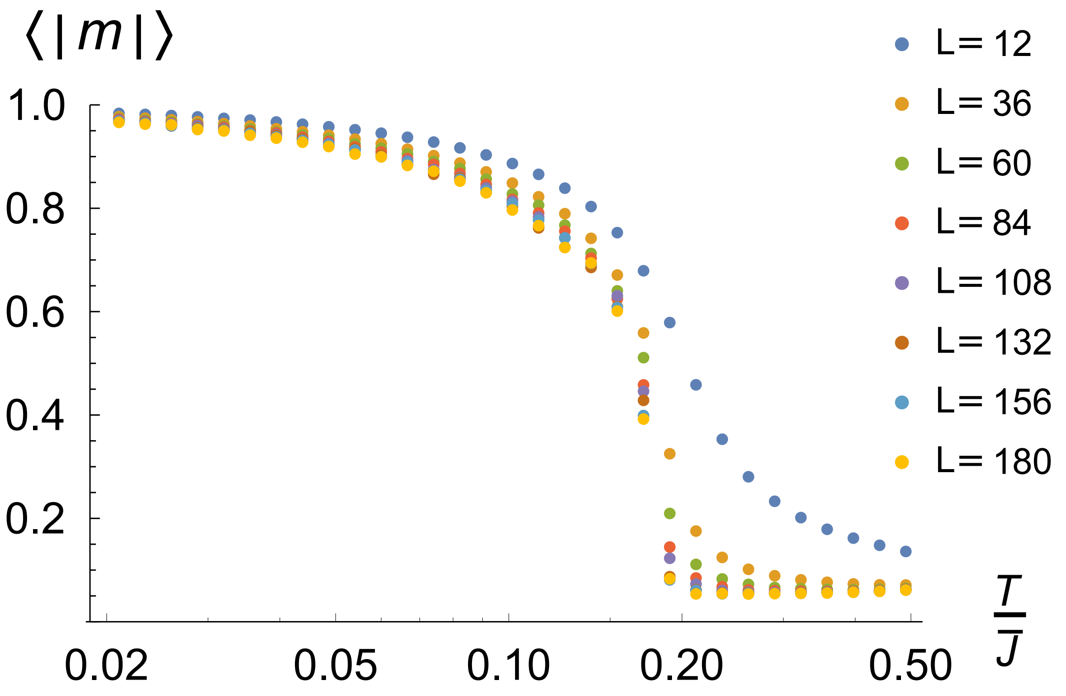

Figure 4.25: Magnetization of emergent degrees of freedom as function of temperature for $J_{th} = 0.92\bar{J}$

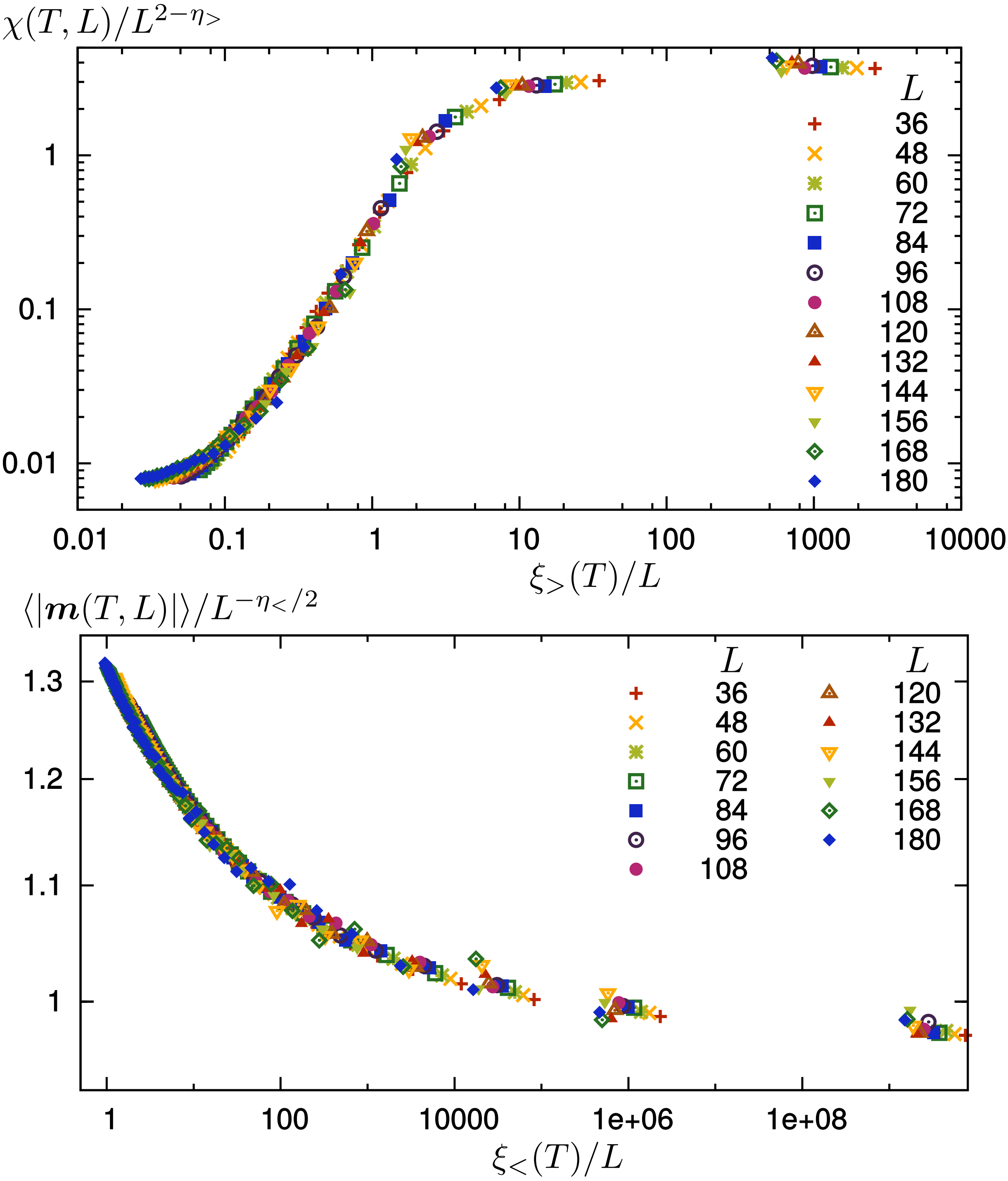

Figure 4.26: Finite size scaling of susceptibility $\chi(T,L) = L^{2-\eta_>} Y_\chi(\xi_>/L)$ as a function of $\xi_>/L$ and magnetization $\langle|\boldsymbol{m}|(T,L)\rangle = L^{-\eta_</2} Y_m(\xi_</L)$ as a function of $\xi_</L$ for $J_{th} = 0.6\bar{J}$, $J_{tt} = 1.0$ and $\bar{J} = 1.22$. Best data collapse is obtained with a BKT scaling ansatz and yields $T_{<,>}$, $a_{<,>}$ and $\eta_{<,>}$ as given in the text.

Chapter 5

Conclusion

The central topic of this thesis is frustration and the role it plays in generating surprising emergent phenomena in spin systems.

Thus in chapter 2 we have studied the conceivably most fundamental kind of frustration, namely the frustration felt by a spin system in the presence of finite spatial curvature. We did this by treating a central pillar of field theoretic studies in the subject of phase transitions, namely the N component ϕ^4 theory, in the geometric setting of hyperbolic space. The analytical treatment of this theory was made possible by the momentum space techniques that we developed in chapter 2 .

The N-component ϕ^4 theory in flat space is an unfrustrated spin system. Its ordered state is a uniaxial ferromagnet. However, in hyperbolic space it is frustrated solely due to the properties of space. We found that in the symmetry broken phase, in which spins want to align in the same direction in spin-space, this ferromagnetic ordering becomes impossible due to the fact that the available space around any given point grows exponentially with distance from the spin. As a consequence all correlation functions show exponential decay even at the critical point. The critical point was identified by the scale-free form of the correlation function once it is represented in the eigenbasis of the hyperbolic Laplacian. Yet, the exponential decay in real-space has the effect that all the familiar infrared divergences of ϕ^4 theory in flat space are regulated by the existence of the additional length scale of hyperbolic space, namely the radius of curvature. We showed that, as a consequence of this, arbitrarily small spatial curvature leads to the emergence of a new fixed point which is characterized by new critical exponents that differ from the flat-space and even mean-field exponents.

In chapters 3 and 4 we studied a different type of frustration in a spin model. This kind of frustration, which goes by the name *geometric frustration*, arises whenever the spins in a system are not able to satisfy all bonds to neighboring spin such as to minimize the interaction energy between these. The quintessential example of this behavior is provided by the triangular lattice, on which spins that couple antiferromagnetically to neighboring spins, order, at zero temperature, in a 120° arrangement. Combining this model with another antiferromagnetic model, namely the honeycomb lattice with nearest neighbor couplings, into the so-called windmill lattice, we obtain highly non-trivial physics. In the limit of very strong intra-sublattice coupling and very small inter-sublattice coupling, these two systems, although coupled by a small antiferromagnetic interaction, have zero temperature ground states that are energetically fully decoupled. They become coupled in an order-by-disorder mechanism at arbitrarily small temperatures and a $U(1)$ relative degree of freedom of the two sublattices emerges.

The prerequisite for the emergent $U(1)$ physics is the decoupled phase of the sublattices. Therefore the question must be answered of whether this decoupled regime exists in a broad region of the phase diagram, or if it destroyed by the existence of phases that have far smaller energies and are therefore preferred. Chapter 3 dealt with this problem by employing an algorithm that extensively searches for ground states as a function of the coupling constants. It was found that the Heisenberg and XY model on this lattice each have eight different ground states. Moreover, the decoupled regime does in fact exist in a rather large portion of the zero temperature phase diagram.

Having dealt with this prerequisite, it was now possible to explore the emergent phenomena in the decoupled phase. This was done in chapter 4, where this was achieved by studying the model in extensively parallelized Monte Carlo simulations that were tailored to the characteristics of the windmill model. Subjecting the magnetization and susceptibility of the emergent spin degrees of freedom to a finite size scaling analysis, we found that the relative degrees of freedom turn out to behave effectively as an XY model in a six-fold potential. In this way we confirmed a speculation that is historically due to A. M. Polyakov, who conjectured that short-range Heisenberg spin systems, although forbidden from developing long-range order may host emergent spins that are capable of developing long-range order.

The central result of chapter 4 is the detailed finite temperature phase diagram of the Heisenberg windmill lattice, which shows the region of the emergent critical phase. The main conclusion is the fact that this isotropic short-range Heisenberg system on a two-dimensional lattice is capable of developing emergent degrees of freedom that are capable of showing, in a large region of the phase diagram, power law correlations. In particular we found the existence of the phase transitions, their critical exponents and universality classes.

Acknowledgements

I am grateful to Prof. Jörg Schmalian for making me a member of his group and for teaching me many things about critical phenomena. The hyperbolic space problem was a refreshing change of direction and refueled my energy. His many words of encouragement and general optimism made the work seem easy and very enjoyable.

I thank Peter Orth for collaborating with me on the windmill spin model for two years. By working on these projects I learned a great deal about phase transitions. Next to the large number of physics-related discussions that we had, I particularly enjoyed the many runs that we undertook in 2013.

Thanks are also due to Prof. Alexander Shnirman for co-refereeing this thesis.

The years at the institute were made particularly enjoyable by the fun atmosphere that its members created. Thanks to Ulf for all the time we spent discussing and joking about everything under the sun. The probability puzzles that we tried to solve together provided just as much joy and generated even further opportunities for jokes.

I enjoyed Pablo's and Philip's company in our shared office and the many discussions we had at and away from the institute. I hope they found me just as tolerable as a room-mate.

Then there are the various adventures of Team Coffee and Team Mate. I thank its many permanent members, among which are Tim, Mareike, Fabienne, Matthias H., Markus, Julia, Matthias B., Egor, Una, Pia and Paddl.

Thanks to Mathias for many discussions about physics and fun math problems. Thanks also to the many other members of the TKM, past and present, who enlivened the mood at the institute.

I am grateful to Pablo, Tim and Ulf for proofreading parts of this thesis and providing very useful remarks.

Over the course of the years Andreas' assistance in matters of computers was invaluable.

I similarly profited from Christian's vast knowledge of programming languages.

Finally I thank my family for all their support.

Appendix A

Normalization of radial functions

In this appendix to chapter 2 we compute the normalization of the $\Pi_{\sigma l}(r)$. Since the differential equation for $\Pi_{\sigma l}$ is of Sturm-Liouville type, we already know that the orthogonality property holds. The normalization constant is defined by

$$N_{\sigma,l}\delta(\sigma-\rho) \quad = \quad \int_0^\infty dr \sinh^2 r \ \Pi_{\sigma l}(r)\Pi_{\rho l}(r).$$

We will compute $N_{\sigma,l}$ by establishing a relation between $N_{\sigma l}$ and $N_{\sigma l+1}$. Starting with the explicit representation (2.22) and defining $u_{\sigma l}(r) \equiv \sinh(r)\Pi_{\sigma l}(r)$ we have

$$u_{\sigma,l+1} = \frac{1}{\sqrt{\sigma^2+(l+1)^2}}\left(u'_{\sigma l} - (l+1)\coth r \ u_{\sigma l}\right).$$

The $u_{\sigma l}$ satisfy

$$\frac{d^2}{dr^2}u_{\sigma l} = \left(-\sigma^2 + \frac{l(l+1)}{\sinh^2 r}\right)u_{\sigma l}.$$

Then

$$\begin{aligned}
N_{\sigma,l+1}\delta(\sigma-\rho) \quad &= \quad \int_0^\infty dr \ u_{\sigma l+1}(r)u_{\rho l+1}(r) \\
&= \quad \frac{1}{\sqrt{\sigma^2+(l+1)^2}}\frac{1}{\sqrt{\rho^2+(l+1)^2}} \\
&\qquad \int_0^\infty dr \ \left(u'_{\sigma l}u'_{\rho l} + (l+1)^2\coth^2 r \ u_{\sigma l}u_{\rho l} - (l+1)\coth r \ (u_{\rho l}u_{\sigma l})'\right)
\end{aligned}$$

and partially integrating the first and third term we have

$$\begin{aligned}
N_{\sigma,l+1}\delta(\sigma-\rho) \quad &= \quad \frac{1}{\sqrt{\sigma^2+(l+1)^2}}\frac{1}{\sqrt{\rho^2+(l+1)^2}} \\
&\qquad \times\int_0^\infty dr \ \left(-u_{\sigma l}u''_{\rho l} + (l+1)^2\coth^2 r \ u_{\sigma l}u_{\rho l} - (l+1)\frac{1}{\sinh^2 r}u_{\rho l}u_{\sigma l}\right) \\
&= \quad \frac{1}{\sqrt{\sigma^2+(l+1)^2}}\frac{1}{\sqrt{\rho^2+(l+1)^2}}
\end{aligned}$$

$$
\begin{aligned}
&\times \int_0^\infty dr\ [-u_{\sigma l}(-\rho^2 + \frac{l(l+1)}{\sinh^2 r})u_{\rho l} + (l+1)^2 \coth^2 r\ u_{\sigma l}u_{\rho l} \\
&\qquad - \frac{(l+1)}{\sinh^2 r} u_{\rho l} u_{\sigma l}] \\
= &\ \frac{1}{\sqrt{\sigma^2 + (l+1)^2}} \frac{1}{\sqrt{\rho^2 + (l+1)^2}} \int_0^\infty dr\ (\rho^2 + (l+1)^2) u_{\sigma l} u_{\rho l} \\
= &\ N_{\sigma,l}\delta(\sigma - \rho)
\end{aligned}
$$

thus all $N_{\sigma,l}$ are identical and it suffices to compute a particular one, say, $N_{\sigma,0}$. The latter is easily obtained, since $u_{\sigma 0} = \sinh(r)\Pi_{\sigma 0}(r) = -\sin(\sigma r)$ and therefore

$$\int_0^\infty dr\ u_{\sigma 0}(r) u_{\rho 0}(r) = \frac{\pi}{2}\delta(\sigma - \rho).$$

Thus we find

$$N_{\sigma l} = \frac{\pi}{2}$$

to be the proper normalization factor.

Appendix B

Analytic calculation of the $T = 0$ ground state energies

In this appendix to chapter 3 we compute analytically the energy for every $T = 0$ ground state in this model. For all the phases that we have found, the spin-configurations are such that the interaction energy of a spin with its neighbors is translationally invariant, *i.e.*, the nearest neighbor sums

$$\sum_j \boldsymbol{S}_i^t \cdot \boldsymbol{S}_j^t, \sum_j \boldsymbol{S}_i^A \cdot \boldsymbol{S}_j^B, \sum_j \boldsymbol{S}_i^t \cdot \boldsymbol{S}_j^{A/B} \tag{B.1}$$

are all independent of i. As a consequence, the computation of the total energy is rather straightforward. One merely needs to consider the energy of a spin and its neighbors and multiply the result by $N/2$ (for spins on the triangular lattice) or N (for spins on the honeycomb lattice). In some of the phases, however, there are configuration parameters that change continuously with the coupling constants. We introduce these as variational parameters that have to be chosen appropriately in order to minimize the total energy.

B.1 Collinear antiferromagnetic phase/canted ferromagnetic phase $(2a)$ and $(2b)$

To calculate the energy of these phases, consider the left configuration in Fig. 3.4. Out of the neighboring 6 honeycomb spins of a triangular spin there are always two spins that have the same orientation (positive scalar product) as the triangular spin. One is an A-site spin, the other a B-site spin. All remaining honeycomb spins are either equal or opposite to one of the two. We introduce as the variational parameters θ_1 and θ_2, the angles that the A- and B-site honeycomb spins make with the triangular lattice spin. For the energy we find

$$\begin{aligned} E_2 &= E_t + E_h + E_{th} && \text{(B.2)} \\ &= -NJ_t - 2NJ_h + NJ_h \cos(\theta_1 + \theta_2) && \text{(B.3)} \\ &\quad -NJ_{th} \left(\cos\theta_1 + \cos\theta_2\right) && \text{(B.4)} \end{aligned}$$

which is minimized by

$$\theta \equiv \theta_1 = \theta_2 = \cos^{-1}\Big(\frac{J_{th}}{2J_h}\Big) \tag{B.5}$$

with energy

$$E_{2a} = -NJ_t - 3NJ_h - N\frac{J_{th}^2}{2J_h}. \tag{B.6}$$

In order for Eq. (B.5) to be meaningful, it is required that $J_{th} \leq 2J_h$. In the opposite regime $J_{th} \geq 2J_h$, we instead have the minimum at $\theta_1 = \theta_2 = 0$. The energy for this locked phase is

$$E_{2b} = -NJ_t - NJ_h - 2NJ_{th}. \tag{B.7}$$

B.2 Ferromagnetic phases $(3a)$ and $(3b)$

To compute the energy of this phase, we note from Fig. 3.5 that the A and B sublattices are each ferromagnetically ordered. Let θ_1 and θ_2 denote the angles between A and triangular sublattice magnetizations and between B and the triangular lattice magnetization, respectively. The total energy in this phase is

$$\begin{aligned} E = {} & 3NJ_t + 3NJ_h \cos(\theta_1 + \theta_2) \\ & + 3NJ_{th} \left(\cos\theta_1 + \cos\theta_2\right) . \end{aligned} \tag{B.8}$$

Minimization yields the angles

$$\cos\theta \equiv \cos\theta_1 \quad = \quad \cos\theta_2 = -\frac{j_{th}}{2j_h} \tag{B.9}$$

and energy

$$E_{3a} \quad = \quad 3NJ_t - 3NJ_h - N\frac{3J_{th}^2}{2J_h}. \tag{B.10}$$

The coupling constants have to satisfy

$$\frac{J_{th}}{2J_h} \leq 1 \tag{B.11}$$

in order for θ to be real.

When this condition is violated, the minimum of the energy function is instead found at

$$\theta = \theta_1 = \theta_2 = \pi \tag{B.12}$$

with

$$E_{3b} = 3NJ_t + 3NJ_h - 6NJ_{th}. \tag{B.13}$$

This is phase $(3b)$ in the phase diagram.

B.3 Double Cone Configuration $(4a)$ and $(4b)$

We parametrize the energy of this phase in terms of the cone opening angles α_h and α_t as well as the advance angle θ. Let the z axis be parallel to the cone axis. Then we can write the total energy as

$$\begin{aligned} E_4 = &-NJ_t - NJ_h + 2NJ_t \sin^2\alpha_t\big(\cos^2\theta + \cos\theta\big) \\ &+ 2NJ_h \sin^2\alpha_h\big(\cos\theta + 1\big) - 2NJ_{th}\Big(\cos\big(\alpha_h - \alpha_t\big) \\ &+ 2\sin\alpha_t \sin\alpha_h \cos\theta\Big)\,. \end{aligned} \tag{B.14}$$

Minimizing with respect to $\{\alpha_t, \alpha_h, \theta\}$ yields the three equations

$$2\sin\alpha_t\cos\alpha_t(\cos^2\theta + \cos\theta) - j_{th}\left[\sin(\alpha_h - \alpha_t) + 2\cos\alpha_t \sin\alpha_h \cos\theta\right] = 0 \tag{B.15}$$
$$2j_h\sin\alpha_h\cos\alpha_h(\cos\theta + 1) - j_{th}\left[\sin(\alpha_t - \alpha_h) + 2\sin\alpha_t\cos\alpha_h\cos\theta\right] = 0 \tag{B.16}$$
$$(1 + 2\cos\theta)\sin^2\alpha_t + j_h\sin^2\alpha_h - 2j_{th}\sin\alpha_t\sin\alpha_h = 0. \tag{B.17}$$

This system of equations can be tremendously simplified by noting that all dependences on α_t and α_h can be expressed in terms of the combinations

$$\rho = \frac{\sin\alpha_h}{\sin\alpha_t} \tag{B.18}$$
$$\sigma = \frac{\cos\alpha_h}{\cos\alpha_t}\,. \tag{B.19}$$

With this the minimization conditions are transformed into

$$2(\cos^2\theta + \cos\theta) + j_{th}(\sigma - \rho - 2\rho\cos\theta) = 0 \tag{B.20}$$
$$2j_h(\cos\theta + 1)\sigma\rho + j_{th}(\rho - \sigma - 2\sigma\cos\theta) = 0 \tag{B.21}$$
$$2\cos\theta + 1 + j_h\rho^2 - 2j_{th}\rho = 0\,. \tag{B.22}$$

In order to find the solutions of this set of equations, we solve Eq. (B.22) for $\cos\theta$ and substitute this solution into the other two equations (B.20) and (B.21)

$$-1 - 2j_h j_{th}\rho^3 + j_h^2\rho^4 + 2j_{th}\sigma = 0 \tag{B.23}$$
$$\rho\left(j_{th} - 2jth^2\sigma + 3j_h j_{th}\rho\sigma + j_h(1 - j_h\rho^2)\sigma\right) = 0 \tag{B.24}$$

One obvious solution comes from the second equation with $\rho = 0$. We will treat this case later. We assume $\rho \neq 0$, then the two resulting equations contain σ linearly and eliminating it results in a 6th order equation for ρ that happens to be solvable and has the roots

$$\rho_1 = \frac{j_{th} - \sqrt{j_{th}^2 - 4j_h}}{2j_h} \tag{B.25}$$
$$\rho_2 = \frac{j_{th} + \sqrt{j_{th}^2 - 4j_h}}{2j_h} \tag{B.26}$$
$$\rho_3 = \frac{j_{th} - \sqrt{j_h + j_{th}^2}}{j_h} \tag{B.27}$$

$$\rho_4 = \frac{j_{th} + \sqrt{j_h + j_{th}^2}}{j_h}. \tag{B.28}$$

The last two solutions ρ_3 and ρ_4 are both doubly degenerate. From these solutions the resulting values for σ and θ are found to be

$$\sigma_1 = \frac{j_{th}(j_{th} - \sqrt{j_{th}^2 - 4j_h})^2}{8j_h^2} \tag{B.29}$$

$$\sigma_2 = \frac{j_{th}(j_{th} + \sqrt{j_{th}^2 - 4j_h})^2}{8j_h^2} \tag{B.30}$$

$$\sigma_3 = \frac{-j_{th} + \sqrt{j_h + j_{th}^2}}{j_h} \tag{B.31}$$

$$\sigma_4 = -\frac{j_{th} + \sqrt{j_h + j_{th}^2}}{j_h} \tag{B.32}$$

and

$$\cos\theta_1 = j_{th}\frac{j_{th} - \sqrt{j_{th}^2 - 4j_h}}{4j_h} \tag{B.33}$$

$$\cos\theta_2 = j_{th}\frac{j_{th} + \sqrt{j_{th}^2 - 4j_h}}{4j_h} \tag{B.34}$$

$$\cos\theta_3 = -1 \tag{B.35}$$

$$\cos\theta_4 = -1. \tag{B.36}$$

Note that $\cos\theta_2 \geq 1$, thus the solution θ_2 is not admissible. The solution θ_3 may also be discarded, because it has a negative value of ρ, whereas $\rho \geq 0$ from the definition and $0 \leq \alpha_h, \alpha_t \leq \pi$.

The solution θ_4 has $\rho_4 = -\sigma_4$. Inserting into this relation the definitions in terms of α_t and α_h we have

$$\sin\alpha_h = \rho_4 \sin\alpha_t \tag{B.37}$$

$$\cos\alpha_h = -\rho_4 \cos\alpha_t \tag{B.38}$$

and by taking squares and adding, $\rho_4 = 1$ is deduced and as a consequence $\alpha_t = \pi - \alpha_h$. Such a phase, however, has energy $E = -NJ_t - NJ_h + 2NJ_{th}$. This energy is always larger than that of phase (1). We can therefore discard this solution as well.

To summarize, the only solution that needs to be considered is $(\rho_1, \sigma_1, \theta_1)$ and we therefore drop the subscript in the following. We can express the angles in terms of ρ and σ as

$$\sin\alpha_t = \sqrt{\frac{1-\sigma^2}{\rho^2 - \sigma^2}} \tag{B.39}$$

$$\sin\alpha_h = \sqrt{\frac{1-\sigma^2}{\rho^2 - \sigma^2}}\rho. \tag{B.40}$$

By inserting these parameters back into the expression for the energy, we find the energy in explicit form as a function of the coupling constants:

$$\begin{aligned}\frac{E_{4a}}{NJ_t} &= -1+\frac{j_{th}^2}{2j_h}-\frac{5}{3}j_{th}^2-\frac{j_{th}^4}{4j_h^2}+\frac{j_{th}^3\sqrt{j_{th}^2-4j_h}}{4j_h^2}+\frac{12j_h^2+j_{th}^2\left(5j_h-12\right)}{12j_h+9j_{th}^2} \\ &\quad +\frac{8j_h(2j_h-1)+2j_{th}^2(4j_h+1)-5j_{th}^4}{\sqrt{j_{th}^2-4j_h}\left(4j_h+3j_{th}^2\right)}j_{th}+\frac{2j_{th}}{\sqrt{j_{th}^2-4j_h}}-\frac{4\sqrt{2}j_{th}^2\sqrt{\epsilon^{(1)}\epsilon^{(2)}}}{j_{th}-\sqrt{j_{th}^2-4j_h}}\end{aligned} \tag{B.41}$$

where

$$\begin{aligned}\epsilon^{(1)} &\equiv \frac{j_{th}^2-j_{th}\sqrt{j_{th}^2-4j_h}-2j_h(j_h+1)}{-j_{th}^4+j_{th}^3\sqrt{j_{th}^2-4j_h}+2j_{th}^2j_h+8j_h^2} \\ \epsilon^{(2)} &\equiv \frac{3j_{th}^4-3j_{th}^3\sqrt{j_{th}^2-4j_h}+8j_h^2(1+j_h)+4j_{th}j_h(j_h+2)\sqrt{j_{th}^2-4j_h}-2j_{th}^2j_h(j_h+7)}{-3j_{th}^4+8j_{th}^2j_h+16j_h^2}.\end{aligned}$$

The necessary condition for the existence of this phase is that the coupling constants are such that all three quantities $\alpha_t, \alpha_h, \theta$ are real. As a first condition we have

$$j_{th}^2 \geq 4j_h \tag{B.42}$$

in order to make the square root expression in ρ, σ and θ real.

The requirement that α_t be real translates into

$$0 \leq \frac{1-\sigma^2}{\rho^2-\sigma^2} \leq 1. \tag{B.43}$$

From the form of ρ and σ in terms of the coupling constants it is straightforward to show that $\sigma \leq \rho$. With this the inequality (B.43) results in the final requirement

$$\sigma \leq 1 \leq \rho. \tag{B.44}$$

There are no further conditions, since α_h is guaranteed to be real if α_t is.

We return to the case $\rho = 0$, which is also one of the solutions of Eqs. (B.20)-(B.22) with

$$\rho = 0 \rightarrow \alpha_h = 0 \tag{B.45}$$

$$\sigma = \frac{1}{2j_{th}} \rightarrow \cos\alpha_t = 2j_{th} \tag{B.46}$$

$$\theta = \frac{2\pi}{3}. \tag{B.47}$$

The energy in terms of the coupling constants has a simpler form

$$E_{4b} = -\frac{3}{2}NJ_t - NJ_h - 2N\frac{J_{th}^2}{J_t} \tag{B.48}$$

This is the other double cone phase that we have denoted (4b) in the phase diagram. The necessary condition for this phase to exist, which follows from the requirement that α_t must be real, is

$$j_{th} \leq \frac{1}{2}. \tag{B.49}$$

B.4 Incommensurate spiral phase (5)

We calculate the energy with the spiral angle θ as a variational parameter. The variational expression for the energy is

$$\begin{aligned} E(\theta) = & -NJ_t + NJ_h - 2NJ_{th} + 2NJ_t \cos^2\theta \\ & + (2NJ_t + 2NJ_h - 4NJ_{th}) \cos\theta. \end{aligned} \tag{B.50}$$

We minimize with respect to θ and obtain

$$\begin{aligned} \cos\theta &= -\frac{1}{2}\left(1 + \frac{J_h}{J_t} - 2\frac{J_{th}}{J_t}\right) \\ E_5 &= -\frac{3}{2}NJ_t - \frac{N}{2J_t}(J_h - 2J_{th})^2 \end{aligned}$$

as minimizing angle and energy. Since θ must be real, it follows that

$$|1 + j_h - 2j_{th}| \leq 2$$

must hold for the existence of the spiral phase.

B.5 Incommensurate alternating spiral phase (XY I)

The total variational energy is given by

$$\begin{aligned} E(\theta) = & -NJ_t + 2NJ_{th} + NJ_h + 2NJ_t(\cos^2\theta - \cos\theta) \\ & - 4NJ_{th}\cos\theta - 2J_h\cos\theta\,. \end{aligned} \tag{B.51}$$

The energy is minimized for

$$\cos\theta = \frac{1}{2} + \frac{J_{th}}{J_t} + \frac{J_h}{2J_t} \tag{B.52}$$

which yields the energy of phase XY I:

$$E_{\text{XY I}} = -\frac{3}{2}NJ_t - N\frac{(J_h + 2J_{th})^2}{2J_t}. \tag{B.53}$$

B.6 Canted ferromagnetic phase (XY II)

This phase is related to phase (4a) and the minimization problem may be solved in close analogy with it. The energy is given in terms of the parameters α_t and α_h:

$$\begin{aligned} E = & NJ_t + NJ_h + 2NJ_t\cos 2\alpha_t + 2NJ_h\cos 2\alpha_h \\ & - 2NJ_{th}\left[\cos(\alpha_t + \alpha_h) + 2\cos(\alpha_t - \alpha_h)\right]\,. \end{aligned} \tag{B.54}$$

The minimization conditions are given by

$$2j_h\rho\sigma = j_{th}(\sigma + \rho) \tag{B.55}$$

$$3\sigma - \rho = \frac{4}{j_{th}}. \tag{B.56}$$

These equations are solved by

$$
\begin{aligned}
\sigma_\pm &\equiv \frac{\cos\alpha_h}{\cos\alpha_t} && \text{(B.57)} \\
&= \frac{2}{3j_{th}} + \frac{j_{th}}{3j_h} \pm \sqrt{\left(\frac{2}{3j_{th}} + \frac{j_{th}}{3j_h}\right)^2 - \frac{1}{j_h}} \\
\rho &\equiv \frac{\sin\alpha_h}{\sin\alpha_t} = 3\sigma - \frac{4}{j_{th}}\,. && \text{(B.58)}
\end{aligned}
$$

The positive sign of σ leads to a solution with an energy that is always larger than that of the other planar phases. Hence we will disregard this configuration and only focus on the negative sign solution σ_- (and drop the subscript on σ). As a first condition we require that the expression under the square root in the formula for σ must not be negative. This is easily shown to be satisfied in exactly two disjoint regions of parameter space

$$
\begin{aligned}
j_{th}^2 &\leq j_h && \text{(B.59)} \\
j_h &\leq j_{th}^2/4\,. && \text{(B.60)}
\end{aligned}
$$

Furthermore, we require, as we did for phase $(4a)$, that α_t is real. If α_t is real, so will be α_h. This condition will hold if either one of the two inequalities

$$
\begin{aligned}
&\sigma < 1 < \rho && \text{(B.61)} \\
&\rho < 1 < \sigma\,. && \text{(B.62)}
\end{aligned}
$$

is satisfied. From the form of σ and ρ in terms of the coupling constants we can show that the first case does not exist for any choice of coupling constants. Thus we require only the second inequality (B.62).

Finally, we compute the energy from the values of the angles α_t and α_h, which are known in terms of σ and ρ, and find

$$
\frac{E_{\text{XY II}}}{NJ_t} = \frac{9j_{th}^2}{4}\sqrt{\epsilon^{(1)}} + \epsilon^{(2)} \tag{B.63}
$$

where

$$
\begin{aligned}
\epsilon^{(1)} &\equiv \frac{\frac{2(j_h^2+1)j_{th}^4}{j_h^2} + 8j_h^2 - \frac{9j_h^2+2j_h+9}{j_h}j_{th}^2 + 8 + \left[\frac{2(j_h^2-1)j_{th}^3}{j_h} - 4(j_h^2-1)j_{th}\right]\sqrt{\frac{j_{th}^2-5j_h}{j_h^2} + \frac{4}{j_{th}^2}}}{j_{th}^4 - 5j_hj_{th}^2 + 4j_h^2} \\
\epsilon^{(2)} &\equiv -\frac{(j_h-1)(8j_h-5j_{th}^2)(2j_h+j_{th}^2)}{4j_h\sqrt{j_{th}^4 - 5j_hj_{th}^2 + 4j_h^2}} + \frac{5(j_h+1)j_{th}^2}{4j_h} + j_h + 1.
\end{aligned}
$$

Appendix C

Stiffness measurements

The critical phase of the windmill model is enclosed on both sides by a BKT transition. The characteristic of such a phase transition is a jump in the spin stiffness ρ of the system at $T = T_c$ by the universal value $\rho/T_c = 2/\pi$. Thus measuring this quantity would arguably provide the most direct proof of the existence of a power law phase. While the stiffness of either spin system, i.e. the triangular and honeycomb lattice spin systems, should flow to zero in a plot of stiffness versus the logarithm of system size, the same plot for the stiffness of the emergent degrees of freedom, the 'relative spin stiffness' of the two sublattice systems, should remain constant inside the power law phase.

The three stiffness components of the triangular lattice with Heisenberg spins were calculated in Monte Carlo simulations by [92]. An analogous Monte Carlo treatment of the stiffness components of Heisenberg spins on the honeycomb lattice does not seem to exist in the literature. Below we show the results of our own simulations.

We begin this appendix by first deriving the formulas by which the stiffnesses for the honeycomb and triangular lattice can be measured. Using these formulas we carried out Monte Carlo simulations and obtained the spin stiffnesses as a function of temperature for different system sizes. The spin stiffness of an infinitely large system of Heisenberg spins on a two-dimensional lattice is zero. However, any finite system possesses a finite stiffness and the scaling behavior has been calculated in the literature.

In the case of the triangular lattice we compare our numerical results with those obtained by Southern and Young in [92]. In the case of the honeycomb lattice we compare our numerical results with RG flow equations obtained to 1-loop order and 2-loop order by Orth et al. in [72, 73]. We obtain in both cases excellent agreement with the results of these authors.

The crucial quantity to calculate in a Monte Carlo simulation of the windmill model is the 'relative spin stiffness'. We were, however, not able to determine sampling formulas for this. We wish to point out that the loose expression 'relative stiffness' is somewhat misleading and it would be more appropriate to consider it as a coupling constant between the two sublattices. The reason for this lies in the interpretation of the spin stiffness. Therefore we first explain how the spin stiffness may be defined.

An operational definition of the spin stiffness is the following: consider a finite system and hold the spins on one end of it fixed, then ρ is defined as the response of the free energy, $\frac{d^2F}{d\theta^2}|_{\theta=0}$, of the system to an infinitesimal twist by an angle $d\theta$ at the other end. This twist on one end will distribute itself over the entire length of the system in order to minimize the free energy cost. In the presence of a system with two sublattices, we may define the stiffness of the individual lattices, by carrying out the twisting operation only on one lattice and not twisting the other lattice. However, twisting only the relative degree of freedom of the spins, without also applying a twist to the individual lattices can obviously not be achieved and this is the primary difficulty in introducing the relative spin stiffness.

In the following we will recast the definition in a somewhat different form that makes it possible to detect the couplings. Then we will derive formulas for the stiffnesses of the honeycomb lattice and triangular lattice, respectively.

Consider the Hamiltonian

$$H = J \sum_{\langle ij \rangle} \boldsymbol{S}_i \cdot \boldsymbol{S}_j$$

of Heisenberg spins on a arbitrary lattice. The spin stiffness (cf. definitions in [92]) is defined by introducing a twist unit-vector $\boldsymbol{n}$ and a direction $\boldsymbol{u}$ along the lattice. A spin $\boldsymbol{S}_j$ is twisted with respect to its neighbor $\boldsymbol{S}_i$ by an amount $\frac{\theta}{L}\boldsymbol{e}_{ij} \cdot \boldsymbol{u}$ around the axis described by $\boldsymbol{n}$, where $\boldsymbol{e}_{ij}$ is the vector connecting site i to site j. The Hamiltonian is rotationally invariant term by term. In particular the relative twist of $\boldsymbol{S}_j$ versus $\boldsymbol{S}_i$ can be implemented by just twisting $\boldsymbol{S}_j$ by the difference between the twist angles of spins $\boldsymbol{S}_i$ and $\boldsymbol{S}_j$. This twisting can be expressed by the substitution

$$\boldsymbol{S}_j \to \exp\left(\frac{\theta}{L}\left(\boldsymbol{e}_{ij} \cdot \boldsymbol{u}\right) \boldsymbol{n}\times\right) \boldsymbol{S}_j$$

transforming the Hamiltonian into

$$H = J \sum_{\langle ij \rangle} \boldsymbol{S}_i \cdot \exp\left(\frac{\theta}{L}\left(\boldsymbol{e}_{ij} \cdot \boldsymbol{u}\right) \boldsymbol{n}\times\right) \boldsymbol{S}_j .$$

Introducing this twist into the Hamiltonian, we may now ask how the free energy behaves as a function of θ. Because of global $O(3)$ symmetry it is clear that the free energy should not depend on the sign of θ, i.e. the modification of the free energy $F(\theta)$ due to twist is reflected by the second derivative of F, but not at any lower order in θ. The second derivative measures the cost of twisting the system at the boundary by a small angle θ. This quantity we define to be the spin stiffness:

$$\rho_s(\boldsymbol{u}, \boldsymbol{n}) \equiv \left(\frac{\partial^2 F}{\partial \theta^2}\right)_{\theta=0}$$

We proceed to derive an expression for ρ_s in terms of correlation functions that can be sampled by Monte Carlo methods. The free energy is found from the partition function

$$\begin{aligned} Z &= \int_{\mathrm{cfg}} \exp(-\beta H) \\ F &= -T \log Z \end{aligned}$$

which produces the following expression for ρ_s

$$\begin{aligned} \frac{\partial F}{\partial \theta} &= -T \frac{1}{Z} Z' \\ \frac{\partial^2 F}{\partial \theta^2} &= -T \frac{Z''}{Z} + T \left(\frac{Z'}{Z}\right)^2 = -T \frac{Z''}{Z} + \beta \left(\frac{\partial F}{\partial \theta}\right)^2 . \end{aligned}$$

As pointed out above, the first derivative of F has to vanish. This can be seen formally as follows:

$$\begin{aligned}
\left(\frac{\partial Z}{\partial\theta}\right)_{\theta=0} &= -\beta\int_{\mathrm{cfg}}\exp(-\beta H)\left(\frac{\partial H}{\partial\theta}\right)_{\theta=0} \\
&= -\frac{\beta}{L}\int_{\mathrm{cfg}}\exp(-\beta H)\sum_{\langle ij\rangle}(\boldsymbol{e}_{ij}\cdot\boldsymbol{u})\boldsymbol{S}_i\cdot(\boldsymbol{n}\times\boldsymbol{S}_j) \\
&= \frac{\beta}{L}\boldsymbol{n}\cdot\int_{\mathrm{cfg}}\exp(-\beta H)\sum_{\langle ij\rangle}(\boldsymbol{e}_{ij}\cdot\boldsymbol{u})\,(\boldsymbol{S}_i\times\boldsymbol{S}_j)\,.
\end{aligned}$$

The configurational integral performed over $\boldsymbol{S}_i\times\boldsymbol{S}_j$ is zero by virtue of the fact that by integrating first with constant angle between $\boldsymbol{S}_i$ and $\boldsymbol{S}_j$, the term $\boldsymbol{S}_i\cdot\boldsymbol{S}_j$ in H does not change but $\boldsymbol{S}_i\times\boldsymbol{S}_j$ points in all possible directions and therefore integrates to 0.
Using this fact the stiffness is found to be

$$\rho_s(\boldsymbol{u},\boldsymbol{n}) = \frac{\partial^2 F}{\partial\theta^2} = \left\langle\left(\frac{\partial^2 H}{\partial\theta^2}\right)_{\theta=0}\right\rangle - \beta\left\langle\left(\frac{\partial H}{\partial\theta}\right)^2_{\theta=0}\right\rangle.$$

For the averages we have

$$\begin{aligned}
\left\langle\left(\frac{\partial H}{\partial\theta}\right)^2_{\theta=0}\right\rangle &= \frac{J^2}{N}\left\langle\left(\sum_{\langle ij\rangle}(\boldsymbol{e}_{ij}\cdot\boldsymbol{u})\boldsymbol{n}\cdot(\boldsymbol{S}_i\times\boldsymbol{S}_j)\right)^2\right\rangle \\
\left\langle\left(\frac{\partial^2 H}{\partial\theta^2}\right)_{\theta=0}\right\rangle &= \frac{J}{N}\left\langle\sum_{\langle ij\rangle}(\boldsymbol{e}_{ij}\cdot\boldsymbol{u})^2\boldsymbol{S}_i\cdot\boldsymbol{n}\times(\boldsymbol{u}\times\boldsymbol{S}_j)\right\rangle \\
&= \frac{J}{N}\left\langle\sum_{\langle ij\rangle}(\boldsymbol{e}_{ij}\cdot\boldsymbol{u})^2\left[(\boldsymbol{S}_i\cdot\boldsymbol{n})(\boldsymbol{S}_j\cdot\boldsymbol{n})-\boldsymbol{S}_i\cdot\boldsymbol{S}_j\right]\right\rangle
\end{aligned}$$

By choosing an orthogonal system of unit vectors $\hat{\boldsymbol{k}}_i$ we can compute the stiffnesses in three different directions:

$$\begin{aligned}
\rho_s(\boldsymbol{u},\hat{\boldsymbol{k}}_\alpha) &= \left\langle\left(\frac{\partial^2 H}{\partial\theta^2}\right)_{\theta=0}\right\rangle - \beta\left\langle\left(\frac{\partial H}{\partial\theta}\right)^2_{\theta=0}\right\rangle \qquad \text{(C.1)} \\
&= -\frac{J}{N}\left\langle\sum_{\langle ij\rangle}(\boldsymbol{e}_{ij}\cdot\boldsymbol{u})^2\left[S_i^\beta\cdot S_j^\beta+S_i^\gamma\cdot S_j^\gamma\right]\right\rangle \\
&\quad -\beta\frac{J^2}{N}\left\langle\left(\sum_{\langle ij\rangle}(\boldsymbol{e}_{ij}\cdot\boldsymbol{u})\left(S_i^\beta\cdot S_j^\gamma-S_i^\gamma\cdot S_j^\beta\right)\right)^2\right\rangle \qquad \text{(C.2)}
\end{aligned}$$

where the indices α,β,γ have to be understood in a cyclic sense.

We now specialize to the triangular lattice. Picking the x-direction for $\boldsymbol{u}$ and the z-direction for $\boldsymbol{n}$, we have for ρ_x:

$$\rho_x = -\frac{J}{N}\left\langle\sum_{\langle ij\rangle_h}\left[S_i^x\cdot S_j^x+S_i^y\cdot S_j^y\right]\right\rangle - \frac{J}{4N}\left\langle\sum_{\langle ij\rangle_{d_1}}\left[S_i^x\cdot S_j^x+S_i^y\cdot S_j^y\right]\right\rangle$$

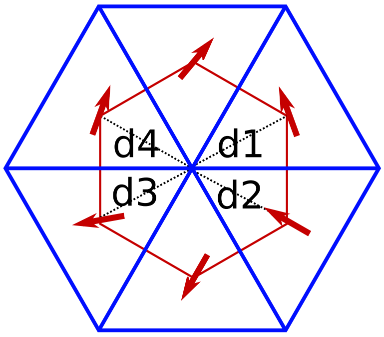

Figure C.1: Labeling of bonds

$$
\begin{aligned}
& -\frac{J}{4N}\left\langle \sum_{\langle ij\rangle_{d_2}} \left[S_i^x \cdot S_j^x + S_i^y \cdot S_j^y\right] \right\rangle \\
& -\beta\frac{J^2}{N}\left\langle \mathcal{J}^2 \right\rangle \\
\mathcal{J} \equiv & \sum_{\langle ij\rangle_h} \left(S_i^x \cdot S_j^y - S_i^y \cdot S_j^x\right) + \frac{1}{2}\sum_{\langle ij\rangle_{d_1}} \left(S_i^x \cdot S_j^y - S_i^y \cdot S_j^x\right) \\
& -\frac{1}{2}\sum_{\langle ij\rangle_{d_2}} \left(S_i^x \cdot S_j^y - S_i^y \cdot S_j^x\right)
\end{aligned}
$$

Here $\langle ij\rangle_h$ means horizontal neighbors, $\langle ij\rangle_{d_1}$ denotes diagonal neighbors from lower left to upper right and $\langle ij\rangle_{d_2}$ are the diagonal neighbors from lower right to upper left. As we can see, they contribute differently to the stiffness components.

For the honeycomb lattice the direction vectors are different for odd and even sites ($\langle ij\rangle_{\text{odd}}$ and $\langle ij\rangle_{\text{even}}$ refer to i being odd and even, respectively). To avoid double counting the sum has to be either over the even or the odd sites, not both:

$$
\begin{aligned}
\rho_s(\boldsymbol{u}, \hat{\boldsymbol{k}}_\alpha) &= -\frac{J}{N}\left\langle \sum_{\langle ij\rangle} (\boldsymbol{e}_{ij} \cdot \boldsymbol{u})^2 \left[S_i^\beta \cdot S_j^\beta + S_i^\gamma \cdot S_j^\gamma\right] \right\rangle \\
&\quad -\beta\frac{J^2}{N}\left\langle \left(\sum_{\langle ij\rangle} (\boldsymbol{e}_{ij} \cdot \boldsymbol{u}) \left(S_i^\beta \cdot S_j^\gamma - S_i^\gamma \cdot S_j^\beta\right) \right)^2 \right\rangle \\
&= -\frac{J}{N}\left\langle \sum_{\langle ij\rangle_{\text{odd}}} (\boldsymbol{e}_{ij} \cdot \boldsymbol{u})^2 \left[S_i^\beta \cdot S_j^\beta + S_i^\gamma \cdot S_j^\gamma\right] \right\rangle \\
&\quad -\beta\frac{J^2}{N}\left\langle \left(\sum_{\langle ij\rangle_{\text{odd}}} (\boldsymbol{e}_{ij} \cdot \boldsymbol{u}) \left(S_i^\beta \cdot S_j^\gamma - S_i^\gamma \cdot S_j^\beta\right) \right)^2 \right\rangle \\
&= -\frac{J}{4N}\left\langle \sum_{\langle ij\rangle_{d_1}} \left[S_i^x \cdot S_j^x + S_i^y \cdot S_j^y\right] + \sum_{\langle ij\rangle_{d_2}} \left[S_i^x \cdot S_j^x + S_i^y \cdot S_j^y\right] \right\rangle
\end{aligned}
$$

$$-\beta\frac{J^2}{4N}\left\langle\left(\sum_{\langle ij\rangle_{d_1}}\left(S_i^x\cdot S_j^y-S_i^y\cdot S_j^x\right)-\sum_{\langle ij\rangle_{d_2}}\left(S_i^x\cdot S_j^y-S_i^y\cdot S_j^x\right)\right)^2\right\rangle$$

Here the sum has been extended over the odd sites. In the last line the directions of $\boldsymbol{u}$ and $\hat{\boldsymbol{k}}_\alpha$ were chosen along the x-axis, as before.
The stiffness in the y-direction is determined by:

$$\begin{aligned}
\rho_s(\hat{\boldsymbol{y}},\hat{\boldsymbol{z}}) &= -\frac{J}{N}\left\langle\sum_{\langle ij\rangle_{\text{odd}}}(\boldsymbol{e}_{ij}\cdot\hat{\boldsymbol{y}})^2\left[S_i^x\cdot S_j^x+S_i^y\cdot S_j^y\right]\right\rangle \\
&\quad -\beta\frac{J^2}{N}\left\langle\left(\sum_{\langle ij\rangle_{\text{odd}}}(\boldsymbol{e}_{ij}\cdot\hat{\boldsymbol{y}})\left(S_i^x\cdot S_j^y-S_i^y\cdot S_j^x\right)\right)^2\right\rangle \\
&= -\frac{J}{N}\left\langle\sum_{i\text{ odd}}\boldsymbol{S}_i\cdot\left((\boldsymbol{e}_{iu(i)}\cdot\hat{\boldsymbol{y}})^2\boldsymbol{S}_{u(i)}+(\boldsymbol{e}_{il(i)}\cdot\hat{\boldsymbol{y}})^2\boldsymbol{S}_{l(i)}+(\boldsymbol{e}_{ir(i)}\cdot\hat{\boldsymbol{y}})^2\boldsymbol{S}_{r(i)}\right)\right\rangle \\
&\quad -\beta\frac{J^2}{N}\left\langle\left(\sum_{i\text{ odd}}\boldsymbol{S}_i\times\left((\boldsymbol{e}_{iu(i)}\cdot\hat{\boldsymbol{y}})\boldsymbol{S}_{u(i)}+(\boldsymbol{e}_{il(i)}\cdot\hat{\boldsymbol{y}})\boldsymbol{S}_{l(i)}+(\boldsymbol{e}_{ir(i)}\cdot\hat{\boldsymbol{y}})\boldsymbol{S}_{r(i)}\right)\right)^2\right\rangle \\
&= -\frac{J}{N}\left\langle\sum_{i\text{ odd}}\boldsymbol{S}_i\cdot\left(\frac{1}{3}\boldsymbol{S}_{u(i)}+\frac{1}{12}\boldsymbol{S}_{l(i)}+\frac{1}{12}\boldsymbol{S}_{r(i)}\right)\right\rangle \\
&\quad -\beta\frac{J^2}{N}\left\langle\left(\sum_{i\text{ odd}}\boldsymbol{S}_i\times\left(\frac{1}{\sqrt{3}}\boldsymbol{S}_{u(i)}-\frac{1}{2\sqrt{3}}\boldsymbol{S}_{l(i)}-\frac{1}{2\sqrt{3}}\boldsymbol{S}_{r(i)}\right)\right)^2\right\rangle
\end{aligned}$$

where the letters u, l, r refer to the upper, left and right neighbors, respectively.
The stiffness of the triangular lattice was measured by Monte Carlo simulation on lattices with $L = 12, 24, 48, 96, 120, 180$ at the temperature $T = 0.2J_t$. The stiffness formula above was used in the Monte Carlo simulation to find the behavior of ρ as a function of $\log L$. We thereby repeat work that was done by Southern and Young in [92]. The figure shows an overlay of our Monte Carlo data with theirs (the Monte Carlo data are the dots) and shows excellent agreement. The solid curve was obtained by these authors after numerically solving the RG flow equations obtained by Azaria et al. [2] and using the stiffnesses of the $L = 12$ system as the initial value of the flow.

The flow equations are given by

$$\begin{aligned}
\frac{d\rho_1}{d\log L} &= -t\left(1-\frac{1}{2}\lambda\right)-\frac{t^2}{\rho_1}\left(\frac{5}{8}\lambda^2-\frac{3}{2}\lambda+1\right) \\
\frac{d\rho_3}{d\log L} &= -t\frac{\lambda^2}{2}-\frac{t^2}{\rho_1}\frac{1}{8}\lambda^3
\end{aligned}$$

where $t = T/2\pi$ and $\lambda = \rho_3/\rho_1$ and the equality $\rho_2 = \rho_1$ provides the remaining stiffness component.
Next we take up the honeycomb lattice and calculate the stiffnesses in a Monte Carlo simulation of the honeycomb lattice. We compare the resulting data with the RG flow equation obtained in [72, 73]. The flow equation, which is obtained using 2-loop RG, is given by

$$\frac{d\rho}{d\log L} = -\frac{1}{2\pi}-\frac{1}{2\pi^2}\frac{1}{\rho^2},$$

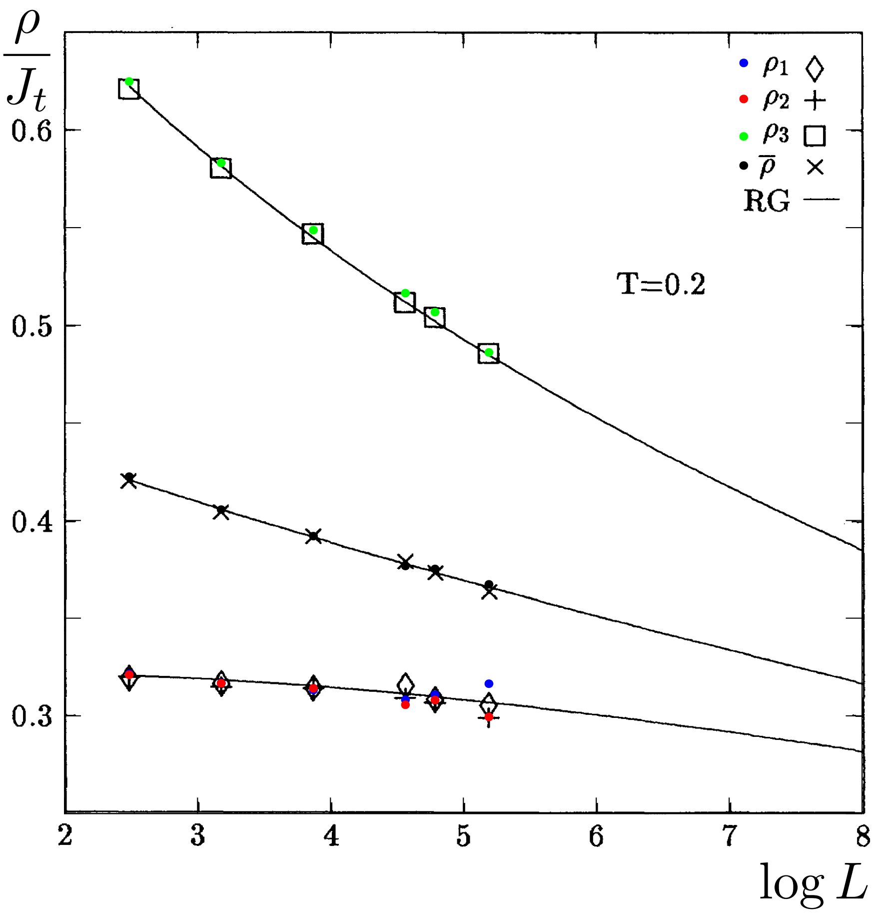

Figure C.2: Stiffness of Triangular Lattice at $T = 0.2J_t$ generated by our Monte Carlo code (dots). The overlaid plot is from [92]. Reprinted with permission from [92] (http://dx.doi.org/10.1103/PhysRevB.48.13170), Copyright (1993) by the American Physical Society.

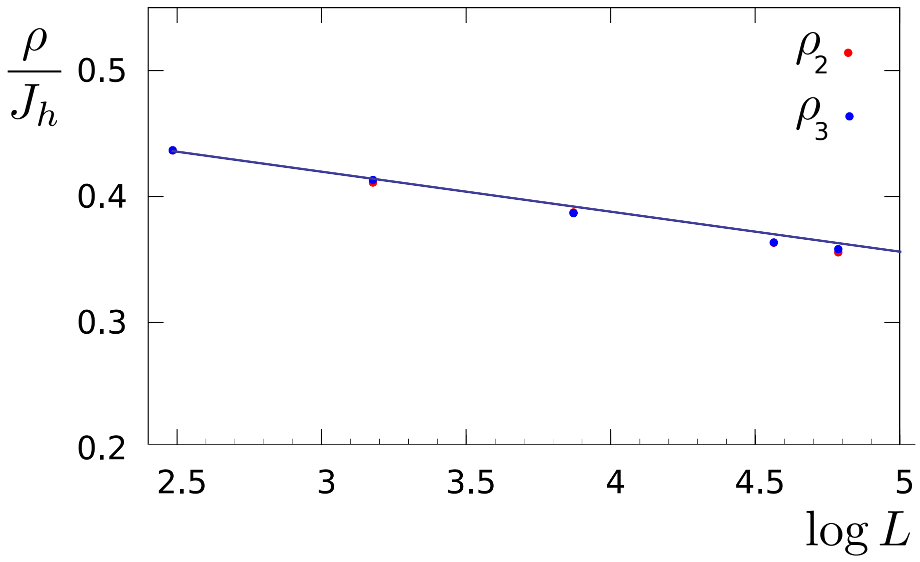

Figure C.3: Stiffness for the Honeycomb lattice. Comparison with 1-loop RG flow equations

where the first term alone is the 1-loop result.

In the Figures C.3 and C.4 we compare the data with both, the 1-loop and 2-loop result, respectively. As one can see the Monte Carlo value of the stiffness is systematically lower than the 1-loop RG results. However, the match becomes much better when compared with the 2-loop RG result.

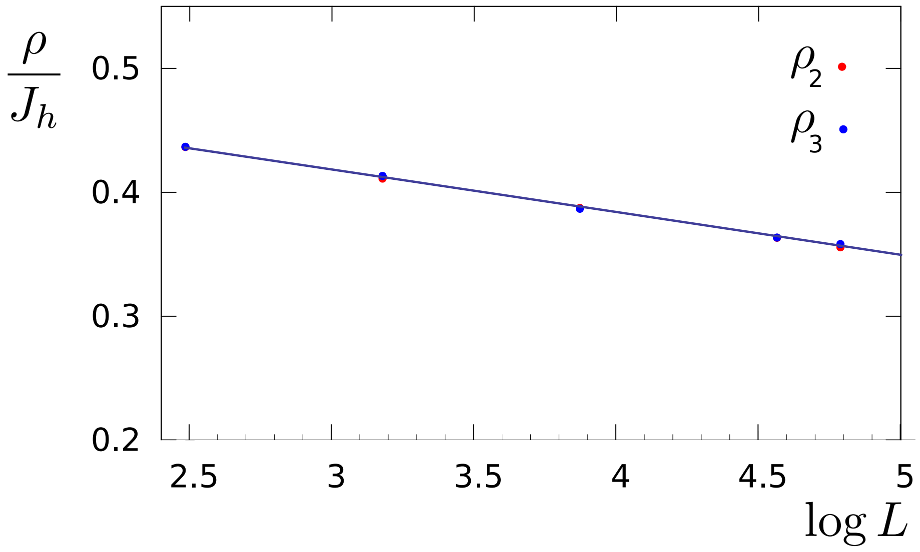

Figure C.4: Stiffness for the Honeycomb lattice. Comparison 2-loop RG flow equations

Appendix D

Luttinger-Tisza Matrix of the windmill lattice

In 1946 J. M. Luttinger and L. Tisza published a work [52], where the problem of minimizing the total energy of interacting dipole moments on a cubic lattice was considered. The form for the interaction between the dipole moments was assumed to be a quadratic form in the components of the dipole moment vectors. In their method developed for this problem, the condition that all dipole vectors must be normalized to unity is softened into the *weak constraint* that only the sum $\sum_i \boldsymbol{S}_i^2$ has to equal N, the number of spins on the lattice. This weak constraint allows the minimization problem to be solved easily. The authors then verify that the solution of this minimization problem also satisfies the *strong constraint* that $\boldsymbol{S}_i^2 = 1$ for all i of the lattice.
Their procedure has found ample application in the determination of ground states of many other spin models. However, in cases where the lattice is not so simple the 'solution' obtained from the minimization problem does not satisfy the strong constraint. In this case the ground states show much more diversity and need to be obtained in other ways, for instance algorithmically, as we did in chapter 3.
In this appendix we derive the Luttinger-Tisza matrix for the windmill lattice and point out the difficulty that impedes a straightforward solution along the lines followed by Luttinger and Tisza for cubic lattices.
We start this analysis by dividing the windmill-lattice into the sublattices triangular, honeycomb A and honeycomb B. Then all lattices become identical triangular lattices that are shifted with respect to each other by the same displacement vector. In terms of spins on these three sublattices we can write the Hamiltonian as

$$H = J_t \sum_{\langle ij \rangle} \boldsymbol{S}_i \cdot \boldsymbol{S}_j + J_{th} \sum_{\langle ij \rangle} \boldsymbol{S}_i \cdot \boldsymbol{S}_j^A + J_{th} \sum_{\langle ij \rangle} \boldsymbol{S}_i \cdot \boldsymbol{S}_j^B + J_h \sum_{\langle ij \rangle} \boldsymbol{S}_i^A \cdot \boldsymbol{S}_j^B$$

where $\boldsymbol{S}$ are the spins on the triangular lattice and $\boldsymbol{S}^{A/B}$ are the spins on the honeycomb A/B-sites. Thus we have three identical copies of lattices interacting with each other and with themselves. The windmill lattice can be considered as a special case where the coupling constants for interaction within the A and B lattices are zero and the interactions of these lattices with the third lattice happens with equal strength. A triangular lattices can be described by the basis vectors

$$\boldsymbol{a}_1 = \begin{pmatrix} 1 \\ 0 \end{pmatrix} a$$

$$\boldsymbol{a}_2 = \begin{pmatrix} 1/2 \\ \sqrt{3}/2 \end{pmatrix} a.$$

We define the reciprocal basis vectors

$$\begin{aligned} \boldsymbol{b}_1 &= \frac{2\pi}{a} \begin{pmatrix} 1 \\ -1/\sqrt{3} \end{pmatrix} \\ \boldsymbol{b}_2 &= \frac{2\pi}{a} \begin{pmatrix} 0 \\ 2/\sqrt{3} \end{pmatrix}. \end{aligned}$$

Then the Fourier transform of the spins is

$$\boldsymbol{S}(\boldsymbol{q}) = \sum_{\boldsymbol{r}} \boldsymbol{S}(\boldsymbol{r}) \exp\left(i\boldsymbol{q} \cdot \boldsymbol{r}\right).$$

Since the lattice has the period as described by the bravais vectors, it is sufficient to let the components q_i in the $\boldsymbol{b}$-basis run from $-1/2$ to $1/2$. Thus in order to obtain $\boldsymbol{S}(\boldsymbol{r})$ from the last equation, we integrate the q_i precisely in this range:

$$\boldsymbol{S}(\boldsymbol{r}') = \int\limits_{-1/2}^{1/2} dq_1 \int\limits_{-1/2}^{1/2} dq_2 \boldsymbol{S}(\boldsymbol{q}) \exp\left(-i\boldsymbol{q} \cdot \boldsymbol{r}'\right) = \int d^2q \boldsymbol{S}(\boldsymbol{q}) \exp\left(-i\boldsymbol{q} \cdot \boldsymbol{r}'\right)$$

and similarly for the other spins.
We begin with the term describing the interactions between two triangular spins. Inserting the Fourier transform yields

$$\begin{aligned} H_{tt} &= J_t \sum_{\langle ij \rangle} \boldsymbol{S}_i \cdot \boldsymbol{S}_j = \frac{J_t}{2} \sum_{\boldsymbol{r},n} \boldsymbol{S}(\boldsymbol{r}) \cdot \boldsymbol{S}(\boldsymbol{r} + \delta\boldsymbol{r}_n) \\ &= \frac{J_t}{2} \int d^2q \int d^2q' \boldsymbol{S}(\boldsymbol{q}) \boldsymbol{S}(\boldsymbol{q}') \sum_{\boldsymbol{r}} \exp\left(-i\frac{2\pi}{a}\left(\boldsymbol{q} + \boldsymbol{q}'\right) \cdot \boldsymbol{r}\right) \sum_n \exp\left(-i\frac{2\pi}{a} \boldsymbol{q}' \cdot \delta\boldsymbol{r}_n\right). \end{aligned}$$

The sum over $\boldsymbol{r}$ represents a Dirac-comb with period 1 in the q_i variables. Since the integration range is $(-1/2, 1/2)$, however, only the tooth at 0 is important and yields a delta function:

$$H_{tt} = \frac{J_t}{2} \int d^2q \int d^2q' \boldsymbol{S}(\boldsymbol{q}) \boldsymbol{S}(-\boldsymbol{q}) \sum_n \exp\left(i\frac{2\pi}{a} \boldsymbol{q} \cdot \delta\boldsymbol{r}_n\right).$$

Furthermore, the sum over the vectors to the neighboring spins $\delta\boldsymbol{r}_n$ is easily evaluated:

$$\begin{aligned} \sum_n \exp\left(i\frac{2\pi}{a} \boldsymbol{q} \cdot \delta\boldsymbol{r}_n\right) &= \exp\left(i\frac{2\pi}{a} \boldsymbol{q} \cdot \boldsymbol{a}_1\right) + \exp\left(-i\frac{2\pi}{a} \boldsymbol{q} \cdot \boldsymbol{a}_1\right) + \exp\left(i\frac{2\pi}{a} \boldsymbol{q} \cdot \boldsymbol{a}_2\right) \\ &\quad + \exp\left(-i\frac{2\pi}{a} \boldsymbol{q} \cdot \boldsymbol{a}_2\right) + \exp\left(i\frac{2\pi}{a} \boldsymbol{q} \cdot (\boldsymbol{a}_1 - \boldsymbol{a}_2)\right) \\ &\quad + \exp\left(i\frac{2\pi}{a} \boldsymbol{q} \cdot (\boldsymbol{a}_2 - \boldsymbol{a}_1)\right) \\ &= 2\cos 2\pi q_1 + 2\cos 2\pi q_2 + 2\cos 2\pi\left(q_1 - q_2\right). \end{aligned}$$

Finally

$$H_{tt} = J_t \int d^2q \boldsymbol{S}(-\boldsymbol{q}) \left[\cos 2\pi q_1 + \cos 2\pi q_2 + \cos 2\pi\left(q_1 - q_2\right)\right] \boldsymbol{S}(\boldsymbol{q}).$$

With the other lattices we proceed in a similar fashion. Let $\boldsymbol{S}^A(\boldsymbol{r})$ and $\boldsymbol{S}^B(\boldsymbol{r})$ stand for the A- and B-site honeycomb-lattice spins that are located in the unit cell spanned by $\boldsymbol{a}_1$ and $\boldsymbol{a}_2$ at $\boldsymbol{r}$.
First we compute the interaction between the triangular and honeycomb lattice A:

$$\begin{aligned}
H_{th_A} &= J_{th}\sum_{\boldsymbol{r},n}\boldsymbol{S}(\boldsymbol{r})\cdot\boldsymbol{S}^A(\boldsymbol{r}+\delta\boldsymbol{r}_n)\\
&= J_{th}\int d^2q\int d^2q'\boldsymbol{S}(\boldsymbol{q})\cdot\boldsymbol{S}^A(\boldsymbol{q}')\exp\left(-i\frac{2\pi}{a}\left(\boldsymbol{q}+\boldsymbol{q}'\right)\boldsymbol{r}\right)\sum_n\exp\left(-i\frac{2\pi}{a}\boldsymbol{q}'\delta\boldsymbol{r}_n\right)\\
&= J_{th}\int d^2q\boldsymbol{S}(\boldsymbol{q})\cdot\boldsymbol{S}^A(-\boldsymbol{q})\sum_n\exp\left(i\frac{2\pi}{a}\boldsymbol{q}\delta\boldsymbol{r}_n\right).
\end{aligned}$$

The sum is performed over the three A-site neighbors of $\boldsymbol{S}(\boldsymbol{r})$:

$$\begin{aligned}
\delta\boldsymbol{r}_i &= \{-\boldsymbol{a}_1-\boldsymbol{a}_2,-\boldsymbol{a}_1,-\boldsymbol{a}_2\}\\
\sum_n\exp\left(i\frac{2\pi}{a}\boldsymbol{q}\delta\boldsymbol{r}_n\right) &= \exp\left(-i2\pi(q_1+q_2)\right)+\exp\left(-i2\pi q_1\right)+\exp\left(-i2\pi q_2\right)
\end{aligned}$$

$$H_{th_A}=J_{th}\int d^2q\boldsymbol{S}(\boldsymbol{q})\cdot\left(\exp\left(-i2\pi(q_1+q_2)\right)+\exp\left(-i2\pi q_1\right)+\exp\left(-i2\pi q_2\right)\right)\boldsymbol{S}^A(-\boldsymbol{q}).$$

For H_{th_B} we have

$$\begin{aligned}
H_{th_B} &= J_{th}\sum_{\boldsymbol{r},n}\boldsymbol{S}(\boldsymbol{r})\cdot\boldsymbol{S}^B(\boldsymbol{r}+\delta\boldsymbol{r}_n)\\
&= J_{th}\int d^2q\boldsymbol{S}(\boldsymbol{q})\cdot\boldsymbol{S}^B(-\boldsymbol{q})\sum_n\exp\left(i\frac{2\pi}{a}\boldsymbol{q}\delta\boldsymbol{r}_n\right)
\end{aligned}$$

$$\begin{aligned}
\delta\boldsymbol{r}_i &= \{\boldsymbol{0},-\boldsymbol{a}_1,-\boldsymbol{a}_2\}\\
\sum_n\exp\left(i\frac{2\pi}{a}\boldsymbol{q}\delta\boldsymbol{r}_n\right) &= 1+\exp\left(-i2\pi q_1\right)+\exp\left(-i2\pi q_2\right)
\end{aligned}$$

and finally

$$H_{th_B}=J_{th}\int d^2q\boldsymbol{S}(\boldsymbol{q})\cdot\boldsymbol{S}^B(-\boldsymbol{q})\left(1+\exp\left(-i2\pi q_1\right)+\exp\left(-i2\pi q_2\right)\right).$$

The last case to consider is the interaction between lattices A and B:

$$\begin{aligned}
H_{h_Ah_B} &= J_h\sum_{\boldsymbol{r},n}\boldsymbol{S}^A(\boldsymbol{r})\cdot\boldsymbol{S}^B(\boldsymbol{r}+\delta\boldsymbol{r}_n)\\
&= J_h\int d^2q\boldsymbol{S}^A(\boldsymbol{q})\cdot\boldsymbol{S}^B(-\boldsymbol{q})\sum_n\exp\left(i\frac{2\pi}{a}\boldsymbol{q}\delta\boldsymbol{r}_n\right)
\end{aligned}$$

Using the conventions explained above for the positions vectors, we have

$$\delta\boldsymbol{r} = \{0,\boldsymbol{a}_1,\boldsymbol{a}_2\}$$

and therefore

$$\sum_n \exp\left(i\frac{2\pi}{a}\boldsymbol{q}\delta\boldsymbol{r}_n\right) \quad = \quad 1+\exp 2\pi i q_1+\exp 2\pi i q_2$$

and obtain the final result:

$$H_{h_A h_B} \quad = \quad J_h \int d^2q \boldsymbol{S}^A(\boldsymbol{q})\cdot\boldsymbol{S}^B(-\boldsymbol{q})\,(1+\exp 2\pi i q_1+\exp 2\pi i q_2)$$

In order to write this as a quadratic form, we introduce the vector

$$\boldsymbol{\mathcal{S}} = \begin{pmatrix} \boldsymbol{S}(\boldsymbol{q}) \\ \boldsymbol{S}^A(\boldsymbol{q}) \\ \boldsymbol{S}^B(\boldsymbol{q}) \end{pmatrix}$$

and its Hermitian conjugate

$$\boldsymbol{\mathcal{S}}^\dagger(\boldsymbol{q}) = \begin{pmatrix} \boldsymbol{S}(-\boldsymbol{q}), & \boldsymbol{S}^A(-\boldsymbol{q}), & \boldsymbol{S}^B(-\boldsymbol{q}) \end{pmatrix}$$

then the total Hamiltonian can be symmetrized by adding complex conjugates and taking one-half, as

$$H = \int d^2q\; \boldsymbol{\mathcal{S}}^\dagger(\boldsymbol{q})\,\mathcal{M}(\boldsymbol{q})\,\boldsymbol{\mathcal{S}}(\boldsymbol{q}) \tag{D.1}$$

with

$$\mathcal{M} = \begin{pmatrix} J_t f(q_1,q_2) & J_{th} g^*(q_1,q_2) & J_{th} h^*(q_1,q_2) \\ J_{th} g(q_1,q_2) & 0 & J_h h^*(q_1,q_2) \\ J_{th} h(q_1,q_2) & J_h h(q_1,q_2) & 0 \end{pmatrix}, \tag{D.2}$$

where

$$f(q_1,q_2) \quad \equiv \quad \cos 2\pi q_1+\cos 2\pi q_2+\cos 2\pi(q_1-q_2)$$

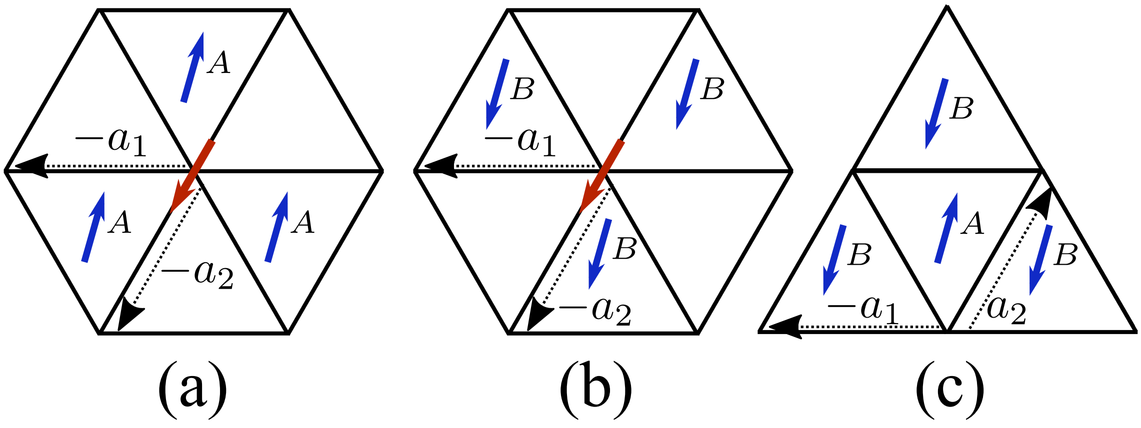

Figure D.1: The vectors $\delta\boldsymbol{r}$, defining the sites of neighboring spins, are found by considering to which unit-cell the spins belong. (a) The three A-site neighbors of a triangular spin. (b) The three B-site neighbors of a triangular spin. (c) The three B-site neighbors of an A-site spin.

$$\begin{aligned} g(q_1,q_2) &\equiv \frac{1}{2}(1+e^{2\pi i q_1}+e^{2\pi i q_2}+e^{2\pi i(q_1+q_2)}) \\ h(q_1,q_2) &\equiv \frac{1}{2}(1+e^{2\pi i q_1}+e^{2\pi i q_2}). \end{aligned}$$

This matrix $\mathcal{M}$ is known as the Luttinger-Tisza matrix. In order to minimize the energy H, we Fourier-transform the sum of the real-space constraints

$$\sum_i \left[|\boldsymbol{S}_i|^2+\left|\boldsymbol{S}_i^A\right|^2+\left|\boldsymbol{S}_i^B\right|^2\right]=3N \tag{D.3}$$

into

$$\int d^2q\,|\boldsymbol{\mathcal{S}}(\boldsymbol{q})|^2 \;=\; \int d^2q\left[|\boldsymbol{S}(\boldsymbol{q})|^2+\left|\boldsymbol{S}^A(\boldsymbol{q})\right|^2+\left|\boldsymbol{S}^B(\boldsymbol{q})\right|^2\right]=3N.$$

The Luttinger-Tisza procedure now consists in diagonalizing the matrix in eq. (D.2) and thereby rewriting eq. (D.1). The matrix $\mathcal{M}$ being Hermitian, we can diagonalize it with a unitary matrix U by introducing

$$\boldsymbol{\mathcal{S}}'=U\boldsymbol{\mathcal{S}}=\begin{pmatrix}\boldsymbol{S}_1(\boldsymbol{q})\\ \boldsymbol{S}_2(\boldsymbol{q})\\ \boldsymbol{S}_3(\boldsymbol{q})\end{pmatrix}$$

which transforms eq. (D.1) into

$$H=\int d^2q\;\boldsymbol{\mathcal{S}}'^{\dagger}(\boldsymbol{q})\,\mathcal{D}(\boldsymbol{q})\,\boldsymbol{\mathcal{S}}'(\boldsymbol{q})=\int d^2q\;\left[D_1|\boldsymbol{S}_1|^2+D_2|\boldsymbol{S}_2|^2+D_3|\boldsymbol{S}_3|^2\right] \tag{D.4}$$

where

$$\mathcal{D}(\boldsymbol{q})\equiv U^{\dagger}(\boldsymbol{q})\mathcal{M}(\boldsymbol{q})U(\boldsymbol{q})\equiv\begin{pmatrix}D_1(\boldsymbol{q}) & 0 & 0\\ 0 & D_2(\boldsymbol{q}) & 0\\ 0 & 0 & D_3(\boldsymbol{q})\end{pmatrix}.$$

Let us furthermore assume that the eigenvalues are sorted in ascending order $D_1(\boldsymbol{q})\leq D_2(\boldsymbol{q})\leq D_3(\boldsymbol{q})$ for each $\boldsymbol{q}$. Most importantly, the weak constraint eq. (D.4) is transformed into

$$\int d^2q\,|U\boldsymbol{\mathcal{S}}(\boldsymbol{q})|^2=\int d^2q\left[|\boldsymbol{S}_1|^2+|\boldsymbol{S}_2|^2+|\boldsymbol{S}_3|^2\right]=3N \tag{D.5}$$

According to the prescription of Luttinger and Tisza we must now minimize the energy in (D.4) under the constraint (D.5). This is obviously accomplished by distributing all the weight $|\boldsymbol{S}_1(\boldsymbol{q})|^2$ into the values of $\boldsymbol{q}$, say certain $\{\boldsymbol{Q}_i\}$, that yield the lowest D_1 and set $|\boldsymbol{S}_1(\boldsymbol{q})|=0$ for all $\boldsymbol{q}\notin\{\boldsymbol{Q}_i\}$ as well as $|\boldsymbol{S}_2(\boldsymbol{q})|^2=|\boldsymbol{S}_3(\boldsymbol{q})|^2=0$ for all $\boldsymbol{q}$. Since the spins in real-space are real-valued the condition $\boldsymbol{S}_1(\boldsymbol{q})=\boldsymbol{S}_1^*(-\boldsymbol{q})$ has to be satisfied. In other words, with $\boldsymbol{Q}$ we also have to include $-\boldsymbol{Q}$ as a minimizing wave-vector.

It is easy to demonstrate that the eigenvalues of $\mathcal{M}(\boldsymbol{q})$ and $\mathcal{M}(-\boldsymbol{q})$ are identical, thus with $\boldsymbol{Q}$ the vector $-\boldsymbol{Q}$ is also in the minimizing set $\{\boldsymbol{Q}_i\}$. First notice that upon switching $\boldsymbol{q}\to-\boldsymbol{q}$ in (D.2), we obtain, by virtue of $f\to f$, $g\leftrightarrow g^*$ and $h\leftrightarrow h^*$, the fact that $\mathcal{M}\to\mathcal{M}^{\mathrm{T}}$. Since $\mathcal{M}$ is a Hermitian matrix, $\mathcal{M}$ and $\mathcal{M}^{\mathrm{T}}$ have the same eigenvalues and the claim follows.

The minimum energy is then given by

$$H_{\min}=3ND_1(\boldsymbol{Q}).$$

Of course, the spectrum of $\mathcal{M}$ may be degenerate and there may be different values of $\boldsymbol{q}$ with $D_1(\boldsymbol{q}) = D_1(\boldsymbol{Q})$. In this case one has more freedom in distributing the weak-constraint weight $3N$ to the $S_1(\boldsymbol{q})$.
The characteristic equation of $\mathcal{M}$ is

$$\begin{aligned}
0 &= E^3(\boldsymbol{q}) + A(\boldsymbol{q})E^2(\boldsymbol{q}) + B(\boldsymbol{q})E(\boldsymbol{q}) + C(\boldsymbol{q}) \\
A(\boldsymbol{q}) &= -f(q_1,q_2)J_t \\
B(\boldsymbol{q}) &= \left[f(q_1,q_2) + \frac{1}{2}f(q_1,-q_2) + \frac{7}{4}\right] J_{th}^2 + \left[3 + 2f(q_1,q_2)\right]\frac{J_h^2}{4} \\
C(\boldsymbol{q}) &= \frac{J_{th}^2 J_h}{4}(3 + 2f(q_1,q_2))(1 + f(q_1,-q_2)) - \frac{J_t J_h^2}{4} f(q_1,q_2)(3 + 2f(q_1,q_2)) \\
f(q_1,q_2) &= \cos 2\pi q_1 + \cos 2\pi q_2 + \cos 2\pi (q_1 - q_2)
\end{aligned}$$

and the lowest eigenvalue D_1 with the corresponding value of $\boldsymbol{q}$ is defined by

$$\begin{aligned}
D_1 &= \min_{\boldsymbol{q}} E(\boldsymbol{q}) \\
\boldsymbol{Q} &= \underset{\boldsymbol{q}}{\text{argmin}}\ E(\boldsymbol{q}).
\end{aligned}$$

In order to demonstrate how the Luttinger-Tisza method fails, let us assume now that we have found a minimizing wave-vector $\pm\boldsymbol{Q}$. This means that we have found a vector $\boldsymbol{\mathcal{S}}$ of the form

$$\boldsymbol{\mathcal{S}}' = U\boldsymbol{\mathcal{S}} = \begin{pmatrix} \boldsymbol{S}_1^{(0)}\delta(\boldsymbol{q}-\boldsymbol{Q}) + \boldsymbol{S}_1^{(0)}\delta(\boldsymbol{q}+\boldsymbol{Q}) \\ 0 \\ 0 \end{pmatrix}$$

with $|\boldsymbol{S}_1^{(0)}|^2 = \frac{3N}{2}$, which is necessary in order to satisfy the condition of weak constraint. Now we transform back, in order to obtain the weights for the individual lattices:

$$\begin{aligned}
\boldsymbol{\mathcal{S}} &= U^\dagger \boldsymbol{\mathcal{S}}' \\
\boldsymbol{S}(\boldsymbol{q}) &= U_{11}^* \left(\boldsymbol{S}_1^{(0)}\delta(\boldsymbol{q}-\boldsymbol{Q}) + \boldsymbol{S}_1^{(0)}\delta(\boldsymbol{q}+\boldsymbol{Q})\right) \\
\boldsymbol{S}^A(\boldsymbol{q}) &= U_{21}^* \left(\boldsymbol{S}_1^{(0)}\delta(\boldsymbol{q}-\boldsymbol{Q}) + \boldsymbol{S}_1^{(0)}\delta(\boldsymbol{q}+\boldsymbol{Q})\right) \\
\boldsymbol{S}^B(\boldsymbol{q}) &= U_{31}^* \left(\boldsymbol{S}_1^{(0)}\delta(\boldsymbol{q}-\boldsymbol{Q}) + \boldsymbol{S}_1^{(0)}\delta(\boldsymbol{q}+\boldsymbol{Q})\right)
\end{aligned}$$

In order to satisfy the weak-constraint equation for the individual lattices, we have to demand $|U_{11}|^2 = |U_{21}|^2 = |U_{31}|^2 = \frac{1}{3}$. This is equivalent to saying that the normalized eigenvector belonging to the lowest eigenvalue should have components with absolute square equal to $1/3$. This will in general not be the case. One then has to conclude that the assumption of a single minimizing mode $\pm\boldsymbol{Q}$ is not valid. Indeed, reviewing the phases that we found algorithmically, one sees that only one phase, namely the spiral phase, is described by a single ordering wave-vector. The other phases are characterized by having more ordering vectors. If there is more than one wave-vector, it means that a compromise was achieved in that energetically less favorable ordering wave-vectors were included in the ground state in order to satisfy the strong constraint, which is the reason why the Luttinger-Tisza analysis does not yield a straightforward answer to the minimization problem.

Appendix E

Analytic calculation of the order-by-disorder potential

In this appendix to chapter 4 we summarize our calculation of the order-by-disorder potential terms. The aim of this calculation is to determine the dependence of the free-energy on the manifold of ground-state configurations (the calculation follows [102, 90, 35, 10]). In order to carry out the calculation we parametrize the spins as small fluctuations around one of the ground states. We choose the plane of spins of the triangular lattice spins in their groundstate to lie in the xy plane. The honeycomb spins have an order parameter, that is described by angles β and α. The fluctuations of the triangular sublattice spins are called (ρ, σ, τ) and those of the honeycomb spins are called (μ, ν). We choose the following parametrization of the fluctuations

$$\begin{aligned}
\boldsymbol{n}^A &= \begin{pmatrix} 1-\frac{\rho_y^2+\rho_z^2}{2} \\ \rho_y \\ \rho_z \end{pmatrix} \\
\boldsymbol{n}^B &= R\begin{pmatrix} 1-\frac{\sigma_y^2+\sigma_z^2}{2} \\ \sigma_y \\ \sigma_z \end{pmatrix} = \begin{pmatrix} -\frac{1}{2}-\frac{\sqrt{3}}{2}\sigma_y+\frac{\sigma_y^2+\sigma_z^2}{4} \\ \frac{\sqrt{3}}{2}-\frac{1}{2}\sigma_y-\frac{\sqrt{3}}{4}(\sigma_y^2+\sigma_z^2) \\ \sigma_z \end{pmatrix} \\
\boldsymbol{n}^C &= R^2\begin{pmatrix} 1-\frac{\tau_y^2+\tau_z^2}{2} \\ \tau_y \\ \tau_z \end{pmatrix} = \begin{pmatrix} -\frac{1}{2}+\frac{\sqrt{3}}{2}\tau_y+\frac{\tau_y^2+\tau_z^2}{4} \\ -\frac{\sqrt{3}}{2}-\frac{1}{2}\tau_y+\frac{\sqrt{3}}{4}(\tau_y^2+\tau_z^2) \\ \tau_z \end{pmatrix}
\end{aligned}$$

$$\begin{aligned}
\boldsymbol{h}^A &= \left(1-\frac{\mu_1^2+\mu_2^2}{2}\right)\boldsymbol{h}_0+\mu_1\boldsymbol{\beta}+\mu_2\boldsymbol{\alpha} \\
\boldsymbol{h}^B &= -\left[\left(1-\frac{\nu_1^2+\nu_2^2}{2}\right)\boldsymbol{h}_0+\nu_1\boldsymbol{\beta}+\nu_2\boldsymbol{\alpha}\right]
\end{aligned}$$

with unit vectors

$$\boldsymbol{h}_0 = \begin{pmatrix} \sin\beta\cos\alpha \\ \sin\beta\sin\alpha \\ \cos\beta \end{pmatrix}, \ \boldsymbol{\beta} = \begin{pmatrix} \cos\beta\cos\alpha \\ \cos\beta\sin\alpha \\ \sin\beta \end{pmatrix}, \ \boldsymbol{\alpha} = \begin{pmatrix} -\sin\alpha \\ \cos\alpha \\ 0 \end{pmatrix}$$

and where $R = R_z(2\pi/3)$ is the rotation matrix that rotates spins around the z-axis by $2\pi/3$. With this parametrization it is a straightforward task to rewrite the Hamiltonian in the following form. The triangular spin Hamiltonian becomes

$$H_t = J_{tt} \sum_i \boldsymbol{n}_i^A \cdot \left(\sum_{j(i)} \boldsymbol{n}_j^B + \sum_{j(i)} \boldsymbol{n}_j^C \right) + J_{tt} \sum_i \boldsymbol{n}_i^B \cdot \sum_{j(i)} \boldsymbol{n}_j^C$$

here the notation $j(i)$ denotes summation over the neighbors j of the spin with index i. This is

$$H_t = -\frac{3}{2} N J_{tt} + \delta H_t$$

with

$$\begin{aligned}
\delta H_t &= J_{tt} \sum_{\langle i,j \rangle} \left[\frac{1}{4} \left(\rho_{iy}^2 + \rho_{iz}^2 + \sigma_{jy}^2 + \sigma_{jz}^2 \right) - \frac{1}{2} \rho_{iy} \sigma_{jy} + \rho_{iz} \sigma_{jz} \right] \\
&\quad + J_{tt} \sum_{\langle i,j \rangle} \left[\frac{1}{4} \left(\rho_{iy}^2 + \rho_{iz}^2 + \tau_{jy}^2 + \tau_{jz}^2 \right) - \frac{1}{2} \rho_{iy} \tau_{jy} + \rho_{iz} \tau_{jz} \right] \\
&\quad + J_{tt} \sum_{\langle i,j \rangle} \left[\frac{1}{4} \left(\sigma_{iy}^2 + \sigma_{iz}^2 + \tau_{jy}^2 + \tau_{jz}^2 \right) - \frac{1}{2} \sigma_{iy} \tau_{jy} + \sigma_{iz} \tau_{jz} \right],
\end{aligned}$$

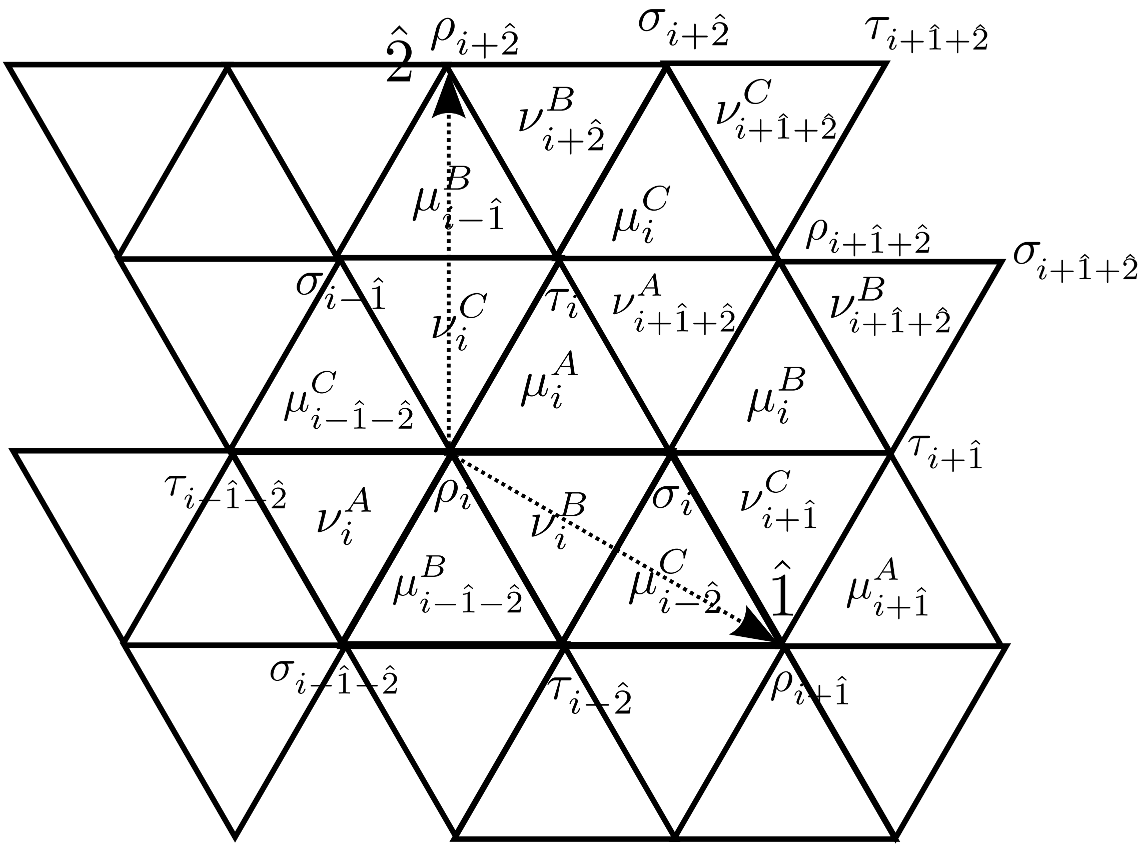

Figure E.1: Labeling of sites inside the enlarged magnetic unit-cell.

where all the linear terms have canceled out. Similarly we have

$$\begin{aligned}
\delta H_h &= J_{hh}\sum_i \frac{3}{2}\left[\left(\mu_{i1}^A\right)^2+\left(\mu_{i2}^A\right)^2+\left(\nu_{i1}^A\right)^2+\left(\nu_{i2}^A\right)^2+\left(\mu_{i1}^B\right)^2+\left(\mu_{i2}^B\right)^2+\left(\nu_{i1}^B\right)^2+\left(\nu_{i2}^B\right)^2\right] \\
& J_{hh}\sum_i \frac{3}{2}\left[\left(\mu_{i1}^C\right)^2+\left(\mu_{i2}^C\right)^2+\left(\nu_{i1}^C\right)^2+\left(\nu_{i2}^C\right)^2\right] \\
& -J_{hh}\sum_i \mu_{i1}^A\left[\nu^A_{i+\hat{1}+\hat{2},1}+\nu_{i1}^B+\nu_{i1}^C\right]+\mu_{i1}^B\left[\nu^A_{i+\hat{1}+\hat{2},1}+\nu^B_{i+\hat{1}+\hat{2},1}+\nu^C_{i+\hat{1},1}\right] \\
& -J_{hh}\sum_i \mu_{i1}^C\left[\nu^A_{i+\hat{1}+\hat{2},1}+\nu^B_{i+\hat{2},1}+\nu^C_{i+\hat{1}+\hat{2},1}\right] \\
& -J_{hh}\sum_i \mu_{i2}^A\left[\nu^A_{i+\hat{1}+\hat{2},2}+\nu_{i2}^B+\nu_{i2}^C\right]+\mu_{i2}^B\left[\nu^A_{i+\hat{1}+\hat{2},2}+\nu^B_{i+\hat{1}+\hat{2},2}+\nu^C_{i+\hat{1},2}\right] \\
& -J_{hh}\sum_i \mu_{i2}^C\left[\nu^A_{i+\hat{1}+\hat{2},2}+\nu^B_{i+\hat{2},2}+\nu^C_{i+\hat{1}+\hat{2},2}\right]
\end{aligned}$$

and finally

$$\begin{aligned}
H_{th} &= J_{th}\sum_i \cos\alpha\rho_{iy}(\mu_{i2}^A+\mu^B_{i-\hat{1}-\hat{2},2}+\mu^C_{i-\hat{1}-\hat{2},2}) \\
&+\cos\beta\sin\alpha\rho_{iy}(\mu_{i1}^A+\mu^B_{i-\hat{1}-\hat{2},1}+\mu^C_{i-\hat{1}-\hat{2},1}) \\
&-\sin\beta\rho_{iz}(\mu_{i1}^A+\mu^B_{i-\hat{1}-\hat{2},1}+\mu^C_{i-\hat{1}-\hat{2},1})-\cos\alpha\rho_{iy}(\nu_{i2}^A+\nu_{i2}^B+\nu_{i2}^C) \\
&-\cos\beta\sin\alpha\rho_{iy}(\nu_{i1}^A+\nu_{i1}^B+\nu_{i1}^C)+\sin\beta\rho_{iz}(\nu_{i1}^A+\nu_{i1}^B+\nu_{i1}^C) \\
&+J_{th}\sum_i \frac{\sqrt{3}\sin\alpha-\cos\alpha}{2}\sigma_{iy}(\mu_{i2}^A+\mu_{i2}^B+\mu^C_{i-\hat{2},2}) \\
&-\frac{\sqrt{3}\cos\alpha+\sin\alpha}{2}\cos\beta\sigma_{iy}(\mu_{i1}^A+\mu_{i1}^B+\mu^C_{i-\hat{2},1})-\sin\beta\sigma_{iz}(\mu_{i1}^B+\mu_{i1}^A+\mu^C_{i-\hat{2},1}) \\
&-\frac{\sqrt{3}\sin\alpha-\cos\alpha}{2}\sigma_{iy}(\nu^A_{i+\hat{1}+\hat{2},2}+\nu_{i2}^B+\nu^C_{i+\hat{1},2}) \\
&+\frac{\sqrt{3}\cos\alpha+\sin\alpha}{2}\cos\beta\sigma_{iy}(\nu^A_{i+\hat{1}+\hat{2},1}+\nu_{i1}^B+\nu^C_{i+\hat{1},1}) \\
&+\sin\beta\sigma_{iz}(\nu^A_{i+\hat{1}+\hat{2},1}+\nu_{i1}^B+\nu^C_{i+\hat{1},1}) \\
&-J_{th}\sum_i \frac{\sqrt{3}\sin\alpha+\cos\alpha}{2}\tau_{iy}(\mu_{i2}^A+\mu^B_{i-\hat{1},2}+\mu_{i2}^C) \\
&+\frac{\sqrt{3}\cos\alpha-\sin\alpha}{2}\cos\beta\tau_{iy}(\mu_{i1}^A+\mu^B_{i-\hat{1},1}+\mu_{i1}^C)-\sin\beta\tau_{iz}(\mu_{i1}^A+\mu^B_{i-\hat{1},1}+\mu_{i1}^C) \\
&+\frac{\sqrt{3}\sin\alpha+\cos\alpha}{2}\tau_{iy}(\nu^A_{i+\hat{1}+\hat{2},2}+\nu^B_{i+\hat{2},2}+\nu_{i2}^C) \\
&-\frac{\sqrt{3}\cos\alpha-\sin\alpha}{2}\cos\beta\tau_{iy}(\nu^A_{i+\hat{1}+\hat{2},1}+\nu^B_{i+\hat{2},1}+\nu_{i1}^C) \\
&+\sin\beta\tau_{iz}(\nu^A_{i+\hat{1}+\hat{2},1}+\nu^B_{i+\hat{2},1}+\nu_{i1}^C).
\end{aligned}$$

We transform this into Fourier space with

$$\rho_i=\rho\left(\boldsymbol{r}_i\right)=\frac{1}{(2\pi)^2}\int d^2q e^{i\boldsymbol{q}\boldsymbol{r_i}}\rho(\boldsymbol{q})$$

and rewrite the resulting total Hamiltonian in matrix form. This matrix has dimensions 18×18. It may, however, be written in extremely compact block form. This will facilitate the calculation of the free energy below. The full Hamiltonian is

$$\delta H = \frac{N}{6(2\pi)^2} \int d^2q \psi^\dagger \begin{pmatrix} J_{tt}M_t & J_{th}M_{th}^\dagger \\ J_{th}M_{th} & J_{hh}M_h \end{pmatrix} \psi.$$

with

$$M_t \;=\; \begin{pmatrix} \frac{15}{2}\mathbb{I} - \frac{j_0 j_0^\dagger}{2} & 0 \\ 0 & 3\mathbb{I} + j_0 j_0^\dagger \end{pmatrix}$$

$$M_h \;=\; \begin{pmatrix} 3\mathbb{I} & -e^{i(q_1+q_2)} j_0^\dagger & 0 & 0 \\ -e^{-i(q_1+q_2)} j_0 & 3\mathbb{I} & 0 & 0 \\ 0 & 0 & 3\mathbb{I} & -e^{i(q_1+q_2)} j_0^\dagger \\ 0 & 0 & -e^{-i(q_1+q_2)} j_0 & 3\mathbb{I} \end{pmatrix}$$

and

$$M_{th} = \begin{pmatrix} j_0 u & j_0 v \\ -j_0^\dagger u & -j_0^\dagger v \\ j_0 w & 0 \\ -j_0^\dagger w & 0 \end{pmatrix}.$$

The entries are themselves matrices:

$$j_0 \;=\; \begin{pmatrix} 1 & 1 & 1 \\ e^{i(q_1+q_2)} & 1 & e^{iq_1} \\ e^{i(q_1+q_2)} & e^{iq_2} & 1 \end{pmatrix}$$

$$u \;=\; \cos\beta \begin{pmatrix} \sin\alpha & 0 & 0 \\ 0 & \sin(\alpha + \frac{4\pi}{3}) & 0 \\ 0 & 0 & \sin(\alpha + \frac{2\pi}{3}) \end{pmatrix}$$

$$v \;=\; -\sin\beta \begin{pmatrix} 1 & 0 & 0 \\ 0 & 1 & 0 \\ 0 & 0 & 1 \end{pmatrix}$$

$$w \;=\; \begin{pmatrix} \cos\alpha & 0 & 0 \\ 0 & \cos(\alpha + \frac{4\pi}{3}) & 0 \\ 0 & 0 & \cos(\alpha + \frac{2\pi}{3}) \end{pmatrix}.$$

The quantity ψ describing the fluctuation amplitudes is given by

$$\psi(Q_1, Q_2) \;=\; \left(\rho_y, \sigma_y, \tau_y, \rho_z, \sigma_z, \tau_z, \mu_1^A, \mu_1^B, \mu_1^C, \nu_1^A, \nu_1^B, \nu_1^C, \mu_2^A, \mu_2^B, \mu_2^C, \nu_2^A, \nu_2^B, \nu_2^C\right).$$

Finally, the correction to the free energy due to the fluctuations in a given ground state, characterized by β and α, is computed by the formula

$$\delta F \;=\; T \int d^2q \log \Delta$$

with determinant

$$\Delta \;=\; \det \begin{pmatrix} J_{tt}M_t & J_{th}M_{th}^{\dagger} \\ J_{th}M_{th} & J_{hh}M_h \end{pmatrix}.$$

A straightforward analytical evaluation of this determinant is complicated by the large dimension of the matrices. However, we may still carry out this computation by making repeated use of the block structure of δH. We use the following block matrix decomposition:

$$\begin{pmatrix} A & B \\ C & D \end{pmatrix} = \begin{pmatrix} 1 & 0 \\ 0 & D \end{pmatrix} \begin{pmatrix} A & B \\ D^{-1}C & 1 \end{pmatrix} = \begin{pmatrix} 1 & 0 \\ 0 & D \end{pmatrix} \begin{pmatrix} 1 & B \\ 0 & 1 \end{pmatrix} \begin{pmatrix} A - BD^{-1}C & 0 \\ D^{-1}C & 1 \end{pmatrix}.$$

Since all three matrices are triangular, the determinant is just

$$\det \begin{pmatrix} A & B \\ C & D \end{pmatrix} = \det D \det \left(A - BD^{-1}C\right),$$

an equality known as the Schur identity. Iterative application of this identity to the block matrices breaks the block structure down, until we are left with a determinant of a 3×3 matrix. We start with the calculation of the determinant for the special case $\beta = \frac{\pi}{2}$. Here the determinant (after discarding α-independent factors) can be written as

$$\sum_{n=0}^{3} \Delta_n \left(\frac{J_{th}}{\bar{J}}\right)^{2n}$$

with $\bar{J} = \sqrt{J_{tt}J_{hh}}$ and q-dependent Δ_n. Computation of the Δ_n shows that only $n = 3$ yields an α-dependence. The two other determinants are independent of α and are therefore not responsible for the selection of the groundstate. Integration over q yields the sought free energy dependence on α. Numerical evaluation of this last integral yields

$$\delta F \equiv \left(\frac{J_{th}}{\bar{J}}\right)^6 \frac{NT}{3} \int \frac{d^2q}{(2\pi)^2} \frac{\Delta_3}{\Delta_0} = -10^{-4} NT \cos^2(3\alpha) \left(\frac{J_{th}}{\bar{J}}\right)^6.$$

Next we compute to lowest-order in $\left(\frac{J_{th}}{\bar{J}}\right)$ the dependence on β. In computing the determinant by Schur's identity, one is left with a determinant of the form

$$\log\det\left[\mathbb{I} + \left(\frac{J_{th}}{\bar{J}}\right)^2 A^{-1}B + \left(\frac{J_{th}}{\bar{J}}\right)^4 A^{-1}C\right],$$

where A, B, C are 3×3 matrices. We are only interested in the lowest-order correction, which will obviously be proportional to $\left(\frac{J_{th}}{\bar{J}}\right)^2$. We find this most conveniently by rewriting the logarithm as a trace:

$$\begin{aligned} \log\det\left[\mathbb{I} + \left(\frac{J_{th}}{\bar{J}}\right)^2 A^{-1}B + \left(\frac{J_{th}}{\bar{J}}\right)^4 A^{-1}C\right] &= \mathrm{Tr}[\log(\mathbb{I} + \left(\frac{J_{th}}{\bar{J}}\right)^2 A^{-1}B + \left(\frac{J_{th}}{\bar{J}}\right)^4 A^{-1}C)] \\ &\equiv \sum T_n \left(\frac{J_{th}}{\bar{J}}\right)^{2n} \qquad \text{(E.1)} \end{aligned}$$

Once the T_n are known, the free energy can be expressed as

$$\delta F \equiv \sum_{n=1}^{6} \delta F_n \left(\frac{J_{th}}{\bar{J}}\right)^{2n} = \frac{NT}{3} \sum_{n=1}^{6} \left(\frac{J_{th}}{\bar{J}}\right)^{2n} \int \frac{d^2q}{(2\pi)^2} T_n$$

Next we compute the T_n by expanding the logarithm in $\left(\frac{J_{th}}{\bar{J}}\right)^2$

$$\mathrm{Tr}[\log(\mathbb{I} + \left(\frac{J_{th}}{\bar{J}}\right)^2 A^{-1}B + \left(\frac{J_{th}}{\bar{J}}\right)^4 A^{-1}C)] = \sum_{1}^{\infty} (-)^{n-1} \frac{\left(\frac{J_{th}}{\bar{J}}\right)^{2n} \mathrm{Tr}\left[(A^{-1}B + \left(\frac{J_{th}}{\bar{J}}\right)^2 A^{-1}C)^n\right]}{n}$$

with

$$\begin{aligned} T_1 &= \mathrm{Tr}\left[A^{-1}B\right] \\ T_2 &= \mathrm{Tr}\left[A^{-1}C\right] - \frac{1}{2}\mathrm{Tr}\left[(A^{-1}B)^2\right] \\ T_3 &= -\mathrm{Tr}\left[A^{-1}BA^{-1}C\right] + \frac{1}{3}\mathrm{Tr}\left[(A^{-1}B)^3\right]. \end{aligned}$$

Here we will only require T_1. Using the stated formula, it is straightforward to calculate the lowest-order dependence of the free energy on β. We find

$$\delta F = 0.131274 \cos(2\beta) NT \left(\frac{J_{th}}{\bar{J}}\right)^2.$$

List of Figures

Bibliography

[1] A. Altland and B. Simons. *Condensed Matter Field Theory.* Cambridge University Press, Cambridge, U.K., 2006.

[2] P. Azaria, B. Delamotte, T. Jolicoeur, and D. Mouhanna. Spin stiffness of canted antiferromagnets. *Phys. Rev. B*, 45:12612–12615, Jun 1992.

[3] Seung Ki Baek, Harri Mäkelä, Petter Minnhagen, and Beom Jun Kim. Ising model on a hyperbolic plane with a boundary. *Phys. Rev. E*, 84:032103, Sep 2011.

[4] Dario Benedetti. Critical behavior in spherical and hyperbolic spaces. *Journal of Statistical Mechanics: Theory and Experiment*, 2015(1):P01002, 2015.

[5] V. L. Berezinskii. Destruction of long-range order in one-dimensional and two-dimensional systems possessing a continuous symmetry group. II. Quantum systems. *Sov. Phys. JETP*, 34:610, 1972.

[6] Curtis G. Callan and Frank Wilczek. Infrared behavior at negative curvature. *Nuclear Physics B*, 340(2–3):366 – 386, 1990.

[7] Luca Capriotti, Andrea Fubini, Tommaso Roscilde, and Valerio Tognetti. Ising Transition in the Two-Dimensional Quantum $J_1 - J_2$ Heisenberg Model. *Phys. Rev. Lett.*, 92:157202, Apr 2004.

[8] J.L. Cardy. General Discrete Planar Models in Two Dimensions: Duality Properties and Phase Diagrams. *J. Phys. A: Math. Gen.*, 13:1507–1515, 1980.

[9] P. M. Chaikin and T. C. Lubensky. *Principles of Condensed Matter Physics.* Cambridge University Press, Cambridge, U.K., 1995.

[10] J. T. Chalker, P. C. W. Holdsworth, and E. F. Shender. Hidden order in a frustrated system: Properties of the Heisenberg Kagomé antiferromagnet. *Phys. Rev. Lett.*, 68:855–858, Feb 1992.

[11] Murty Challa and D. Landau. Critical behavior of the six-state clock model in two dimensions. *Phys. Rev. B*, 33:437–443, Jan 1986.

[12] P. Chandra, P. Coleman, and A. I. Larkin. Ising transition in frustrated Heisenberg models. *Phys. Rev. Lett.*, 64(1):88–91, Jan 1990.

[13] G.-W. Chern and O. Tchernyshyov. Magnetic charge and ordering in Kagome spin ice. *Phil. Trans. R. Soc. A*, 370:5718, 2012.

[14] Gia-Wei Chern, Paula Mellado, and O. Tchernyshyov. Two-Stage Ordering of Spins in Dipolar Spin Ice on the Kagome Lattice. *Phys. Rev. Lett.*, 106:207202, May 2011.

[15] Gia-Wei Chern and R. Moessner. Dipolar Order by Disorder in the Classical Heisenberg Antiferromagnet on the Kagome Lattice. *Phys. Rev. Lett.*, 110:077201, Feb 2013.

[16] R. Coldea, D. A. Tennant, K. Habicht, P. Smeibidl, C. Wolters, and Z. Tylczynski. Direct Measurement of the Spin Hamiltonian and Observation of Condensation of Magnons in the 2D Frustrated Quantum Magnet Cs_2CuCl_4. *Phys. Rev. Lett.*, 88:137203, Mar 2002.

[17] R. Coldea, D. A. Tennant, A. M. Tsvelik, and Z. Tylczynski. Experimental Realization of a 2D Fractional Quantum Spin Liquid. *Phys. Rev. Lett.*, 86:1335–1338, Feb 2001.

[18] H. S. M. Coxeter. *Introduction to geometry.* Wiley classics library, Wiley, 1969.

[19] S. Weinberg D. R. Nelson and T. Piran. *Statistical mechanics of membranes and surfaces (second edition).* World Scientific Pub Co Inc, 2004.

[20] C. Domb. On the Theory of Cooperative Phenomena in Crystals. *Advances in Physics 9 , 245*, 1960.

[21] Martin Eckstein, Marcus Kollar, Krzysztof Byczuk, and Dieter Vollhardt. Hopping on the bethe lattice: Exact results for densities of states and dynamical mean-field theory. *Phys. Rev. B*, 71:235119, Jun 2005.

[22] E. Fermi. *Thermodynamics.* Dover books in physics and mathematical physics. Dover Publications, 1956.

[23] R. M. Fernandes, A. V. Chubukov, J. Knolle, I. Eremin, and J. Schmalian. Preemptive nematic order, pseudogap, and orbital order in the iron pnictides. *Phys. Rev. B*, 85:024534, Jan 2012.

[24] R. M. Fernandes, L. H. VanBebber, S. Bhattacharya, P. Chandra, V. Keppens, D. Mandrus, M. A. McGuire, B. C. Sales, A. S. Sefat, and J. Schmalian. Effects of Nematic Fluctuations on the Elastic Properties of Iron Arsenide Superconductors. *Phys. Rev. Lett.*, 105:157003, Oct 2010.

[25] Michael E. Fisher and Michael N. Barber. Scaling Theory for Finite-Size Effects in the Critical Region. *Phys. Rev. Lett.*, 28:1516–1519, Jun 1972.

[26] Rebecca Flint and Patrick A. Lee. Emergent Honeycomb Lattice in $LiZn_2Mo_3O_8$. *Phys. Rev. Lett.*, 111:217201, Nov 2013.

[27] V. Fock. Zur Theorie des Wasserstoffatoms. *Zeitschrift für Physik* ***98****(3-4), 145–154*, 1935.

[28] Maw Lin Foo, Yayu Wang, Satoshi Watauchi, H. W. Zandbergen, Tao He, R. J. Cava, and N. P. Ong. Charge ordering, commensurability, and metallicity in the phase diagram of the layered Na_xCoO_2. *Phys. Rev. Lett.*, 92:247001, Jun 2004.

[29] Andrej Gendiar, Roman Krcmar, Sabine Andergassen, Michal Daniška, and Tomotoshi Nishino. Weak correlation effects in the Ising model on triangular-tiled hyperbolic lattices. *Phys. Rev. E*, 86:021105, Aug 2012.

[30] Antoine Georges, Gabriel Kotliar, Werner Krauth, and Marcelo J. Rozenberg. Dynamical mean-field theory of strongly correlated fermion systems and the limit of infinite dimensions. *Rev. Mod. Phys.*, 68:13–125, Jan 1996.

[31] N. Goldenfeld. *Lectures on Phase Transitions and the Renormalization Group*. Westview Press, Boulder, CO, USA, 1992.

[32] S. Gubser, I. Klebanov, and A. Polyakov. Gauge theory correlators from non-critical string theory. *Physics Letters B* **428**, 1998.

[33] L. X. Hayden, T. A. Kaplan, and S. D. Mahanti. Frustrated Classical Heisenberg and XY Models in Two Dimensions with Nearest-Neighbor Biquadratic Exchange: Exact Solution for the Ground-State Phase Diagram. *Phys. Rev. Lett.*, 105:047203, Jul 2010.

[34] M. Hemmida, H.-A. Krug von Nidda, N. Büttgen, A. Loidl, L. K. Alexander, R. Nath, A. V. Mahajan, R. F. Berger, R. J. Cava, Yogesh Singh, and D. C. Johnston. Vortex dynamics and frustration in two-dimensional triangular chromium lattices. *Phys. Rev. B*, 80:054406, Aug 2009.

[35] Christopher L. Henley. Ordering due to disorder in a frustrated vector antiferromagnet. *Phys. Rev. Lett.*, 62:2056–2059, Apr 1989.

[36] Koji Hukushima and Koji Nemoto. Exchange Monte Carlo Method and Application to Spin Glass Simulations. *J. Phys. Soc. Jpn.*, 65(6):1604, 1996.

[37] S. V. Isakov and R. Moessner. Interplay of quantum and thermal fluctuations in a frustrated magnet. *Phys. Rev. B*, 68:104409, Sep 2003.

[38] Bhilahari Jeevanesan and Peter P. Orth. Classical ground states of Heisenberg and XY antiferromagnets on the windmill lattice. *Phys. Rev. B*, 90:144435, Oct 2014.

[39] Jorge V. José, Leo P. Kadanoff, Scott Kirkpatrick, and David R. Nelson. Renormalization, vortices, and symmetry-breaking perturbations in the two-dimensional planar model. *Phys. Rev. B*, 16(3):1217–1241, 1977.

[40] Gregor Jotzu, Michael Messer, Rémi Desbuquois, Martin Lebrat, Thomas Uehlinger, Daniel Greif, and Tilman Esslinger. Experimental realisation of the topological Haldane model. *arXiv:1406.7874*, 2014.

[41] Helmut G Katzgraber. Introduction to Monte Carlo Methods. *arXiv preprint arXiv:0905.1629*, 2009.

[42] J. M. Kosterlitz. The critical properties of the two-dimensional xy model. *J. Phys. C: Solid St. Phys.*, 7:1046, 1974.

[43] J. M. Kosterlitz. Phase Transitions in Long-Range Ferromagnetic Chains. *Phys. Rev. Lett.*, 37(23):1577–1580, Dec 1976.

[44] J. M. Kosterlitz and D. J. Thouless. Ordering, metastability and phase transitions in two-dimensional systems. *J. Phys. C: Solid St. Phys.*, 6:1181, 1973.

[45] R Krcmar, A Gendiar, K Ueda, and T Nishino. Ising model on a hyperbolic lattice studied by the corner transfer matrix renormalization group method. *Journal of Physics A: Mathematical and Theoretical*, 41(12):125001, 2008.

[46] R. Krcmar, T. Iharagi, A. Gendiar, and T. Nishino. Tricritical point of the J_1-J_2 Ising model on a hyperbolic lattice. *Phys. Rev. E*, 78:061119, Dec 2008.

[47] M. Kurata, R. Kikuchi, and T. Watari. A Theory of Cooperative Phenomena. III. Detailed Discussions of the Cluster Variation Method. *The Journal of Chemical Physics*, 1953.

[48] M. F. Lapa and C. L. Henley. Ground States of the Classical Antiferromagnet on the Pyrochlore Lattice. arXiv:1210.6810, 2012.

[49] C. Laumann, A. Scardicchio, and S. L. Sondhi. Cavity method for quantum spin glasses on the Bethe lattice. *Phys. Rev. B*, 78:134424, Oct 2008.

[50] E. Lifshitz and I. Khalatnikov. Investigations in relativistic cosmology. *Advances in Physics* **12***(46), 185–249*, 1963.

[51] Shi-Zeng Lin, Yoshitomo Kamiya, Gia-Wei Chern, and Cristian D. Batista. Stiffness from Disorder in Triangular-Lattice Ising Thin Films. *Phys. Rev. Lett.*, 112:155702, Apr 2014.

[52] J. M. Luttinger and L. Tisza. Theory of Dipole Interaction in Crystals. *Phys. Rev.*, 70:954–964, Dec 1946.

[53] S.-K. Ma. Critical Exponents above T_c to $O(\frac{1}{n})$. *Phys. Rev. A* **7***, 2172–2187*, Jun 1973.

[54] J. M. Maldacena. The Large N limit of superconformal field theories and supergravity. *Adv.Theor.Math.Phys.* **2***, 231–252*, 1998.

[55] E. Marinari and G. Parisi. Simulated Tempering: A New Monte Carlo Scheme. *EPL*, 19(6):451, 1992.

[56] T. McQueen, Q. Huang, J. W. Lynn, R. F. Berger, T. Klimczuk, B. G. Ueland, P. Schiffer, and R. J. Cava. Magnetic structure and properties of the $s = 5/2$ triangular antiferromagnet α-NaFeO_2. *Phys. Rev. B*, 76:024420, Jul 2007.

[57] R. Melzi, P. Carretta, A. Lascialfari, M. Mambrini, M. Troyer, P. Millet, and F. Mila. Li$_2$VO$(Si, Ge)O_4$, a Prototype of a Two-Dimensional Frustrated Quantum Heisenberg Antiferromagnet. *Phys. Rev. Lett.*, 85:1318–1321, Aug 2000.

[58] N. D. Mermin and H. Wagner. Absence of Ferromagnetism or Antiferromagnetism in One- or Two-Dimensional Isotropic Heisenberg Models. *Phys. Rev. Lett.*, 17:1307–1307, Dec 1966.

[59] Laura Messio, Bernard Bernu, and Claire Lhuillier. Kagome antiferromagnet: A chiral topological spin liquid? *Phys. Rev. Lett.*, 108:207204, May 2012.

[60] Nicholas Metropolis, Arianna W Rosenbluth, Marshall N Rosenbluth, Augusta H Teller, and Edward Teller. Equation of state calculations by fast computing machines. *The journal of chemical physics*, 21(6):1087–1092, 1953.

[61] Y Miyatake, M Yamamoto, J J Kim, M Toyonaga, and O Nagai. On the implementation of the 'heat bath' algorithms for Monte Carlo simulations of classical Heisenberg spin systems. *J. Phys. C*, 19(14):2539, 1986.

[62] R. Moessner and J. T. Chalker. Properties of a Classical Spin Liquid: The Heisenberg Pyrochlore Antiferromagnet. *Phys. Rev. Lett.*, 80:2929–2932, Mar 1998.

[63] R. Mosseri and J. Sadoc. The Bethe lattice: a regular tiling of the hyperbolic plane. *Journal de Physique Lettres* ***43****(8), 249–252*, 1982.

[64] M. Mourigal, W. T. Fuhrman, J. P. Sheckelton, A. Wartelle, J. A. Rodriguez-Rivera, D. L. Abernathy, T. M. McQueen, and C. L. Broholm. Molecular Quantum Magnetism in $LiZn_2Mo_3O_8$. *Phys. Rev. Lett.*, 112:027202, Jan 2014.

[65] D. R. Nelson. *Defects and geometry in condensed matter physics.* Cambridge University Press, 2002.

[66] David R. Nelson. Liquids and Glasses in Spaces of Incommensurate Curvature. *Phys. Rev. Lett.*, 50:982–985, Mar 1983.

[67] David R. Nelson. Order, frustration, and defects in liquids and glasses. *Phys. Rev. B*, 28:5515–5535, Nov 1983.

[68] MEJ Newman and GT Barkema. *Monte Carlo Methods in Statistical Physics.* Oxford University Press: New York, USA, 1999.

[69] Zohar Nussinov. Avoided phase transitions and glassy dynamics in geometrically frustrated systems and non-Abelian theories. *Phys. Rev. B*, 69:014208, Jan 2004.

[70] Zohar Nussinov, Joseph Rudnick, Steven A. Kivelson, and L. N. Chayes. Avoided critical behavior in $O(n)$ systems. *Phys. Rev. Lett.*, 83:472–475, Jul 1999.

[71] A. Olariu, P. Mendels, F. Bert, B. G. Ueland, P. Schiffer, R. F. Berger, and R. J. Cava. Unconventional Dynamics in Triangular Heisenberg Antiferromagnet $NaCrO_2$. *Phys. Rev. Lett.*, 97:167203, Oct 2006.

[72] Peter P. Orth, Premala Chandra, Piers Coleman, and Jörg Schmalian. Emergent Critical Phase and Ricci Flow in a 2D Frustrated Heisenberg Model. *Phys. Rev. Lett.*, 109:237205, Dec 2012.

[73] Peter P. Orth, Premala Chandra, Piers Coleman, and Jörg Schmalian. Emergent criticality and Friedan scaling in a two-dimensional frustrated Heisenberg antiferromagnet. *Phys. Rev. B*, 89:094417, Mar 2014.

[74] P. P. Soltan-Panahi, J. Struck, P. Hauke, A. Bick, W. Plenkers, G. Meineke, C. Becker, P. Windpassinger, M. Lewenstein, and K. Sengstock. Multi-component quantum gases in spin-dependent hexagonal lattices. *Nat. Phys.*, 7:434, 2011.

[75] A. M. Polyakov. Interaction of Goldstone particles in two dimensions. Applications to ferromagnets and massive Yang-Mills fields. *Phys. Lett. B*, 59(1):79, October 1975.

[76] A. M. Polyakov. *Gauge fields and strings*, volume 3 of *Contemporary concepts in physics*. Harwood Academic Publishers, Chur, Switzerland, 1987.

[77] Craig Price and Natalia B. Perkins. Finite-temperature phase diagram of the classical Kitaev-Heisenberg model. *Phys. Rev. B*, 88:024410, Jul 2013.

[78] Craig C. Price and Natalia B. Perkins. Critical Properties of the Kitaev-Heisenberg Model. *Phys. Rev. Lett.*, 109:187201, Nov 2012.

[79] T. Radu, H. Wilhelm, V. Yushankhai, D. Kovrizhin, R. Coldea, Z. Tylczynski, T. Lühmann, and F. Steglich. Bose-Einstein Condensation of Magnons in Cs_2CuCl_4. *Phys. Rev. Lett.*, 95:127202, Sep 2005.

[80] A. P. Ramirez. Strongly geometrically frustrated magnets. *Annu. Rev. Mater. Sci.*, 24:453, 1994.

[81] Michael Rubinstein and David R. Nelson. Dense-packed arrays on surfaces of constant negative curvature. *Phys. Rev. B*, 28:6377–6386, Dec 1983.

[82] S. Sachdev. *Quantum Phase Transitions*. Cambridge University Press, Cambridge, U.K., 1999.

[83] Subir Sachdev and David R. Nelson. Theory of the structure factor of metallic glasses. *Phys. Rev. Lett.*, 53:1947–1950, Nov 1984.

[84] Anders W Sandvik. Computational studies of quantum spin systems. *arXiv preprint arXiv:1101.3281*, 2011.

[85] François Sausset, Gilles Tarjus, and Pascal Viot. Tuning the Fragility of a Glass-Forming Liquid by Curving Space. *Phys. Rev. Lett.*, 101:155701, Oct 2008.

[86] François Sausset and Gilles Tarjus. Growing Static and Dynamic Length Scales in a Glass-Forming Liquid. *Phys. Rev. Lett.*, 104:065701, Feb 2010.

[87] Guilhem Semerjian, Marco Tarzia, and Francesco Zamponi. Exact solution of the Bose-Hubbard model on the Bethe lattice. *Phys. Rev. B*, 80:014524, Jul 2009.

[88] J. P. Sheckelton, F. R. Foronda, LiDong Pan, C. Moir, R. D. McDonald, T. Lancaster, P. J. Baker, N. P. Armitage, T. Imai, S. J. Blundell, and T. M. McQueen. Local magnetism and spin correlations in the geometrically frustrated cluster magnet $LiZn_2Mo_3O_8$. *Phys. Rev. B*, 89:064407, Feb 2014.

[89] J. P. Sheckelton, J. R. Neilson, D. G. Soltan, and T. M. McQueen. Possible valence-bond condensation in the frustrated cluster magnet $LiZn_2Mo_3O_8$. *Nat. Mat.*, 11:493, 2012.

[90] E. Shender. Antiferromagnetic garnets with fluctuationally interacting sublattices. *Sov. Phys. JETP*, 56:178, 1982.

[91] Sophia R. Sklan and Christopher L. Henley. Nonplanar ground states of frustrated antiferromagnets on an octahedral lattice. *Phys. Rev. B*, 88:024407, Jul 2013.

[92] B. W. Southern and A. P. Young. Spin stiffness in frustrated antiferromagnets. *Phys. Rev. B*, 48:13170–13173, Nov 1993.

[93] Oleg A. Starykh, Wen Jin, and Andrey V. Chubukov. Phases of a Triangular-Lattice Antiferromagnet Near Saturation. *Phys. Rev. Lett.*, 113:087204, Aug 2014.

[94] J. Struck, C. Ölschläger, R. Le Targat, P. Soltan Panahi, A. Eckardt, M. Lewenstein, P. Windpassinger, and K. Sengstock. Quantum Simulation of Frustrated Classical Magnetism in Triangular Optical Lattices. *Science*, 333(6045):996–999, 2011.

[95] J. Struck, M. Weinberg, C. Ölschläger, P. Windpassinger, J. Simonet, K. Sengstock, R. Höppner, P. Hauke, A. Eckardt, M. Lewenstein, and L. Mathey. Engineering Ising-XY spin-models in a triangular lattice using tunable artificial gauge fields. *Nat. Phys.*, 9:738, 2013.

[96] Y Taguchi, Y Oohara, H Yoshizawa, N Nagaosa, and Y Tokura. Spin chirality, Berry phase, and anomalous Hall effect in a frustrated ferromagnet. *Science*, 291(5513):2573–2576, 2001.

[97] G Tarjus, S A Kivelson, Z Nussinov, and P Viot. The frustration-based approach of supercooled liquids and the glass transition: a review and critical assessment. *Journal of Physics: Condensed Matter*, 17(50):R1143, 2005.

[98] L. Tarruell, D. Greif, T. Uehlinger, G. Jotzu, and T. Esslinger. Creating, moving and merging Dirac points with a Fermi gas in a tunable honeycomb lattice. *Nature (London)*, 483:302, 2012.

[99] I. Terasaki, Y. Sasago, and K. Uchinokura. Large thermoelectric power in $NaCo_2O_4$ single crystals. *Phys. Rev. B*, 56:R12685–R12687, Nov 1997.

[100] M. F. Thorpe. Bethe lattices. *Excitations in Disordered Systems NATO Advanced Study Institute Series B78 , 85–107*, 1982.

[101] L. Viciu, Q. Huang, E. Morosan, H.W. Zandbergen, N.I. Greenbaum, T. McQueen, and R.J. Cava. Structure and basic magnetic properties of the honeycomb lattice compounds $Na_2Co_2TeO_6$ and $Na_3Co_2SbO_6$. *Journal of Solid State Chemistry*, 180(3):1060 – 1067, 2007.

[102] J. Villain. Order from Disorder. *J. Phys France*, 38:385, 1977.

[103] Fa Wang and Ying Ran. Nearly flat band with Chern number $c = 2$ on the dice lattice. *Phys. Rev. B*, 84:241103, Dec 2011.

[104] G. H. Wannier. Antiferromagnetism. the triangular ising net. *Phys. Rev.*, 79:357–364, Jul 1950.

[105] Cédric Weber, Luca Capriotti, Grégoire Misguich, Federico Becca, Maged Elhajal, and Frédéric Mila. Ising Transition Driven by Frustration in a 2D Classical Model with Continuous Symmetry. *Phys. Rev. Lett.*, 91:177202, Oct 2003.

[106] Jeff Weeks. Curved spaces - software to visualize curved spaces.

[107] E. Witten. Anti De Sitter Space and Holography. *Adv.Theor.Math.Phys.* **2**, *253–291*, 1998.

[108] J. Zinn-Justin. *Quantum Field Theory and Critical Phenomena.* Oxford University Press, New York, NY, USA, 2002.